



KTH Electrical Engineering

Ultra Wideband: Communication and Localization

VIJAYA PARAMPALLI YAJNANARAYANA

Doctoral Thesis in Electrical Engineering
Stockholm, Sweden 2017

TRITA-EE 2016:184

ISSN 1653-5146

ISBN 978-91-7729-201-2

KTH, School of Electrical Engineering

Department of Signal Processing

SE-100 44 Stockholm

SWEDEN

Akademisk avhandling som med tillstånd av Kungl Tekniska högskolan framlägges till offentlig granskning för avläggande av teknologie doktorsexamen i Elektroteknik fredagen den 17 Februari 2017 klockan 13:00 i hörsal Q2, Osquldas väg 10, Stockholm.

© 2017 Vijaya Parampalli Yajnanarayana, unless otherwise noted.

Tryck: Universitetsservice US AB

To my daughter, Aditi

Abstract

Future communication networks will have seamless and ubiquitous connectivity among several communicating devices using different radio technologies. These devices could include cell phones, TVs, refrigerators, computers, tablets, etc. Key to this vision is low-power, low-cost and low-complexity transceivers. Ultra-wideband (UWB) has an unprecedented opportunity here to impact future communication technologies. The wide bandwidth of UWB enables innovative system designs to trade bandwidth efficiency for other merits such as device complexity, power consumption, etc. Large bandwidth also enables high precision localization and robust communication systems. In this thesis, we have focused on the signal processing aspects of UWB signals to aid communication and localization.

The first part of this thesis develops methods for UWB communication. The UWB transceivers employed in the sensor networks are typically made up of low cost hardware platforms. In order to meet the stringent regulatory body constraints, the physical layer signaling technique should be optimally designed. We propose two signaling schemes which are variants of pulse position modulation (PPM) signaling for impulse radio (IR) UWB communication. The constraints arising from the low cost hardware platform are considered along with the regulatory body requirements while developing the physical layer signaling for UWB. We also propose detectors for the signaling schemes and evaluate the performance of these detectors.

IR-UWB can be used for precise range measurements as it provides a very high time resolution. This enables accurate time of arrival (TOA) estimations from which precise range values can be derived. Utilizing the range information of the nodes in the network to aid UWB communication is not a well-studied problem. We propose methods which use range information to arrive at optimal schedules for an all-to-all broadcast problem. Results indicate that throughput can be increased on average by three to ten times for typical network configurations compared to the traditional methods. Next, we discuss hypothesis testing in the context of UWB transceivers. We show that, when multiple detector outputs from a hardware platform are available, fusing the results from them can yield better performance in hypothesis testing than relying on a single detector output. We propose a multi-detector UWB hardware platform and discuss different fusion techniques to fuse the detector outputs.

In the second part of this thesis, the emphasis is placed on localization and joint estimation of location and communication parameters. Here, we focus on estimating

the TOA of the signal. The wide bandwidth of the UWB signal requires high speed analog to digital converts (ADC) which makes the cost of the digital transceivers prohibitively high. To address this problem, we take two different strategies. In the first approach, we consider energy detectors operating at sub-Nyquist rates as they can be designed using cost effective analog circuits and are power efficient. However, they lack precision in range measurements. We propose a multichannel receiver with each channel having a low-cost energy detector operating at a sub-Nyquist rate. We show that the number of energy detector channels needed to meet the digital matched filter's performance is high at low signal to noise ratios (SNR) and reduces as SNR increases, and finally converges to four as SNR increases asymptotically. We also show that a Kalman filter with suitable choice of state and measurement equations can perform the dual task of tracking the TOA as well as fusing the multiple energy detector outputs. In the second approach, we consider a compressive sampling based technique. Here, we propose a new acquisition front end, using which the sampling rate of the ADC can be significantly reduced. Two TOA estimation algorithms are proposed which can operate on the sub-Nyquist samples to estimate TOA. Results indicate that the performance can match the maximum likelihood (ML) based TOA estimation with only 1/4-th the sampling rate. Also, we show that performance at low SNRs can be improved by using the a-priori information from channel and geographical constraints of the target.

We extended the idea of compressive sampling based TOA estimation towards joint estimation of TOA and PPM symbols. Here, two signaling methods along with the algorithms are proposed based on the dynamicity of the target. They provide similar performance to the ML based estimation, however with a significant savings in the ADC resources.

Sammanfattning

Framtidens kommunikationsnätverk kommer att erbjuda användarvänlig och lättillgänglig kommunikation mellan olika enheter baserad på radioteknologi. Exempel på enheter som skulle kunna kommunicera är mobiltelefoner, TV-apparater, kylskåp, datorer, surfplattor, etc. Nyckeln till denna vision är billiga sändtagare med låg strömförbrukning och låg komplexitet. Ultra wideband radio (UWB) har här en unik chans att påverka framtida kommunikationsteknologier. Den breda bandbredden hos UWB möjliggör en innovativ systemdesign där den effektiva bandbredden kan vägas emot andra karakteriserande egenskaper såsom enhetskomplexitet, strömförbrukning, etc. En hög bandbredd möjliggör även lokalisering med hög precision och robusta kommunikationssystem. I denna avhandling har vi fokuserat på signalbehandlingsaspekter hos UWB-signaler som används för kommunikation och lokalisering.

Den första delen av avhandlingen utvecklar metoder för UWB-kommunikation. De UWB-sändtagare som används i sensornätverk är typiskt baserade på billiga hårdvaruplattformar. För att kunna möta stringenta regulativa spatiala krav så krävs en optimal design av signaltekniken i det fysiska skiktet. Vi föreslår två signalscheman som är varianter av pulspositionsmodulering (PPM) för impulsradio-baserad (IR) UWB-kommunikation. Under utvecklandet av signaltekniken för UWB i det fysiska skiktet tar vi hänsyn till både de restriktioner som följer av den billiga hårdvaruplattformen, samt regulativa spatiala krav. Vi föreslår även detektorer för signalschemana och utvärderar prestandan hos dessa detektorer.

IR-UWB kan tack vare sin höga tidsupplösning användas för avståndsmätning med hög precision. Detta möjliggör noggrann ankomsttidsestimering från vilken precisa avståndsvärden kan erhållas. Användandet av avståndsinformation från noder i nätverket för att stötta UWB-kommunikation är ett problem som tidigare inte fått mycket uppmärksamhet. Vi föreslår metoder som använder avståndsinformationen för att erhålla optimala scheman för ett alla-till-alla-sändningsproblem. Resultatet indikerar att genomströmningen kan ökas med i genomsnitt tre till tio gånger för typiska nätverkskonfigurationer jämfört med traditionella metoder. Därefter diskuterar vi hypotesprövning för UWB sändtagare. Vi visar att när utdata från multipla detektorer är tillgänglig från en hårdvaruplattform så kan man genom att sammanfoga resultat från dessa detektorer erhålla bättre prestanda under hypotesprövning än när man förlitar sig på utdata från endast en detektor. Vi föreslår en multidetektor-UWB-hårdvaruplattform och diskuterar olika tekniker för att sam-

manfoga utdata från detektorerna.

I den andra delen av denna handling så ligger tyngdpunkten på lokalisering och gemensam estimering av lokaliserings- och kommunikationsparametrar. Vi fokuserar på att estimerar signalens ankomsttid. Den bredda bandbredden hos UWB signalen kräver analog-till-digital-omvandlare med hög hastighet vilket innebär att kostnaden för de digitala sändtagarna verkar begränsande. Två strategier presenteras för att lösa detta problem. I den första metoden studerar vi energidetektorer som implementeras med en sub-Nyquist frekvens, eftersom de är energisnåla och kan designas med hjälp av kostnadseffektiva analoga kretsar. De saknar dock precision i avståndsmätningarna. Vi föreslår en multikanal-mottagare där varje kanal har en lågkostnads-energidetektor implementerad med en sub-Nyquist frekvens. Vi visar att antalet kanaler för energidetektorer som behövs för att uppnå prestandan hos digitala matchade filter är hög vid låga signal-brusförhållanden, minskar då signal-brusförhållandet ökar, och slutligen konvergerar mot fyra då signal-brusförhållandet ökar asymptotiskt. Vi visar även att ett Kalmanfilter med ett lämpligt val av tillstånds- och mättekvationer kan både estimerar ankomsttiden och sammanfoga utdatat från de multipla energidetektorerna. I den andra metoden studerar vi tekniker baserade på komprimerad sampling. Vi föreslår en ny anskaffningsfront, med vilken samplingsfrekvensen hos analog-till-digital-omvandlaren kan minskas betydligt. Två algoritmer för ankomsttidsestimering som kan appliceras på sub-Nyquist samples föreslås. Resultat indikerar att prestandan matchar maximum likelihood (ML)-baserad ankomsttidsestimering med endast en fjärdedel av dess samplingsfrekvens. Dessutom så visar vi att prestandan vid låga signal-brusförhållanden kan förbättras genom att använda a priori-information från kanalen och geografiska bivillkor på målenheten.

Vi utvidgar idén om ankomstestimering baserad på komprimerad sampling till gemensam estimering av ankomsttid och PPM-symboler. Två signaleringsmetoder med respektive algoritmer föreslås baserat på målenhetens dynamik. Dessa tillhandahåller liknande prestanda som ML-baserad estimering, men med betydande besparingar av analog-till-digital-omvandlarens resurser.

Acknowledgments

First and foremost, I am grateful to my advisor Prof. Peter Händel for providing me with an opportunity to work in the Department of Signal Processing at KTH. I am thankful for all the freedom he gave me to explore various research topics. Despite his busy schedule, he was always available for discussion. Most of all, I was always impressed with the feedback from him on my papers. He always had new and interesting perspectives on them which helped me to improve the current work and derive new ideas for future research. I am also thankful to my co-advisor, Dr. Satyam Dwivedi for his guidance and support. Interactions and discussions I had with him were extremely helpful.

I have been fortunate to collaborate with brilliant colleagues like Dr. Klas Magnusson, Dr. Rasmus Brandt, and Dr. Alessio De Angelis for my research papers. Many thanks for working with me. I also want to thank Dr. Jeffrey Larson and Dr. Saikat Chatterjee for teaching convex optimization and sparse signal processing. These topics helped me a lot in my research.

I am grateful to Zaki Ahmed, Per Johanesson and Britta Johanesson for all the practical help they provided, particularly during the difficult year of 2013. I am thankful to Per and Britta for those wonderful trips, snacks, parties, etc., and the hospitality they extended when my family visited Sweden. Many thanks to Zaki for those delightful discussions in the cafe. I also would like to thank Marie, Arun, Pol, Nima, and Ahti for proof reading the thesis and Johan for the Swedish translation of the abstract. I would like to thank Prof. Mikael Skoglund for performing the quality check of the thesis. Many thanks to Tove Schwartz for assistance in administrative affairs.

I wish to thank Prof. Andreas Springer of Johannes Kepler University (JKU), Linz, Austria, for taking time to act as opponent to this thesis. I also thank Prof. Ana Rusu, Associate Prof. Henk Wymeersch, and Dr. Bo Göransson for taking part in the grading committee.

I would like to express my deepest gratitude to my mother Prema and my father P.Y. Aithal for their love and support. Finally, many thanks to my beloved wife Pavithra, for her ever patient approach to life, and my bundle of joy, Aditi, for giving a new perspective to life every time.

Vijaya Yajnanarayana
Stockholm, February 2017

Contents

Contents	xi
Nomenclature	xv
List of Figures	xix
1 Introduction	1
1.1 What is UWB?	1
1.2 History of UWB	3
1.3 UWB Characteristics	4
1.4 Applications	7
1.5 Commercial UWB systems	8
1.6 UWB Research at KTH	9
1.7 Motivations and Objectives	11
1.8 Thesis Outline and Contribution	13
2 Preliminaries	19
2.1 Detection Theory	19
2.2 Estimation Theory	20
2.3 Convex Optimization	23
2.4 Traveling Salesman Problem	24
2.5 Algorithm Complexity	25
2.6 Sparse Signal Processing	25
3 Hardware Aware IR-UWB signaling	29
3.1 Background	29
3.2 Pulse Construction and System Model	32
3.3 UWB Constraints	34
3.4 UWB Hardware	36
3.5 Modulator	36
3.6 Detector Performance	42
3.7 Conclusion	49

4	Location Aided UWB Communication	51
4.1	Background	51
4.2	System Model and Problem Formulation	55
4.3	Algorithms	60
4.4	Effect of Synchronization and Range errors	68
4.5	Comparison with CDMA systems	70
4.6	Simulation Study	72
4.7	Conclusion	78
4.A	Proof that nodes $i - 1$ and $i + 1$ do not interfere in the convex problem	80
4.B	Average Complexity of IPA	81
5	Detection and Fusion techniques for IR-UWB transceivers	83
5.1	Background	83
5.2	System Model	87
5.3	Detector Performance	89
5.4	Fusion Rules for IR-UWB Signal Detection	93
5.5	Performance Evaluation of Fusion Methods	96
5.6	Conclusion	98
5.A	Performance of Matched Filter	99
5.B	Performance of Energy Detector	101
5.C	Performance of Amplitude Detector	104
6	UWB TOA Estimation using Kalman filter	107
6.1	Background	107
6.2	Model	109
6.3	Detectors	111
6.4	AWGN Channel Analysis	113
6.5	Multipath Channel Analysis	117
6.6	Multi detector Fusion Using Kalman Filter	120
6.7	Simulation Study	122
6.8	Conclusion	125
7	Compressive Sampling Based UWB TOA Estimator	129
7.1	Background	129
7.2	Signal Model	132
7.3	ML based TOA estimation	133
7.4	UWB Channels	134
7.5	Sparse representation of UWB signal	136
7.6	Method for sub-Nyquist TOA Estimation	137
7.7	Simulation Study	139
7.8	Conclusions	144
8	Compressive Sampling Based Joint PPM and TOA Estimator	147

8.1	Background	147
8.2	System Model	148
8.3	Sub-Nyquist TOA Estimator	149
8.4	Joint TOA and PPM Symbol Estimation	149
8.5	Numerical Results	154
8.6	Conclusions	156
9	Summary and Future Research	157
9.1	Conclusions	157
9.2	Future Research	159
	Bibliography	161

Nomenclature

Abbreviations and Acronyms

UWB	Ultra-Wideband
IR-UWB	Impulse Radio UWB
GSM	Global System for Mobile Communications
LTE	Long-Term Evolution
3G	Third Generation
RF	Radio Frequency
FCC	Federal Communications Commission
mmWave	milli-meter wave
OFDM	Orthogonal Frequency Division Multiplexing
MC	Multi-Carrier
SS	Spread Spectrum
IR	Impulse Radio
LOS	Line of Sight
NLOS	Non Line of Sight
PSD	Power Spectral density
FFT	Fast Fourier Transform
GPS	Global Positioning Systems
SNR	Signal to Noise Ratio
WSN	Wireless Sensor Networks
EIRP	Effective Isotropically Radiated Power
ENT	Ear Nose Throat
FPGA	Field Programmable Gate Array
SPI	Serial Peripheral Interface
TDC	Time to Digital Conversion
SER	Symbol Error Rate
TOA	Time of Arrival

TDOA	Time Difference of Arrival
AWGN	Additive White Gaussian Noise
PDF	Probability Density Function
MAP	Maximum a Posteriori probability
MSE	Mean of the Squared Error
CRLB	Cramer-Rao Lower Bound
NP	Non-deterministic Polynomial-time
LKH	Lin-Kernighan heuristic
BPDN	Basis Pursuit Denoising
OMP	Orthogonal Matching Pursuit
USB	Universal Serial Bus
wUSB	wireless USB
IEEE	Institute of Electrical and Electronics Engineers
TH	Time-Hopping
IID	Independent and Identically Distributed
LNA	Low Noise Amplifier
BPF	Band Pass Filter
ADC	Analog to Digital Converter

Notations

x	Scalar variable
\mathbf{x}	Vector variable
$\ \mathbf{x}\ _p$	p -norm of \mathbf{x}
\mathbb{R}^N	N -dimensional real field
\mathbb{C}^N	N -dimensional complex field
$\ \mathbf{x}\ $	2-norm of \mathbf{x}
\mathbf{A}	Matrix variable
\mathbf{A}^{-1}	Matrix Inverse of \mathbf{A}
$[\mathbf{A}]_{i,j}$	Element corresponding to i row and j column
\mathbf{A}^T	Matrix transpose
\mathbf{A}^*	Conjugate transpose
\mathbf{A}^\dagger	Pseudo inverse
$\Pr(\mathcal{E})$	Probability of the event \mathcal{E}
$p(x)$	PDF of x
$\mathcal{N}(\boldsymbol{\mu}, \mathbf{C})$	Gaussian distribution with mean, $\boldsymbol{\mu}$ and covariance, \mathbf{C}
$\mathbb{E}[\cdot]$	Expectation of a random variable
$\text{Var}[\cdot]$	Variance of a random variable
$\{a, b, c\}$	Set with elements a , b and c
$[a, b]$	Closed interval between a and b
(a, b)	Open interval between a and b
$\mathcal{O}(\cdot)$	Big-O notation
$\mathbf{A}_{\mathcal{I}}$	Matrix formed by choosing the columns from support set \mathcal{I}
$\mathbf{Q}(\cdot)$	Tail Probability of standard normal function
$\mathbf{Q}_{\chi^2_\nu(\lambda)}(\cdot)$	Tail probability of the non-central chi-square distribution
$\arg \max$	The argument that achieves maximum

List of Figures

1.1	Spectral mask specified by FCC showing the equivalent isotropic radiated power (EIRP) versus frequency for indoor UWB system. . .	2
1.2	Illustration of Saleh-Valenzuela channel model.	6
1.3	UWB communication and localization applications.	9
1.4	UWB medical applications. Reproduced with permission from authors of [CSB14].	10
1.5	In-house UWB hardware platform [ADH13].	12
1.6	Schematic overview of the technical chapters presented in the thesis.	17
2.1	A convex function.	23
2.2	A convex set.	24
2.3	Role of l_1 -norm in sparse estimation.	26
3.1	Iconic model of the in-house developed impulse radio UWB-platform.	30
3.2	System model consisting of transmitter, channel and receiver. . . .	34
3.3	Spectral mask specified by FCC showing the equivalent isotropic radiated power (EIRP) versus frequency for indoor UWB system. .	35
3.4	Train of pulses with randomized pulse interval and its PSD.	37
3.5	An illustration of no-memory signaling.	38
3.6	Choice of optimal modulation parameter for no-memory signaling. .	39
3.7	No-memory signaling and its PSD.	39
3.8	An illustration of with-memory signaling.	41
3.9	With-memory signaling and its PSD.	43
3.10	Quantized time bins used by the hard decision detector.	43
3.11	Comparison of theoretical and simulation performance in terms of SER for hard decision detection based demodulator for the no-memory signaling.	45
3.12	Comparison of performance of no-memory and with-memory signaling in terms of SER.	47
4.1	Illustration of fire fighters agents sharing information continuously with other agents [NZSH13].	54

4.2	A graphical illustration of a geometric configuration of a swarm network of micro quadcopters.	55
4.3	Peer-to-peer ad-hoc sensor network with 3 nodes. d_{AB} , d_{BC} and d_{CA} are the path lengths between nodes A , B and C	56
4.4	Concurrent transmission on a shared common channel without scheduling.	57
4.5	Messages from node i and j arriving at node k	61
4.6	The cyclic TSP solution and the 3 possible linear orders for a 3-node network.	62
4.7	Iteration 1 for the 3 node network shown in Figure 4.3 with the configuration defined in Table 4.1.	66
4.8	Iteration 2 for the 3 node network shown in Figure 4.3 with the configuration defined in Table 4.1.	66
4.9	Two distinct 3-node configurations.	68
4.10	Network geometry with 6 nodes scattered randomly in a 2-D plane and plots of message packets arrival to them.	70
4.11	Performance of proposed methods as a function of N for no outliers configuration.	73
4.12	Performance of proposed methods as a function of N for no outliers configuration with nodes far-apart.	74
4.13	Bitrate per sensor, R_s , of proposed methods and CDMA approach as a function of N . Notice that the proposed methods yield better performance relative to CDMA.	75
4.14	Network geometry with 6 nodes scattered randomly in a 2-D plane and plots of message packets arrival to them for network with few nodes as outliers	77
4.15	Performance of proposed methods as a function of N for with few nodes as outliers.	79
4.16	Effect of proposed methods due to imprecise range and clock jitter.	80
4.17	The 3rd order polynomial fit to the average complexity curve, along with the residual error for the various order polynomial fit.	81
5.1	Depiction of direct sampling receiver architecture with multi detector fusion.	86
5.2	Transmit signal structure constitutes of N_T transmit frames.	87
5.3	Generic detector structure.	90
5.4	Detection performance at various SNRs and ROC for a matched filter detector.	91
5.5	Detection performance at various SNRs and ROC for the energy detector.	92
5.6	Detection performance at various SNRs and ROC for the amplitude detector.	94
5.7	Depiction of different decision fusion methods.	94
5.8	The performance of different detectors in theory and simulation.	97

5.9	Probability of detection and error performance for various fusion techniques using the configuration defined in Table 5.2.	98
5.10	Probability of detection and error performance using the fusion rule defined in (5.4.8) (MAP fusion), OR Fusion and ED decision alone without any fusion using the configuration defined in Table 5.2. . . .	98
6.1	Joint fusion and tracking structure using multi-channel receiver. . .	109
6.2	Variation of energy samples, x_n , verses block index, n . Parameters $T_f = 200$ ns, $T_b = 1$ ns, SNR = 0 dB and $N_{\text{obs}} = 200$ are considered.	113
6.3	Variation of MSE with SNR for a single channel energy detector and matched filter based receivers. MSE is evaluated by averaging the estimated TOA for 1000 random τ_{toa} drawn from $\mathcal{U}[0, T_f = 200 \text{ ns}]$. Matched filter asymptotically reaches the CRLB bound.	115
6.4	Variation of MSE with SNR for single channel energy detector. . . .	117
6.5	Averaged channel energy profile for 802.15.4a CM1 channel model. 100 different channel realizations are averaged.	118
6.6	Fusion of multiple detector estimates for a dynamic TOA model using Kalman filter.	119
6.7	Variation of MSE with time for the TOA estimates of digital matched filter and multi-channel sub-Nyquist energy detector based receiver (N indicates number of channels).	121
6.8	Steady state MSE verses time, for digital matched filter and multi-channel energy detector receivers (N indicates number of channels).	123
6.9	Number of sub-Nyquist energy detector channels need to match the performance of matched filter operating at Nyquist rate.	124
6.10	Variation of MSE with time for IEEE 802.14.4a CM1 channel model for digital matched filter and multi-channel energy detector receivers.	125
6.11	Steady state MSE verses time for IEEE 802.14.4a CM1 channel model, for digital matched filter and multi-channel energy detector based receivers.	126
6.12	Energy of the samples used in the TOA estimation for digital matched filter and multi-channel receivers.	127
7.1	The PMF and PDF of λ and τ_{pld} respectively for IEEE 802.15.4a CM1 model.	135
7.2	Block diagram of the compressive sampling (CS) system for TOA estimation.	136
7.3	The block diagram of the simulation bed for the performance evaluation of TOA estimation algorithms.	140
7.4	The performance of the proposed method with number of paths searched, K , and under-sampling ratio, \mathcal{U}	141
7.5	The Performance of the proposed and ML based TOA estimation algorithms at various acquisition frequencies.	142

7.6	Performance of the proposed and ML based TOA estimation algorithms using various dictionaries.	143
7.7	Performance comparison of the proposed algorithms in the presence of <i>a priori</i> information.	144
8.1	Block diagram of the compressive sampling (CS) system for TOA estimation. The $\beta_i(t), i = 1, \dots, M$, denotes the continuous time i.i.d normal processes with zero mean and unit variance.	149
8.2	Transmit signal for the proposed Algorithm 8.1. The T_d is the delay spread of the channel and Δ is the PPM modulation index (width of the PPM-bins).	151
8.3	Transmit signal for the proposed Algorithm 8.2. The T_d is the delay spread of the channel, Δ is the PPM modulation index (width of the PPM-bins) and $N_b = 1$ is considered.	153
8.4	The performance of Algorithm 8.1 and ML method at various SNRs. For ML estimation, sampling rate of $F_s = 8$ GHz is employed. For compressive sampling algorithm sampling rates of $F_u = 2$ GHz, and 1 GHz are employed. The $\Lambda = T_s$	155
8.5	The performance of Algorithm 8.2 and ML method at various SNRs. For ML estimation, the sampling rate of $F_s = 8$ GHz is employed. . .	156

Introduction

In the year 2021, it is predicted that there will be 15 billion devices that will be connected. While some of the devices will be cellular, a large part will use other radio technologies [ER15]. In this context, ultra-wideband (UWB) technology, has an unprecedented opportunity to impact communication systems.

The radio technologies for communication systems generally employ a non-overlapping radio frequency (RF) spectrum. That is, every radio technology like GSM, 3G, LTE, Bluetooth etc., uses a distinct RF spectrum. A typical UWB system employs a large bandwidth. In the 0 – 10 GHz band, there are several radio technologies, and several new ones are emerging. As a result, RF spectrum is becoming more premium and more scarce. Communication systems using UWB offer a promising solution in this band as they can co-exist with other radio technologies sharing the same RF band. Regulatory bodies impose stringent emission requirements to prevent the UWB signals interfering with other radio technologies. Another interesting development is the availability of the mmWave spectrum without stringent emission requirements. This has benefited the evolution of UWB technology in the 30 – 80 GHz spectrum.

1.1 What is UWB?

There are multiple definitions for a UWB signal. Most of the definitions on what can be construed as UWB signal depends on the spectrum regulatory bodies. The federal communications commission (FCC) defines the UWB signal as a signal which meets at least one of the following criteria:

- The 10 dB fractional bandwidth is greater than 0.20.
- The 10 dB bandwidth is equal to or greater than 0.5 GHz, regardless of the fractional bandwidth.

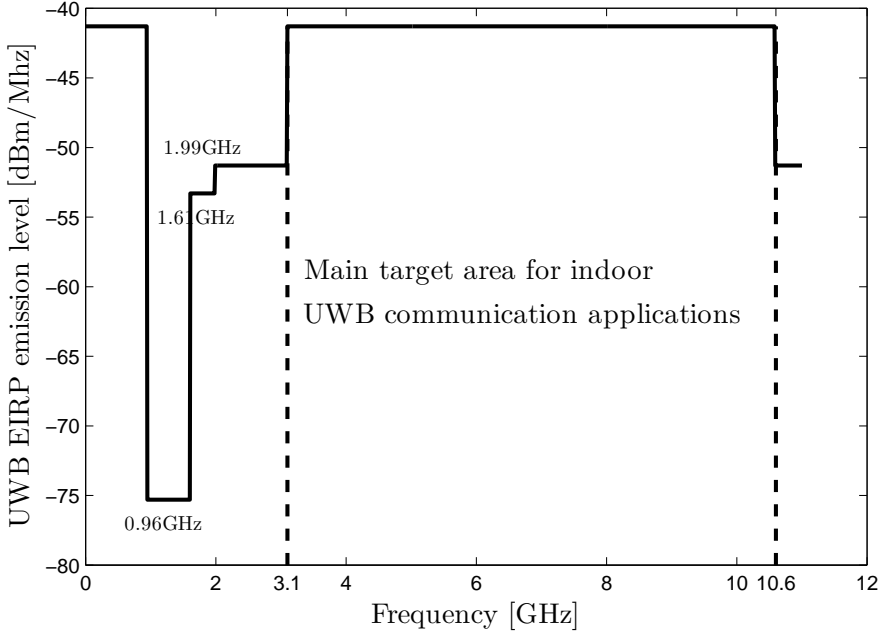


Figure 1.1: Spectral mask specified by FCC showing the equivalent isotropic radiated power (EIRP) versus frequency for indoor UWB system.

The fractional bandwidth of a signal provides the signal bandwidth in relation to the carrier frequency. It is defined as

$$\frac{2(F_H - F_L)}{(F_H + F_L)}, \quad (1.1.1)$$

where F_H and F_L indicate the highest and lowest frequency component of the transmitted UWB signal, respectively.

The wide bandwidth used by the UWB signals can overlap with other radio technologies. Thus, the regulatory bodies impose very stringent constraints on the UWB emissions in order to protect the victim receivers. These are specified through spectral masks which are generally defined for the 0 – 10 GHz band. Although there exist multiple emission norms for UWB signals, here we concentrate on FCC regulations. This is due to the fact that most of the other definitions are derived from the FCC rules, and these regulations are the most popular regulations for UWB. The FCC regulations are defined in [FCC02].

FCC regulations control the UWB emissions through the constraints on maximal average power P_{av} , and maximal peak power P_{pk} . The average power, P_{av}

is measured using a spectrum analyzer with resolution bandwidth (RBW) $B_{av} = 1$ MHz. Maximal average power constraints are specified through spectral masks. The Figure 1.1 shows the FCC mandated spectral mask for indoor UWB emissions. P_{pk} should not exceed 0 dBm when measured using a spectrum analyzer with RBW set to 50 MHz.

The availability of unlicensed mmWave spectrum has brought renewed interest in UWB technology. The mmWave signals have a frequency range that goes from 30 GHz to 300 GHz. More bandwidth is available at these frequencies compared to 0 – 10 GHz. The UWB emissions in the unlicensed mmWave spectrum do not have stringent emission norms due to the higher oxygen absorption which limits the long-distance interference to the other devices. For example, FCC allows the devices to transmit power up to 10 W in the 57 – 64 GHz band [Nag07].

1.2 History of UWB

The first wireless communication involved spark gap transmission experiments conducted by Marconi and Hertz in the late 1890s. The bandwidth consumed by these experiments was huge and can be considered as ultra wideband communication. This experimental setup can be considered as a crude form of impulse radio system¹. Marconi employed this method to transmit Morse code sequences across the Atlantic ocean.

Even though wireless communications started with ultra wideband transmissions, there were many challenges ranging from electronic components to antenna design to make this a prominent transmission technique at the time. These technological limitations pushed wireless communications toward carrier modulated narrowband signals. The carrier frequencies employed were typically several orders of magnitude larger than the signal bandwidth itself.

Developments in areas such as measurement technology helped the evolution of UWB technology. For example, impulse measurement techniques which can be used to characterize the transient behavior of the microwave networks required small sub-nanosecond pulses. This led to the development of circuits to generate sub-nanosecond pulses in 1960s [MG07]. The requirements for electronic warfare further developed UWB technology. This resulted in utilizing the pulse generation techniques for applications such as radar devices, to enable higher spatial resolution for the radars.

The first patent for UWB wireless communication was filed in 1973 [Ros73]. Here the authors envisaged the development of a transceiver for short-range wireless communications without licensing. The idea was too advanced for that time, as there were several hurdles to adopting the proposed idea. These included the electronic components that can operate at such large bandwidths. For the next few decades, narrowband signals dominated the communication landscape.

¹Impulse radio is a particular flavor of UWB which uses extremely short impulse like pulses.

At the end of the 20th century, the first impulse radio proposal was made in the seminal paper of Win and Scholtz [WS98]. This triggered much interest in academia and industry, as the spectrum in the 0 – 10 GHz band was crowded and UWB was a potential technology which could coexist with the existing spectral bands. Around the same time in 2002, the FCC part 15 ruling allowing unlicensed usage furthered the interest in the technology. However, much of the action in the area died down due to challenges in the development of cost effective radio which could satisfy the spectrum regulatory bodies' stringent requirements.

Due to the development in the electronic technology and evolution of the signal processing methods, today cost effective UWB radios can be designed which satisfy the stringent requirements of the spectrum regulatory bodies. Coupled with this, the availability of the unlicensed mmWave spectrum for UWB with less stringent requirements has renewed interest in the UWB technology. This thesis, among other things, also focuses on the signal processing methods, to further the progress in this area.

1.3 UWB Characteristics

1.3.1 Multi-carrier UWB schemes

There are many ways to generate UWB signals. One approach is to combine the spread spectrum (SS) and multi-carrier (MC) techniques. Here the incoming data is spread using different spreading codes and up-converted on to different frequencies [PH96]. Another approach is to use multi-band orthogonal frequency division multiplexing (OFDM), where an OFDM signal is produced with approximately 528 MHz bands. The multi-carrier techniques have increased complexity and require several mixers or digital fast Fourier transform (FFT) to place the different signal components in the required frequencies [BKM⁺06]. As a result of these disadvantages, multi-carrier techniques are rarely used for UWB.

1.3.2 Impulse radio UWB schemes

Impulse radio UWB (IR-UWB) systems employ discontinuous pulses for transmission. These pulses are extremely narrow and occupy a wide bandwidth. Since these narrow pulses are only few nano-seconds wide (impulse like), the system is called IR-UWB. In these systems the information can be embedded in the position, forming a pulse position modulated (PPM) signaling scheme, or in amplitude forming pulse amplitude modulated (PAM) signaling schemes. A typical transmitted symbol is spread over N pulses. This provides a processing gain similar to spread spectrum techniques. The typical duty cycle of the pulses used is very low and therefore, the receivers only need to “listen” to the channel for a small fraction of the period between pulses. This can reduce the interference from the continuous source as it is only relevant when the receiver is attempting to detect a pulse [BKM⁺06].

Many pulse shapes have been explored in IR-UWB research, and commonly employed pulse shapes include Gaussian, Laplacian, and Hermitean [MGK02]. However, in practice it is difficult to generate these shapes in hardware. In many UWB systems, the generated pulse shape can be approximated to a Gaussian doublet. In these systems, a square pulse is generated by turning the diode on and off, which leads to a pulse shape which is not rectangular but with its edges smoothed off. This happens due to the imperfect doping of the diode, antenna effects, etc. The resulting shape generated can be approximated by a Gaussian shape.

Even though the methods and algorithms discussed in this thesis can be extended to other UWB techniques, our primary focus is on IR-UWB based communication and localization systems.

1.3.3 Propagation characteristics

There are two common approaches that are generally taken to define the propagation characteristics of the UWB signals. The first method is called the *deterministic approach*. Here, first the obstacles' geometric shape, type and its electro-magnetic (EM) properties in the propagation environment are defined. Subsequently, the channel response can be arrived at by using EM simulation tools via ray-tracing techniques [YGCZ03, YZC03, SGI08]. This technique has several disadvantages as it is site-specific and also, when the environment changes, the channel model becomes useless. To overcome this, one can make actual channel measurements for common types of channels, like indoor line of sight (LOS), indoor non-LOS (NLOS), industrial LOS, etc. and derive a statistical model from the measurements. This type of channel modeling is called *statistical channel modeling* and many popular IEEE UWB standards use this form of channel modeling.

One of the most widely used statistical channel models for indoor propagation was proposed by Saleh and Valenzuela [SV87]. This model is adopted in IEEE 802.15.4a CM1 standard for providing a stochastic channel model for various UWB environments [MCC⁺04, Mol05]. As per this model, the discrete-time impulse response of the UWB channel has clusters that follow Poisson arrival with parameter, Λ , and the multipath components (MPCs) within the cluster follow a Laplacian distribution with parameter λ . The mean cluster energy decays exponentially with parameter Γ . The choice of Λ , λ and Γ defines various UWB propagation environments. A pictorial representation of this model is shown in Figure 1.2.

A model with C clusters having R rays (MPCs) can be mathematically expressed as

$$h(t) = \sum_{i=1}^C \sum_{j=1}^R a_{i,j} \delta(t - T_i - \gamma_{i,j}), \quad (1.3.1)$$

where, T_i represents the arrival time of the i -th cluster and $\gamma_{i,j}$ represents the time duration of the j -th ray in the i -th cluster in relation to T_i . Note that by definition $\gamma_{i,1} = 0$ and T_1 denotes the arrival time of the first ray of the first cluster.

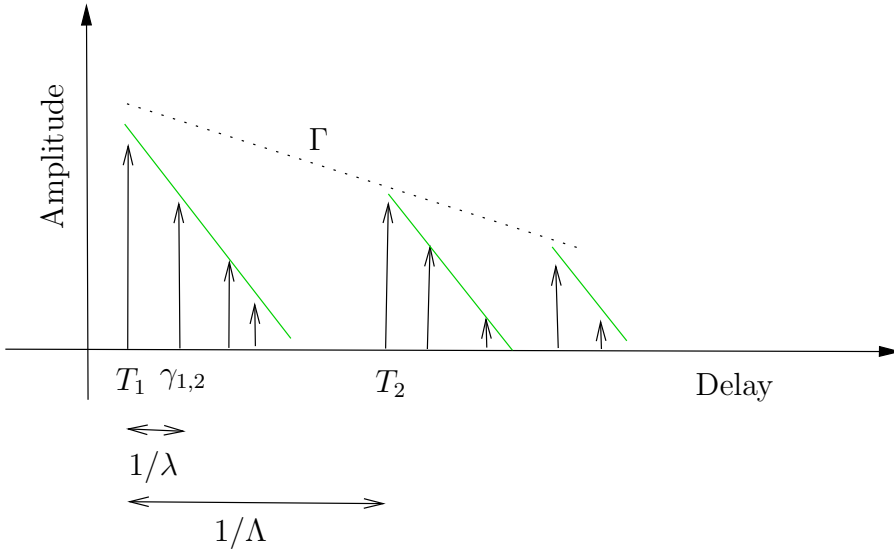


Figure 1.2: Illustration of Saleh-Valenzuela channel model.

1.3.4 Standardization

In this section, we will briefly describe the standardization activities in the area of the UWB communication. There are two main standards that have emerged from IEEE standards group. The IEEE 802.15.3a, which caters to high data rate applications and the IEEE 802.15.4a, which caters to low data rate applications.

IEEE 802.15.3a

The primary goal of this standard was to develop a UWB physical layer (PHY) standard to cater to high rate applications. The applications envisaged by the task group included, among other things, cable-less media transfer, imaging, and multi-media streaming. The main goal was to provide a short range, high speed, alternate PHY for the existing IEEE 802.15.3 medium access control (MAC) standard. The primary work of this standard committee included the development of the channel model which can be used for UWB system evaluation. The standard supported 110 Mbps up to 10m and used OFDM technology [BKM⁺06].

IEEE 802.15.4a

The primary goal of this standard was to develop a UWB standard to cater to low rate applications. The potential applications included wireless sensor networks,

home automation, etc. The IEEE 802.15.4a TG4 group, which studied the requirements for the low rate UWB applications, provided standard channel models for various low rate environments like indoor LOS, industry LOS, indoor NLOS, etc. These models are one of the most popular ways to evaluate the UWB systems. There is also a non-IEEE standards group called multiband OFDM alliance (MBOA), which is an alliance of academia and industry, for UWB based on OFDM techniques. The IEEE 802.15.3a group is not active. In this thesis, the proposed methods are evaluated in the context of the IEEE 802.15.4a standard to demonstrate their benefits.

1.4 Applications

There are several applications for UWB technology, primarily in the area of localization, communication and medicine.

1.4.1 UWB in Localization

The development of global positioning systems (GPS) has revolutionized positioning and tracking technology. However, indoor environments still pose significant challenges for GPS systems. This is because the complex physical characteristics of the environments, such as walls, windows, etc., pose a significant obstacle in decoding the satellite signals. A typical GPS signal occupies a bandwidth of only 2 MHz, resulting in overlapped MPCs. This makes it extremely difficult to accurately measure the time of arrival (TOA) from the satellites, especially in harsh indoor environments.

Range estimates are crucial for localization, as location information can be derived from the range values from multiple anchors using triangulation. Accurate range estimates are typically obtained by using TOA methods. The best performance in terms of mean-square-error (MSE) for an unbiased estimator is given by the Cramer-Rao lower bound (CRLB) and for a time of arrival (TOA) estimation problem this is given by [GTG⁺05, DCW08]:

$$\sigma_{\tau}^2 \geq \frac{1}{8\pi^2 \text{SNR} \beta^2}, \quad (1.4.1)$$

where, β is the effective signal bandwidth defined by

$$\beta^2 = \left[\frac{\int_{-\infty}^{\infty} f^2 |S(f)|^2 df}{\int_{-\infty}^{\infty} |S(f)|^2 df} \right], \quad (1.4.2)$$

where $S(f)$ is the Fourier transform of the transmit pulse $s(t)$. Since UWB uses extremely large bandwidths with very high time resolution, they can be used for precise range estimation. Therefore UWB is a good candidate for indoor localization and can provide the high level of position accuracy required for indoor positioning. This has also enabled several applications in the area of inventory tracking, assisted living and intelligent transportation systems.

1.4.2 UWB in Communication

There are two application scenarios in which UWB can be used. They are as follows:

- Short range high data rate applications.
- Long range low data rate applications.

From the famous Shannon-Hartley theorem, the capacity of the system can be increased either by increasing the channel bandwidth or signal to noise ratio (SNR) or both. Since UWB systems employ wide bandwidths, it is possible to achieve high data rate. However, the transceiver, in order to be compliant with the spectrum regulatory bodies' emission requirements, needs to be of low power. This will limit the range of the wireless communication and thus, UWB is ideal for high-rate, low range applications. UWB can be used in wireless USB, multi-media streaming, machine-to-machine communication, etc.

UWB also provides flexibility to trade bandwidth with range, security, multi-user setup, etc. This can enable several low rate applications in wireless sensor networks (WSNs). The UWB signal has interesting propagation characteristics as it can penetrate well in harsh environments, making it an ideal candidate for search and rescue systems. Many systems such as first responder systems, intelligent transportation systems, etc. require both localization and communication. UWB, with its ability to provide robust data communication coupled with highly accurate localization capability, is an ideal candidate for these systems [NZSH13, RRS⁺11]. Figure 1.3 depicts a snapshot of potential UWB communication and localization applications.

1.4.3 UWB in Medicine

UWB's noise-like behavior with extremely low effective isotropically radiated power (ERIP) makes UWB signals useful for biomedical applications. UWB signals are commonly used in medical imaging and medical sensing. The UWB medical radar can be used for monitoring cardiac motion, blood pressure, the respiratory system, etc. Typical medical imaging applications can include, for example, breast cancer detection and obstetrics imaging. The UWB is also used in intensive care units to monitor coma patients, to detect when they come out of the coma, so that much need medical attention can be provided when they wake up. The UWB signal's ability to provide accurate indoor localization can be used to monitor patients suffering from chronic disease. UWB can also be used for non-intrusive disease diagnosis of the ear-nose-throat (ENT) organs [CSB14]. Figure 1.4 shows a snapshot of various applications in which UWB signals can be employed.

1.5 Commercial UWB systems

Early commercial UWB systems including Ubisense and Timedomain used non-standard or custom made communication and localization solutions [Tdm16, Ubi16].

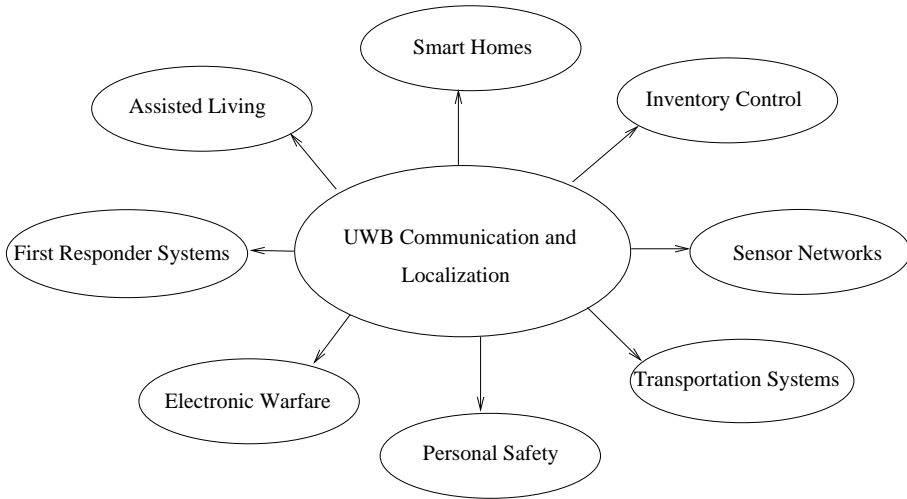


Figure 1.3: UWB communication and localization applications.

They used centralized architecture with anchors. These anchors are connected through cables and their locations are known. The transmitter tags which require localization are mounted on the targets such as a person, object, sensor, etc. The centralized anchors are capable of determining the ranges and bearings to transmitter tags using time difference of arrival (TDOA) and angle of arrival (AOA), respectively. The TDOA/AOA values from the anchor to the tags are used to localize the target.

The evolution of the IEEE 802.15.4 standard for UWB PHY enabled interoperability and made products future-proof. Companies like Bespoon, Decawave, etc., developed chip sets which can be used to design IEEE 802.15.4 standard-specific UWB products. Recent trend is to use these chipsets in the UWB system design. Some of these chip companies also are entering in to consumer market. For example, spoonphone from Bespoon is a full blown smartphone, packed with state-of-the-art sensors that will enable several smartphone applications which need precision localization [Com16a].

1.6 UWB Research at KTH

Extensive research on UWB communication and localization has been performed at the Department of Signal Processing, KTH, in Sweden. An in-house low cost UWB sensor hardware platform has been designed in the lab. The architecture of this platform is shown in Figure 1.5. The analog UWB measurement section is connected to the field-programmable gate array (FPGA) using a serial peripheral

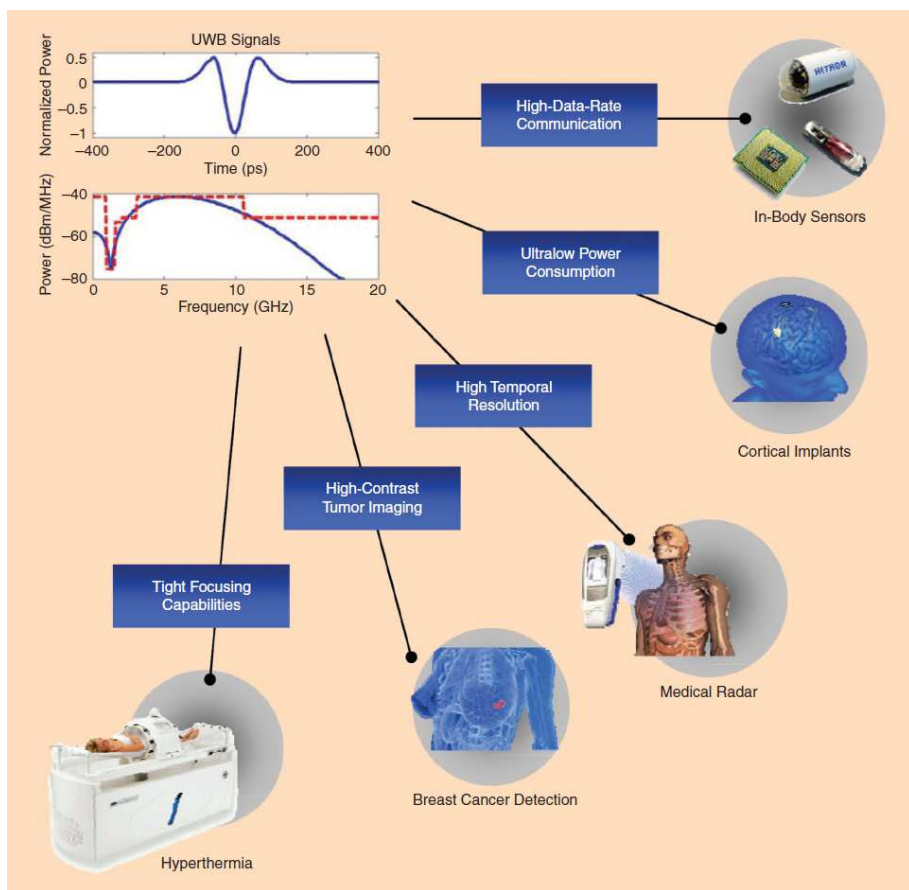


Figure 1.4: UWB medical applications. Reproduced with permission from authors of [CSB14].

interface (SPI). This architecture is based on time to digital conversion (TDC), which was originally designed for ranging round-trip time calculations. However, the same can be used to measure the time between the pulse intervals, thereby enabling demodulation of PPM signals and thus, it can also be used for UWB communication. The UWB transceiver has a pulse generator which is realized using a step-recovery diode, and is triggered by the start signal from the FPGA. The output of the energy detector, after being compared with the voltage threshold in the on-chip comparator, provides the stop signal for the TDC measurement. Further details of this UWB sensor hardware architecture, along with the measurement results, can be found in [ADH13]. Many novel proposals discussed in this dissertation are applicable to the future evolution of this flexible UWB hardware platform. The self-localization and distributed cooperative localization methods developed in the lab are discussed in [DAH12,ZADH13].

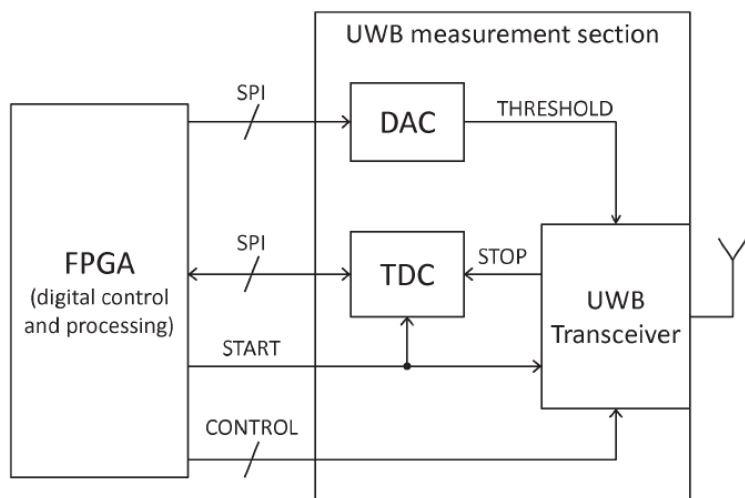
1.7 Motivations and Objectives

Significant attention has been given to UWB research subsequent to the FCC adopting the unlicensed UWB operation in the USA in 2002 [FCC02]. Much of the research has been an extension of the spread spectrum concepts to UWB. One example of this is developing the signaling methods based on time-hopping for multiple access and security. Several practical challenges have not been considered in the research of physical layer signaling for UWB. The UWB transceivers employed in the UWB sensor network are typically made up of low cost hardware platforms. The constraints that emerge from these low cost hardware platforms need to be considered along with the regulatory body requirements while developing the physical layer signaling.

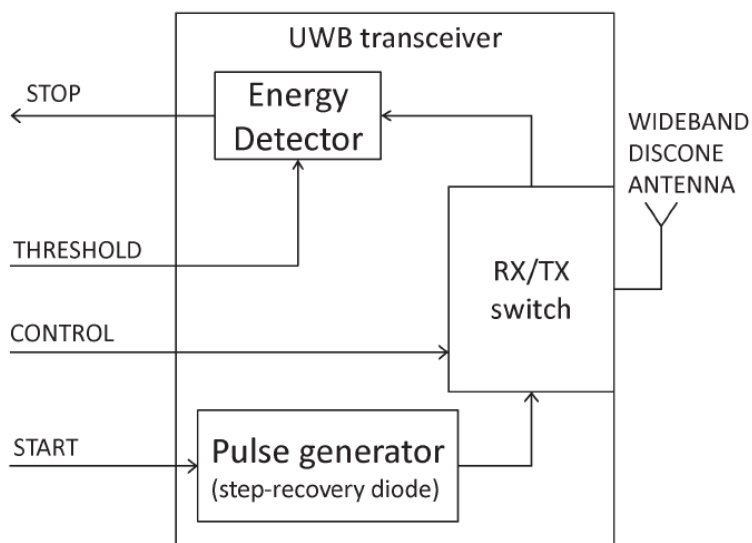
There have been several research studies on using UWB signals for communication and localization. However, utilizing the location information of the sensor nodes for UWB communication is not a well studied problem. Many UWB sensor networks require cyclic all-to-all communication for information dissemination across the network. Utilizing the sensor location in such communication can provide significant benefits. This aspect is explored little in the UWB literature.

In many hardware platforms, a single UWB transceiver mounted on the sensors is used for multiple applications such as ranging, sensing and communication. Each detector in these platforms, such as amplitude detectors (AD), energy detectors (ED), etc. uses particular statistics of the received samples for UWB pulse detection based on the application. The performance of hypothesis testing for these detectors as a function of various UWB physical layer parameters, such as number of pulses, energy of the pulse and pulse shape, is not a well researched topic. The fusion of these detector outputs when there is no strict binding between the application and detector can improve the hypothesis testing performance.

Accurate time of arrival (TOA) is essential in several applications including localization and communication. The digital matched filter based detector is the



(a) Sensor unit



(b) UWB transceiver

Figure 1.5: In-house UWB hardware platform [ADH13].

method of preference, because of its superior performance in additive white Gaussian noise (AWGN) and multi-path channels. However, UWB signals occupy extremely large bandwidth and thus requires high-speed analog-to-digital converters (ADCs). These are very expensive, and low-cost alternatives are preferred. Also, typically the target is dynamic in nature, therefore how to estimate the TOA of a dynamic target using multiple low cost energy detector chains is of particular interest.

A simple approach to TOA estimation for LOS UWB channels is to choose the location of the peak in the received signal as the TOA estimate. However, the main source of error here will be due to the strongest multipath components arriving later than the first path. This problem is typically addressed using thresholding [GS05,DCW08,DCW06]. When these algorithms are implemented using digital transceivers, they require a sampling rate much higher than the Nyquist rate. The estimation of the TOA using sub-Nyquist sampling is not addressed in UWB literature. This can significantly ease the bottleneck of the ADC design due to the wide bandwidth of the UWB signal.

Many applications, such as first responder systems require both localization and communication. How to design the physical layer signals to aid joint estimation of TOA and data symbols in the sub-Nyquist domain is of particular interest. This can ease the requirements on the RF front-end sampling rate and can reduce the cost of the UWB receivers.

The above discussion naturally leads to the following research topics which are addressed in this thesis:

1. Hardware aware spectral efficient physical layer signaling for UWB,
2. Location aware communication,
3. Multi-detector hardware platform with fusion methods,
4. Joint fusion and estimation of TOA from dynamic target using multiple low-cost detector chains,
5. A compressive sampling approach to UWB TOA estimation,
6. Joint estimation of TOA and data-symbol in sub-Nyquist domain.

1.8 Thesis Outline and Contribution

This section provides an outline of the thesis with a brief summary of the material presented in each chapter. This thesis consists of 9 chapters, the summary of which are as follows.

Chapter 2

Chapter 2 deals with the preliminaries. Here we will briefly discuss the concepts and tools that are needed to understand the rest of the thesis. We start with a brief introduction to optimization methods where we discuss the convex optimization and traveling salesman problem. Then we proceed toward statistical signal processing, where we discuss the basics of detection and estimation theory. Followed by this is an introduction to sparse signal processing.

Chapter 3 – 8 discuss the main contributions of this thesis. Each chapter is complete by itself and to understand the material the reader does not need the content of previous or subsequent chapters. However, the chapters themselves address problems which are related. The connections between the chapters is shown in Figure 1.6. Each chapter begins with a “Background” section, which gives the overall context to the discussion that follows and ends with a “Conclusion” section which summarizes the chapter along with the main concepts from that chapter.

Chapter 3

Chapter 3 discusses the physical layer signal construction for UWB. There exists extensive research on the design of hardware platforms and algorithms for localization and communication strategies. However, there is limited research on how to optimize the physical layer signaling for UWB communication in view of constraints from cost-effective hardware and regulatory bodies in the context of UWB. In this chapter, two signaling schemes are discussed, with one requiring higher complexity in modulation and demodulation, which can increase the range by nearly 4 times without compromising the bitrate. This chapter also discusses demodulators for the proposed schemes and derives the theoretical performance in terms of symbol error rates (SER) for them. This chapter is based on the following papers:

- [A] V. Yajnanarayana, S. Dwivedi, A. De Angelis, and P. Händel, “Spectral efficient IR-UWB communication design for low complexity transceivers,” *EURASIP Journal on Wireless Communications and Networking*, vol. 2014:158, no. 1, pp. 1-13, 2014.
- [B] V. Yajnanarayana, S. Dwivedi, and P. Händel, “Design of impulse radio UWB transmitter with improved range performance using PPM signals,” *2014 IEEE International Conference on Electronics, Computing and Communication Technologies (CONECCT)*, Bangalore, India, Jan 2014, pp. 1-5.
- [C] V. Yajnanarayana, S. Dwivedi, A. De Angelis, and P. Händel, “Design of impulse radio UWB transmitter for short range communications using PPM signals,” *2013 IEEE International Conference on Electronics, Computing and Communication Technologies (CONECCT)*, Bangalore, India, Jan 2013, pp. 1-4.

Chapter 4

Chapter 4 deals with multiple access scheduling. A typical multiple access scheduling decides how the channel is shared among the nodes in the network. Typical scheduling algorithms aim at increasing the channel utilization and thereby throughput of the network. In this chapter, we describe several algorithms for generating an optimal schedule, in terms of channel utilization, for multiple access by utilizing range information in a fully connected network. A detailed analysis for the proposed algorithms' performance in terms of their complexity, convergence, and effect of nonidealities in the network is also discussed. The performance of the proposed schemes is compared with non-aided methods to quantify the benefits of using the range information in the UWB communication. The methods discussed in this chapter have several favorable properties for scalable systems. We show that the proposed techniques yield better channel utilization and throughput as the number of nodes in the network increases. This chapter is based on the following paper:

- [D] V. Yajnanarayana, K. Magnusson, R. Brandt, S. Dwivedi, and P. Händel, "Optimal Scheduling for Interference Mitigation by Range Information," Manuscript submitted to *IEEE Transactions on Mobile Computing*, 2016.

Chapter 5

Optimal detection of UWB pulses in a UWB transceiver employing multiple detector types is proposed and analyzed in Chapter 5. To enable the transceiver to be used for multiple applications, the designers can have different types of detectors such as an energy detector, amplitude detector, etc., built in to single transceiver architecture. We discuss several fusion techniques for fusing decisions made by individual IR-UWB detectors. In order to get early insight into the theoretical achievable performance of these fusion techniques, we assess the performance of these fusion techniques for commonly used detector types such as matched filter, energy detector and amplitude detector under Gaussian assumption. These are valid for ultra short distance communication and in UWB systems operating in millimeter wave (mmwave) band with high directivity gain. In this chapter, we show that the performance can be improved by fusing decisions from multiple detector types compared to a stand-alone detector. This chapter is based on the following papers.

- [E] V. Yajnanarayana and P. Händel, "Performance Evaluation of IR-UWB Detectors and Fusion Techniques for UWB Transceiver Platforms," *International Journal of Ultra Wideband Communications and Systems*, in press.
- [F] V. Yajnanarayana, S. Dwivedi and P. Händel, "IR-UWB Detection and Fusion Strategies using Multiple Detector Types," *2016 IEEE Wireless Communications and Networking Conference (WCNC)*, Doha, Qatar, Apr. 2016, pp. 1-6.

Chapter 6

In Chapter 6, we discuss the fusion of dynamic TOA from multiple low complexity detectors like energy detectors operating at sub-Nyquist rate through Kalman filtering. We show that by having a multi-channel receiver, with each channel having an energy detector, we can achieve the performance of a digital implementation with a matched filter. In this chapter, we also derive an analytical expression for the number of sub-Nyquist energy detector channels needed to achieve the performance of a digital implementation with a matched filter. Using simulations, we also demonstrate the validity of our analytical approach. Results indicate that the number of energy detectors needed will be high at low SNRs and converge to a constant number as the SNR increases. We also study the performance of the strategy proposed using the IEEE 802.15.4a CM1 multipath channel model and show in simulations that two sub-Nyquist detectors are sufficient to match the performance of a digital matched filter. This chapter is based on the following paper:

- [G] V. Yajnanarayana, S. Dwivedi and P. Händel, “Multi detector fusion of dynamic TOA estimation using Kalman filter,” *2016 IEEE International Conference on Communications (ICC)*, Kuala Lumpur, Malaysia, May 2016, pp. 1-6.

Chapter 7

Chapter 7 discusses two compressive sampling based time TOA estimation algorithms using a sub-Nyquist rate receiver. We also describe a novel compressive sampling dictionary design for the compact representation of the received UWB signal. One of the proposed algorithm exploits the *a priori* information with regard to the channel and the range of the target. The performance of the algorithms is compared against the maximum likelihood (ML) based receiver using IEEE 802.15.4a CM1 line of sight (LOS) UWB channel model. The discussed methods yield similar performance to the ML TOA estimation at high SNRs. However, the computational complexity and the sampling rate requirements are lesser compared to the ML estimator. In this chapter, we also analyze the performance of the algorithm with respect to practical constraints such as the size of the holographic dictionary and sampling rates. A new algorithm which can exploit both the *a priori* information regarding the UWB channel and the geographical constraints on the target that may be available at the receiver is also discussed. This algorithm can substantially boost performance compared to the algorithm without *a priori* information at low SNRs. This chapter is based on the following paper:

- [H] V. Yajnanarayana and P. Händel, “Compressive Sampling Based UWB TOA Estimator,” Manuscript submitted to *EURASIP Journal on Advances in Signal Processing*, 2016

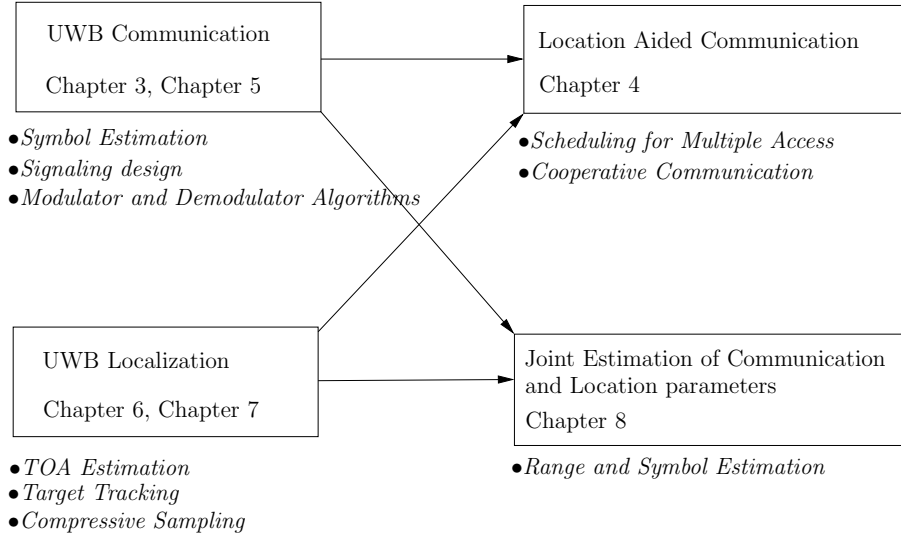


Figure 1.6: Schematic overview of the technical chapters presented in the thesis.

Chapter 8

Chapter 8 describes a sub-Nyquist rate receiver which can jointly estimate TOA and data symbols. We borrow the ideas from the previous chapter to first represent the received UWB signal in a new domain in which it is sparse. Then, we design physical layer waveforms and estimation algorithms to exploit this sparsity for joint estimation of TOA and PPM data symbols. The performance of the receiver is compared against the ML based receiver using the IEEE 802.15.4a CM1 LOS UWB channel model. The proposed algorithm yields a performance similar to the ML based algorithms with only a fraction of the sampling rate at high SNRs (>25 dB). This chapter is based on the following paper:

- [I] V. Yajnanarayana and P. Hädel, “Joint Estimation of TOA and PPM Symbols using Sub-Nyquist Sampled IR-UWB signal,” *IEEE Communication Letters*, in revision.

Chapter 9

Finally, Chapter 9 summarizes the author’s general conclusions and possible directions for future research.

Copyright Notice

As specified in the Section 1.8, material presented in this thesis is based on the author's previous work which is published or submitted to conferences and journals held by or sponsored by IEEE, Springer and InderScience publishers. They hold the copyright of the published papers and will hold the copyright of the submitted papers if they are accepted.

Preliminaries

In this chapter, we will introduce basic concepts that are needed to understand the rest of thesis. We will start with the fundamentals of detection and estimation theory.

2.1 Detection Theory

Detection theory deals with the problem of choosing a particular hypothesis from the observation, \mathbf{x} . Typically a hypothesis maps to a particular phenomenon that is being detected. For example, in the context of a UWB signal, we can formulate a hypothesis for whether a particular frame has a UWB pulse or not. If there are only two hypotheses, H_0 and H_1 for a phenomenon, then the detection problem reduces to a binary hypothesis test. For a binary hypothesis, the following types of errors can occur when deciding based on the observation:

- A type-1 error or false alarm, which occurs when the observation is decoded as H_1 , for an H_0 event. Probability of false alarm, $P_{FA} = \Pr(H_1; H_0)$ ¹.
- A type-2 error or miss, which occurs when the observation is decoded as H_0 , for an H_1 event. Probability of miss, $P_M = \Pr(H_0; H_1)$.

Both type-1 and type-2 errors cannot be reduced simultaneously. A typical approach is to fix the false alarm (type-1 error) and seek an optimal detector to minimize the type-2 error. Note that minimizing the type-2 error is the same as maximizing the detection probability, $P_D = (1 - \Pr(H_0; H_1)) = \Pr(H_1; H_1)$. This setup is called the Neyman-Pearson (NP) approach to hypothesis testing. We can formalize this into a theorem as follows:

Theorem 2.1.1. *For a given false alarm, $P_{FA} = \alpha$, to maximize, P_D , decide toward H_1 if,*

$$L(\mathbf{x}) = \frac{p(\mathbf{x}; H_1)}{p(\mathbf{x}; H_0)} > \gamma, \quad (2.1.1)$$

¹We define $\Pr(H_i; H_j)$ as the probability of choosing H_i hypothesis when H_j has occurred.

where the threshold, γ , is obtained from

$$P_{FA} = \int_{\mathbf{x}: L(\mathbf{x}) > \gamma} p(\mathbf{x}; H_0) d\mathbf{x} = \alpha. \quad (2.1.2)$$

The equation (2.1.1) is called the likelihood ratio test [Kay98].

2.1.1 Bayesian Approach

In many applications, the prior probabilities of the hypotheses are known. For example, in UWB communication using M -ary PPM scheme, we know that the symbols (hypotheses) are equiprobable with probability, $1/M$. If the objective is to minimize the error or misclassification, then the optimal rule is the maximum *a posteriori* probability (MAP) rule. That is, for a multi-hypotheses case with the M possible hypotheses, decide H_i , if

$$\begin{aligned} \Pr(H_i|\mathbf{x}) &> \Pr(H_j|\mathbf{x}), \\ \forall i, j \in \{1 \dots M\} \text{ and } j \neq i. \end{aligned} \quad (2.1.3)$$

If we re-write (2.1.3), using Bayes theorem, we get

$$\Pr(H_i|\mathbf{x}) = \frac{p(\mathbf{x}|H_i)\Pr(H_i)}{p(\mathbf{x})}. \quad (2.1.4)$$

If all the hypotheses are equiprobable, then maximizing the $\Pr(H_i|\mathbf{x})$ is the same as maximizing $p(\mathbf{x}|H_i)$ with the choice of H_i . Under this condition the MAP rule reduces to, decide H_i if

$$\begin{aligned} p(\mathbf{x}|H_i) &> p(\mathbf{x}|H_j), \\ \forall i, j \in \{1 \dots M\} \text{ and } j \neq i. \end{aligned} \quad (2.1.5)$$

This is called the maximum likelihood (ML) rule. In Chapter 5, we will consider a direct sampling receiver structure and use the concepts discussed in this section to arrive at a binary hypothesis about the presence of a UWB pulse in the received samples.

2.2 Estimation Theory

The estimation theory deals with arriving at a quantitative conclusion about a parameter, $\boldsymbol{\theta}$, from the observation, \mathbf{x} . An example of this is estimating the value of the TOA from a received UWB frame. The joint probability distribution function (PDF), $p(\boldsymbol{\theta}, \mathbf{x})$, denotes the complete statistical description of the parameters and observations.

The posterior PDF, $p(\boldsymbol{\theta}|\mathbf{x})$, is the quantity of interest in many estimation problems. Applying Bayes rule, the posterior PDF can be written as

$$p(\boldsymbol{\theta}|\mathbf{x}) = \frac{p(\mathbf{x}|\boldsymbol{\theta})p(\boldsymbol{\theta})}{p(\mathbf{x})}, \quad (2.2.1)$$

$$= \alpha p(\mathbf{x}|\boldsymbol{\theta})p(\boldsymbol{\theta}), \quad (2.2.2)$$

where $\alpha = 1/p(\mathbf{x})$ is a normalizing constant.

In the above formulation, we assumed that the parameter, $\boldsymbol{\theta}$, is random and unknown. However, in certain estimation problems, $\boldsymbol{\theta}$, can be deterministic. Under these conditions, good estimators can be designed by mathematically modeling the observation \mathbf{x} , through the parametrized, PDF, $p(\mathbf{x}; \boldsymbol{\theta})$.

2.2.1 Performance of an estimator

An estimator is a function, g , which maps the observation space to the parameter space, i.e., $g: \mathcal{S}_{\mathbf{x}} \rightarrow \mathcal{S}_{\boldsymbol{\theta}}$. We want to have this mapping function to have an error, $\boldsymbol{\epsilon} \triangleq (\boldsymbol{\theta} - \hat{\boldsymbol{\theta}})$ which is as small as possible. In particular, we look at the mean of the squared error (MSE), that is

$$\mathbf{M} = \mathbb{E} \left[(\boldsymbol{\theta} - \hat{\boldsymbol{\theta}})^2 \right], \quad (2.2.3)$$

where, $\mathbb{E}[\cdot]$ is an expectation operator and $\|\cdot\|$ is the 2-norm. In a Bayesian set up with the unknown random parameter, the optimal estimator is the conditional mean $\boldsymbol{\mu}_{\boldsymbol{\theta}|\mathbf{x}} \triangleq \mathbb{E}_{\boldsymbol{\theta}|\mathbf{x}}[\boldsymbol{\theta}]$ and for such an estimator, the variance is given by the conditional covariance, $\mathbf{C}_{\boldsymbol{\theta}|\mathbf{x}}$.

If the parameter is deterministic and unknown, then an unbiased estimate is usually preferred. That is, $\hat{\boldsymbol{\theta}} = g(\mathbf{x})$, and such an estimator has a property

$$\mathbb{E}[\hat{\boldsymbol{\theta}}] = \boldsymbol{\theta}. \quad (2.2.4)$$

The variance (MSE) of any unbiased estimator is at least as high as the inverse of the Fisher information. Where Fisher information is defined as

$$\mathbf{I}(\boldsymbol{\theta}) = -\mathbb{E} \left[\frac{\partial^2 p(\mathbf{x}; \boldsymbol{\theta})}{\partial^2 \boldsymbol{\theta}} \right], \quad (2.2.5)$$

$$\mathbf{M}_{i,i} \geq [\mathbf{I}^{-1}(\boldsymbol{\theta})]_{i,i}. \quad (2.2.6)$$

The bound defined in (2.2.6) is called Cramer-Rao lower bound (CRLB).

2.2.2 Estimation Methods

Typical estimation methods depend on the model assumptions. Consider the four scenarios [Zac13]:

- (i) Likelihood $p(\mathbf{x}|\boldsymbol{\theta})$ and prior $p(\mathbf{x})$ are available.
- (ii) Only likelihood $p(\mathbf{x}|\boldsymbol{\theta})$ is available.
- (iii) First and second order statistics of the $\boldsymbol{\theta}$ and \mathbf{x} are available.
- (iv) The observation can be modeled as $\mathbf{x} = h(\boldsymbol{\theta}) + \mathbf{w}$.

In the first scenario, a Bayesian minimum MSE (MMSE) estimator can be designed using the conditional mean, $\boldsymbol{\mu}_{\boldsymbol{\theta}|\mathbf{x}}$. However, in many cases it is not possible to solve the complex integrals that arise in this setup. Hence, a more computationally amenable setup consisting of maximizing a posterior distribution (MAP) formulation is considered. This can be written as

$$\hat{\boldsymbol{\theta}}_{\text{MAP}} = \arg \max_{\boldsymbol{\theta}} p(\boldsymbol{\theta}|\mathbf{x}). \quad (2.2.7)$$

The second approach is typically applied in the absence of information about the prior distribution of the $\boldsymbol{\theta}$. In these circumstances, it is common to treat the parameter as a deterministic but unknown value and obtain the estimator by maximizing the likelihood distribution. That is

$$\hat{\boldsymbol{\theta}}_{\text{ML}} = \arg \max_{\boldsymbol{\theta}} p(\mathbf{x}; \boldsymbol{\theta}) \quad (2.2.8)$$

The third model assumption leads to a linear framework, where the estimate is a linear function of the observation, that is $\hat{\boldsymbol{\theta}} = \mathbf{H}\mathbf{x}$. The value of \mathbf{H} can be obtained by

$$\begin{aligned} \mathbf{H}^* &= \arg \min_{\mathbf{H}} \mathbf{C}_{\hat{\boldsymbol{\theta}}}(\mathbf{H}), \\ \hat{\boldsymbol{\theta}}_{\text{LMMSE}} &= \mathbf{H}^* \mathbf{x} \end{aligned} \quad (2.2.9)$$

where, $\mathbf{C}_{\hat{\boldsymbol{\theta}}}(\mathbf{H}) = \mathbb{E}[(\boldsymbol{\theta} - \mathbf{H}\mathbf{x})(\boldsymbol{\theta} - \mathbf{H}\mathbf{x})^T]$. It can be shown that only first and second order statistics of $\boldsymbol{\theta}$ and \mathbf{x} are needed for this estimator rather than the PDFs. These form a class of estimators called linear MMSE (LMMSE) estimators.

The fourth model assumes no statistical distributions, but only a function, $h(\cdot)$, which can model the observations as a function of the $\boldsymbol{\theta}$. In these situations the estimate can be obtained by

$$\hat{\boldsymbol{\theta}}_{\text{LS}} = \arg \min_{\boldsymbol{\theta}} (\epsilon^2), \quad (2.2.10)$$

where $\epsilon^2 = (\mathbf{x} - h(\boldsymbol{\theta}))^T (\mathbf{x} - h(\boldsymbol{\theta}))$. This class of estimators are called a least squares (LS) estimators. If we modify the ϵ^2 as $(\mathbf{x} - h(\boldsymbol{\theta}))^T \mathbf{W} (\mathbf{x} - h(\boldsymbol{\theta}))$ with a weighted matrix \mathbf{W} , then the estimator is called weighted least squares estimator. In Chapter 6, Chapter 7 and Chapter 8 we employ the LMMSE, ML and LS based estimation principals discussed in this section.

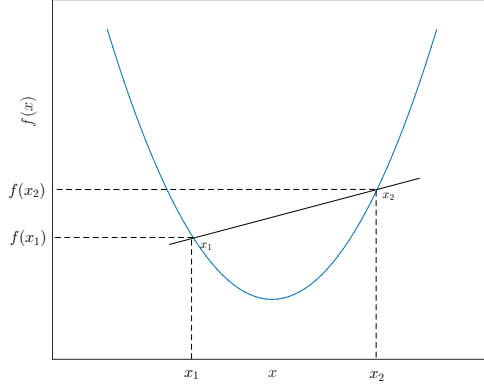


Figure 2.1: A convex function.

2.3 Convex Optimization

A function $f : \mathbb{R}^N \rightarrow \mathbb{R}$, is said to be convex, if it satisfies

$$f(c\mathbf{x}_1 + (1 - c)\mathbf{x}_2) \leq cf(\mathbf{x}_1) + (1 - c)f(\mathbf{x}_2), \quad (2.3.1)$$

for any $\mathbf{x}_1, \mathbf{x}_2 \in \mathbb{R}^N$ and $c \in [0, 1]$. Figure 2.1 shows a convex function, $f : \mathbb{R} \rightarrow \mathbb{R}$. The implication of (2.3.1) is that the function value should lie on or below the straight line (since $N = 1$ is considered here) joining any two points x_1 and x_2 .

A set, \mathcal{S} , is said to be a convex set, if we have convex combination of any two elements of a set is also contained in the set. That is, if $\mathbf{x}, \mathbf{y} \in \mathcal{S}$, then for $c \in [0, 1]$, we have

$$c\mathbf{x} + (1 - c)\mathbf{y} \in \mathcal{S}. \quad (2.3.2)$$

Convex and non-convex sets are illustrated in Figure 2.2. A convex optimization problem is an optimization problem defined as follows

$$\begin{aligned} & \underset{\mathbf{x}}{\text{minimize}} && f(\mathbf{x}) \\ & \text{subject to} && \mathbf{x} \in \mathcal{S}, \end{aligned} \quad (2.3.3)$$

where f is a convex function and \mathcal{S} is a convex set. The convex problem has a property that the local minimum is also a global minimum. This enables efficient methods to solve them. A class of problems within convex problems has a particular structure wherein the objective function and the constraints are linear, such

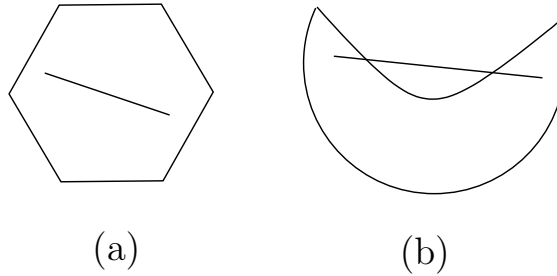


Figure 2.2: The set of all points inside and on the hexagon shown in (a) forms a convex set and the points of (b) does not form a convex set as some convex combination of its elements does not lie within the set.

problems are called linear programs. A typical linear program has a structure

$$\begin{aligned} & \underset{\mathbf{x}}{\text{minimize}} && \mathbf{a}^T \mathbf{x} \\ & \text{subject to} && \mathbf{A} \mathbf{x} \leq \mathbf{b}, \end{aligned} \tag{2.3.4}$$

where, \mathbf{a} , \mathbf{b} are known vectors and \mathbf{A} is a known matrix. The \leq is used in a loose sense here to depict that every element of vector $\mathbf{A} \mathbf{x}$ is less than the corresponding element of vector \mathbf{b} . The linear programs can be solved efficiently using simplex or interior-point methods [BV04].

As we will see in Chapter 4, many UWB communication access problems can be relaxed into a convex optimization problem. In many of these problems, one can exploit the structure in the problem to arrive at the optimal solution efficiently (less computational time for a given input size).

2.4 Traveling Salesman Problem

In this section, we state the traveling salesman problem (TSP). Consider a list of cities with routes defined between them. The TSP attempts to derive the shortest possible route that will visit all the cities exactly once and return to the origin city. The solution of this problem is NP-hard (refer to the Section 2.5 about computational complexity).

The all-to-all broadcast is used in various types of networks for information dissemination across the network to accomplish various tasks such as localization, routing, distributed control and computation. We will show in Chapter 4 that these types of communication can be posed as a traveling salesman problem.

The TSP is known to be NP-hard [RP89, Law76, Lov79], but there are algorithms that can find exact solutions for small problems, and other algorithms that can find approximate solutions for larger problems [Joh82, Lap92]. Many techniques employ

heuristic approaches for finding the approximate solution [Hel00, Ree93, RSL77]. One of the popular heuristics is the Lin-Kernighan heuristic (LKH). There are implementations available for these methods of solving TSP problems. For example, we used the implementation of [Hel00] in Chapter 4 to solve the TSP problem.

2.5 Algorithm Complexity

An algorithm is a sequence of steps taken to manipulate the input to achieve a desired output. The complexity of an algorithm deals with the amount of resources required and the dependence of these resources on the size of the input. The resource here could be time, memory, gates, etc. However, for many problems, it is common to use time as a resource.

For a certain class of problems, algorithms can be designed to solve them in polynomial-time. For these problems it is common to estimate the complexity in an asymptotic sense. Typically for these problems the big-O notation is used to quantify complexity. For example, if the polynomial-time for the algorithm, with size N is given by $2N^2 + 3N + 5$, then the algorithm is said to be of $\mathcal{O}(N^2)$. There is a certain class of problems, for which there does not exist (at least not yet known) algorithms that can solve them in polynomial time. This class of problems are called non-deterministic polynomial-time (NP-hard) problems. The TSP problem discussed above is one such problem.

2.6 Sparse Signal Processing

The UWB signals occupy a wide bandwidth and this requires ADCs to operate at a very high rate. These ADCs are costly, suffer from poor resolution and are power hungry. Sparsity of the received UWB signal in certain domains, can be exploited to reduce the number of samples needed to make statistical inference. This naturally leads to the reduced sampling rate and, therefore, reduced use of ADCs resources.

Definition 2.6.1 ($\mathcal{I}_{\mathbf{x}}$ support of \mathbf{x}). Support of \mathbf{x} is defined as a set consisting of indices of non-zero elements of \mathbf{x} . That is

$$\mathcal{I}_{\mathbf{x}} \triangleq \{i : x_i \neq 0\}, \quad (2.6.1)$$

where, x_i , denotes the i -th element of the vector \mathbf{x} .

Definition 2.6.2 (l_0 norm). The l_0 norm of \mathbf{x} ($\|\mathbf{x}\|_0$), is the number of non-zero elements in the set \mathbf{x} . That is, it is the cardinality of the support set, therefore,

$$\|\mathbf{x}\|_0 = |\mathcal{I}_{\mathbf{x}}|. \quad (2.6.2)$$

Definition 2.6.3 (l_p norm). The l_p norm of \mathbf{x} ($\|\mathbf{x}\|_p$), with $p \geq 1$, is defined as

$$\|\mathbf{x}\|_p^p = \sum_{i=1}^N |x_i|^p, \quad (2.6.3)$$

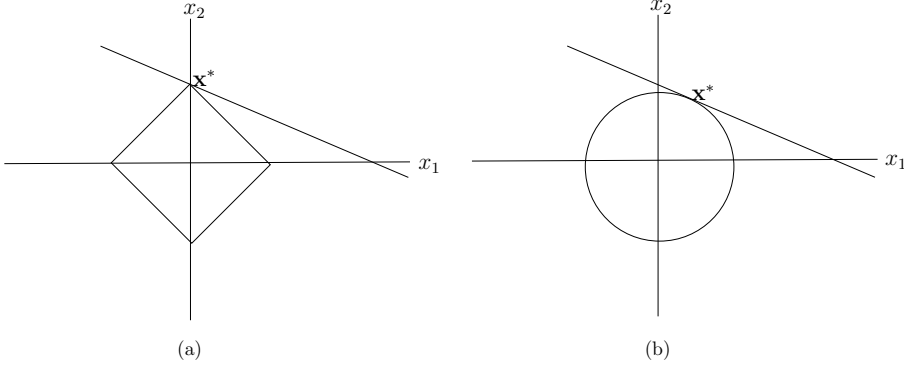


Figure 2.3: The intersection of l_1 and l_2 ball with $\mathbf{x} = \{x_1, x_2\}$. The line indicates the solution set of an equation with 2 variables. Notice that l_1 solution (shown in (a)) has one of the coordinates as 0 compared to l_2 solution (shown in (b))

where N is the number of elements in the vector \mathbf{x} .

Consider the measurement vector, $\mathbf{y} \in \mathbb{R}^M$, which is observed after linearly transforming the signal vector, $\mathbf{x} \in \mathbb{R}^N$, as shown below.

$$\mathbf{y} = \mathbf{A}\mathbf{x}, \quad (2.6.4)$$

where, $\mathbf{A} \in \mathbb{R}^{M \times N}$, is the measurement matrix and $M < N$. A standard compressive sampling problem deals with finding sparse \mathbf{x} , given the measurement \mathbf{y} and measurement matrix \mathbf{A} . Also, typically, \mathbf{A} has i.i.d. entries taken from a normal distribution. One way to find the sparse solution is to solve the following optimization problem

$$\begin{aligned} \arg \min_{\mathbf{x}} \|\mathbf{x}\|_0 \\ \text{subject to } \mathbf{y} = \mathbf{A}\mathbf{x}. \end{aligned} \quad (2.6.5)$$

The solution for this is NP-hard. A computationally amenable formulation can be achieved by modifying the objective function from l_0 to l_1 as given below.

$$\begin{aligned} \arg \min_{\mathbf{x}} \|\mathbf{x}\|_1 \\ \text{subject to } \|\mathbf{y} = \mathbf{A}\mathbf{x}\|. \end{aligned} \quad (2.6.6)$$

The intuition on picking l_1 norm here is its ability to promote sparsity as can be understood by Figure 2.3.

When the measurements \mathbf{y} are noisy, then the model becomes

$$\mathbf{y} = \mathbf{A}\mathbf{x} + \mathbf{e}. \quad (2.6.7)$$

Algorithm 2.1: OMP algorithm**Input:** $\mathbf{y}, \mathbf{A}, K, \Delta, \mathbf{e}_0 = \mathbf{y}, k = 0, \mathcal{I}_0 = \{\emptyset\}$ **Output:** Recoverd \mathbf{x} ($\hat{\mathbf{x}}$).

```

1 repeat
2    $t = \arg \max |\langle \mathbf{h}_i, \mathbf{e}_k \rangle|, i = 1, \dots, N$ 
3    $k = k + 1$ 
4    $\mathcal{I}_k = \mathcal{I}_{k-1} \cup t$ 
5    $\mathbf{e}_k = \mathbf{y} - \mathbf{A}_{\mathcal{I}_k} \mathbf{A}_{\mathcal{I}_k}^\dagger \mathbf{y}$ 
6 until  $k \leq K$ 
7 return  $\hat{\mathbf{x}} = \mathbf{A}_{\mathcal{I}_K}^\dagger \mathbf{y}$ 

```

In this case, one needs to choose the \mathbf{x} , which fits the model as well as it should be sparse. This can be accomplished by reformualting the problem as

$$\arg \min_{\mathbf{x}} \frac{1}{2} \|\mathbf{y} - \mathbf{A}\mathbf{x}\|_2^2 + \lambda \|\mathbf{x}\|_1. \quad (2.6.8)$$

This is a well known problem formulation and is called a basis pursuit denoising (BPDN) problem. The λ parameter weighs the importance of the model fit and the sparsity level.

Greedy pursuit algorithms can also be used to solve the problem defined in (2.6.5). The central idea in these algorithms is to find the underlying support set of \mathbf{x} , by match filtering the columns of \mathbf{A} with the residual signal in an iterative way. The residual signal in each iteration is the error in the least-square fit with \mathbf{y} , with the chosen supports. This algorithm is called orthogonal matching pursuit (OMP). An OMP algorithm to recover a K -sparse \mathbf{x} from \mathbf{y} is as given in the Algorithm 2.1.

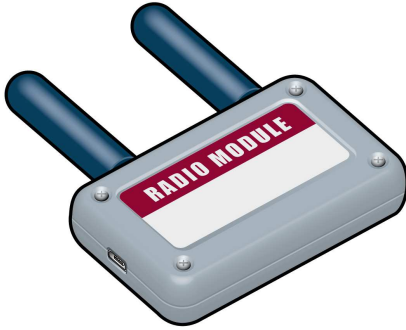
As shown in Chapter 1, Section 1.3.3, the propagation characteristics of the UWB signal results in a channel which can be modeled using Saleh-Valenzuela channel model. This means that the UWB channel has multi-paths arriving as clusters in the Poisson distributed way and the multipath components (MPCs) within the cluster follows a Laplacian model. Since the pulses themselves are narrow in time (impulse-like), the received signal is inherently sparse in time. As we will see in Chapter 7 and Chapter 8, the UWB signal can be represented in a compact way by choosing an appropriate basis.

Hardware Aware IR-UWB signaling

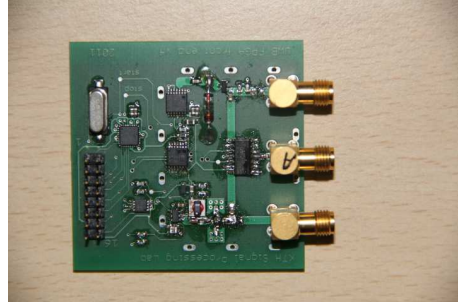
Ultra wideband (UWB) radio for communication has several challenges. From the physical layer perspective, a signaling technique should be optimally designed to work in synergy with the underneath hardware to achieve maximum performance. In this chapter, we will discuss a variant of pulse position modulation (PPM) for physical layer signaling, which can achieve raw bitrate in excess of 150 Mbps on a low complexity in-house developed impulse radio UWB-platform. The signaling system is optimized to maximize bitrate under practical constraints of low complexity hardware and regulatory bodies. We propose a detector and derive its theoretical performance bounds, and compare the performance in simulation in terms of symbol error rates (SER). Modifications to the signaling, which can increase the range by 4 times with a slight increase in the computational complexity is proposed. Detectors for this modification and a comparative study of the performance of the proposed UWB physical layer signaling schemes in terms of symbol error rates are also discussed in this chapter.

3.1 Background

There are several radio technologies operating in 0 – 10 GHz band, and several new ones are emerging as a result RF spectrum is becoming more premium and more scarce. Communication systems using ultra wideband (UWB) offer a promising solution which can co-exist with other radio technologies. This coexistence also saves expensive spectrum licensing fees [BKM⁺06, NP09]. The Federal Communications Commission (FCC) adopted license free UWB operation in the United States of America [FCC02]. This has resulted in 7.5 GHz of spectrum available for UWB systems. One of the direct consequences of this large bandwidth is the ability to achieve very high data rates, as given by the Shannon-Hartley theorem. Wide bandwidth also enables innovative system design such as trading data rate to avoid costly channel estimation techniques in [HT02], or designing the analog transmit



(a) Radio module



(b) Printed circuit board (PCB)

Figure 3.1: Iconic model of the in-house developed impulse radio UWB-platform of size 6 cm x 4 cm for ranging and communication using separate RX and TX antennas from Greenwavescientific. (details are available at [Gwa16].)

and receive structure with non-idealities in [Orn20]. In general, there is a wide scope of data rate, range and other parameters that can be traded off based on the application [Lue12, ZOS⁺09, Mol05].

There are several ways in which a signal can be spread to large bandwidths. The most popular methods include frequency hopping (FH) [YH02], orthogonal frequency-division multiplexing (OFDM) [BBD⁺10], direct-sequence spread spectrum (DS-SS) [FKO⁺] and time-hopping impulse radio (TH-IR) [WS00]. UWB based on OFDM and TH-IR have gone in to IEEE 802.15.3a and IEEE 802.15.4a standards. TH-IR schemes are most popular as they provide better performance and complexity trade-offs [ZOS⁺09].

The use of impulse signaling was proposed by Win and Scholtz in the 1990s. Their work published in [Sch93, WS98, WS00] contributed significantly toward the adaptation of TH-IR for UWB. High bandwidth enables the UWB transceiver to generate narrow impulse signals, this fine time resolution can yield accurate position localization and ranging. This has enabled the application of UWB for high precision ranging and localization. Figure 3.1 shows a graphical depiction of an in-house developed IR-UWB platform for ranging and communication. It uses a low cost pulse generator to generate sub-nano second pulses using step recovery diode (SRD), as described in [ADGC11]. The characterization and modeling of the UWB platform for a distance measurement system can be found in [ADM⁺09] [SDAH11]. A detailed architectural description and experimental ranging results from a prototype of the platform have been published in [ADH13]. The power and range of the transceiver can be easily traded by controlling the amplitude, duty cycle and number of pulses per bit of transmission.

There are several commercial companies which develop IR-UWB products, including [Com16c, Com16d, Com16e, Com16a, Com16b]. Companies like Decawave and Bespoon develop 802.15.4a standard specific IR-UWB products [DW1, Com16a]. The physical layer signals of these UWB radios are defined by the standard. There are some companies like Timedomain and Ubisense which develop non-standard or custom made communication and localization solutions [Tdm16, Ubi16]. In these UWB radios, the physical layer signaling does not adhere to any standards. The work proposed in this chapter considers a methodology to maximize the communication rate through custom physical layer signaling, subject to hardware and regulatory constraints.

The main motivation for this chapter is from the requirement that many UWB applications need to perform localization and communication using the same radio module [RHFME10, Lue12]. The UWB radios of Timedomain and Ubisense both have localization and communication capabilities; however, these radios have minimal communication capabilities of few Kbps and physical layer signaling in them is not made public. This chapter is also motivated by the fact that although extensive research can be found on the design of hardware platforms and algorithms for localization and communication strategies [ADH13, Lue12, GTG⁺05], but how to optimize the physical layer signaling for communication in view of constraints from cost effective hardware and regulatory bodies is not a well studied problem. The achievable bitrate for the discussed methods in this chapter depends on the hardware parameters of the UWB platform. The proposed methods suggest that the in-house developed UWB radio shown in Figure 3.1 can achieve bitrates up to 150 Mbps. The in-house UWB platform uses pulse round-trip time (RTT) for localization. It has a range of about 10m with an accuracy of 30 cm in practical scenarios. It has a digital processing section based on a field-programmable gate array (FPGA), which interfaces with the analog UWB sections to generate required analog pulsed waveforms for transceiver operation. The modulator and demodulator algorithms proposed in this chapter can be programmed in FPGA, for processing UWB communication signals. This chapter proposes two signaling schemes with one requiring higher complexity in modulation and demodulation, however can increase the range by nearly 4 times without compromising on the bitrate. This is believed to have an interest in its own right, as it corresponds to (or outperforms) today's state of the art. Although, the discussion in this chapter considers the in-house developed UWB radio (Figure 3.1) for demonstrating the techniques, the results are of general importance which can enable engineers to follow similar methodology to exploit the hardware and spectrum to achieve a higher possible range and bitrate.

In this context, through this chapter we propose a method for communication using low cost and low complexity hardware architecture which can perform ranging, localization and communication. The main topics of this chapter are summarized below:

- A method to design a custom physical layer signaling to maximize the data rate by optimal choice of modulation parameters, given the constraints from hard-

ware and regulatory bodies is illustrated. An algorithm for such a modulator with no memory between symbols called a no-memory modulator is proposed.

- A spectrally more efficient modulator, which can improve the range of the communication by introducing the memory between symbols called with-memory modulator is proposed. This has a marginal increase in the complexity of modulator and demodulator algorithms with an increase in range by 4 times.
- A no-memory modulator is analyzed by deriving an expression for the symbol error rate (SER) performance. A detector algorithm for the no-memory modulator is proposed, and its SER performance is verified through simulation.
- The detector algorithm for the with-memory modulator is proposed and detector performance of no-memory and with-memory signaling are compared in simulation.

This chapter is organized as follows: In Section 3.2, we discuss the system model and pulse shapes used in the impulse radio. Section 3.3 discusses UWB constraints. Section 3.4 is on low complexity UWB hardware platform for localization and communication. Section 3.5 details the design of physical layer signal construction and modulator algorithms. Section 3.6 describes detectors and their performance in terms of symbol error rates. Finally, Section 3.7 details the conclusions from the design and demonstrated results.

3.2 Pulse Construction and System Model

A wide range of pulse shapes have been explored for UWB communication from rectangular to Gaussian [GMHK02]. The Gaussian pulses and their derivatives, usually called monopulses, are effective due to the ease of construction and good resolution in both time and frequency. In many cost effective hardware designs, these shapes are generated without any dedicated circuits. A simple transistor or diode, which is turned “on” and “off” to generate a narrow rectangular pulse will form an approximate Gaussian shape due to the imperfections in micro-electronic design [MG07].

The time domain Gaussian pulse with mean μ and variance σ^2 can be written as

$$\frac{1}{\sqrt{2\pi\sigma^2}} e^{-\frac{(t-\mu)^2}{2\sigma^2}}. \quad (3.2.1)$$

A more useful form of this equation for system design is defined in [MG07]. This is a scaled version of (3.2.1) with zero mean and variance $\tau^2/4\pi$. This is given by

$$s(t) = -e^{-2\pi(\frac{t}{\tau})^2}. \quad (3.2.2)$$

In a typical UWB device, when the signal passes through the UWB antenna, it will have a differentiation effect on the signal. A similar effect is observed when the receiver receives the pulses. The first and second order Gaussian pulses are given by

$$s'(t) = \frac{ds(t)}{dt} = \frac{4\pi t}{\tau^2} e^{\frac{-2\pi t^2}{\tau^2}}, \quad (3.2.3)$$

$$s''(t) = \frac{d^2s(t)}{dt^2} = -4\pi e^{\frac{-2\pi t^2}{\tau^2}} \left(\frac{-\tau^2 + 4\pi t^2}{\tau^4} \right). \quad (3.2.4)$$

For analytical and simulation analysis, we have used the power normalized second order Gaussian pulse as given below:

$$p^2(t) = \frac{(s''(t))^2}{\int_{-\infty}^{\infty} (s''(t))^2 dt}. \quad (3.2.5)$$

Several modulation techniques are proposed in the literature using narrow pulses [WLJ⁺09a, WS00]. Primarily they are variants of PPM, binary phase shift keying (BPSK) or on-off keying (OOK). Since our objective is to employ low complexity hardware structure to perform synchronized ranging and communication, a variant of PPM based signaling for communication is used. This can reuse the hardware structure (having RTT calculation logic for ranging) for detection and demodulation of physical layer signal. This is further illustrated in Section 3.4.

The system model comprises of three parts; transmitter, channel and receiver, as shown in Figure 3.2. The transmitter generates the PPM variant signal. This is a modified pulse specified in [WS00] with 1 symbol per pulse and no time hopping. The transmitted output signal is given by

$$W_{tr}(t) = \sqrt{E_p} \sum_n p(t - nT_s - d_n\Delta - \gamma_n), \quad (3.2.6)$$

where T_s is the symbol period, $d_n \in [0, \dots, L-1]$, is the n th symbol, $p(t)$ is the normalized pulse such that $\int_{-\infty}^{\infty} p^2(t)dt = 1$, E_p is the energy of the pulse, γ_n is a parameter coming from the constraints of the typical UWB hardware which will be explained later, Δ is the modulation index and $\log_2 M$ is the modulation order. Though in our model each symbol is defined by one pulse, it can be easily extended to multiple pulses for each symbol so that communication rate and detectability can be traded.

In UWB applications which use ranging for localization, the detectors rely on the first arriving path or line of sight (LOS). This is in contrast to the traditional channel measurement and modeling. However, for extremely short distance high speed communication with highly directional antennas, we can adopt a deterministic single path channel [Mol05]. These short distance high speed UWB applications include transferjet and wireless USB (wUSB). The message information is embedded in the time axis of PPM signals. Due to the high time resolution of UWB signals, the performance of the system is sensitive to the timing jitter (random

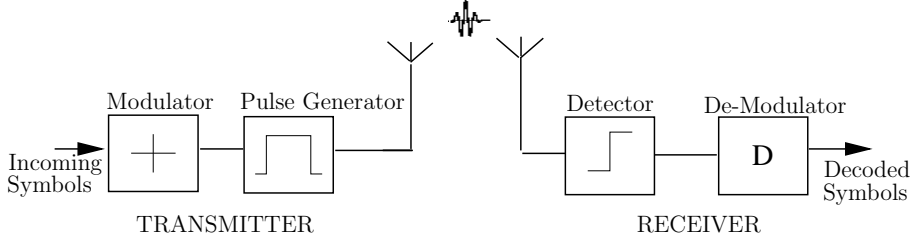


Figure 3.2: System model consisting of transmitter, channel and receiver.

shift on time axis) and synchronization [GA03, GMPK07]. The effect of channel, imperfect timing/synchronization and receiver front end thermal noise will cause errors while demodulating the PPM signals. We combine the effect of channel, imperfect timing/synchronization, together with receiver front end to introduce a random jitter along with noise $n(t)$ as shown in (3.2.7). For analytical and simulation purposes, we assume Gaussian distribution with zero mean and variance σ_j^2 for jitter [WLW09]. Thus, the received signal is given by

$$W_{rx}(t) = \sqrt{E_r} \sum_n p(t - nT_s - d_n\Delta - \gamma_n - j(n)) + n(t), \quad (3.2.7)$$

where E_r is the energy of the received pulse, $j(n) \sim \mathcal{N}(0, \sigma_j^2)$ is the random jitter in the received signal and $n(t)$ is the receiver noise on the received signal.

The third part of the system model is the detector/demodulator, which demodulates the signal represented in (3.2.7). In the signal model, a single user UWB system with no multiple access interference is assumed. However, it is straight forward to extend the techniques proposed in this chapter for multi-user system.

In the subsequent sections, we will show how to optimally design the modulator and detector to the constraints of hardware and regulatory bodies. We will also evaluate the theoretical performance of the demodulator for the chosen modulator. In the next section, we will discuss some of the challenges in the transmission and detection of UWB pulses from the regulatory bodies and hardware perspective.

3.3 UWB Constraints

The FCC regulations are among the most popular regulations for UWB, and most of the regulations in other countries are derived from these regulations. The FCC regulations, [FCC02], define a UWB system as any intentional radiator having an absolute 10 dB bandwidth greater than 500 MHz, or a relative bandwidth greater than 20%. Since UWB systems have to co-exist with other narrowband technologies, the compliance requirements from regulatory bodies for UWB systems are very

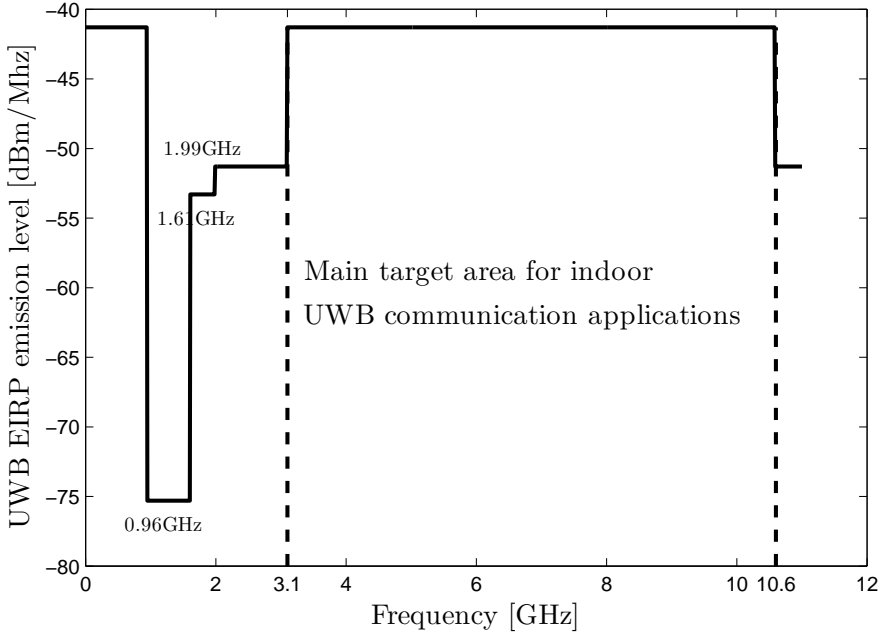


Figure 3.3: Spectral mask specified by FCC showing the equivalent isotropic radiated power (EIRP) versus frequency for indoor UWB system.

stringent to ensure that they do not interfere with the existing narrowband systems. This makes the design of UWB for communication challenging. These requirements are generally specified through constraints on maximal average power P_{av} , and maximal peak power P_{pk} . The average power, P_{av} is measured using a spectrum analyzer (SA) with resolution bandwidth (RBW) $B_{av} = 1$ MHz. The maximal average power constraints are specified through spectral masks. Figure 3.3 shows the FCC mandated spectral mask for indoor UWB emissions. P_{pk} should not exceed 0 dBm when measured using an SA with RBW set to 50 MHz.

The pulse repetition rate (PRF) (that is, $1/T_s$ in (3.2.6)) of the IR-UWB signal plays a significant role on how the UWB device impacts other narrow band receivers in its range; these receivers are called victim receivers [FCC02]. If the PRF is larger than the bandwidth of the victim receiver, then the emission may appear as noise like to the victim receiver. This effect is proportional to the average power of the UWB signal within the receiver's bandwidth. If pulse rate is smaller than the victim receivers bandwidth, then UWB signal would appear like impulse noise to the victim receiver and the effect is proportional to the peak power of the UWB signal. Thus, at low PRF the output levels are constrained by the limit on the peak emission

levels, and at high PRF by the limit on the average emission levels [FCC02].

In [TAW05], the authors specify the existence of two distinct regimes where only one of the two power constraints are active for the IR-UWB signal. For PRF less than 1 MHz, peak constraints are active; for PRF greater than 1 MHz, average power constraints are active. The signaling proposed in this chapter is optimized for high rate data communication and hence, high PRF is assumed as $\gg 1$ MHz yielding only the average power constraint relevant.

3.4 UWB Hardware

Larger bandwidth of ultra wideband signals also enables suboptimal receiver designs, which are more efficient from cost and complexity perspective. Some of these low cost designs can be found at [ADH13, KNX⁺12]. We briefly discussed this in Chapter 1. In this chapter, we propose the hardware architecture platform of [ADH13] for communication. The modulator algorithm on FPGA will generate control signals required to trigger the step recovery diode to generate UWB pulses. On the receive side, the transceiver has an energy detector. Whenever the signal energy crosses a certain threshold, it sends a “Start/Stop” signal to time-to-digital converter (TDC). TDC measures the interval between the pulses, which carries information in the PPM variant physical layer signaling. This information is further processed by the demodulator algorithm on FPGA to demodulate the symbol. Estimating the RTT on unmodulated signal can be used to localize objects as discussed in [ADH13]. Thus, this low complexity transceiver can be used for both localization and communication [YDAH13].

In general, in a low complexity UWB transmitter, it is not possible to transmit arbitrary close pulses because of the recovery time required for the micro electronic devices used in them. This creates a constraint on the signaling that the pulses need to be separated by at least a minimum distance equal to the recovery time. This is the reason for having γ_n in (3.2.6). Also, at the detector it is not possible to resolve between arbitrarily close pulses. Thus the modulation index Δ in (3.2.6) cannot be arbitrarily small.

3.5 Modulator

A periodic train of impulses will result in a spectral comb formation in the power spectral density (PSD) function. This results in inefficient usage of power and reduces the range of UWB nodes as the spectral peaks can cross the power levels specified in Figure 3.3. One way to overcome the spectral comb formation is to randomize the pulse interval. As an illustrative example, we can choose the probability density function (PDF) of pulse repetition period T_{PRF} as a uniform distribution

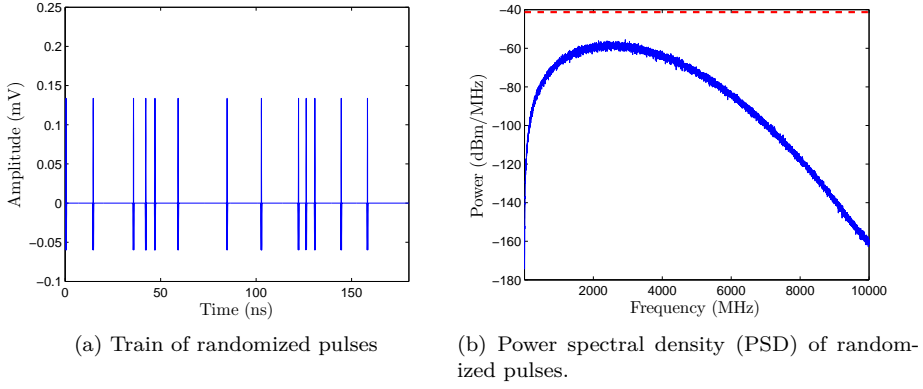


Figure 3.4: Train of pulses with randomized pulse interval and its PSD. $T_s = 18$ ns is employed and 1000 pulses are considered for computing PSD. Dashed line in (b) indicates -41.3 dBm/MHz.

given by

$$p(T_{\text{PRT}}) = \begin{cases} \frac{1}{2T_s - T} & \text{If } T \leq T_{\text{PRT}} \leq 2T_s, \\ 0 & \text{Otherwise.} \end{cases} \quad (3.5.1)$$

Here T , which is $\ll T_s$ is the pulse width of the pulses. T_{PRT} is varied from T instead of 0 to avoid collision between pulses. A train of these pulses is shown in Figure 3.4a and its power spectrum is shown in Figure 3.4b. For this kind of signaling on average, the pulse rate will be close to $1/T_s$ and the power spectrum will be smooth, as shown in Figure 3.4b ($T_s = 18$ ns, $T = 1$ ns).

As discussed in Section 3.4, it is not possible from the hardware perspective to generate arbitrarily close pulses. Also, from the detector perspective it is not possible to resolve the timing between arbitrarily close pulses. For example, in the hardware architecture proposed in [ADH13], the step recovery diode used in the transmitter has a fixed recovery time preventing the generation of close pulses; and TDC used in the detector has a fixed time resolution preventing the detection of close pulses. One way to design the signaling is to have γ_n in (3.2.6) equal to the minimum separation needed between the pulses T_{ms} , and modulation index Δ in (3.2.6) equal to the detectors sensitivity (TDC time resolution). Thus, the resulting transmitted signal assuming 1 symbol per pulse is given by

$$W_{\text{tr}}(t) = \sum_n p(t - nT_s - d_n\Delta - T_{\text{ms}}). \quad (3.5.2)$$

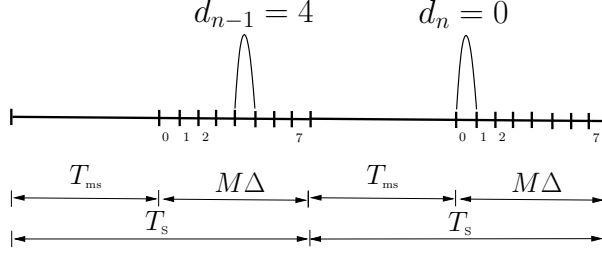


Figure 3.5: Signal employed to have γ_n in (3.2.6) equal to the minimum separation needed between the pulses T_{ms} and modulation index Δ in (3.2.6) is equal to the detectors sensitivity. Here $M = 8$ is assumed. No memory is employed in the signaling between symbols, hence it is called no-memory signaling.

Figure 3.5 shows the illustration of this signaling. Each symbol has a fixed gap of T_{ms} in the beginning between $[0, T_{ms}]$ and the modulated RF pulse in the interval $M\Delta$ between $(T_{ms}, T_s]$. The symbol time T_s and bitrate R_b is given by

$$T_s = T_{ms} + \Delta M, \quad (3.5.3)$$

and

$$R_b = \frac{\log_2 M}{T_s}. \quad (3.5.4)$$

For any UWB hardware, the T_{ms} and Δ are fixed. They come from the two UWB hardware constraints discussed above. The modulation parameter M can be picked to maximize the bitrate. To do this, (3.5.4) is evaluated and the optimal M that maximizes the bitrate, R_b , is chosen. The variation of R_b versus M for various ratio's of T_{ms}/Δ (indicating different transceiver hardware) is shown in Figure 3.6a. The bitrate R_b for the optimal choice of M versus T_{ms}/Δ is shown in Figure 3.6b. The bitrate peak to around 160 Mbps at $M = 8$ when the typical parameter values of $T_{ms} = 10$ ns and $\Delta = 1$ ns for the in-house UWB-platform is considered.

The modulator algorithm which modulates the input symbol vector, \mathbf{d} , is shown in Algorithm 3.1. The algorithm is initialized with X and Y denoting the TDC resolution and diode recovery time respectively [ZSZ10, ADH13]. The method generateRFPulse in line 6 of the algorithm is used to generate the train of RF pulses as shown in (3.5.2). In the in-house prototype UWB platform, this is accomplished by generating a trigger control signal from FPGA to the step recovery diode in the transmitter [ADH13]. Since no memory is employed between symbols in this signaling, it is called no-memory signaling. This modulator was introduced and briefly described in [YDAH13].

A variant of the M-PPM signal shown in (3.5.2) with $T_{ms} = 10$ ns and modulation index $\Delta = 1$ ns is generated. 5 pulses of this signal are shown in Figure 3.7a.

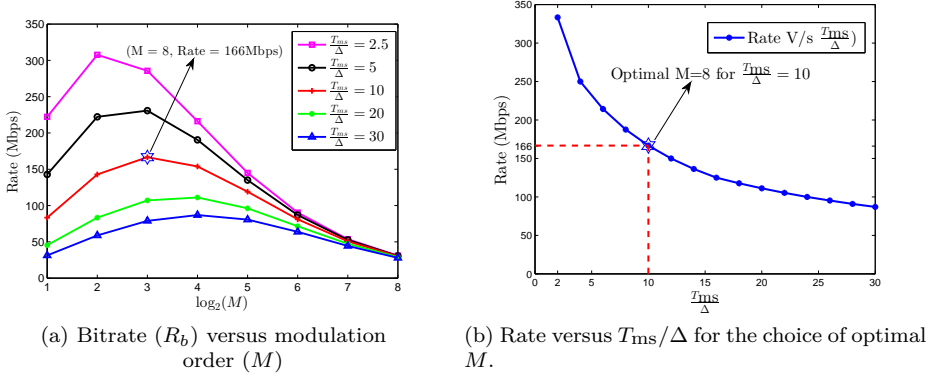


Figure 3.6: Bitrate R_b varies with the modulation order M . Choice of optimal M , where bitrate peaks depends on T_{ms}/Δ . Bitrate peaks at $M = 8$ for the nominal parameter values for the in-house hardware consisting of $T_{ms} = 10$ ns and $\Delta = 1$ ns.

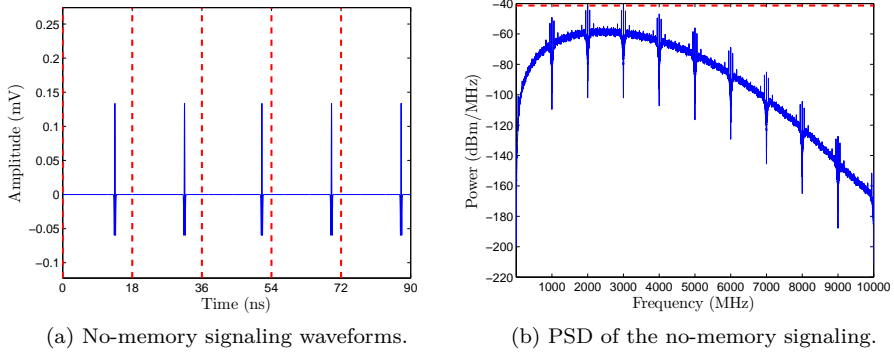


Figure 3.7: No-memory signaling and its PSD with $M = 8$, $\Delta = 1$ ns, and $T_{ms}/\Delta = 10$. For computing PSD, 1000 pulses are considered. The dashed vertical line in (a) indicates the symbol boundary, and the dashed horizontal line in (b) indicates -41.3 dBm/MHz, average power constraint defined by the FCC.

Algorithm 3.1: No-memory Signaling for UWB Modulator

```

1 Algorithm NoMemoryModulator(d)
2    $\Delta \leftarrow X$  ▷ Initialize to TDC Resolution
3    $T_{\text{ms}} \leftarrow Y$  ▷ Initialize to diode recovery time
4    $n \leftarrow 1$ 
5   while  $n \leq \text{Length}(\mathbf{d})$  do
6     generateRFPulse( $n, d_n, T_{\text{ms}}, \Delta$ )
7     ▷ Generate pulse  $p(t - nT_s - d_n\Delta - T_{\text{ms}})$ 
8      $n \leftarrow n + 1$ 
9   return

```

Each symbol duration, $T_s = 18 \text{ ns}$, resulting in $\text{PRF} \gg 1 \text{ MHz}$ causing only average power constraint being active. Each symbol constitutes a fixed constant gap of $T_{\text{ms}} = 10 \text{ ns}$, and 3 bits of information are modulated in the remaining $M\Delta = 8 \text{ ns}$ (since $\Delta = 1 \text{ ns}, M = 8$). We cannot achieve as smooth PSD as in Figure 3.4b, because now pulse train has deterministic gaps between pulses (T_{ms}) and the pulse positions are quantized (Δ) for it to work with the chosen UWB hardware; However, the data can be assumed to be random because of interleaving and randomization in the symbol rate chain of the physical layer. This leads to a relatively smooth PSD. The PSD of this signaling scheme is shown in Figure 3.7b.

The signaling employed above has a fixed gap, T_{ms} in every symbol, as shown in (3.5.2). This ensures that minimum separation between pulses is greater than or equal to the recovery time of the diode. If the modulator structure is altered to remember the position of the transmitted pulse for the previous symbol, then the minimum gap needed for the current symbol can be reduced. We define this reduced gap as T'_{ms} and it is illustrated in Figure 3.8. In Figure 3.8, gap T'_{ms} is reduced by 3Δ by remembering the position of the pulse in the previous symbol. The total separation between the pulses is $T_{\text{ms}} = T'_{\text{ms}} + 3\Delta$. Since the total duration of the symbol is constant, the reduction in the gap will result in an increased region for modulated RF pulses. Therefore, this increases the time interval bin widths (modulation index) of the PPM scheme, which in turn increases the demodulator's performance. Figure 3.8 shows the increase in bin widths for the second symbol ($d_n = 0$) as gap, T'_{ms} reduced by 3Δ . Since in this method the transmitter needs to remember the past transmitted symbol to decide on T'_{ms} for the current symbol, we call this signaling as with-memory signaling. The algorithm for implementing this modulator is shown in Algorithm 3.2. It is initialized with X and Y denoting the TDC resolution, Δ and diode recovery time, T_{ms} . The algorithm takes a vector of symbols, \mathbf{d} , and calls generateRFPulse with different bin widths Δ_n and gap T'_{ms} to generate the train of RF pulses defined in (3.5.2).

The two primary benefits of this signaling are summarized below.

1. There is better detectability due to an increase in the bin widths (modulation

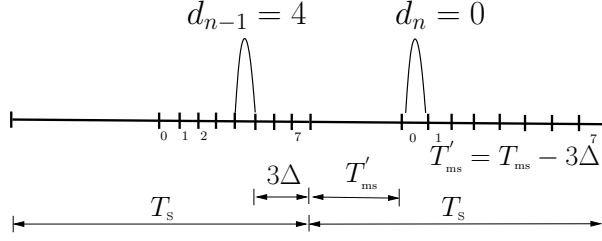


Figure 3.8: With-memory signaling for UWB modulator showing the reduction in the gap T'_ms in the current symbol by remembering the position of the pulse in the previous symbol. $M = 8$ is assumed.

Algorithm 3.2: With-memory Signaling for UWB Modulator

```

1 Algorithm WithMemoryModulator(d)
2    $\Delta_1 = X$  ▷ Initialize to TDC resolution
3    $T'_{ms} = T_{ms} = Y$  ▷ Initialize to diode recovery time
4    $n \leftarrow 2$ 
5   generateRFPulse(1,  $d_1$ ,  $T'_{ms}$ ,  $\Delta$ )
6   ▷ Generate pulse  $p(t - T_s - d_1\Delta_1 - T'_{ms})$ .
7   while  $n \leq \text{Length}(d)$  do
8      $T'_{ms} \leftarrow T_{ms} - ((M - 1) - d_{n-1})\Delta_{n-1}$ 
9     if  $T'_{ms} < 0$  then
10       $T'_{ms} \leftarrow 0$ 
11       $\Delta_n \leftarrow \frac{T_s - T'_{ms}}{M}$ 
12      generateRFPulse( $n$ ,  $d_n$ ,  $T'_{ms}$ ,  $\Delta_n$ )
13      ▷ Generate pulse  $p(t - nT_s - d_n\Delta_n - T'_{ms})$ .
14       $n \leftarrow n + 1$ 
15   return

```

index) as explained before. Later in this chapter, we compare the performance (in terms of SER) of this signaling with no-memory signaling.

2. The with-memory signaling leads to a better randomization of the pulses. In contrast to no-memory signaling, there are no deterministic gaps and pulses spread to all regions of the symbol interval.

The impact of the second point above is further smoothing of the PSD. Figure 3.9a shows 5 symbols in the time domain, and Figure 3.9b shows the PSD of with-

memory signaling using 1000 randomly generated bits. The order M is chosen as 8, recovery time $T_{\text{ms}} = 10$ ns and modulation index $\Delta = 1$ ns, as discussed above.

Comparing Figure 3.9b and Figure 3.7b indicates significant smoothening of the PSD by using with-memory signaling. This will enable the transmitter to generate pulses at a higher amplitude without violating the mask specification of the regulatory bodies, thereby increasing the range of communication. Furthermore, Figure 3.9a and Figure 3.7a indicates that the pulse amplitude can be increased by approximately 4 times compared to the no-memory signaling, without violating the regulatory bodies specifications, with the hardware having similar constraints. For the deterministic single-path propagation model, the path loss, PL, is given by

$$\text{PL} = \frac{(4\pi df)^2}{c}, \quad (3.5.5)$$

where f is the frequency of operation, d is the range, and c is the speed of light [Sko08]. The received power, P_{rx} , for transmitted power, P_{tx} , is given by

$$P_{\text{rx}} = \frac{P_{\text{tx}}}{\text{PL}}. \quad (3.5.6)$$

An amplitude increase of 4 times results in 16 times (12 dB) increase in power. Since path loss is proportional to the square of the distance as given by (3.5.5), for any given received power and frequency of operation, if d_1 and d_2 are ranges for transmitters employing no-memory and with-memory signaling, then

$$\frac{P_{\text{tx}}}{d_1^2} = \frac{16P_{\text{tx}}}{d_2^2}, \quad (3.5.7)$$

which leads to

$$d_2 = 4d_1. \quad (3.5.8)$$

Equation (3.5.8) means that the range in the with-memory signaling can be increased by 4 times compared to the no-memory signaling. This increased range comes with a cost of increased complexity in the modulator, as shown in Algorithm 3.2.

In the next section, we will evaluate the performance of the demodulator for the proposed signaling scheme.

3.6 Detector Performance

In this section, we propose a detector for the modulators proposed before and evaluate its performance. For analytical discussion, we assume that the symbol timing acquisition procedure has been performed prior to data transmission. For the no-memory signaling modulator with $M = 8$, a hard decision demodulator is designed. The demodulator uses the quantized 8 time interval bins as defined in Table 3.1. This is also illustrated in Figure 3.10.

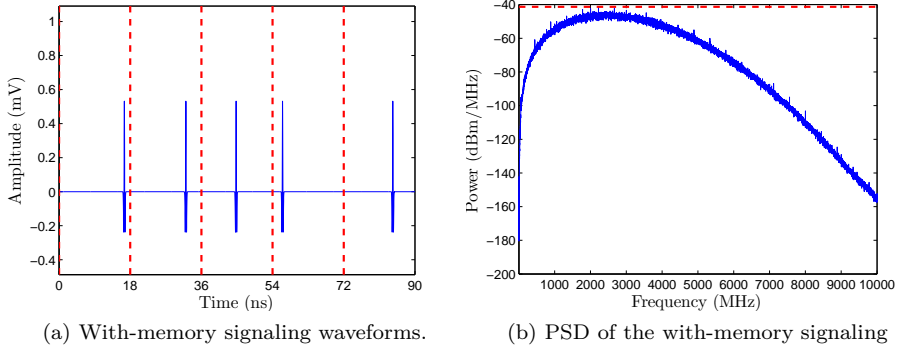


Figure 3.9: With-memory signaling and its PSD with $M = 8$, $\Delta = 1$ ns and $T_{\text{ms}}/\Delta = 10$. For computing PSD, 1000 pulses are considered. The dashed vertical line in (a) indicates the symbol boundary, and the dashed horizontal line in (b) indicates -41.3 dBm/MHz, average power constraint defined by the FCC.

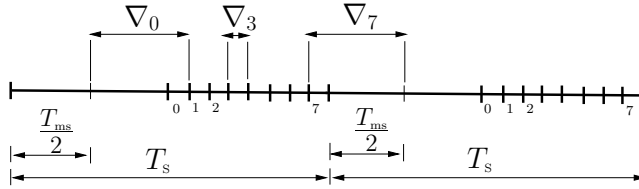


Figure 3.10: Quantized time bins used by the hard decision detector. The corner bins are wider than the middle bins.

Quantized time Intervals for hard decision demodulation	
∇_0	$[(\frac{T_{\text{ms}}}{2}) - (T_{\text{ms}} + \Delta)]$
∇_i	$[(i\Delta - ((i + 1)\Delta)]$ for $i \in [1, \dots, 6]$
∇_7	$[(T_{\text{ms}} + 7\Delta) - (T_s + \frac{T_{\text{ms}}}{2})]$

Table 3.1: Time Intervals used for hard decision demodulation.

Algorithm 3.3: Hard decision demodulation for no-memory signaling

```

1 Algorithm HardDecision(r)
2   for  $j \leftarrow 1$  to Length(r) do
3      $\nabla \leftarrow \text{PeakPosition}(\mathbf{r}[j])$ 
4        $\triangleright$  Find the position of the peak for symbol  $j$ 
5       if  $\nabla \in \nabla_i, i \in [0, \dots, 7]$  then
6          $\triangleright \nabla_i$ s are defined in Table 3.1
6          $\text{ds}[j] \leftarrow i$ 
6   return

```

The intervals for two corner bins are larger because the detector can exploit the dead time T_{ms} left for the diode recovery. The algorithm for the hard decision demodulation is shown in Algorithm 3.3. The algorithm demodulates the received vector, \mathbf{r} , into a vector, \mathbf{ds} . The function “PeakPosition” in line 3 of the algorithm returns the peak position of the received pulse for symbol- j . The function “Length”, returns the number of symbols and $\mathbf{r}[j]$ denotes the address of the j -th symbol.

The performance bounds for the no-memory signaling can be derived in terms of SER. The received signal is as defined in (3.2.7). For no-memory signaling transmitter, the received signal at the receiver will have $\gamma_n = T_{\text{ms}}$ and is given by

$$W_{\text{rx}}(t) = \sqrt{E_r} \sum_n p(t - nT_s - d_n\Delta - T_{\text{ms}} - j(n)) + n(t). \quad (3.6.1)$$

As shown in the Table 3.1, from the detector perspective there are three different types of symbols. The first symbol 0 and the last symbol 7 have a much larger detection probability, since their decision intervals (∇_0, ∇_7) are large. The middle symbols [1 – 6] have the same and smaller decision intervals $\nabla_i = \Delta, i \in [1, 6]$. In general, if the modulation order is M , and all symbols are equally likely, then the corner symbols will occur each with a probability of $1/M$ and middle symbols with $(M - 2)/M$. If P_{e1} is the probability of a symbol error for the middle symbol, and P_{e2} and P_{e3} are the probabilities of symbol errors for the corner symbols, then the probability of symbol error P_e is the average of the three types of errors; P_{e1} , P_{e2} , and P_{e3} (refer to Table 3.1 and Figure 3.10). Therefore,

$$\begin{aligned}
P_e &= \left(\frac{M-2}{M}\right) P_{e1} + \left(\frac{1}{M}\right) P_{e2} + \left(\frac{1}{M}\right) P_{e3}, \\
&= \left(\frac{M-2}{M}\right) P_{e1} + \left(\frac{2}{M}\right) P_{e2}.
\end{aligned} \quad (3.6.2)$$

Where, we assumed $P_{e2} = P_{e3}$ in the second equality, Further, substituting for P_{e1}

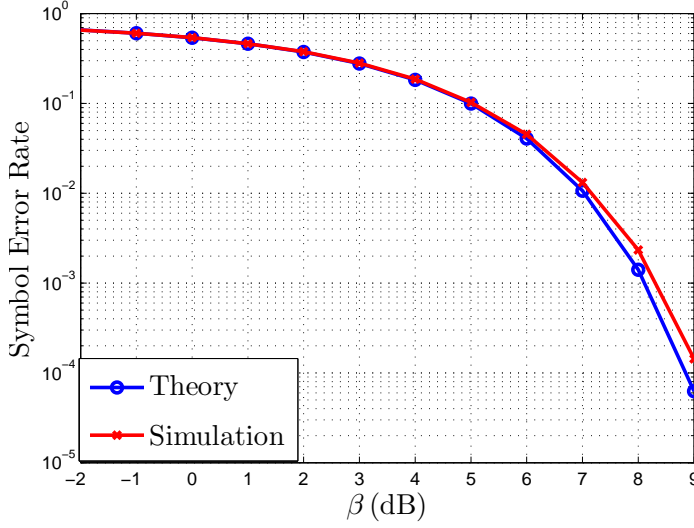


Figure 3.11: Comparison of theoretical and simulation performance in terms of SER for hard decision detection based demodulator for the no-memory signaling.

and P_{e2} in (3.6.2) we get,

$$\begin{aligned}
 P_e &= 2 \left(\frac{M-2}{M} \right) \Pr \left(x > \frac{\Delta}{2} \right) \\
 &\quad + \frac{2}{M} \left(\Pr \left(x > \frac{\Delta}{2} \right) + \Pr \left(x > \frac{\Delta + T_{ms}}{2} \right) \right) \\
 &= 2 \left(\frac{M-1}{M} \right) \Pr \left(x > \frac{\Delta}{2} \right) \\
 &\quad + \frac{2}{M} \Pr \left(x > \frac{\Delta + T_{ms}}{2} \right).
 \end{aligned} \tag{3.6.3}$$

When the signal in (3.6.1) is passed through a peak detector, the combined effect of the jitter $j(n)$ and noise $n(t)$ on the peak detector will cause an error in the peak position. This error in the peak position $w(n)$ can be assumed to be Gaussian distributed with mean 0 and variance σ^2 . Therefore we get

$$\begin{aligned}
 \Pr \left(x > \frac{\Delta}{2} \right) &= \frac{1}{\sqrt{2\pi\sigma^2}} \int_{\frac{\Delta}{2}}^{\infty} \exp \left(\frac{-x^2}{2\sigma^2} \right) dx \\
 &= Q \left(\frac{\beta}{2} \right),
 \end{aligned} \tag{3.6.4}$$

where $Q(\cdot)$ denotes the tail probability of the standard normal distribution. The parameter β is the ratio of bin width Δ to standard deviation σ of the random errors in the peak position. Similarly,

$$\begin{aligned} \Pr\left(x > \frac{\Delta + T_{\text{ms}}}{2}\right) &= \frac{1}{\sqrt{2\pi\sigma^2}} \int_{\frac{\Delta + T_{\text{ms}}}{2}}^{\infty} \exp\left(\frac{-x^2}{2\sigma^2}\right) dx \\ &= Q\left(\frac{\Delta + T_{\text{ms}}}{2\sigma}\right) \\ &= Q\left(\frac{(1 + \alpha)\beta}{2}\right). \end{aligned} \quad (3.6.5)$$

Here in the third equality, transceiver specific ratio $(T_{\text{ms}}/\Delta) = \alpha$ is assumed. Substituting (3.6.4) and (3.6.5) in (3.6.3), the symbol error probability P_e is given by

$$P_e = 2 \left\{ \left(\frac{M-1}{M} \right) Q\left(\frac{\beta}{2}\right) + \frac{1}{M} Q\left(\frac{(1+\alpha)\beta}{2}\right) \right\}, \quad (3.6.6)$$

where $\beta = \Delta/\sigma$ and $\alpha = T_{\text{ms}}/\Delta$.

The performance of the proposed detector is evaluated in simulations with $M = 8$, $\Delta = 1 \text{ ns}$ and $T_{\text{ms}} = 10 \text{ ns}$ ($\alpha = 10$). The simulation consisted of 200000 randomly generated symbols. The SER for various β values are shown in Figure 3.11. A strong correlation for P_e between theory and simulation is observed.

Algorithm 3.4: Hard decision demodulation for with-memory signaling

```

1 Algorithm HardDecisionDemod(r)
  ▷ Demodulate the 1st symbol
2    $\Delta \leftarrow \frac{T_s - T_{\text{ms}}}{M}$ 
3    $\nabla = \text{PeakPosition}(\mathbf{r}[1])$ 
4   if  $\nabla \in \nabla_i \quad i \in 0, \dots, 7$  then
5      $\text{ds}[1] \leftarrow i$ 
6   for  $j = 2 \rightarrow \text{Length}(\mathbf{r})$  do
7      $T'_{\text{ms}} = T_{\text{ms}} - ((M-1) - \text{ds}[j-1])\Delta$ 
8      $\Delta \leftarrow \frac{T_s - T'_{\text{ms}}}{M}$ 
9      $\nabla = \text{PeakPosition}(\mathbf{r}[j])$ 
10    if  $\nabla \in \nabla_i \quad i \in 0, \dots, 7$  then
11       $\text{ds}[j] \leftarrow i$ 
12  return

```

▷ ∇_i s are defined in Table 3.1
 ▷ New Δ computed above is used

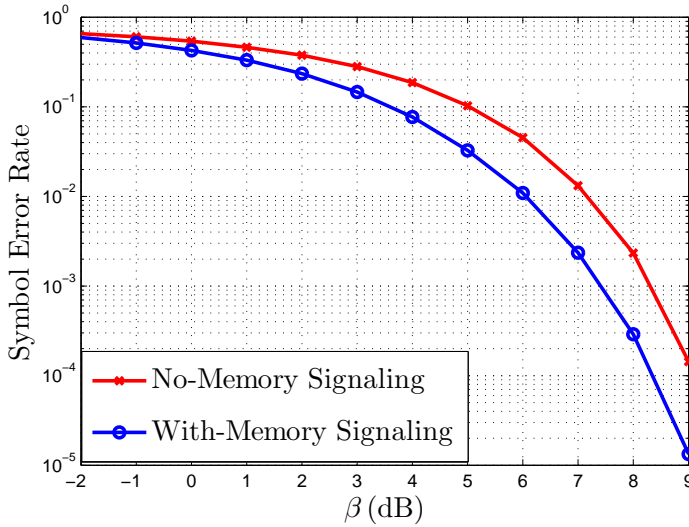


Figure 3.12: Comparison of performance of no-memory and with-memory signaling in terms of SER.

Earlier, we proposed a modified signaling with memory in the modulator (with-memory signaling), which claimed to have two benefits:

1. A better detectability due to an increase in the bin widths (modulation index), as explained before.
2. Better randomization of the pulses. Unlike in the no-memory signaling, there are no deterministic gaps and pulses are spread to all regions of the symbol interval.

The impact of the second point is further smoothing of the PSD, which is demonstrated earlier with the PSD plots. To quantify the performance improvement due to the first point, detector performance of with-memory signaling and no-memory signaling needs to be compared. We implemented a hard decision detection algorithm for the with-memory signaling. This algorithm is described in Algorithm 3.4. The algorithm demodulates the received vector, \mathbf{r} , into a vector \mathbf{ds} . Parameters T_{ms} and T_s in the algorithm should be the same as those used in the with-memory modulator algorithm defined in Algorithm 3.2. The PeakPosition in line 4 of the algorithm returns the peak position of the received pulse. This algorithm is similar to the no-memory demodulator defined in Algorithm 3.3, except that the bin width Δ_i changes between symbols, and it depends on the previous bin width and previously decoded symbol.

It is not straightforward to obtain a closed-form analytical expression for the performance of the with-memory signaling. In the with-memory signaling, on average $T'_{\text{ms}} < T_{\text{ms}}$. If we assume that all the symbols are equally likely, then the average symbol value ($\in [0, M-1]$) for the previous symbol is $(M-1)/2$, therefore on average T'_{ms} is given by

$$T'_{\text{ms}} = T_{\text{ms}} - \frac{(M-1)}{2} \Delta. \quad (3.6.7)$$

Therefore, average bin width for with-memory signaling is given by

$$\Delta' = \frac{T_s - T'_{\text{ms}}}{M} \quad (3.6.8)$$

$$= \frac{T_{\text{ms}} - T'_{\text{ms}} + M\Delta}{M}, \quad (3.6.9)$$

where in the second equality follows after substituting for T_s from (3.5.3). Further applying (3.6.7) to (3.6.9) we get

$$\Delta' = \left(\frac{3M-1}{2M} \right) \Delta. \quad (3.6.10)$$

If we define β' as the ratio of Δ'/σ then we have

$$\beta' = \left(\frac{3M-1}{2M} \right) \beta. \quad (3.6.11)$$

Substituting (3.6.11) in (3.6.6) we get the symbol error probability for the with-memory signaling and is given by

$$P_e = 2 \left\{ \left(\frac{M-1}{M} \right) Q \left(\frac{(3M-1)\beta}{4M} \right) + \frac{1}{M} Q \left(\frac{(1+\alpha)(3M-1)\beta}{4M} \right) \right\}. \quad (3.6.12)$$

From (3.6.10), for $M = 8$ we get an average bin width for the $\Delta' = 1.43\Delta$, This increase in the bin width will result in better detectability of symbols at receiver. In simulation it was observed that the bin width increases by $\Delta' = 1.32\Delta$. This reduction in the bin width is due to line 9 - 12 in the modulator Algorithm 3.2, where in order to ensure one pulse per symbol period, T'_{ms} is forced to zero resulting in the reduction of bin width for the transmitted symbol. The performance of the detector for with-memory signaling is evaluated in simulation with 200000 randomly generated samples, and the results are compared with no-memory signaling. Figure 3.12 compares the performance of the hard decision detectors for the no-memory and with-memory signaling schemes. A gain of approximately 1 dB can be achieved in terms of SNR at SER of 10^{-2} by using the with-memory signaling.

The presented SER performance for the proposed signaling schemes are valid for the transceivers which are in line of sight (LOS) with short distance between

them and having highly directional antennas as discussed in Section 3.2. For these systems we can assume a simple AWGN channel model. However, for systems having fading channels with multi-path, channel equalization and time of arrival (TOA) estimation need to be performed prior to demodulation. The SER performance of the proposed signaling schemes in such systems depends on the performance of the channel equalization and TOA estimation algorithms.

3.7 Conclusion

In this chapter, we proposed a custom signaling which is a variant of PPM signaling for IR-UWB communication. We also proposed an alternative signaling called with-memory signaling, which requires memory in the modulator and demodulator however can further smoothen PSD compared to no-memory signaling. The result of this is illustrated in Figure 3.9b. We showed that range can be increased by four times compared to no-memory signaling, without violating the regulatory body constraints. This gain comes with a cost of increased complexity in the modulator and demodulator, as discussed in the modulator and demodulator Algorithms 3.2 and 3.4 respectively. We also derived the theoretical closed form expression for a hard decision demodulator with no-memory signaling. We compared the performance of the simulations with the derived theoretical result; This is illustrated in Figure 3.11. We implemented a detector for the with-memory signaling proposed in this chapter. The detector performance of with-memory signaling is compared with the detector performance for no-memory signaling. We showed that with-memory signaling can improve the detector performance by approximately 1 dB at 10^{-2} SER. Results are illustrated in the Figure 3.12.

The performance of the proposed signaling methods of this chapter are demonstrated in simulations in order to assess the performance gains without many platform dependencies. The proposed schemes are valid for any low cost UWB hardware platform employing a step recovery diode at the transmitter and having a need for minimum time resolution between pulses at the detector for detection. The transceiver in Figure 3.1 will be an integral part of our next generation infrastructure free indoor position system [NZSH13]. The radio here should be used not only for ranging but also for the wireless communication and thus fulfill a need for the proposed method. Today, we can use commercial UWB ranging like TimeDomain for this purpose, however these systems do not have high bitrate communication capabilities. The results of the proposed signaling methods indicate the possibility of achieving a higher bitrate in excess of 150 Mbps with low probability of error in detection as suggested by the performance curves using the parameters from our transceiver hardware. With these findings, one can further develop the work to implement the proposed algorithms in to our transceiver system and evaluate the performance of in-house transceiver hardware discussed in Chapter 1. The proposed algorithms and methods are explained in the context of in-house UWB hardware; however, the results are of general importance which could enable engineers to ap-

ply similar methods and algorithms towards the design of UWB communication system.

Location Aided UWB Communication

The multiple access scheduling decides how the channel is shared among the nodes in the network. Typical scheduling algorithms aims at increasing the channel utilization and thereby throughput of the network. This chapter describes several algorithms for generating an optimal schedule in terms of channel utilization for multiple access by utilizing range information in a fully connected network. We also provide detailed analysis of the proposed algorithms performance in terms of their complexity, convergence, and effect of non-idealities in the network. The performance of the proposed schemes are compared with non-aided methods to quantify the benefits of exploiting the range information in the communication. The proposed methods have several favorable properties for the scalable systems. We show that the proposed techniques yields better channel utilization and throughput as the number of nodes in the network increases. The discussed methods in this chapter indicate that the throughput can be increased on average by **3 – 10** times for typical network configurations.

4.1 Background

The recent advances in sensor technology have resulted in development of low-cost, low-power sensors, which are capable of sensing, data processing, and communication. Many sensor networks have a large number of sensor nodes, which are densely deployed over a wide geographical region to track a certain physical phenomenon [HHKK04, RLK⁺09]. These sensors could have a fixed topology, as in the case of smart sensors used in structural health monitoring [NJ07], or have a dynamic topology, as in the case of sensors mounted on autonomous robots (see applications discussed in [AR98, MGF⁺05, KMPK13]).

In sensor networks, there are many situations where every node needs to transmit a message to every other node at regular intervals. This type of communication is typically required for information dissemination across the network to accomplish

various tasks such as localization, routing, distributed control and computation. For example, in [NZSH13, RRS⁺11] firefighter agents share information at regular intervals through point to multi-point communication, where every agent broadcasts sensor data, like position, temperature, visibility, etc., to all other agents. This provides every firefighter with relevant information about other firefighters, thereby increasing the efficiency of operation. This is illustrated in Figure 4.1.

This type of communication can also be found in the cooperating swarm of micro unmanned aerial vehicles (UAVs). These are low payload carrying, scaled down quadrotor platforms with relevant sensors mounted on them [KMPK13]. Constant updates (communication) between sensors are essential in many UAV networks, as they need to coordinate to accomplish the required tasks. These updates could include sensor data, position information, etc. Fig. 4.2 shows a graphical depiction of quadcopters in a particular geometric formation. Similar regular broadcast communication by sensor nodes can also be found in other swarm networks as discussed in [AR98, NRP⁺05, MGF⁺05]. Reporting the health of each sensor node to all other nodes in wireless sensor networks (WSN) as described in [BA02] also requires regular communication. In underwater acoustic (UWA) sensor networks broadcast communication of similar nature is used for time-synchronization, coordination, self-configuration and localization [KMH11, APM04]. All these networks employ some form of all-to-all broadcast communication between nodes.

Sensor networks in which each sensor has to share information constantly with the other sensors through all-to-all broadcast can be accomplished efficiently by communicating through a shared broadcast channel. As the density of the sensor network increases, the effective bitrate per sensor, R_s , drops, since the total bitrate, R_b , supported by the shared broadcast channel is fixed. In many sensor networks, there exists a long propagation delay in communication in relation to the scheduled access duration (packet length)¹ of the shared channel. This can arise either due to low propagation speed of the physical layer signal in the medium or large distances between sensors (geometric size of the topology). For example, in UWA sensor networks, the propagation of acoustic signal in water is five orders of magnitude slower than in wireless radio channel, coupled with the large distances between sensors in oceans make the above scenario common in these networks. Similar scenarios exist in few wireless sensor networks (WSN) employing impulse radio UWB (IR-UWB) and millimeter wave (mmWave) technologies. In IR-UWB and mmWave channels with high directivity gain can have delay spread of order of few tens of nano-seconds, thus can have small access schedules [KWA⁺04, ZNCO⁺14, MSR15].

In this chapter, we develop an efficient broadcast schedule to access the shared channel by exploiting the propagation delays between sensor nodes. We define one report cycle (update cycle), T_R , as the total time during which all the nodes in the sensor network have transmitted and received one message packet to and from all the other nodes in the network. We use this performance metric to assess the performance of various schemes discussed in this chapter.

¹Packet length and access duration are used interchangeably.

The main aim of this chapter is to detail novel methods that optimize the multiple access schedule by exploiting the spatial-temporal aspect of the channel for the problem discussed above. As will be shown in Section 4.2, this can be posed as an optimization problem, the solution for which is non-convex and computational complexity scales exponentially with the increase in the number of nodes. There are several works in UWA networks, where this problem is addressed, particularly for accomplishing tasks such as self localization. For example, in [SJ01], the interference free all-to-all broadcast in the UWA sensor networks is posed as an optimization problem, which is similar to the problem formulation in Section 4.2. A suboptimal solution is obtained in [SJ01] using a heuristic method, which relaxes the constraints to enable schedule computation for the nodes in a sequential order. However, a better schedule can be obtained by increasing the computational complexity by changing the optimization problem, so that it can be solved using convex methods, traveling salesman problem (TSP) and iterative path-adjusting methods proposed in this chapter. This is discussed further in Section 4.3.

All of the proposed methods discussed in this chapter require a centralized sensor network with a powerful coordinator node, which exploits the position information from all participating nodes for all-to-all broadcast schedule construction. In the networks, where the centralized configuration is not possible or position information of the nodes is unavailable, the algorithms proposed in [RFS15, FZTS11] can be employed. However, as will be shown in Section 4.6, solving the broadcast schedule optimization problem using position information can significantly improve performance.

There also exists standard time division multiple access (TDMA) schemes such as slotted floor acquisition multiple access (FAMA) where regulated transmissions for all the nodes can be accomplished [MS06]. However, in a regular time division channel, the shared common channel is slotted in time and each one of the N nodes of the sensor network will have access to a time slot which is a uniform fraction of the report cycle, T_R . As shown in Section 4.2, as the radius of the sensor network topology and the number of nodes in it increase, the throughput per sensor and the update rate decrease. By exploiting the range information, orthogonality can still be maintained for overlapping time slots which leads to higher capacity. For an ideal positioning of the nodes, the throughput can be increased by N times, leading to a significant performance gain. Even when the positions of the nodes are randomly distributed, the performance boost can be substantial in practice. For the realistic examples studied in this chapter, the throughput is increased by an order of magnitude (10 times for 100 node configurations with outliers as discussed in Section 4.6) compared with a regular scheme.

The main discussion topics of this chapter are as summarized below.

- We introduce three novel methods, which exploit the range information for efficient communication for the all-to-all broadcast problem discussed.
- We analyze these methods in terms of computational complexity.

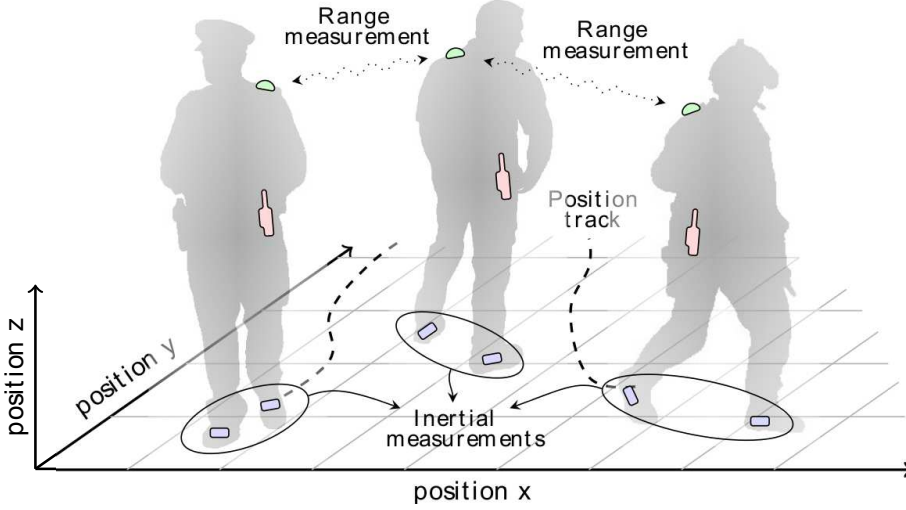


Figure 4.1: Illustration of fire fighters agents sharing information continuously with other agents [NZSH13].

- We discuss the performance analysis of these methods for different topologies and contrast them with standard multiple access protocols such as code division multiple access (CDMA).
- We discuss the robustness of these methods to the non-idealities such as range and synchronization errors.

We will demonstrate the methods using a simple 3 node network shown in Figure 4.3. This will aid us in explaining the algorithms clearly. Subsequently, we will demonstrate the performance of the proposed methods in different network topologies of varied sizes. We use the report cycle, T_R , as a metric to assess performance, with the objective to minimize this parameter.

The rest of the chapter is organized as follows: In Section 4.2, we discuss the system model and formulate the problem. In Section 4.3, we propose algorithms which exploit the range information to provide efficient communication between nodes. In Section 4.4, we study the effect of synchronization and range errors on the proposed algorithms. In Section 4.5, we compare the effective bitrate per sensor, R_s , of the proposed algorithms with the code division multiple access (CDMA) approach. In Section 4.6, we evaluate the proposed methods for a large number of nodes with different topologies and demonstrate the performance gain of exploiting the range information. Finally, in Section 4.7 we discuss the conclusions.

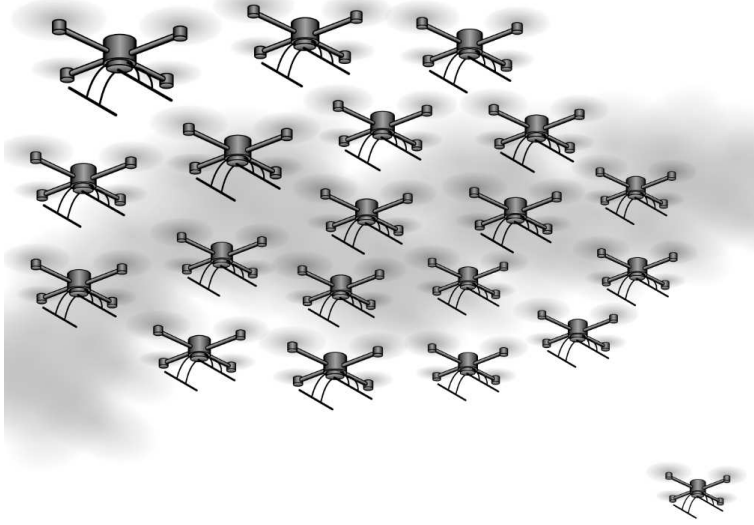


Figure 4.2: A graphical illustration of a geometric configuration of a swarm network of micro quadcopters.

Parameter	Value
d_{AB}	95 m
d_{BC}	110 m
d_{CA}	105 m
\mathcal{L}	30 m
τ	100 ns
μ	3×10^8 m/s

Table 4.1: Configuration for the topology in Figure 4.3.

4.2 System Model and Problem Formulation

Consider a general setup of a fully connected sensor network with N nodes. For the sake of the discussion, we set the access duration (message packet length) per node to be $\tau = 100$ time units. We define the path equivalent message length as $\mathcal{L} = \mu\tau$ length units, where μ is the velocity of the physical layer signal in the propagation medium. The message packets are said to be correctly received, if the packets do not interfere, i.e., there is no collision of packets at the receiving node.

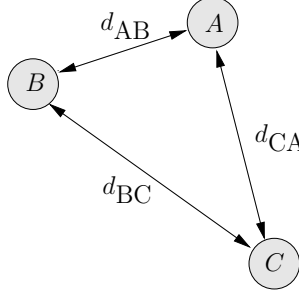


Figure 4.3: Peer-to-peer ad-hoc sensor network with 3 nodes. d_{AB} , d_{BC} and d_{CA} are the path lengths between nodes A , B and C .

4.2.1 Orthogonalization with scheduled transmission

In a network of N nodes, if we assume that the $K = \binom{N}{2}$ range values are available, one approach to orthogonalize the transmission is by creating a sequential schedule, where each node gets to transmit a message every T_D time units, where T_D is given by

$$T_D = \frac{D}{\mu} + \tau, \quad (4.2.1)$$

where D is the maximum of the K range values, that is

$$D = \max_{i,j} \{d_{ij}\}, \forall i, j \in [1, \dots, N], i \neq j. \quad (4.2.2)$$

With this approach, one report cycle, T_R is given by

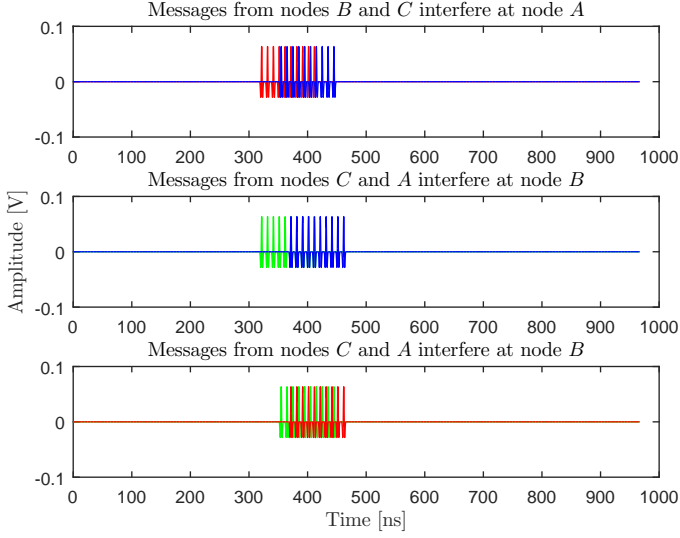
$$T_R = NT_D. \quad (4.2.3)$$

To exemplify the above discussion, consider a 3 node peer-to-peer network as shown in Figure 4.3. For the sake of discussion, the nodes are labeled as A , B , and C . From (4.2.1) and (4.2.2), we get

$$T_D = \frac{\max\{d_{AB}, d_{BC}, d_{CA}\}}{\mu} + \tau = \frac{d_{BC}}{\mu} + \tau. \quad (4.2.4)$$

From (4.2.3), notice that the report cycle, T_R , increases linearly with the number of nodes in the network (N) and the radius of the network topology (D). Therefore, as the number of nodes or the geometric size of the network increases, T_R will increase, resulting in inefficient utilization of the shared common channel; thus, requiring an improved communication method.

In many networks, the geometry of the sensor placements is such that the difference in propagation time for the message packets to arrive at nodes are larger



(a) Interfering message packets due to concurrent transmission.

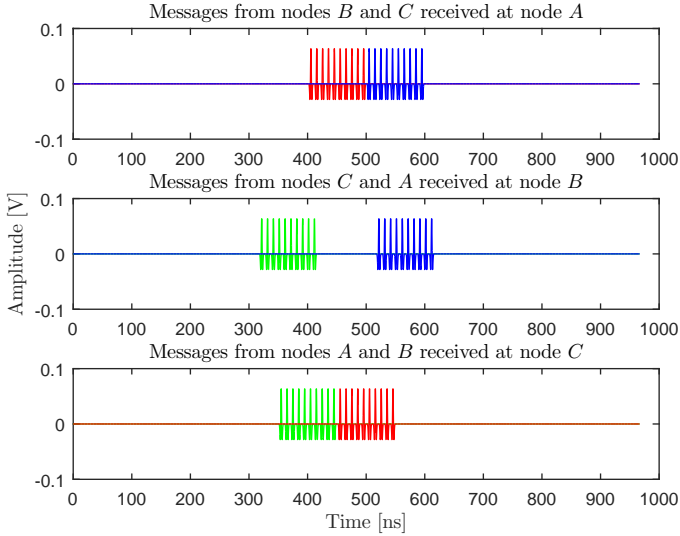
(b) Arrival of packets without interference at A , B and C nodes after introducing delays of $\Delta_B = 84$ ns and $\Delta_C = 150$ ns in B and C nodes, respectively.

Figure 4.4: Concurrent transmission on shared common channel will result in interference as shown in (a). If we solve the optimization problem defined in (4.2.6) then the interference can be mitigated as shown in (b). The signal representing the message packet from nodes A , B and C , $(p_i(t) \mid i \in \{A, B, C\})$ is shown in green, red, and blue respectively. The $\tau = 100$ ns, $\mu = 3 \times 10^8$ m/s, and $\mathcal{L} = 30$ m is considered in the illustration.

than the duration of the message packets themselves. These situations arise in many sensor networks which have small message packets to be shared with other sensors, resulting in a small value of \mathcal{L} . This situation could also arise in future 5G networks, where the physical layer packet lengths of devices in a macro cell are much smaller (on the order of a few microseconds) compared to the cell dimensions (on the order of a few kilometers) [Rap09, RSM⁺13, AIS⁺14, PZD⁺14]. We can reduce the report cycle of the network by exploiting this fact. Consider a sensor network in which the path difference between any two nodes is greater than \mathcal{L} . Then, concurrent transmissions will result in message packets arriving at different times at each node, hence all transmissions are orthogonal. In general, for an N node network to ensure concurrent orthogonal transmissions, the network should fulfill the conditions

$$\begin{aligned} |d_{ki} - d_{kj}| &\geq \mathcal{L} \\ \forall i, j, k \in [1, 2, \dots, N] \mid i, j &\neq k \text{ and } i \neq j, \end{aligned} \quad (4.2.5)$$

where i, j and k denote the distinct nodes in the network and d_{ki} and d_{kj} denote the distance from the k -th node to node i and node j respectively. Thus, the report cycle, T_R , is equal to the maximum path delay, T_D , in the network, instead of NT_D for scheduled transmission as discussed before.

For example, consider the 3 node network shown in Figure 4.3. Suppose, the dimensions of d_{AB} , d_{BC} , and d_{CA} does not follow the specifications of Table 4.1 and if $|d_{AB} - d_{AC}| \geq \mathcal{L}$, then the signal transmitted simultaneously at nodes B and C will arrive at node A at different times, and hence A can correctly receive them. Similarly, $|d_{BA} - d_{BC}| \geq \mathcal{L}$ and $|d_{CA} - d_{CB}| \geq \mathcal{L}$ will ensure correct message packet reception at nodes B and C respectively. Thus, all the three nodes can concurrently transmit, and the report cycle can be completed in T_D .

In general sensor networks, (4.2.5) is rarely fulfilled. When a network with N nodes has a particular geometric configuration, which does not meet condition (4.2.5), we can reduce T_R by introducing a delay Δ_i to each node $i \in [1, 2, \dots, N]$. The Δ_i s are adjusted such that the message packets do not interfere at the receiving nodes. The Δ_i s form the time schedule during which the i -th node needs to transmit. The optimal schedule is obtained by solving the following optimization problem.

$$\begin{aligned} &\underset{\{\Delta_i\}}{\text{minimize}} \quad \max_{i,k} (\Delta_i + \delta_{ki}) \\ &\text{subject to} \quad J = J_1 + J_2 + \dots + J_N = 0, \end{aligned} \quad (4.2.6)$$

where

$$\begin{aligned} J_k &= \left| \int \sum_{ij} p_i(t - \delta_{ki} - \Delta_i) p_j(t - \delta_{kj} - \Delta_j) dt \right| \\ &\forall i, j, k \in [1, 2, \dots, N] \mid i, j \neq k \text{ and } i \neq j. \end{aligned}$$

Here, $p_i(t)$, $i \in [1, 2, \dots, N]$, denotes the physical layer signal of the message packet, J_k denotes the interference due to the received message packets at node k , and J indicates the total interference in the system. The δ_{ki} represents the path-delay

between the k -th node and i -th node and is given by d_{ki}/μ . The report cycle with this approach is given by

$$T_R = \max_{i,j}(\Delta_i + \delta_{ji}) + \tau, \forall i, j \in [1, \dots, N] \text{ and } i \neq j. \quad (4.2.7)$$

To illustrate the solution of the optimization problem (4.2.6), we once again consider the 3 node network shown in Figure 4.3. The configuration defined in Table 4.1 is used for path lengths. In Table 4.1, the path differences between nodes do not meet the constraint defined in (4.2.5). That is, if all the nodes transmit simultaneously, they will interfere with each other. For example, if at time $t = 0$, all the nodes A , B and C concurrently transmit their message packets, then the received signal at nodes A , B and C are shown in Figure 4.4a.

To accomplish short report cycle without interference in the example discussed above, the optimization (4.2.6) is solved using the grid search method with $\tau = 100$ ns, $\mu = 3 \times 10^8$ m/s, and $\mathcal{L} = 30$ m. In this method, we set $\Delta_A = 0$; assuming that all nodes are synchronized to node A , J is computed by varying Δ_B and Δ_C over the interval $[0, T_D]$, where T_D is given by (4.2.1). The solution for the optimization problem using the grid search method yields $\Delta_B = 84$ ns and $\Delta_C = 150$ ns. With these delays introduced in nodes B and C , the signals are not interfering, as shown in Figure 4.4b. Node C , will transmit last after a delay of 150 ns and the resulting report cycle using (4.2.7) is 620 ns.

4.2.2 System Aspects

Consider a centralized sensor network, with a powerful coordinator node, which broadcasts a beacon message with a time-stamp and the registration request. The ordinary nodes will respond with their location information after synchronizing their clock using the time stamp in the beacon². This communication can employ a conventional TDMA scheme on a control channel. The coordinator solves the optimization problem (4.2.6) using the range values of the participating nodes to prepare the broadcast schedules for the nodes. This information is encapsulated into a control packet and transmitted to all participating nodes. Periodically the central node need to collect the information from the participating nodes to resolve the optimization problem to cater to the change in topology due to the node mobility or node failures in the network. Note that the physical control channel on which the registration request and the broadcast schedules are communicated are different from the shared common channel used for all-to-all communication. Even with a powerful coordinator the solution of (4.2.6) is not possible as the scale of the network grows. In the later sections, we will discuss how a practical solution for (4.2.6) can be achieved.

Even though the nodes clocks are synchronized during the initialization process, the synchronization can be lost due to the clock drift, jitter etc. In many sensor

²Ordinary nodes can use TDOA method to account for the transmission delay during synchronization.

networks, synchronization is accomplished using a message passing technique as proposed in timing-sync (TSYNC) or reference broadcast synchronization (RBS) protocols [GKS03, EGE02a]. Network synchronization ensures that all the nodes in the network have the same time scale. We also assume that exact range information is available. Recently, there has been some work on estimation algorithms for joint ranging and synchronization. These are proposed in [DAZH15, RvdV15]. These algorithms can yield joint accuracy levels up to few centimeters for range and few nanoseconds for synchronization. We study the behavior of the proposed algorithms in the presence of range and synchronization errors in Section 4.4.

4.3 Algorithms

Using the grid search method to solve (4.2.6) is costly, as the algorithm complexity, $O(q^N)$, increases exponentially with the number of nodes in the network. Here, q indicates the size of the quantized grid of interval $[0, T_D]$ used in the grid search. In this section, we propose three distinct methods to solve the above problem, each having benefits over the other depending on the network geometry, complexity, etc.

4.3.1 Convex algorithm (CA)

The optimization problem defined in (4.2.6) is not a convex problem since the equality constraints are not affine. The problem can however be made convex by introducing additional constraints. Consider the arrival of messages at node k from nodes i and j as shown in Figure 4.5. We can treat the arrived message packets as boxes of width τ , and thus the message packets will not interfere if the corresponding boxes do not overlap. If we have predetermined the order in which the message packets should arrive at a particular node, we can make sure that the corresponding boxes do not overlap using a simple linear inequality. For example, in Figure 4.5, the inequality would be $\Delta_i + \delta_{ki} + \tau \leq \Delta_j + \delta_{kj}$. Thus, we have isolated the non-convexity of the optimization problem into selecting the order in which the message packets should arrive at the different nodes. Suppose, we consider a sequential schedule, in which node $i + 1$, will transmit after node i , then we can construct the optimization problem as

$$\text{minimize } \max_{\{\Delta_i\}} \quad \Delta_i + \delta_{ki} \quad (4.3.1)$$

$$\text{subject to} \quad \Delta_i + \delta_{ki} + \tau \leq \Delta_{i+1} + \delta_{k,i+1} \quad (4.3.2)$$

$$\Delta_i \geq 0 \quad (4.3.3)$$

In (4.3.2), i goes from 1 to $N - 1$, as there is no node with index $N + 1$, and $k \neq i, i + 1$.

This is a convex optimization problem, as the objective function is convex, and all the inequality constraints are convex. The problem can be solved as a

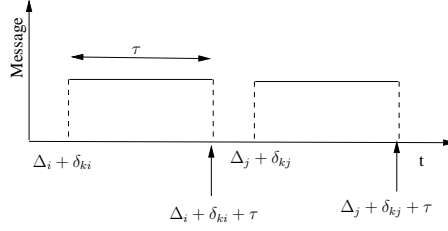


Figure 4.5: Messages from node i and j arriving at node k .

general linear program [BT97, BV04], but algorithms with lower complexity can be constructed by exploiting the structure of the problem. We found that the most efficient way to solve (4.3.1) is to minimize the delays Δ_i sequentially in order of increasing i . We note that Δ_{i+1} is minimized when it is zero or when (4.3.2) is tight for at least one k . For the first node, the smallest possible delay is $\Delta_1 = 0$ and for subsequent nodes the smallest possible delays are given by

$$\Delta_{i+1} = \max \left\{ 0, \Delta_i + \max_k \{ \delta_{ki} - \delta_{k,i+1} \} + \tau \right\}. \quad (4.3.4)$$

This results in a solution where none of the delays can be decreased without violating either (4.3.2) or (4.3.3), meaning that we have found an optimum of (4.3.1). The algorithm can be thought of as sliding the boxes corresponding to transmission $i + 1$ to the left along the time axis until one of them hits 0 or a box from transmission i .

In the above formulation, we have only considered interference between messages from nodes which come directly after each other in the node order. Given that node i does not receive a message from itself, it may be possible for messages from node $i - 1$ and node $i + 1$ to interfere when they are received at node i . This can however never happen, as (4.3.2) implies that

$$\Delta_{i-1} + \delta_{i,i-1} + \tau \leq \Delta_{i+1} + \delta_{i,i+1}, \quad (4.3.5)$$

for $i = 2, 3, \dots, N - 1$. This is shown in Appendix 4.A. Given that N delays need to be computed and that N path delays must be considered in each computation, the algorithm has a complexity of $O(N^2)$.

If the node order is set to A, B, C, in the configuration defined in Table 4.1, this method produces the same solution as the grid search method, within the grid search tolerance³. Even though the formulated problem is convex, for the N -node scenario, sequential ordering may not be the optimal order with the lowest

³Note that the convex solution does not always produce the optimal solution, and thus may not always match the result from the grid search method.

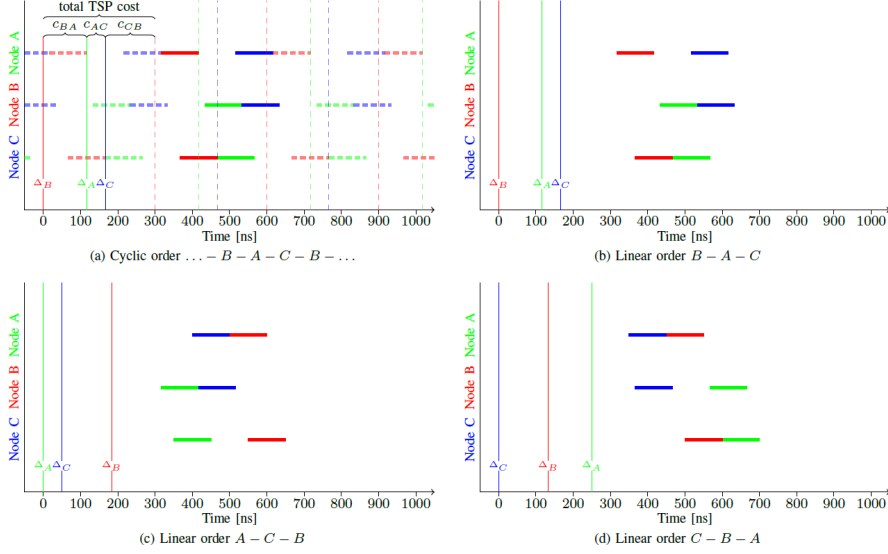


Figure 4.6: The cyclic TSP solution (a) and the 3 possible linear orders that can be created from it (b)-(d), for the network in Figure 4.3. The filled in horizontal bars show one cycle of received messages. The times of transmission are shown as solid vertical lines. In previous and future cycles, received messages and times of transmission are shown as dashed bars and dashed lines respectively. The TSP-costs along the cheapest tour can be visualised as the time differences between the transmissions. The duration of one cycle is 30 ns. In (b), (c), and (d), the report cycles are approximately 633 ns, 650 ns, and 700 ns respectively.

report cycle. Selecting an optimal order is in itself a combinatorial optimization problem [Law76, Lov79]. However, for most practical scenarios, we can select an arbitrary order and solve the convex problem as demonstrated in Section 4.6.

4.3.2 Optimizing the node order by solving a TSP

The problem of selecting a good node order can be formulated as an asymmetric traveling salesman problem (TSP) [Law85], where the cost matrix is derived from the path delays. To be able to do this, we modify the problem so that the nodes transmit in a cyclic order where a second message from the first node is placed directly after the first message from the last node. Then we solve a TSP problem which minimizes the time between two transmissions from the same node. Finally, we consider the N different ways in which the cyclic order can be broken into a linear order, and select the alternative which minimizes the report cycle in the

original problem.

The objective of the traveling salesman problem is to find the cheapest tour which visits a number of cities exactly once. The input to the problem is a cost matrix, \mathbf{C} , where its element c_{ij} is the cost of going from city i to city j [Law85]. In our problem, we let each city correspond to a node in the network. We define the cost matrix so that c_{ij} is the minimum difference between the delays of node j and node i , allowed by (4.3.2), given that j comes directly after i in the node order. Given that we are looking at a cyclic order, node 1 takes the role of node $N + 1$ in (4.3.2), and we do not need to take the constraints (4.3.3) into consideration. If node j comes directly after node i in the selected order, we have that

$$\Delta_j = \Delta_i + \max_k \{\delta_{ki} - \delta_{kj}\} + \tau. \quad (4.3.6)$$

In other words, the delay of any node is equal to the delay of the previous node, plus the cost

$$c_{ij} = \max_k \{\delta_{ki} - \delta_{kj}\} + \tau. \quad (4.3.7)$$

By adding up all of the costs associated with the successive node pairs in the transmission order (TSP tour), we therefore get the time between two transmissions made by the same node. The problem of minimizing the time between two transmissions made by the same node can therefore be formulated as a TSP where the cost matrix is defined by c_{ij} . For the 3 node configuration shown in Figure 4.3, the algorithm is graphically illustrated in Figure 4.6.

The TSP is known to be NP-hard [RP89, Law76, Lov79], but there are algorithms that can find exact solutions for small problems, and other algorithms that can find approximate solutions for larger problems [Joh82, Lap92]. Many techniques employ heuristic approaches for finding the approximate solution [Hel00, Ree93, RSL77]. The best approximate algorithms, often produce optimal or very close to optimal solutions, for large networks with hundreds of nodes. Furthermore, the approximate algorithms can be run multiple times with different starting points and thereby achieve much better performance [Per94]. We have chosen to use the TSP solver LKH [Hel00], which is based on the Lin-Kernighan heuristic. For a problem with 100 nodes, LKH requires less than a second to produce a solution which has a high probability of being optimal. In LKH, all of the costs in matrix \mathbf{C} , must be integers and therefore we mapped the costs in each problem to the interval between 0 and 10^6 using an affine mapping and rounded them to the closest integers. We used version 2.0.7 of LKH with the default settings for all problems.

The report cycle will depend on which node in the TSP cycle is selected as node 1. Therefore we consider all of the N possible choices for node 1 and solve the convex problem defined in Section 4.3.1 for each one of them to see which alternative results in the shortest report cycle. Given that we can reuse the costs that we computed in (4.3.7) when we compute the delays in (4.3.4), the problem of choosing a first node has complexity $O(N^2)$. The overall complexity is therefore dominated by the TSP solver, which has an average complexity that scales approximately

as $O(N^{2.2})$ [Hel00]. We may introduce some sub-optimality by transforming the problem into a problem with transmitters in a cyclic order, and LKH may also not find the exact optimum of the TSP. The gap to optimality would however be negligible for most practical applications.

4.3.3 Iterative path-adjusting algorithm (IPA)

The CA reduces the algorithm complexity by allowing sub-optimality due to the fixed ordering. On the other hand, the TSP algorithm improves over the CA, by choosing a better order without increasing the average algorithmic complexity. One problem with both the algorithms is their inefficiency when (4.2.5) holds for most of the nodes (i.e., nodes are scattered far-apart compared to \mathcal{L}). For a random node configuration, we can in theory ensure that (4.2.5) holds by making the message length τ small enough. If τ is decreased by $d\tau$, the report cycle of the algorithms will however only decrease by $Nd\tau$, as the algorithms cannot change the order in which messages are to be received at the nodes. This results in poor performance when τ is small in comparison to the path delays of the network. To overcome this problem, we propose an alternative algorithm called iterative path-adjusting algorithm (IPA). We show in the later sections that this algorithm outperforms the convex formulation with strict ordering as defined in (4.3.2), and the TSP algorithm, when the sensor nodes are scattered wide apart.

In this algorithm, we adjust the path differences between nodes, d_{ki} and d_{kj} to satisfy (4.2.5) in an iterative way. Adjusting the path difference is the same as introducing delays at nodes i and j , so that the signals from i and j do not interfere at node k . The algorithm is described below in three steps followed by an example on a 3-node network.

- 1 Start the first iteration with $l = 0$ ($l + 1$ denotes the iteration number) and $k = 1$, with $d_{ki}^0 = d_{ki}$. For a topology having N nodes, add additional path lengths $d_{\Delta i_k}^{l+1}$ and $d_{\Delta j_k}^{l+1}$, $\forall i, j \in [1, 2, \dots, N]$, $i, j \neq k$, $i \neq j$ to nodes i and j to satisfy (4.2.5). Thus, the new path lengths are given by

$$d_{ki}^{l+1} = d_{ki}^l + d_{\Delta i_k}^{l+1}, \quad (4.3.8)$$

$$d_{kj}^{l+1} = d_{kj}^l + d_{\Delta j_k}^{l+1}. \quad (4.3.9)$$

Note that to satisfy (4.2.5), the path-length needs to be added to one of the nodes i or j . In this algorithm, we set $d_{\Delta i_k}^{l+1} = 0$ and add additional path length $d_{\Delta j_k}^{l+1}$ only to node j .

- 2 Repeat Step 1, by selecting all nodes one by one ($k = 1, 2, \dots, N$) in the network. Each time, carry over additional path lengths added $d_{ki}^l + d_{\Delta i_k}^{l+1}$ and $d_{kj}^l + d_{\Delta j_k}^{l+1}$. The total adjusted path lengths at the end of iteration l are given by

$$d_{\Delta k}^{l+1} = d_{\Delta k}^l + \sum_i d_{\Delta i_k}^{l+1}, \quad (4.3.10)$$

for $k \in [1, 2, \dots, N]$ and $k \neq i$. This completes an iteration.

- 3 Repeat Step 1 and Step 2 until the total adjusted path length for each node does not change across iterations, meaning that the following condition holds for all $k \in [1, 2, \dots, N]$.

$$d_{\Delta k}^{l+1} = d_{\Delta k}^l. \quad (4.3.11)$$

This indicates that (4.2.5) is met for all nodes simultaneously.

The proposed method is illustrated with the 3 node network shown in Figure 4.3, with the configuration defined in Table 4.1. Figure 4.7 (a) shows that the addition of an additional path length of $20 = (30 - (d_{AC} - d_{AB}))$ is required at node C to meet the constraints in (4.2.5) so that signals from B and C do not collide at A . Similarly, Figure 4.7 (b) and Figure 4.7 (c) add additional path lengths to the previous topology to avoid collisions at nodes B and C respectively. At the end of the 1st iteration, the total path lengths for all of the nodes are given in Figure 4.7 (d).

The second iteration is illustrated in Figure 4.8. Notice that we carried the new topology with added path lengths from the previous iteration ($d_{\Delta A}^1, d_{\Delta B}^1, d_{\Delta C}^1$) to iteration 2 and at the end of iteration 2, the total added path lengths are $(d_{\Delta A}^2, d_{\Delta B}^2, d_{\Delta C}^2) = (0, 25, 45)$. Now the iteration is stopped as it meets the conditions defined in Step 3.

Translating the path lengths into path delays by dividing by the speed of light, c , results in $(\Delta_A, \Delta_B, \Delta_C) \approx (0, 84, 150)$ [ns]. This is the same result as with the grid search and convex methods. This algorithm is analyzed in the next Section.

4.3.4 Analysis of IPA

In order for the arriving signals not to interfere, (4.2.5) needs to be satisfied. We define the path matrix, \mathbf{M} , where each element of \mathbf{M} , d_{ki} , denotes the distance between node k and node i . The IPA adjusts the path matrix in such a way that the path lengths to node k from other nodes (represented by the k -th row in the matrix \mathbf{M}), have path differences greater than \mathcal{L} . For an N node network, the algorithm starts with the original path matrix, \mathbf{M}^0 , as given in (4.3.12). The path adjusted matrix after the l -th iteration is represented as \mathbf{M}^l .

$$\mathbf{M}^0 = \begin{bmatrix} 0 & d_{12} & \cdots & d_{1N} \\ d_{21} & 0 & \cdots & d_{2N} \\ \vdots & \vdots & \ddots & \vdots \\ d_{N1} & d_{N2} & \cdots & 0 \end{bmatrix}. \quad (4.3.12)$$

Note that $d_{kk} = 0, \forall k \in (1, 2, \dots, N)$. Also, matrix \mathbf{M}^0 is symmetric, that is $d_{ki} = d_{ik}$. The path adjusted matrix, \mathbf{M}^l , has elements, d_{ij}^l . The i -th row of the

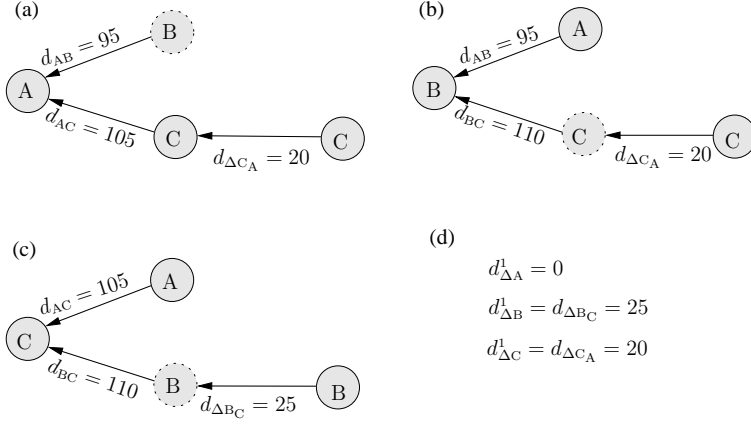


Figure 4.7: Iteration 1 for the 3 node network shown in Figure 4.3 with the configuration defined in Table 4.1.

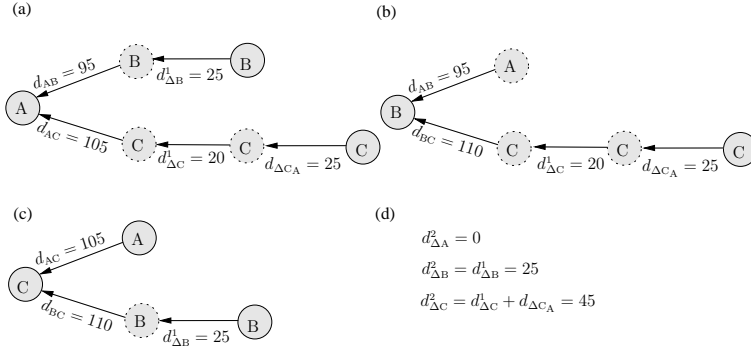


Figure 4.8: Iteration 2 for the 3 node network shown in Figure 4.3 with the configuration defined in Table 4.1.

path adjusted matrix \mathbf{M}^l is denoted as

$$\underline{d_{ix}^l} = \begin{bmatrix} d_{i1}^l & d_{i2}^l & \cdots & d_{iN}^l \end{bmatrix}, \quad (4.3.13)$$

similarly, the i -th column is denoted as

$$\underline{d_{xi}^l} = \begin{bmatrix} d_{1x}^l & d_{2x}^l & \cdots & d_{Nx}^l \end{bmatrix}^T, \quad (4.3.14)$$

where τ denotes the transpose operator.

To perform step 1 of the algorithm, there are many possibilities for additional path lengths $d_{\Delta_{i_k}}^l$ and $d_{\Delta_{j_k}}^l$, such that the arriving signals at node k , have effective path length difference greater than \mathcal{L} . In the discussions of this chapter, in order to make the arriving signals to node k from nodes i and j satisfy $|d_{ki}^l - d_{kj}^l| \geq \mathcal{L}$, we will add path lengths only to j , if $j > i$. That is,

$$\text{if } |d_{ki}^l - d_{kj}^l| < \mathcal{L} \text{ and } j > i \text{ then} \quad (4.3.15)$$

$$d_{\Delta_{i_k}}^{l+1} = 0, \quad (4.3.16)$$

$$d_{\Delta_{j_k}}^{l+1} = \mathcal{L} - (d_{kj}^l - d_{ki}^l), \quad (4.3.17)$$

$$\underline{d}_{xj}^{l+1} = [\underline{d}_{xj}^l + d_{\Delta_{j_k}}^{l+1} \underline{1}], \quad (4.3.18)$$

$$\forall i, j \in [1, 2, \dots, N], i, j \neq k, i \neq j, \text{ and } j > i.$$

Where, $\underline{1}$ is $[1, 1, \dots, 1]^T$ and the process, defined in (4.3.15) to (4.3.18) is repeated for $k = 1, 2, \dots, N$ sequentially to complete an iteration. The iterations with $l = 0, 1, 2, \dots$ are performed until in (4.3.17), $d_{\Delta_{j_k}}^{l+1} = 0, \forall i, j, k \in [1, 2, \dots, N], i, j \neq k$ and $i \neq j$ is met. At each iteration, the elements from \mathbf{M}^l are used for (4.3.15) to (4.3.18).

During each iteration, when (4.3.15) is met, the additional path is added only to one of the nodes (the node on the right). Therefore, as the iterations increase, the path adjusted matrix, \mathbf{M} , will converge to the state with its elements

$$\begin{aligned} |d_{ki}^{l^*} - d_{kj}^{l^*}| &\geq \mathcal{L}, \\ \forall i, j, k \in [1, 2, \dots, N], i, j &\neq k \text{ and } i \neq j, \end{aligned} \quad (4.3.19)$$

where, $l^* + 1$ denotes the number of iterations required for convergence. At this state the arriving signals to any node k from nodes i and j will satisfy (4.2.5). The effective adjusted path is given by

$$d_{\Delta_i}^{l^*} = \underline{d}_{1x}^{l^*}(i) - \underline{d}_{1x}^0(i), \quad (4.3.20)$$

and the equivalent added delay for node, i , is $\Delta_i = d_{\Delta_i}^{l^*}/\mu$.

The average algorithmic complexity for IPA is evaluated by a least square polynomial fit to the average computational time (in ticks) consumed by the algorithm for networks of different sizes. The procedure followed, along with the results, are discussed in Appendix 4.B. From the results of the Appendix 4.B, the average complexity of the IPA algorithm is $O(N^3)$.

A summary of the average complexities of the proposed methods is shown in Table 4.2. For CA, the average case and the worst case complexity are the same, therefore in networks, where the real-time guaranties are needed CA is more amenable than TSP and IPA. The IPA opens up for a higher flexibility regarding the order of the transmissions. Thus, it provides better throughput compared to the convex

Algorithm	Average case complexity
Grid Search	$O(q^N)$ (q is the size of the quantized grid)
CA	$O(N^2)$ (After exploiting the structure in the LP problem)
TSP	$O(N^{2.2})$ (Using LKH solver)
IPA	$O(N^3)$

Table 4.2: Summary of average complexity of the proposed methods.

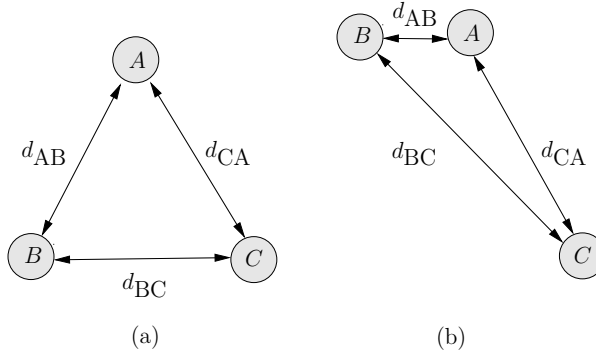


Figure 4.9: Two distinct 3-node configurations.

algorithm as shown in Section 4.6. In mobile sensor networks, the convex approach with fixed ordering among the nodes opens up for schedule-based communication and ranging; thus, node information need not be encoded in the packets [DZAH13]. On the other hand, IPA requires transmission overhead since the node information has to be included in the packets, as the order of packet reception is not predetermined. However, the overhead of encoding the node information in the packet ($\log_2 N$ bits) is not significant.

The performances of the orthogonalization, CA, TSP, and IPA under large scale networks with different geometric formations are studied in the Section 4.6.

4.4 Effect of Synchronization and Range errors

In the discussion so far, we assumed that the sensor clocks are synchronized and the available set of range estimates (d_{ij} s) are accurate. Accurate network synchroniza-

tion can be achieved by synchronizing the sensor clocks to the global positioning system (GPS) clocks or in GPS deficient systems by using the protocols discussed in Section 4.2. Accurate range estimation can be accomplished by using TOA methods. The best performance in terms of mean-square-error (MSE) for an unbiased estimator is given by the Cramer Rao lower bound (CRLB) and for a time of arrival (TOA) estimation problem this is given by [GTG⁺05, DCW08]:

$$\sigma_\tau^2 \geq \frac{1}{8\pi^2 \text{SNR} \beta^2}, \quad (4.4.1)$$

where, β is the effective signal bandwidth defined by

$$\beta^2 = \left[\frac{\int_{-\infty}^{\infty} f^2 |S(f)|^2 df}{\int_{-\infty}^{\infty} |S(f)|^2 df} \right], \quad (4.4.2)$$

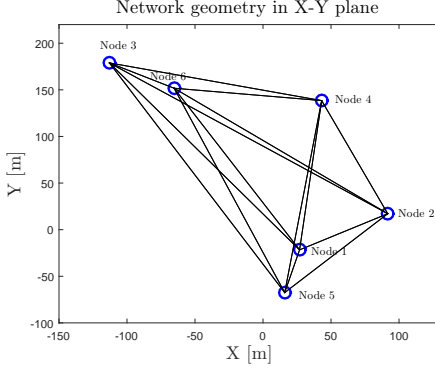
where, $S(f)$ is the Fourier transform of the transmit pulse, $s(t)$. Since many technologies like UWB use extremely large bandwidths, they can be used for precise range estimation. Practical UWB hardware with ranging and communication capabilities with range estimation accuracy of a few centimeters are discussed in [ADH13, YDAH14].

In practice, clock synchronization is not perfect and there will be range errors. These will result in message packets colliding at the receiving nodes. The synchronization error can be approximated as a zero mean normal distribution as shown in [EGE02b, PSJ04]. In wideband RF systems [BP00, JH00], problems such as multipath fading, background interference, and irregular signal propagation characteristics make range estimates inaccurate. The range error can also be approximated as a zero mean normal distribution [LR03, LT02].

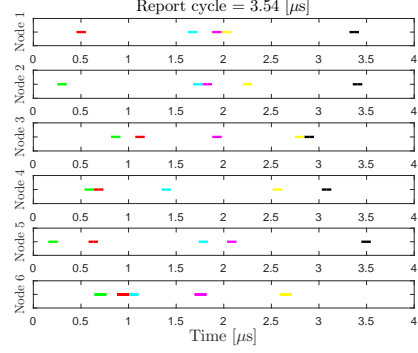
We assume that synchronization and range errors are independent and the net effect will result in the packet arrival time to be randomly shifted from the intended position. The distribution of this random shift from the true position can be approximated to a Gaussian distribution, $\mathcal{N}(0, \sigma_e^2)$. This shift in time of arrival of the message packets at the receiving node can cause interference due to packet collisions. This problem can be reduced by adding a guard interval, ϵ , to the equations of the CA, TSP, and IPA. This can be done by expanding the message packet length τ to $\tau' = \tau + \epsilon$ in (4.3.2) and (4.2.5). Where, ϵ can be used to trade off between tolerable interference and the report cycle time (update rate). It can be shown that

$$\epsilon = \sqrt{2}\sigma_e \text{erfc}^{-1}(2(1 - \mathcal{P})), \quad (4.4.3)$$

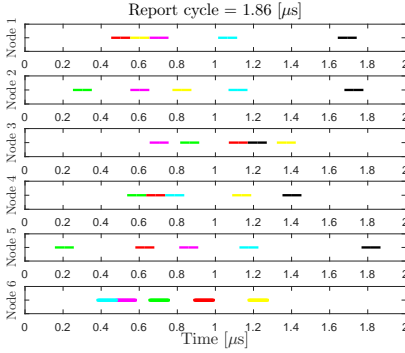
where, $1 - \mathcal{P}$ denotes the percentage during which neighboring packets collide due to the range and synchronization errors. For example, to have 95% collision avoidance between neighboring packets, we need to have $\epsilon = 1.65\sigma_e$. The network level performance in presence of range and synchronization errors, using the above method, for proposed algorithms are studied in Section 4.6.



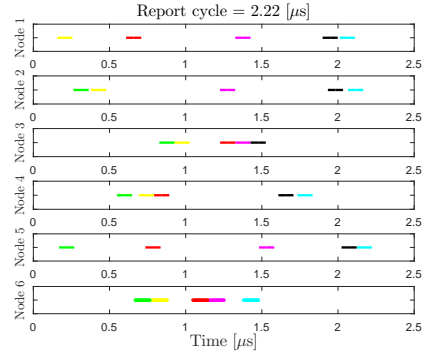
(a) Network Topology



(b) Convex Algorithm



(c) IPA



(d) TSP

Figure 4.10: Network geometry with 6 nodes scattered randomly in a 2-D plane. Received message packets at each node after introducing the computed delays from Table 4.3 for network topology in Figure 4.10a are shown for different algorithms. Notice that the message packets do not interfere. The color of the message packet is mapped to the node as shown in Table 4.4

4.5 Comparison with CDMA systems

In CDMA based multiple access, each node i is assigned a unique spreading code, \mathbf{u}_i , such that $\mathbf{u}_i \perp \mathbf{u}_j$, $\forall i \neq j$. Each sensor transmit the packets continuously by spreading the message with its code. At the receiver, each sensor node de-spreads the signal using its unique code. Thus, in principal the report cycle can be completed in $N\tau$ [s].

However, this scheme is not well suited for the all-to-all broadcast scenario de-

scribed in Section 4.1, due to the interference originating from the near-far problem of CDMA [Vit95]. Unlike in many CDMA systems, this problem cannot be resolved using the classical power-control feedback. To further illustrate this, consider two 3-node networks shown in Fig 4.9. In Fig 4.9 (a), $d_{AB} = d_{BC} = d_{CA}$ and when all the nodes transmit messages concurrently with same power level, the received message signals from all the nodes are at the same power level, and orthogonality of the different spreaded signals holds. Thus, the signal belonging to different sensors in all-to-all broadcast can be de-spread without any interference at all the nodes. In general, for an N node network to have interference free communication, we need the topology to have, $d_{ij} = \xi$, where ξ , is some constant. This is a rare scenario and typically does not occur in practice. Now, consider a network, Fig 4.9(b), with $d_{BC} > d_{CA} > d_{AB}$, and a parallel transmission of an all-to-all broadcast with same power level at all nodes. The sensor node B receives signals from A and C at different power levels, and thus B will face severe interference when separating the signals from A and C . Similar situation occur for the received signal at A and C . The feedback power control does not solve the problem for all-to-all broadcast, as adapting the power in one node to remove interference can create interference to other nodes. As the number of nodes increases, the interference free parallel transmission becomes infeasible⁴.

Another scenario where continuous transmission is not possible are in networks which require cyclical communication. Here the transmission in the current cycle of a sensor depends on the data it received from all the other sensor nodes in the previous cycle of all-to-all communication. This kind of communication is found in distributed control and distributed computation applications as discussed in [KLO10, NZSH13, RRS⁺11].

However, we can exploit the spatial-temporal aspect of the underlying channel, where the propagation delay between nodes are much longer than the access interval. Here each of the N nodes transmit concurrently for a duration of τ , once every T_D seconds. Due to the random topology, and large propagation time, the arrived pulses are spread out in time, thereby reducing the interference. It can be shown that if a spreading code of length, $M \geq N$ is used and the shared common channel can support a bitrate of R_b [bps], the effective bitrate per sensor, R_s , is given by

$$R_s^{\text{CDMA}} \leq \frac{R_b \tau}{M T_D}. \quad (4.5.1)$$

For the proposed algorithms in the chapter, in each report cycle, T_R , each node in the network will get to transmit a message packet once for the duration, τ , seconds. Therefore the effective throughput per sensor can be computed as

$$R_s = \frac{R_b \tau}{T_R}. \quad (4.5.2)$$

⁴For some network geometries, the interference free all-to-all communication problem can be solved as an optimization problem.

Node	Delay Values (Δ_{is}) [ns]		
	CA	IPA	TSP
1	0	0	11.9
2	200.9	200.8	356.8
3	807.8	199.2	1196.3
4	1341.7	117.4	789.0
5	1821.3	395.7	0
6	2665.6	987.8	1243.8

Table 4.3: Computed delay values from proposed methods for the geometric formation defined in Figure 4.10a.

Message packet from node	Color
1	Green
2	Red
3	Cyan
4	Magenta
5	Yellow
6	Black

Table 4.4: Mapping of colors to nodes in Figure 4.10 and Figure 4.14.

In the Section 4.6, we demonstrate in simulation the effective bitrate per sensor, R_s , as a function of the number of nodes, N , to show how the position information exploited in the proposed algorithms offer better performance compared to a CDMA based approach.

4.6 Simulation Study

In the beginning of Section 4.2.1, we mentioned that we can orthogonalize the message packets by separating consecutive transmissions by a time interval equal to the maximum path delay in the network. For the configuration in Table 4.1, the report cycle, T_R , can be computed as below.

$$T_D = \frac{\max(d_{AB}, d_{BC}, d_{CA})}{\mu} + \tau = 470 \text{ ns} . \quad (4.6.1)$$

$$T_R = N \cdot T_D = 1410 \text{ ns}. \quad (4.6.2)$$

However, if the path difference between nodes in the network topology satisfies (4.2.5), then all the nodes can concurrently transmit; thus one report cycle can be

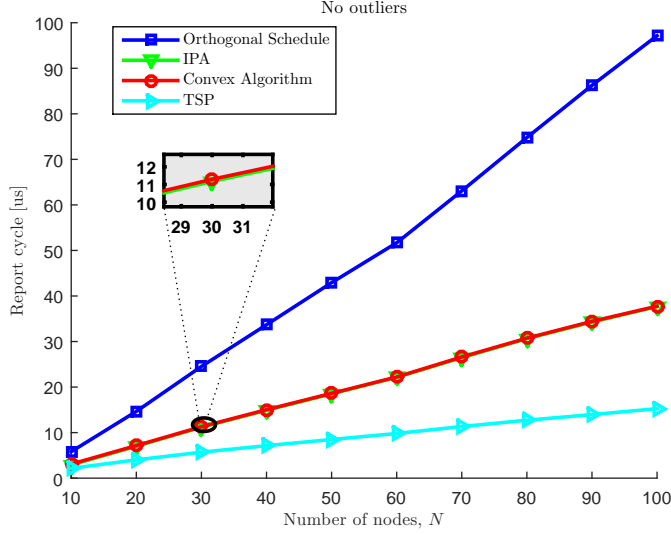


Figure 4.11: Performance of proposed methods as a function of N . Notice that as the number of nodes increases, the proposed techniques yield better performance relative to the orthogonal schedule.

completed in the time duration equal to the maximum path delay in the network plus the packet length, that is 470 ns. More often (4.2.5) is not met. Under these circumstances we can minimize the report cycle by solving (4.2.6). We modified the problem so that it can be casted as a convex optimization problem. For the configuration in Table 4.1, we showed that, $(\Delta_A = 0 \text{ ns}, \Delta_B = 84 \text{ ns}, \Delta_C = 150 \text{ ns})$ solves (4.3.1), therefore node C will transmit last after a delay of 150 ns and complete the report cycle. So one report cycle for the configuration in Table 4.1 is

$$T_R = \max_{ij}(\Delta_i + \delta_{ji}) + \tau, \quad (4.6.3)$$

$$\forall i, j \in [A, B, C] \text{ and } i \neq j$$

$$T_R = 150 + 370 + 100 = 620 \text{ ns}. \quad (4.6.4)$$

Thus, the reduction in the report cycle equals 56%.

To study the performance of the proposed methods for large networks, we form two different formations; one with outliers, where a few sensor nodes are far apart from the rest; and another with no-outliers, where the sensor nodes are scattered uniformly. The performance is reported in terms of the time required to complete one report cycle using the proposed methods.

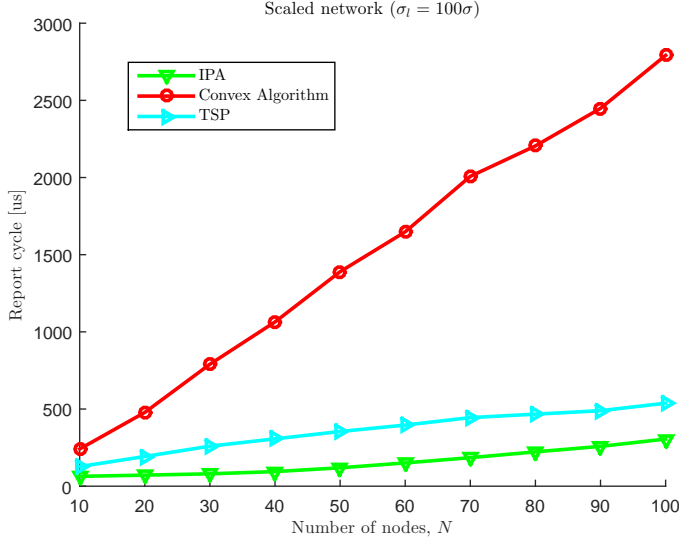


Figure 4.12: Performance of proposed methods as a function of N . Notice that as the number of nodes increases, the IPA algorithm yield better performance relative to TSP when the network radius is larger compared to packet length.

4.6.1 Random geometric formation with no outliers

For performance analysis with no outliers, we create a random geometric formation by scattering the nodes in a plane. The coordinates (x, y) are drawn from a Gaussian distribution as shown below.

$$(x, y) \sim (\mathcal{N}(0, \sigma^2), \mathcal{N}(0, \sigma^2)). \quad (4.6.5)$$

A typical topology of 6 nodes with $\sigma = 50$ [m] is shown in Figure 4.10a. The transmission schedules for interference mitigation, using different proposed algorithms are given in Table 4.3.

With these delays introduced, the received packets will not interfere with each other. The received packets at each node are shown in Figure 4.10b, 4.10c, and 4.10d for CA⁵, IPA and TSP algorithms. Each color in Figure 4.10 is mapped to the messages from a specific node, as shown in the Table 4.4.

Report cycle, T_R , for the given set of delay values computed using CA, TSP and IPA are given by $\max_{i,j}(\Delta_i + \delta_{ij}) + \tau$. For the example network shown in Figure 4.10a,

⁵In simulations, we employ a sequential order for CA, *i.e.*, in (4.3.4), i , is varied from $1, \dots, N-1$, with $\Delta_1 = 0$.

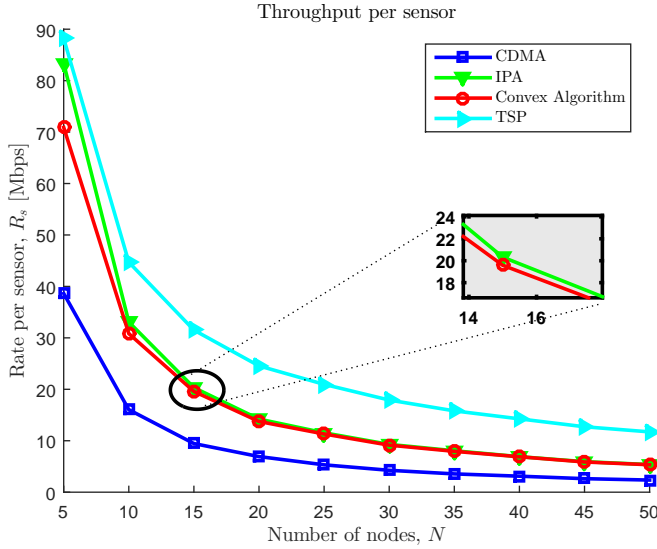


Figure 4.13: Bitrate per sensor, R_s , of proposed methods and CDMA approach as a function of N . Notice that the proposed methods yield better performance relative to CDMA.

the report cycles are given by $3.54 \mu\text{s}$, $2.22 \mu\text{s}$, and $1.86 \mu\text{s}$ for CA, TSP, and IPA respectively.

From Figure 4.10b and Figure 4.10c, notice that the IPA is less constrained than the convex approach; the convex formulation requires that the order of the received message packets is the same at each receiving node. This is not the case for the IPA algorithm. This ensures tighter schedules and explains the better performance of the IPA algorithm.

To assess the performance over a large number of nodes N , we performed Monte-Carlo simulations. We swept the number of nodes, N , from 10 to 100 in steps of 10 and for each N , 32 distinct random geometric formations were constructed as per (4.6.5). The averaged report cycle is reported in Figure 4.11.

Figure 4.11 compares the proposed algorithms to the technique of orthogonalization with scheduled transmission discussed in Section 4.2.1. Notice that for a 100 node randomly scattered network with $\sigma = 50$ [m], T_R is reduced to approximately 1/10 for the TSP algorithm and 1/3 for the fixed order convex algorithm and the IPA algorithm. However, if the radius of the network is scaled by a factor of 100 by changing the variance $\sigma_l = 100\sigma$, the IPA performs better than the TSP algorithm as explained in the earlier section and confirmed in simulation by Figure 4.12.

The effective rate per sensor for the CDMA approach and the proposed algo-

Node	Delay Values (Δ_{is}) [ns]		
	CA	IPA	TSP
1	0	0	401.6
2	266.0	266	667.6
3	0	0	0
4	1444.7	78.1	1444.7
5	939.4	0	939.4
6	2528.5	759.4	147.7

Table 4.5: Computed delay values from proposed methods for the geometric formation defined in Figure 4.14a.

rithms are as given by (4.5.1)⁶ and (4.5.2). Figure 4.13, shows the rate per sensor for CDMA and the proposed algorithms, assuming $R_b = 1$ Gbps and $\tau = 100$ ns. Notice that the proposed algorithms yield better performance in terms of bitrate per sensor, R_s , compared to CDMA.

4.6.2 Random geometric formation with outliers

In this section, we will study the performance of geometric formations of the sensor network with a few sensor nodes far apart from the rest. To create this topology, we construct N nodes distributed according to a mixture of two Gaussian distributions. These distributions are as given below.

$$(x, y) = (\mathcal{N}(0, \sigma^2), \mathcal{N}(0, \sigma^2)) \quad (4.6.6)$$

$$(x_o, y_o) = (\mathcal{N}(0, \sigma_o^2), \mathcal{N}(0, \sigma_o^2)) \quad (4.6.7)$$

The node location is selected from (4.6.6) with probability of 2/3, and from (4.6.7) with probability 1/3. We set $\sigma = 50$ and $\sigma_o = 300$; thus for a large N , 1/3 of the nodes will be outliers. A typical topology with 6 nodes is shown in Figure 4.14a.

The transmission schedules for interference mitigation, by solving the CA, IPA, and TSP are given in Table 4.5.

With these delays introduced, the received packets will not interfere with each other. The received packets at each node are shown in Figure 4.14b, Figure 4.14c and 4.14d for the CA, IPA and the TSP algorithms discussed. Each color in Figure 4.14 is mapped to the message from a specific node, as shown in Table 4.4. For the example network shown in Figure 4.14a, the report cycles are approximately given by $4.73 \mu\text{s}$, $4.23 \mu\text{s}$, and $3.29 \mu\text{s}$ for the CA, TSP, and IPA respectively.

To assess the performance over a large number of nodes N , we performed Monte-Carlo simulations similar to the no-outlier case with 32 distinct random geometric

⁶In simulations, for (4.5.1) equality is considered.

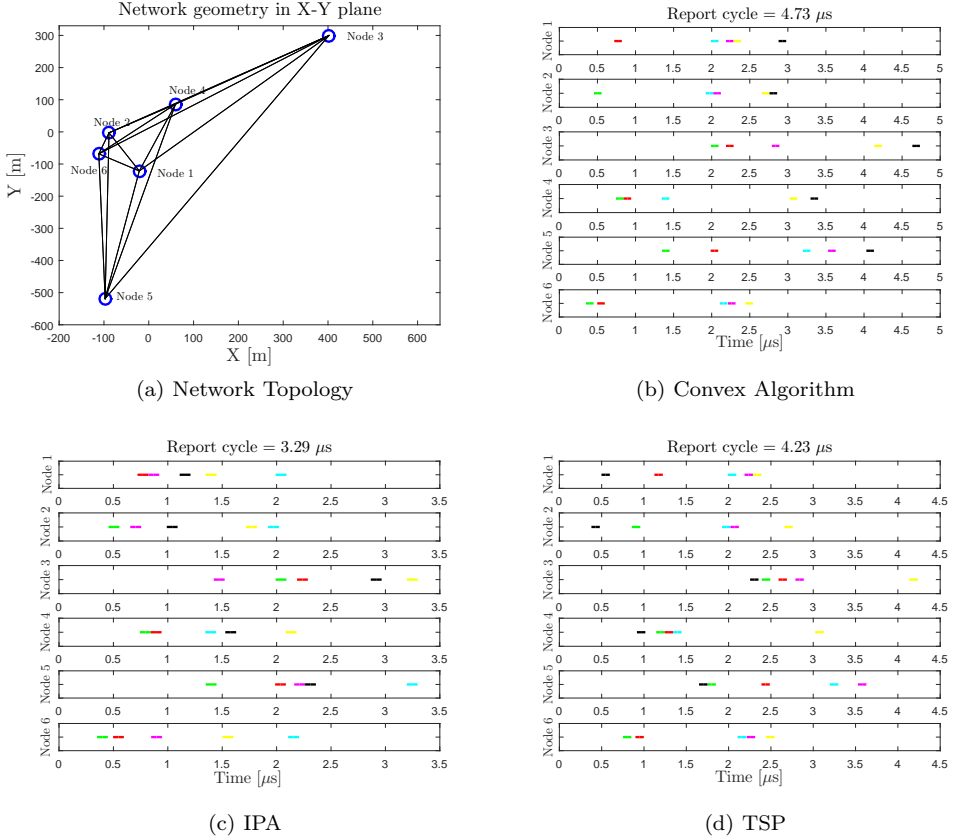


Figure 4.14: Network geometry with nodes scattered randomly in a 2-D plane with outliers. Received message packets at each node after introducing the computed delays from Table 4.5 for the network topology in Figure 4.14a are shown for different algorithms. Notice that the message packets do not interfere. The color of the message packet is mapped to the node as shown in Table 4.4.

formations constructed from the mixture distribution of (4.6.6) and (4.6.7) with probabilities of $2/3$ and $1/3$ respectively. The average report cycle is reported in Figure 4.15.

Figure 4.15 compares the proposed algorithms to the technique of orthogonalization through scheduled transmission discussed in Section 4.2.1. Notice that for a network with 100 nodes, T_R is on average reduced to $1/8$ using TSP algorithm. This means that the net communication or update rate can be increased by a factor of 8 on average for the network topology with outliers. Thus, a sensor network with geometric formations having a few outlier nodes can have higher communication

rate using the proposed algorithms. The further away these outlier nodes are, the greater the benefits will be, as the algorithms can pack the information packets more efficiently there by optimally utilizing the shared common channel.

4.6.3 Performance in the presence of synchronization and range errors

With the configurations for the no-outlier topology as discussed in the Section 4.6.1, we performed Monte-Carlo simulations to assess the average sensitivity of the algorithms to range and synchronization errors. If there were no synchronization and range errors, then the network would have exchanged $N(N - 1)$ packets of width τ , without any interference, using the proposed algorithms. However, due to the errors, packets can interfere and we define the fraction of interference free communication in the network, F , as

$$F = 1 - \frac{\sum_i \mathcal{I}_i}{N(N - 1)\tau}, \quad (4.6.8)$$

where \mathcal{I}_i , denotes the overlapped area of the packets at the receiving node i . The trade-off between the guard interval, ϵ , and report cycle, T_R , is to first pack the transmissions as closely as possible to reduce T_R and then increase the guard interval, ϵ , in the optimization problem, based on the environment to decrease the sensitivity to range and synchronization errors. Figure 4.16, shows the average performance of F , using Monte-Carlo simulations for 20 nodes with 100 distinct topologies constructed using the no-outlier case described earlier, with $\tau = 100$ [ns].

4.7 Conclusion

In this chapter, we discussed a methodology for utilizing the range information to arrive at transmission schedules for high density sensor networks. Connected sensor networks need high rates of communication on a shared channel in order to have high update rates. Therefore, an optimal schedule for accessing the shared common channel needs to be designed for efficient communication. To accomplish this, an optimization problem is formulated using range information for interference mitigation. A solution for the optimization problem is found by CA, TSP and IPA methods. The proposed methods are compared to the traditional time-sharing technique of separating consecutive transmissions by a time interval equal to the duration of maximum path delay in a network. The performances of the algorithms are assessed for different types of networks with varied sizes. Two different geometric formations are considered, one with a random placement of nodes with no outliers and one with outliers. The results are demonstrated in Figure 4.11 and Figure 4.15. A comparison with CDMA based multiple access is also presented in Figure 4.13. The analysis of performance degradation due to non-idealities such as synchronization and range errors is reported in Figure 4.16.

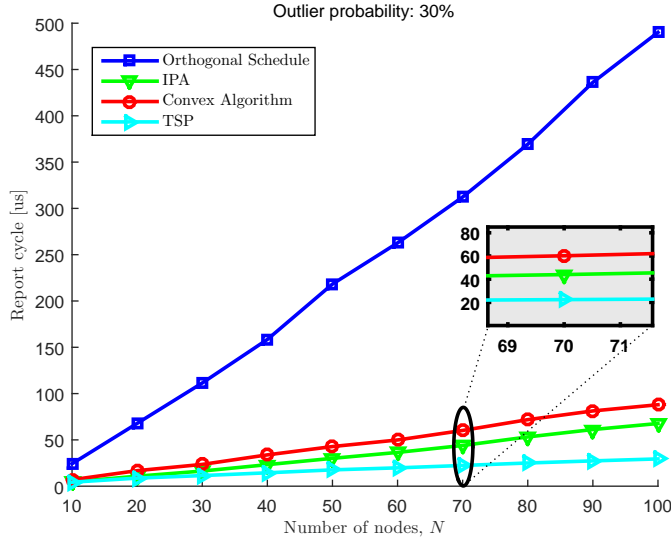


Figure 4.15: Performance of proposed methods as a function of N . Notice that as the number of nodes increases, the proposed techniques yield better performance relative to the orthogonal schedule.

The three proposed algorithms performs better than CDMA or orthogonalization by scheduling one node for maximum path delay in the network. As demonstrated in Figure 4.15, the performance gains are higher, if the networks have few outliers in them. Each of the proposed algorithms has a clear edge over others depending on the type of the network. For example, TSP performs better than IPA and CA for general networks, however, when the network is geometrically larger in relation to the path equivalent message length, \mathcal{L} , then IPA performs better than the TSP and CA as suggested by Figure 4.12. IPA never performs worse than the convex algorithm. From the simulation results, it appears that the IPA will give the same solution as the CA in the worst case scenario, however, the formal proof is not known to the authors. The proposed methods assumes full connectivity, extending the methods for a partially connected network is a topic of further research.

Table 4.2 summarizes the average complexities of the algorithms. For IPA and TSP, the worst case complexities are not known and for CA, the worst case and the average case complexities are same. Thus, IPA and TSP may not be useful in networks where real-time guarantees are needed for the schedule computations. The impact of the synchronization and range errors on the algorithms are studied. As expected, the tighter schedules are more susceptible to the interference due to the imperfect ranging and synchronization. Typical system design involves, first packing

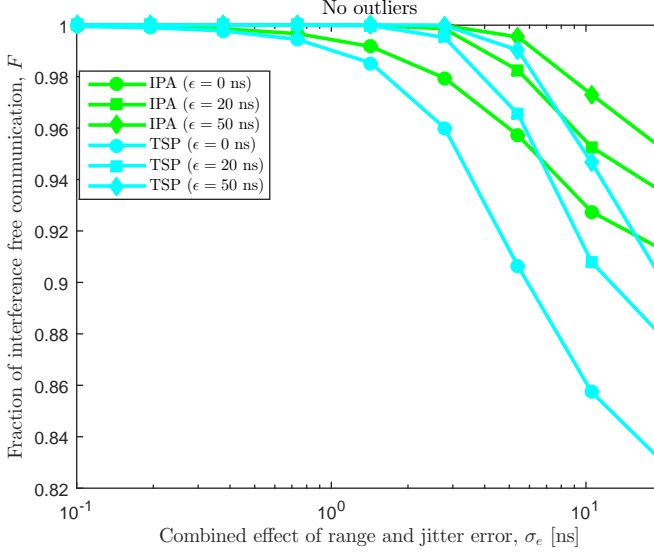


Figure 4.16: Interference in the system of 20 Nodes, in presence of imprecise range and clock jitter. By increasing the guard interval, ϵ , by setting higher \mathcal{P} , as in (4.4.3), the interference performance can be traded with report cycle. For large σ_e , the collisions are unavoidable despite the guard interval.

the transmissions as closely as possible to have low report cycle using the algorithms discussed and then increasing the guard interval, ϵ , to decrease the interference as illustrated in Figure 4.16.

The performances of the proposed methods are demonstrated in simulations in order to assess the performance gains without platform or network dependencies. The in-house transceiver discussed in the Chapter 1, can yield very precise range information on the order of a few centimeters, as reported in [ADH13]. These transceivers could be mounted on the sensors for joint ranging and communication [YDAH13, YDAH14, ADH13]. The results from the simulations of the proposed schemes indicate that a significant improvement in performance in terms of communication rate can be achieved by using the proposed schemes of this chapter.

4.A Proof that nodes $i - 1$ and $i + 1$ do not interfere in the convex problem

In this appendix, we will prove

$$\Delta_{i-1} + \delta_{i,i-1} + \tau \leq \Delta_{i+1} + \delta_{i,i+1}, \quad (4.A.1)$$

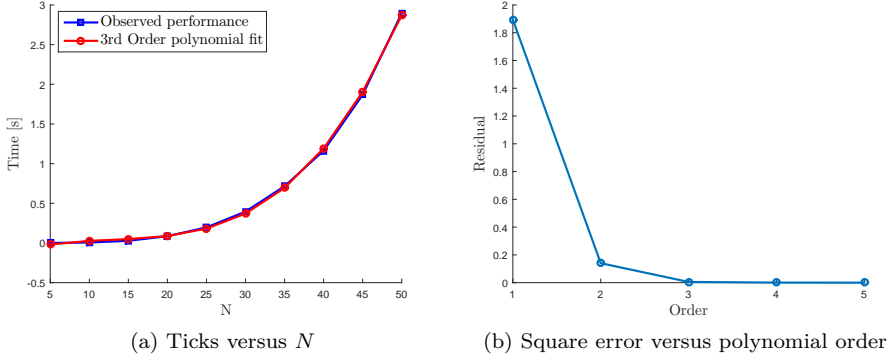


Figure 4.17: The 3rd order polynomial fit to the average complexity curve, along with the residual error for the various order polynomial fit.

which says that messages from node $i - 1$ and node $i + 1$ cannot interfere when they are received at node i in the convex problem. To do this, we consider the constraint in the convex optimization problem, for node $i - 1$ and node i , and get

$$\Delta_{i-1} + \delta_{k,i-1} + \tau \leq \Delta_i + \delta_{k,i} \text{ for } k \neq i - 1, i \quad (4.A.2)$$

and

$$\Delta_i + \delta_{k,i} + \tau \leq \Delta_{i+1} + \delta_{k,i+1} \text{ for } k \neq i, i + 1. \quad (4.A.3)$$

By setting $k = i + 1$ in (4.A.2) and $k = i - 1$ in (4.A.3) we get the following two equations

$$\Delta_{i-1} + \delta_{i+1,i-1} + \tau \leq \Delta_i + \delta_{i+1,i} \quad (4.A.4)$$

$$\Delta_i + \delta_{i-1,i} + \tau \leq \Delta_{i+1} + \delta_{i-1,i+1}. \quad (4.A.5)$$

Adding the left hand sides and the right hand sides of (4.A.4) and (4.A.5), and using the fact that $\delta_{ik} = \delta_{ki}$ we get

$$\Delta_{i-1} + \delta_{i,i-1} + 2\tau \leq \Delta_{i+1} + \delta_{i,i+1}. \quad (4.A.6)$$

This shows that (4.A.1) holds and it also shows that the inequality is always strict given that $\tau > 0$.

4.B Average Complexity of IPA

In this Appendix, we try to arrive at the average complexity of the IPA algorithm. We first create a random topology, by scattering the nodes in a two-dimensional

plane. The coordinates (x, y) are drawn from a Gaussian distribution as shown below:

$$(x, y) \sim (\mathcal{N}(0, \sigma^2), \mathcal{N}(0, \sigma^2)) . \quad (4.B.1)$$

We sweep the number of nodes, N , from 5 to 50 and for each N , we calculate the average time elapsed (ticks) for the IPA algorithm for 32 distinct topologies constructed using $\sigma = 5$ [m]. The elapsed times are measured on Intel Core i5 4300U CPU at 1.9 GHz machine with 8 GB RAM running the Windows 8.1 pro operating system. The blue curve in Figure 4.17a shows the average time elapsed versus N for IPA. To get the average complexity, we try to fit this graph with polynomials of various orders. We also evaluate the residual square error (square of the L2-norm of the residual vector) for various order polynomial fits, this is shown in Figure 4.17b, which indicates that the residual error becomes negligible for an order 3 or more polynomial fit. The red curve in Figure 4.17a, shows that the 3rd order polynomial, $1 \times 10^{-4}x^3 - 2.1 \times 10^{-3}x^2 + 3.07 \times 10^{-2}x - 0.12$, gives a perfect fit, indicating that the average complexity of the IPA algorithm is $O(N^3)$.

Detection and Fusion techniques for IR-UWB transceivers

In this chapter, we analyze the performance of a multi-pulse impulse radio based ultra-wideband (IR-UWB) detector in an AWGN setting and provide different fusion strategies for fusing these detector outputs. To enable the transceiver to be used for multiple applications, designers have different types of detectors such as energy detectors, amplitude detectors, etc., built in to a single transceiver architecture. In order to get early insight into theoretically achievable performance of these fusion techniques, we assess the performance of these fusion techniques for commonly used detector types like matched filter, energy detector and amplitude detector under a Gaussian assumption. The proposed methods are valid for ultra short distance communication and in UWB systems operating in millimeter wave (mmWave) band with high directivity gain. We also derive the detection performance equation for each of the detectors in terms of false alarm rate, shape of the pulse, and number of UWB pulses used in the detection, and apply these in the fusion algorithms. We show that the performance can be improved by approximately 4 dB in terms of signal to noise ratio (SNR) for high probability of detection of a UWB signal ($> 95\%$), by fusing decisions from multiple detector types compared to a standalone energy detector, in a practical scenario.

5.1 Background

As discussed in Chapter 1, IR-UWB schemes employ narrow impulse signals, which can yield high time resolution, and hence can be used for accurate position localization and ranging. Narrow pulse duration coupled with low amplitude due to the restrictions from regulatory agencies like Federal Communications Commission (FCC) makes the detection of these pulses challenging [FCC02, AR09, YDH14]. In general, transmit signaling employs multiple pulses and the receiver aggregates certain characteristics from these pulses like energy, amplitude, position, etc., to make statistical inferences on the transmitted information like range (localization)

or transmitted symbol value (communication) etc. [WS00, WLJ⁺09a]. The performance of the receiver depends on how well the received pulse statistics are utilized for a chosen application [YDH14, WLJ⁺09b].

In many hardware platforms, a single UWB transceiver mounted on sensors is used for multiple applications like ranging, localization, communication, etc., each using particular statistics of the received samples for UWB pulse detection [NZSH13]. For example, long distance communication using UWB may employ an energy detector over a large number of pulses; whereas short distance tracking applications may use an amplitude detector on a few pulses. To enable the transceiver to be used for multiple applications, the designers have different types of detectors like amplitude detectors, energy detectors, etc., built into a single transceiver. In this chapter, we will consider the structure of a digital sampling receiver shown in Figure 5.1. Each detector¹ uses its own detection algorithm on the received samples to infer a hypothesis from the received samples and report it to the higher layers for further processing. These are typically implemented in FPGA for faster processing, and hence, only the computed hard or soft-value decisions are available. In some applications, there are no stringent constraints to bind the usage of a particular detector type; for example, demodulation of short range low data rate communication. In these situations, instead of resorting to a single detector type to arrive at the hypothesis, decision information from all of the different types of detectors can be concurrently utilized to make a more informed decision on the hypothesis. This will utilize transceiver infrastructure better, and since every detector decision is new information about the signaled hypothesis, it should yield better reliability and improved performance.

We formulate a binary hypothesis problem of IR-UWB pulse detection, where decisions from different types of detectors are fused using different fusion methods before deciding on the hypothesis as shown in Figure 5.1. We demonstrate the methods using three commonly employed UWB detector-types ($L = 3$ in Figure 5.1), with an energy detector (ED), matched filter (MF), and an amplitude detector (AD) for Detector-1, Detector-2 and Detector-3 respectively. The binary decisions signaling the hypothesis from these three detectors $\mathbf{d} = [d_1, d_2, d_3]$ are fed to the fusion algorithm to arrive at the binary decision regarding the hypothesis, d_{fused} .

To illustrate the benefits of the scheme, we perform the following steps. First, we derive performance equations for the most commonly used IR-UWB detector types like a matched filter (MF), an amplitude detector (AD) and an energy detector (ED). Here, we derive the analytical expression for probability of detection, P_D , as a function of false alarm rate, P_{FA} , signal-to-noise ratio (SNR), shape of the pulse, etc., for a multi-pulse UWB signal corrupted by additive white Gaussian noise (AWGN). To our knowledge, such an analytical expression is not available in the literature and is believed to be of an interest for the reader in its own right. We discuss the performance of the detectors through the performance plots

¹Detectors and detector types are interchangeably used. In Figure 5.1, each detector in the set, (Detector-1, ..., Detector-L) are of different type.

and verify the theoretical derivations in simulations. Subsequently, we discuss the fusion algorithms for a set of different detectors types (Detector-1, \dots , Detector-L), yielding binary decisions signaling the hypothesis, \mathbf{d} (refer to Figure 5.1). Then, we use these expressions in the fusion algorithms discussed earlier with $L = 3$ and Detector-1, Detector-2 and Detector-3 as MF, ED and AD respectively to assess the performance. We show that, if there are multiple detectors available in the UWB transceiver platform, then decision information from these detectors can be concurrently utilized and intelligently fused based on the application criteria to make a more informed decision on the hypothesis, thus leading to progress in the hypothesis testing concerning UWB pulse detection.

In the proposed receiver structure of Figure 5.1, the received signal is filtered by an RF band-pass filter (BPF) and is amplified using a wideband LNA. The signal is then converted into the digital domain by a high sampling rate analog-to-digital converters (ADC) and digitally processed. The digital receiver structure offers several benefits such as flexibility in design, reconfigurability and scalability [CGC10]. However, since IR-UWB signals occupy large bandwidth and have high time resolution, the design of an IR-UWB digital transceiver is challenging. In order to exploit the regulatory body specifications optimally, the transceivers must operate at a 3.1 – 10 GHz range or in the unlicensed millimeter wave (mmWave) frequency. The wideband BPF design should cover the whole of the useful UWB frequency band. The microwave filter's design, based on a microstrip multi-mode resonator (MMR) and hybrid coplanar waveguide/microstrip structure can cover these ranges. The work in [ZSM05, HHK05, SHN03, IA04] proposes several wideband BPF filter designs for the intended purpose. The wideband LNA amplifies the signal to the operating levels of the ADC. The work in [LN04, WWZ14] discusses the various design aspects of the wideband LNA for UWB radios.

The most complex and costly part of the IR-UWB digital receiver is the ADC. IR-UWB pulses are extremely narrow (orders of a few ns) and occupy very high bandwidth, therefore high speed ADCs are needed for faithful digital representation of the IR-UWB pulses. Typically, such high speed ADCs are designed using a flash ADC [NBC02] or a bank of polyphase ADCs [OB05]. The recent progress in ADC technology, as suggested by [Mur16], indicates that such high speed ADC having a good resolution with signal-to-noise-and-distortion ratio (SNDR) of higher than 30 dB can be achieved for a bandwidth of 10 GHz. This has enabled digital designs for IR-UWB technology. The digital samples from the ADC will be processed by a digital baseband processing block for detection. The baseband processing block consists of a bank of interleavers and detectors. The received frames are time interleaved to avoid coherence between the detector channels. Even though, in practice, this cannot be always accomplished, in those scenarios, the methods proposed are only the upper bound on the achievable performance. For example, in [LG90], the model structures based on the linear regressors for the analysis of tracking algorithms are assumed independent in analysis, but are dependent in practice.

The proposed transceiver structure shown in Figure 5.1 is applicable to the future evolution of our in-house flexible UWB hardware platform as discussed in

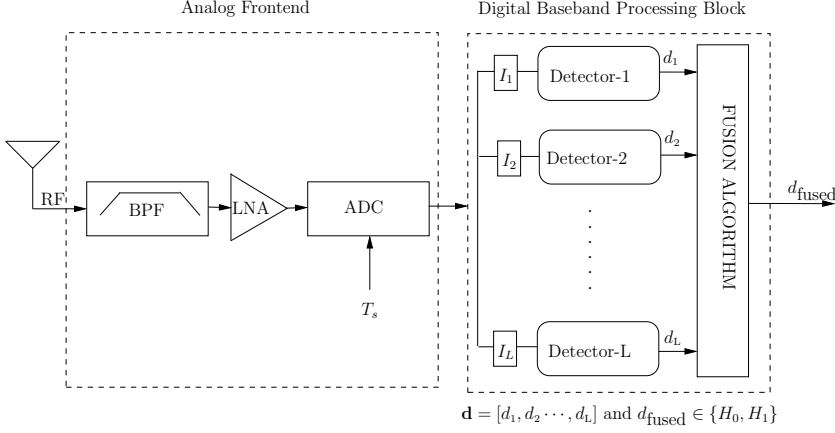


Figure 5.1: Depiction of direct sampling receiver architecture with multi detector fusion. (Detector-1, \dots , Detector-L) are the different detector types available in the transceiver. $d_i, i \in [1, \dots, L]$, indicates the binary decisions made by the different detectors^[1] with regard to the hypothesis. d_{fused} , indicates the fused binary decision for the chosen hypothesis.

Chapter 1 [ADH13, YDAH14]. This platform can be used for joint ranging and communication applications. The platform has a digital processing section comprising an FPGA, where the proposed techniques of this chapter can be implemented. Even though the applicability of the techniques are demonstrated in simulation, the results provide an early insight in to achievable performance. The variants of the proposed structure in Figure 5.1 for hypotheses testing are also employed in [LLH03] and [Wan11]. In [LLH03], the authors discuss UWB hypothesis testing for a bank of similar analog detectors, whereas in [Wan11], the authors propose a distributed fusion of results from multiple UWB sensors, by allocating a different number of pulses to each sensor, under the constraint of maximum number of allocated pulses, such that the error is minimized. Thus, both are different from the proposed application of this chapter.

The rest of the chapter is organized as follows. In Section 5.2, we will discuss the system model. Here, we will define the signal model which will be used in the rest of the chapter. In Section 5.3, we will derive the analytical expression for P_D as a function of P_{FA} , and SNR for matched filter, energy detector and amplitude detector for a multi-pulse IR-UWB signal. Section 5.4 discuss different fusion strategies. In Section 5.5, we will evaluate the performance of the different fusion strategies using the performance equation of the individual detectors derived in Section 5.3. Finally in Section 5.6, we discuss the conclusions.

Parameter	Description
P_{FA}	Probability of false alarm
SNR	Signal to noise ratio
N_p	Number of UWB pulses used in detection
E_p	Energy of the UWB pulses
$s(t)$	Shape of the UWB pulses

Table 5.1: Parameters on which detector's performance depends.

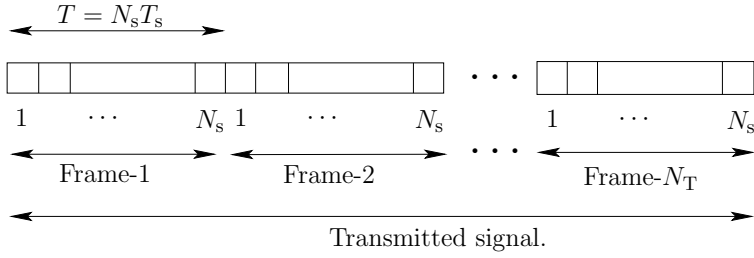


Figure 5.2: Transmit signal structure constitutes of N_T transmit frames. Under hypothesis H_1 , each frame consists of N_s samples of UWB pulse $s(t)$. Under hypothesis H_0 , nothing is transmitted.

5.2 System Model

We consider a binary hypothesis for detection, with H_0 representing that the signal is absent and H_1 representing that the signal is present. Each of the different types of detectors like MF, ED, etc. in the UWB transceiver construct a test statistic from the received samples, based on which inference is made about H_0 or H_1 by comparing the test statistic to a threshold, γ . Different detector types have different ways to construct the test statistic, and thus have varying degrees of performance like probability of detection, P_D , probability of error, P_e , etc. Apart from the chosen test statistic, the performance of the particular detector also depends on all or a few of the parameters listed in the Table 5.1. In Section 5.3, we will derive the analytical expression for probability of detection, P_D , for the ED, MF, and AD detectors as a function of parameters defined in Table 5.1.

The transmitted signal under hypothesis H_1 consists of N_T frames, such that

$$N_T \geq N_p^i \quad \forall i \in \{1, 2, \dots, L\},$$

where N_p^i denotes the number of frames used by Detector- i in the hypothesis test. Each frame consists of one IR-UWB pulse, and during hypothesis H_0 nothing is

transmitted (N_T empty frames). Each UWB pulse is of fixed duration, T , represented by $s(t)$, sampled at the rate, $1/T_s$, and has $N_s = T/T_s$, samples. The transmit signal structure is as shown in Figure 5.2. Thus, both hypotheses can be mathematically expressed as

$$\begin{aligned} & \sum_{n=0}^{N_T-1} \sum_{i=0}^{N_s-1} s(t-nT)\delta(t-nT-iT_s) \quad \text{under } H_1, \\ & 0 \quad \text{under } H_0 \end{aligned} \quad (5.2.1)$$

where $\delta(t)$ denotes the Dirac delta function and the model uses N_T identical frames in each hypothesis test cycle. This is similar to the time hopped impulse radio (TH-IR) UWB models proposed in [Sch93, WS98, WS00], except that we are not considering time hopping, as it has no effect on the statistics collected by the detector across multiple frames. The function $s(t-nT)\delta(t-nT-iT_s)$ represents the i -th discrete sample of the n -th frame under hypothesis H_1 and is denoted by $s(n, i)$. The received signal is corrupted by Gaussian noise. Thus, the received signal used in the hypothesis test under both hypotheses is given by

$$\begin{aligned} & \sum_{n=0}^{N_T-1} \sum_{i=0}^{N_s-1} x(t-nT)\delta(t-nT-iT_s) \quad \text{under } H_1 \\ & \sum_{n=0}^{N_T-1} \sum_{i=0}^{N_s-1} w(t-nT)\delta(t-nT-iT_s) \quad \text{under } H_0 \end{aligned}, \quad (5.2.2)$$

where $x(t)$ is the received pulse shape. The function, $x(t-nT)\delta(t-nT-iT_s)$, represents the i -th sample of the n -th received frame under hypothesis H_1 and is denoted by $x(n, i)$. Similarly, $w(t-nT)\delta(t-nT-iT_s)$, represents the Gaussian noise corresponding to the i -th sample of the n -th received frame and is denoted by $w(n, i)$. We assume a single-path line-of-sight (LOS) channel, thus, the received samples, $x(n, i) = \beta s(n, i) + w(n, i)$, where, β , indicates the path loss.

Typically, the UWB channels are subject to multi-path propagation where a large number of paths can be observed at the receiver [PR14]. However, if the transceivers are in close proximity with clear line of sight, the detectors here rely on the first arriving path or LOS; this is in contrast to traditional channel measurement and modeling. If the UWB transceiver is operating at millimeter wave frequencies, due to the combined effect of higher directivity gain due to the RF-beamforming and higher absorption characteristics of the channel results in single-path LOS channels for distances less than 100 meters. The IEEE 802.15.3c standard channel measurements for a residential LOS channel model also corroborate the same [GQMT07, IEE09, TMR11]. For the transceiver operating in the frequency band less than 10 GHz, due to higher reflections, refractions and scattering characteristics of the channel, the assumption of a single-path LOS channel is valid only for extremely short distances of order of less than 10 meters [ADH13, Cot14, Mol05, YDAH14]. These short distance high speed UWB applications include transferjet and wireless USB (wUSB) [Tra16, All16]. Also, adopting the simple model proposed here will

make the discussion mathematically tractable. Without loss of generality, we use $\beta = 1$. In the signal model proposed in (5.2.1) and (5.2.2), we assume perfect synchronization, otherwise there will be degradation of the individual detectors (and fused) performance. In many systems, the synchronization can be accomplished using methods proposed in [GKS03, EGE02a]. In the next section, we will derive the detection performance of these detectors, which will be used in later sections to evaluate fusion performance.

5.3 Detector Performance

The performance of the MF, ED, and AD detectors is studied in [Tur60, VT04, Urk67, Kay98] for a general deterministic signal. Energy detection based sub-Nyquist UWB detectors are studied in [GS05, GSO06]. However, the performance analysis of the MF, ED, and AD detection for a digital UWB signal as a function of parameters shown in Table 5.1 is not available in literature to the best knowledge of the authors. In this Section, we will derive analytical expressions for probability of detection, P_D , as a function of parameters in Table 5.1 and use them in later sections to assess the performance of the fusion rules.

As discussed in Section 5.2, each transmit frame constitutes a UWB pulse, $s(t)$, sampled at $1/T_s$. We define frame energy, E_{p_n} , as

$$E_{p_n} = \sum_{i=0}^{N_s-1} s^2(n, i). \quad (5.3.1)$$

We assume all the frames in the transmission are of the same pulse shape, $s(t)$, so (5.3.1) is independent of n , thus $E_p = E_{p_n}$. As discussed in (5.2.2), the received signal under both hypotheses, H_1 and H_0 , is corrupted by AWGN noise samples, $w(n, i)$. We assume that these noise samples are independent and identically distributed (IID) with $w(n, i) \sim \mathcal{N}(0, \sigma^2/N_s)$, where \mathcal{N} denotes the normal distribution, such that the total noise energy in the frame is given by

$$\sum_{i=0}^{N_s-1} \mathbf{E}[w^2(n, i)] = \sigma^2. \quad (5.3.2)$$

Here, \mathbf{E} denotes the expectation operator. We define signal-to-noise ratio, SNR, as

$$\text{SNR} = \frac{E_p}{\sigma^2}. \quad (5.3.3)$$

Typical detector structure used in Figure 5.1 is as shown in Figure 5.3. Each detector will construct a test statistic, T_k , such that

$$T_k = \sum_{n=0}^{N_p^k} \sum_{i=0}^{N_s-1} f_k(r(n, i)), \quad (5.3.4)$$

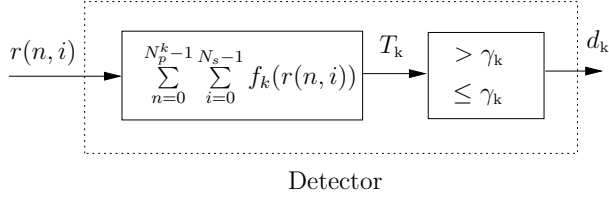


Figure 5.3: Generic detector structure. The different detector types use a different function $f_k(\cdot)$, to construct the test statistic, T_k . Since in this chapter, we use three distinct detector types, matched filter (MF), energy detector (ED), and amplitude detector (AD), we have $k \in \{\text{MF}, \text{ED}, \text{AD}\}$. The $r(n, i)$ denotes the received samples. The $r(n, i) = x(n, i)$ and $r(n, i) = w(n, i)$ during hypotheses H_1 and H_0 respectively.

from the received samples and compare it with a threshold to decide on a hypothesis. Depending on the test statistic generation function, $f_k(\cdot)$, we have different types of detectors like matched filter, energy detector, amplitude detector, etc.. In this chapter, we use MF, ED, and AD detectors, thus we have $k \in \{\text{MF}, \text{ED}, \text{AD}\}$. N_p^k denote number of frames used by the detector- k , in the hypothesis testing. The $r(n, i)$ denotes the received samples and is equal to $x(n, i)$ and $w(n, i)$ during hypotheses H_1 and H_0 respectively.

5.3.1 Matched Filter

For the matched filter, the test statistic generation function, $f_k(\cdot)$, is given by

$$f_{\text{MF}}(r(n, i)) = r(n, i)s(n, i). \quad (5.3.5)$$

The performance in terms of probability of detection for the matched filter, P_D^{MF} , as a function of probability of false alarm, $P_{\text{FA}}^{\text{MF}}$, and SNR is derived in Appendix 5.A and it is given by

$$P_D^{\text{MF}} = \mathbf{Q} \left(\mathbf{Q}^{-1}(P_{\text{FA}}) - \sqrt{N_s N_p^{\text{MF}} \text{SNR}} \right), \quad (5.3.6)$$

where \mathbf{Q} is the tail probability of the Gaussian distribution and SNR is as defined in (5.3.3). Equation (5.3.6) is used to evaluate the performance at various SNRs and is shown in Figure 5.4a and receiver operating characteristics (ROC) is shown in Figure 5.4b.

5.3.2 Energy Detector

In the energy detector, the test statistic generation function, $f_k(\cdot)$, is given by

$$f_{\text{ED}}(r(n, i)) = r^2(n, i). \quad (5.3.7)$$

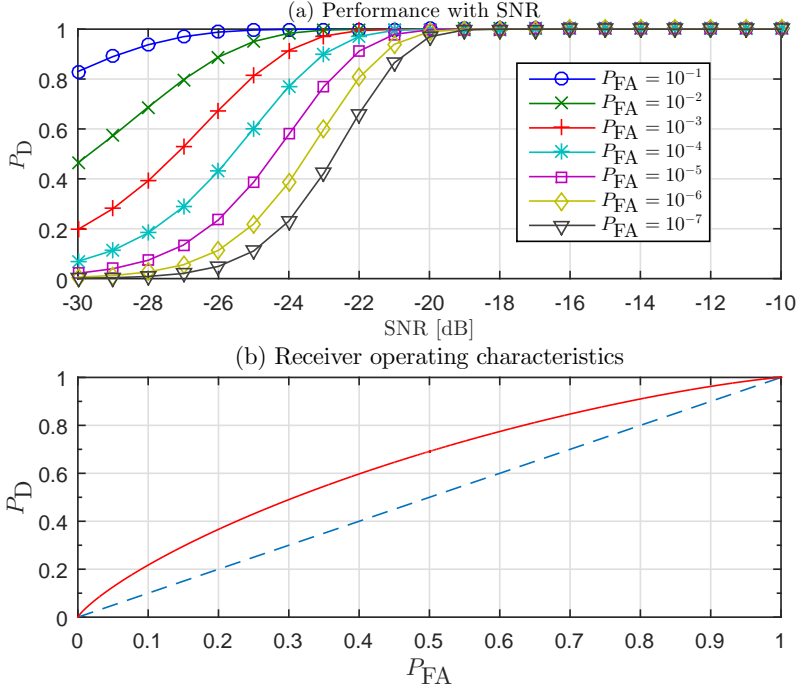


Figure 5.4: Detection performance at various SNRs and ROC for a matched filter detector. For (a) and (b) plots, $N_p^{\text{MF}} = 10$ and $\text{SNR} = -30$ [dB] are considered.

The performance in terms of probability of detection for the energy detector, P_D^{ED} , as a function of probability of false alarm, P_{FA}^{ED} , and SNR is derived in Appendix 5.B and it is given by

$$P_D^{\text{ED}} = \mathbf{Q}_{\chi^2_\nu(\lambda)}^{-1} \left(\sqrt{2N_p^{\text{ED}}N_s} \mathbf{Q}^{-1}(P_{FA}^{\text{ED}}) + N_p^{\text{ED}}N_s \right) \quad (5.3.8)$$

where $\mathbf{Q}_{\chi^2_\nu(\lambda)}$ is the tail probability of the non-central chi-square distribution with degrees of freedom, $\nu = N_p^{\text{ED}}N_s$, and the centrality parameter, $\lambda = N_p^{\text{ED}}N_s\text{SNR}$. The SNR is defined as in (5.3.3). Equation (5.3.8) is used to evaluate the performance at various SNRs and is shown in Figure 5.5a and receiver operating characteristics (ROC) is shown in Figure 5.5b. In deriving the equation (5.3.8) several assumptions are made; later we will verify this analytical equation in simulations.

5.3.3 Amplitude Detector

In the amplitude detector, the test statistic generation function, $f_k(\cdot)$, is given by

$$f_{\text{AD}}(r(n, i)) = |r(n, i)|. \quad (5.3.9)$$

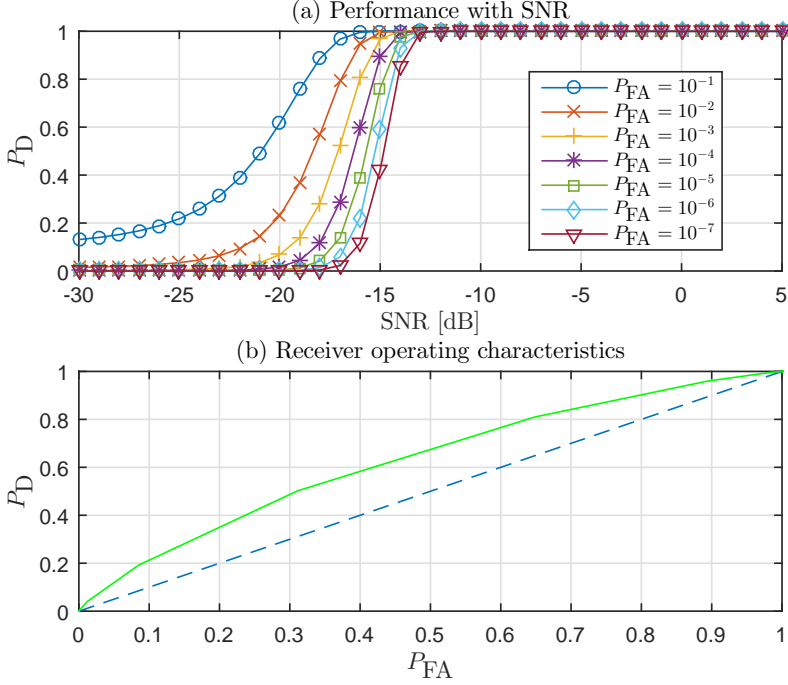


Figure 5.5: Detection performance at various SNRs and ROC for the energy detector. For (a) and (b) plots, $N_p^{\text{ED}} = 1000$ and $\text{SNR} = -25$ [dB] are considered.

The performance in terms of probability of detection for the amplitude detector, P_D^{AD} , as a function of probability of false alarm, P_{FA}^{AD} , and SNR is derived in Appendix 5.C and it is given by

$$P_D^{\text{AD}} = \mathbf{Q} \left(\mathbf{Q}^{-1} \left(\frac{P_{FA}^{\text{AD}}}{2} \right) - \alpha \sqrt{N_p^{\text{AD}} E_p \text{SNR}} \right) + \mathbf{Q} \left(\mathbf{Q}^{-1} \left(\frac{P_{FA}^{\text{AD}}}{2} \right) + \alpha \sqrt{N_p^{\text{AD}} E_p \text{SNR}} \right) \quad (5.3.10)$$

where α is defined as

$$\sum_{i=0}^{N_s-1} s(i) = \alpha E_p, \quad (5.3.11)$$

As shown by (5.3.11) and (5.3.10), the performance of the amplitude detector depends on the shape of the UWB pulse used. We have considered a normalized second order Gaussian pulse as described in [YDAH13, YDH14, MG07]. This is given

by

$$s(t) = -4\pi e^{\frac{-2\pi t^2}{\tau^2}} \left(\frac{-\tau^2 + 4\pi t^2}{\tau^4} \right), \quad (5.3.12)$$

where τ is used to control the impulse spread. Energy normalized pulse, $E_p = 1$, with $\tau = 3.33$ ns, sampled at 5 GHz will result in $\alpha = 4.49$. Thus, for this pulse shape the performance of the amplitude detector is given by

$$\begin{aligned} P_D^{AD} = & \mathbf{Q} \left(\mathbf{Q}^{-1} \left(\frac{P_{FA}^{AD}}{2} \right) - 4.49 \sqrt{N_p^{AD} E_p \text{SNR}} \right) \\ & + \mathbf{Q} \left(\mathbf{Q}^{-1} \left(\frac{P_{FA}^{AD}}{2} \right) + 4.49 \sqrt{N_p^{AD} E_p \text{SNR}} \right). \end{aligned} \quad (5.3.13)$$

Equation (5.3.13) is used to evaluate the performance at various SNRs and is shown in Figure 5.6a and receiver operating characteristics (ROC) is shown in Figure 5.6b.

From (5.3.6), (5.3.8), and (5.3.13), the performance of the matched filter, energy detector and amplitude detector depends on the environment (SNR) and on the system configuration or tuning variables like number of frames considered in the hypothesis testing, N_p and probability of false alarm, P_{FA} . In the matched filter and energy detector, the performance is agnostic to the system specifications like pulse shape, which are fixed for a given hardware. However, in the amplitude detector, detection performance depends on the shape of the pulse as shown in (5.3.10) and (5.3.11). For parameters from the Table 5.2, the probability of detection, P_D , versus SNR using the analytical expression (5.3.6), (5.3.8), and (5.3.13) is as shown in the blue color plots of Figure 5.8.

5.4 Fusion Rules for IR-UWB Signal Detection

We consider a general counting rule, that is, deciding for H_1 if the sum of the decisions, $\sum_{i=1}^L d_i$, exceeds the threshold, k . If we define the decision of the i -th detector in Figure 5.1 as $d_i = 0$ and $d_i = 1$ for hypothesis H_0 and H_1 respectively, then the special cases of these include simple fusion rules such as “AND” ($k = L$), “OR” ($k = 1$), and “Majority-Voting” ($k = L/2$). These fusion rules are depicted in Figure 5.7a, Figure 5.7b and Figure 5.7c. These rules are simple to implement and have been proved to possess robustness features with respect to performance as shown in [CMR15, CR14].

The counting rule based fusion is biased either toward hypothesis H_1 (UWB pulse detection in our model), or toward H_0 . For example, fusing using the “OR” rule will have superior detection performance, but will also have a larger false alarm rate. Similarly, the “AND” fusion rule is conservative in UWB pulse detection, but has a superior false alarm rate performance. These aspects are further illustrated with numerical examples in later sections. If we define the mis-classification of the hypothesis as an error and the objective is to minimize the probability of error, P_e , then the decision rules discussed above are sub-optimal. This is the motivation to

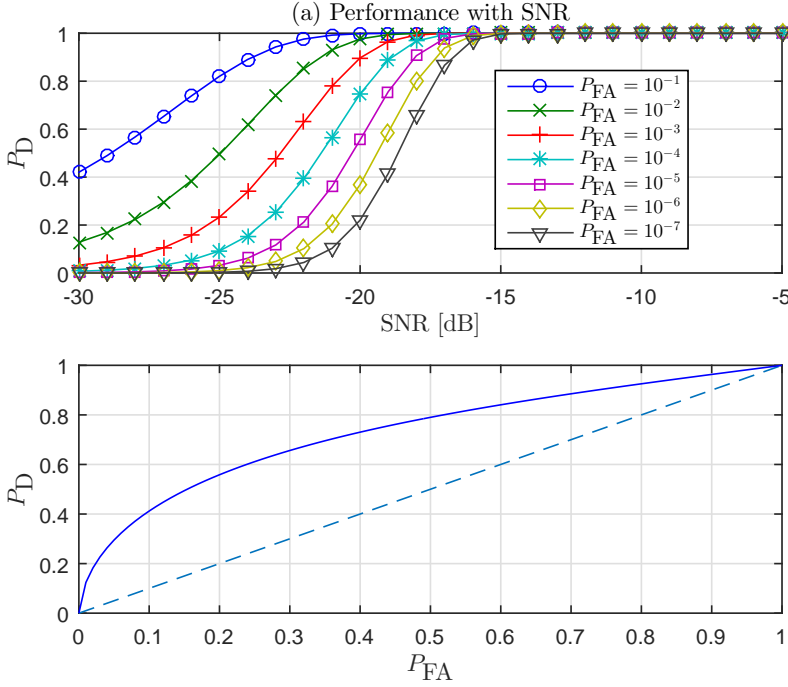


Figure 5.6: Detection performance at various SNRs and ROC for the amplitude detector. For (a) and (b) plots, $N_p^{AD} = 100$ and $\text{SNR} = -30$ [dB] are considered.

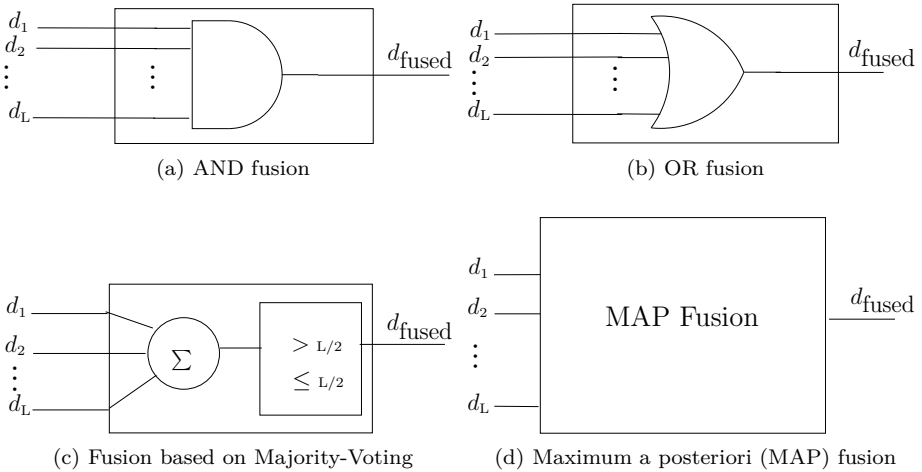


Figure 5.7: Depiction of different decision fusion methods.

design a fusion technique that is optimal in the probability of error sense. For any prior probability for H_0 and H_1 , the fusion rule that minimizes the probability of error is given by the maximum a posteriori (MAP) formulation given below

$$\Pr(H_1|\mathbf{d}) \underset{H_0}{\overset{H_1}{\geq}} \Pr(H_0|\mathbf{d}), \quad (5.4.1)$$

where \mathbf{d} is a L -size vector of binary values signaling the hypothesis of the decisions made by different detectors (refer to Figure 5.1). We can write (5.4.1) as

$$\log \left(\frac{\Pr(H_1|\mathbf{d})}{\Pr(H_0|\mathbf{d})} \right) \underset{H_0}{\overset{H_1}{\geq}} 0. \quad (5.4.2)$$

If we define sets \mathcal{I} , \mathcal{S}_{H_1} and \mathcal{S}_{H_0} as

$$\mathcal{I} := \{1, 2, \dots, L\}, \quad (5.4.3)$$

$$\mathcal{S}_{H_1} := \{i : d_i = 1\}, \quad (5.4.4)$$

$$\mathcal{S}_{H_0} := \mathcal{I} \setminus \mathcal{S}_{H_1} := \{i : d_i = 0\}, \quad (5.4.5)$$

where d_i is the binary decision of the detector- i ($i \in \mathcal{I}$), then,

$$\Pr(H_1|\mathbf{d}) = \frac{P_1}{p(\mathbf{d})} \prod_{i \in \mathcal{S}_{H_1}} P_D^i \prod_{i \in \mathcal{S}_{H_0}} (1 - P_D^i). \quad (5.4.6)$$

Here, we assumed that the decisions of each of the detectors are independent of each other. P_1 is the probability of hypothesis H_1 and $p(\cdot)$ denotes the probability density function (PDF). P_D^i is the probability of detection of the detector- i in Figure 5.1. Similarly, we can write

$$\Pr(H_0|\mathbf{d}) = \frac{P_0}{p(\mathbf{d})} \prod_{i \in \mathcal{S}_{H_1}} P_{FA}^i \prod_{i \in \mathcal{S}_{H_0}} (1 - P_{FA}^i). \quad (5.4.7)$$

P_0 is the probability of hypothesis H_0 . P_{FA}^i is the false alarm of the i -th detector. In many applications such as in communication, hypothesis testing is used for symbol decoding, where both the hypotheses are equally likely. Substituting (5.4.6) and (5.4.7) in (5.4.2) and assuming both hypotheses are equally likely, we get the decision rule as

$$\begin{aligned} \log \left(\frac{\Pr(H_1|\mathbf{d})}{\Pr(H_0|\mathbf{d})} \right) = \\ \sum_{i \in \mathcal{S}_{H_1}} \log \left(\frac{P_D^i}{P_{FA}^i} \right) + \sum_{i \in \mathcal{S}_{H_0}} \log \left(\frac{(1 - P_D^i)}{(1 - P_{FA}^i)} \right) \underset{H_0}{\overset{H_1}{\geq}} 0. \end{aligned} \quad (5.4.8)$$

Unlike the counting rule based fusion (k out of L rule), the MAP fusion rule employed in (5.4.8) requires P_D^i s and P_{FA}^i s at the fusion module (refer to Figure 5.1). In practice this is not always available. This method is also briefly described in [YDH16]. In the next section, we will evaluate the performance of the proposed structure in Figure 5.1 in a simulation under practical setting.

Detector Type	P_{FA}	N_p
Matched Filter	10^{-7}	100
Energy Detector	10^{-1}	1000
Amplitude Detector	10^{-4}	100

Table 5.2: Configuration of parameters for different detectors used in the fusion.

5.4.1 Simulation Study

In deriving the energy detector performance equation (5.3.8), we assumed that a sufficiently large number of pulses are considered. Similarly, for the amplitude detector performance equation (5.3.13), we assumed a particular UWB pulse shape. In this section, we will simulate the detectors and demonstrate the validity of these approximations, for a practical UWB signal setup. We use a signal model in which each frame is of 10 ns duration, having one normalized second order Gaussian pulse as defined in (5.3.12) with $\tau = 3.33$ ns, sampled at 5 GHz. We consider number of frames, N_p , and the false alarm rate, P_{FA} , from Table 5.2 for different detector types. The received samples are corrupted by AWGN noise with variance $1/\text{SNR}$ (since pulses are normalized, that is $E_p = 1$). Monte-Carlo simulations are done using 1000 independent realizations. The detector performance in simulations shown in red, matches the analytical expressions in (5.3.6), (5.3.8) and (5.3.13), shown in blue in Figure 5.8. This validates the derived performance expressions for a practical UWB signal configuration.

5.5 Performance Evaluation of Fusion Methods

When the same radio is used for multiple applications, detectors in them are tuned with different parameter values for P_{FA} , N_p , etc. For example, if the application needs a faster response, then the N_p used will be small; similarly if the application needs robust detection, then it may require a larger N_p . In general, the parameters N_p and P_{FA} are tuned based on the applications. As a result of this, different detectors are optimal in different SNR regions. For example, consider that operating parameters such as P_{FA} and N_p are as shown in Table 5.2. Evaluating equations (5.3.6), (5.3.8) and (5.3.10) with P_{FA} and N_p as defined in Table 5.2, the probability of detection for different detectors is as shown in the blue plots of Figure 5.8. We will consider three different types of detectors discussed earlier, i.e., matched filter, energy detector, and amplitude detector. With this set of detectors, we have $L = 3$, and for “AND”, “OR”, and “Majority-Voting”, we should have $k = 3$, $k = 1$, and $k > 2$ respectively for the counting rule based fusion rule discussed in Section 5.4.

We performed Monte-Carlo simulations with similar signal configurations described in Section 5.4.1. We generated 1000 random signals corresponding to hypotheses H_1 and H_0 as defined in (5.2.1). The probability of correct detection of

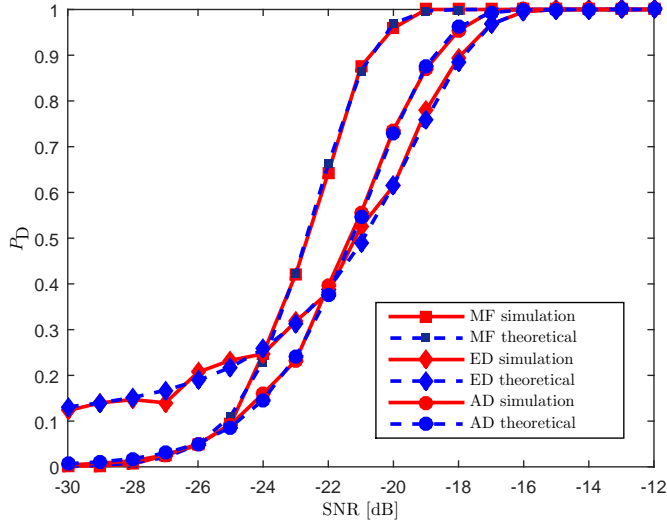


Figure 5.8: The performance of different detectors in theory and simulation are shown. A normalized second order Gaussian pulse of width 10 ns sampled at 5 GHz, is used in the simulation. Thousand random realizations are used in building the probability of detection statistics, with parameters from Table 5.2. The theoretical expressions match the simulation result for all the detectors.

hypothesis, H_1 , when H_1 was indeed signaled, P_D , and the probability of misclassification of hypotheses, P_e , was evaluated using the fusion rules discussed in Section 5.4. The P_{FA} , and N_p , for each detector type are taken from Table 5.2. Results for fused P_D , and P_e , are as shown in Figure 5.9a and Figure 5.9b respectively. Notice that for a fixed SNR, the probability of detection is high for the “OR” fusion, however, the probability of error is also high for the “OR” fusion. This indicates a higher probability of false alarm and probability of miss.

The performance is also evaluated using the MAP fusion rule (5.4.8), for a detector set, (MF, ED, AD), yielding decision vector \mathbf{d} (refer to Figure 5.1), with the configuration taken from Table 5.2. The probability of detection and probability of error are as shown in Figure 5.10a and Figure 5.10b, respectively. Notice that the MAP fusion method (defined by (5.4.8)) is close to “OR” fusion in detection performance, with superior probability of error performance as shown in Figure 5.10b. Comparing the performance of the energy detector alone with the MAP fusion rule for multiple detectors in Figure 5.10a and Figure 5.10b, indicates that a gain of 4 dB in terms of signal to noise ratio (SNR) can be achieved for probability of detection greater than 95% with low probability of error ($< 5\%$).

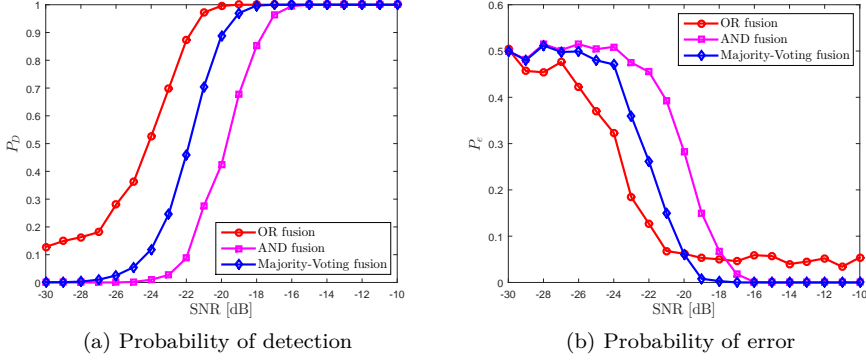


Figure 5.9: Probability of detection and error performance for various fusion techniques using the configuration defined in Table 5.2.

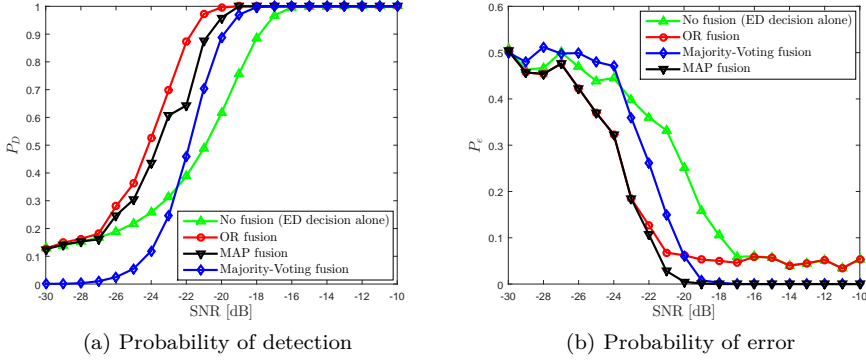


Figure 5.10: Probability of detection and error performance using the fusion rule defined in (5.4.8) (MAP fusion), OR Fusion and ED decision alone without any fusion using the configuration defined in Table 5.2.

5.6 Conclusion

In this chapter, we analyzed the UWB detection performance of matched filter, energy detector and amplitude detector. We derived the analytical expression for probability of detection, P_D , for each of the detectors as a function of parameters defined in Table 5.1. These are shown in (5.3.6), (5.3.8), and (5.3.10). We verified these expressions in simulations; this is shown in Figure 5.8. We analyzed the performance in terms of detection probability and probability of error for different fusion methods like “AND”, “OR”, and “Majority-Voting”. This is shown in

Figure 5.9a and Figure 5.9b. Using Bayes rule, we derived an optimal fusion rule (5.4.8) for UWB detection, which is optimal in the probability of error sense and compared its performance. This is shown in Figure 5.10a and Figure 5.10b.

Results indicate that by making a suitable choice of fusion rule, a trade off between detection and false alarm can be achieved. For example, Figure 5.9a shows that OR fusion is more biased toward detection, however, it also results in higher errors (due to false alarms, refer to Figure 5.9b). If the error performance is critical for the UWB application, then MAP fusion formulation gives superior performance in terms of errors as shown in Figure 5.10b. In general, if there are multiple detectors available in the UWB transceiver platform, then decision information from these detectors can be concurrently utilized and intelligently fused based on the application criteria to make a more informed decision on the hypothesis. In contrast to a standalone detector, the proposed fusion methods enable highly accurate hypothesis testing for UWB signal, thereby improving the performance of the UWB transceiver in applications such as communication and localization.

5.A Performance of Matched Filter

In this Section, we will derive the analytical expression for probability of detection, P_D^{MF} , for a matched filter. We will use N_p^{MF} received frames in each hypothesis test cycle, having a UWB pulse of energy E_p , as defined in (5.3.1) for H_1 hypothesis and having only noise during the H_0 hypothesis. Due to the AWGN channel, the received samples at the receiver have noise which is distributed as $w(n, i) \sim \mathcal{N}(0, \sigma^2/N_s)$, as discussed in Section 5.3. The total noise energy in the received frame is σ^2 as shown in (5.3.2). The ratio of frame energy, E_p , and the noise energy in the received frame, σ^2 , is defined as SNR as shown in (5.3.3).

In a matched filter, the test statistic, T_{MF} , is compared against a threshold γ_{MF} (refer to Figure 5.3). Thus, the hypotheses test can be formulated as

$$T_{\text{MF}} \underset{H_0}{\overset{H_1}{\gtrless}} \gamma_{\text{MF}}, \quad (5.A.1)$$

where T_{MF} is given by

$$T_{\text{MF}} = \sum_{n=0}^{N_p^{\text{MF}}-1} \sum_{i=0}^{N_s-1} r(n, i)s(n, i). \quad (5.A.2)$$

The $r(n, i)$ and $s(n, i)$ are defined in Sections 5.3 and 5.2, respectively. Since $r(n, i) = s(n, i) + w(n, i)$ and $r(n, i) = w(n, i)$ under H_1 and H_0 hypotheses, re-

spectively, we can write

$$T_{\text{MF}} = \begin{cases} \sum_{n=0}^{N_{\text{p}}^{\text{MF}}-1} \sum_{i=0}^{N_{\text{s}}-1} s^2(n, i) + w(n, i)s(n, i) & \text{under } H_1, \\ \sum_{n=0}^{N_{\text{p}}^{\text{MF}}-1} \sum_{i=0}^{N_{\text{s}}-1} w(n, i)s(n, i) & \text{under } H_0. \end{cases} \quad (5.A.3)$$

Since each transmit frame carries the same energy, E_{p} , we can write

$$\sum_{n=0}^{N_{\text{p}}^{\text{MF}}-1} \sum_{i=0}^{N_{\text{s}}-1} s^2(n, i) = N_{\text{p}}^{\text{MF}} E_{\text{p}}.$$

Thus, the matched filter test statistic under hypothesis H_1 ,

$$T_{\text{MF}}^{\text{H}_1} = N_{\text{p}}^{\text{MF}} E_{\text{p}} + \sum_{n=0}^{N_{\text{p}}^{\text{MF}}-1} \sum_{i=0}^{N_{\text{s}}-1} w(n, i)s(n, i). \quad (5.A.4)$$

The $T_{\text{MF}}^{\text{H}_1}$ is a Gaussian random variable with mean

$$\mathbf{E} [T_{\text{MF}}^{\text{H}_1}] = N_{\text{p}}^{\text{MF}} E_{\text{p}}, \quad (5.A.5)$$

and variance

$$\begin{aligned} \mathbf{Var} [T_{\text{MF}}^{\text{H}_1}] &= \mathbf{Var} [N_{\text{p}}^{\text{MF}} E_{\text{p}}] + \sum_{n=0}^{N_{\text{p}}^{\text{MF}}-1} \sum_{i=0}^{N_{\text{s}}-1} \mathbf{Var} [s(n, i)w(n, i)], \\ &= \sum_{n=0}^{N_{\text{p}}^{\text{MF}}-1} \sum_{i=0}^{N_{\text{s}}-1} s^2(n, i) \mathbf{Var} [w(n, i)], \\ &= \frac{N_{\text{p}}^{\text{MF}} \sigma^2 E_{\text{p}}}{N_{\text{s}}}, \end{aligned} \quad (5.A.6)$$

where $\mathbf{Var} [\cdot]$ denotes the variance of the random variable. Similarly, the test statistic under hypothesis H_0 , $T_{\text{MF}}^{\text{H}_0}$ is a Gaussian random variable with mean and variance

$$\mathbf{E} [T_{\text{MF}}^{\text{H}_0}] = \mathbf{E} \left[\sum_{n=0}^{N_{\text{p}}^{\text{MF}}-1} \sum_{i=0}^{N_{\text{s}}-1} s(n, i)w(n, i) \right] \quad (5.A.7)$$

$$= 0, \quad (5.A.8)$$

$$\mathbf{Var} [T_{\text{MF}}^{\text{H}_0}] = \mathbf{Var} \left[\sum_{n=0}^{N_{\text{p}}^{\text{MF}}-1} \sum_{i=0}^{N_{\text{s}}-1} s(n, i)w(n, i) \right] \quad (5.A.9)$$

$$= \frac{N_{\text{p}}^{\text{MF}} \sigma^2 E_{\text{p}}}{N_{\text{s}}}. \quad (5.A.10)$$

Combining equations (5.A.5) to (5.A.10), the PDF of the matched filter test statistic can be written as

$$p(T_{\text{MF}}) = \begin{cases} \mathcal{N}\left(N_{\text{p}}^{\text{MF}} E_{\text{p}}, \frac{N_{\text{p}}^{\text{MF}} \sigma^2 E_{\text{p}}}{N_{\text{s}}}\right) & \text{under } H_1, \\ \mathcal{N}\left(0, \frac{N_{\text{p}}^{\text{MF}} \sigma^2 E_{\text{p}}}{N_{\text{s}}}\right) & \text{under } H_0. \end{cases} \quad (5.A.11)$$

Thus, for a fixed threshold γ_{MF} , we can show that the match filter detector's probability of false alarm, $P_{\text{FA}}^{\text{MF}}$ and probability of detection, P_{D}^{MF} is given by

$$P_{\text{FA}}^{\text{MF}} = \Pr(T_{\text{MF}} > \gamma_{\text{MF}}; H_0) = \mathbf{Q}\left(\frac{\gamma_{\text{MF}}}{\sqrt{\frac{N_{\text{p}}^{\text{MF}} \sigma^2 E_{\text{p}}}{N_{\text{s}}}}}\right), \quad (5.A.12)$$

$$P_{\text{D}}^{\text{MF}} = \Pr(T_{\text{MF}} > \gamma_{\text{MF}}; H_1) = \mathbf{Q}\left(\frac{\gamma_{\text{MF}} - N_{\text{p}}^{\text{MF}} E_{\text{p}}}{\sqrt{\frac{N_{\text{p}}^{\text{MF}} \sigma^2 E_{\text{p}}}{N_{\text{s}}}}}\right) \quad (5.A.13)$$

where \mathbf{Q} is the tail probability of the Gaussian distribution. By solving for γ_{MF} in (5.A.12) for a fixed false alarm and substituting it in (5.A.13), we get the analytical form for the probability of detection. It is given by

$$P_{\text{D}}^{\text{MF}} = \mathbf{Q}\left(\mathbf{Q}^{-1}(P_{\text{FA}}^{\text{MF}}) - \sqrt{N_{\text{s}} N_{\text{p}}^{\text{MF}} \text{SNR}}\right), \quad (5.A.14)$$

where SNR is as defined in (5.3.3).

5.B Performance of Energy Detector

In this Section, we will derive the analytical expression for the probability of detection, P_{D} , for the energy detector. We proceed with the same definitions for E_{p} , SNR, and σ^2 as in Appendix 5.A.

In the energy detector, the test statistic, T_{ED} , is compared against a threshold, γ_{ED} (refer to Figure 5.3). Thus, the hypothesis test can be formulated as

$$T_{\text{ED}} \underset{H_0}{\overset{H_1}{\geq}} \gamma_{\text{ED}}, \quad (5.B.1)$$

where T_{ED} is given by

$$T_{\text{ED}} = \sum_{n=0}^{N_{\text{p}}^{\text{ED}}-1} \sum_{i=0}^{N_{\text{s}}-1} r^2(n, i). \quad (5.B.2)$$

$r(n, i)$ is defined in Section 5.3. Since $r(n, i) = s(n, i) + w(n, i)$ and $r(n, i) = w(n, i)$ under H_1 and H_0 hypothesis, respectively, we can write

$$T_{\text{ED}} = \begin{cases} \sum_{n=0}^{N_{\text{p}}^{\text{ED}}-1} \sum_{i=0}^{N_{\text{s}}-1} (s(n, i) + w(n, i))^2 & \text{under } H_1, \\ \sum_{n=0}^{N_{\text{p}}^{\text{ED}}-1} \sum_{i=0}^{N_{\text{s}}-1} w^2(n, i) & \text{under } H_0. \end{cases} \quad (5.B.3)$$

If we define the energy detector test statistic under hypothesis H_0 as $T_{\text{ED}}^{\text{H}_0}$, then

$$T_{\text{ED}}^{\text{H}_0} = \sum_{n=0}^{N_{\text{p}}^{\text{ED}}-1} \sum_{i=0}^{N_{\text{s}}-1} w^2(n, i). \quad (5.B.4)$$

We can modify the random variable, $T_{\text{ED}}^{\text{H}_0}$ to $(T_{\text{ED}}^{\text{H}_0} N_{\text{s}})/\sigma^2$, such that

$$\frac{T_{\text{ED}}^{\text{H}_0} N_{\text{s}}}{\sigma^2} = \sum_{n=0}^{N_{\text{p}}^{\text{ED}}-1} \sum_{i=0}^{N_{\text{s}}-1} l^2(n, i), \quad (5.B.5)$$

where $l(n, i)$ is an IID with $\mathcal{N}(0, 1)$. Thus, the PDF of $(T_{\text{ED}}^{\text{H}_0} N_{\text{s}})/\sigma^2$ is given by,

$$p\left(\frac{T_{\text{ED}}^{\text{H}_0} N_{\text{s}}}{\sigma^2}\right) \sim \mathcal{X}_{N_{\text{p}}^{\text{ED}} N_{\text{s}}}^2(0), \quad (5.B.6)$$

where \mathcal{X}^2 denotes the chi-square distribution with degree $\nu = N_{\text{p}}^{\text{ED}} N_{\text{s}}$ and central-ity parameter $\lambda = 0$. In (5.B.6), the additive nature of chi-square distribution is utilized.

Similarly, the energy detector test statistic under hypothesis H_1 , $T_{\text{ED}}^{\text{H}_1}$, is given by

$$T_{\text{ED}}^{\text{H}_1} = \sum_{n=0}^{N_{\text{p}}^{\text{ED}}-1} \sum_{i=0}^{N_{\text{s}}-1} r^2(n, i). \quad (5.B.7)$$

Since $r(n, i) = s(n, i) + w(n, i)$ under H_1 , the received samples under hypothesis H_1 will have the distribution $r(n, i) \sim \mathcal{N}(s(n, i), \sigma^2/N_{\text{s}})$.

If X_1, \dots, X_k , are k Gaussian random variables, with mean and variance, μ_i and σ_i^2 respectively, for $i \in [1, \dots, k]$, then the random variable $\sum_{i=1}^k (x_i/\sigma_i)^2$, is a chi-square random variable with degree of freedom, k , and centrality parameter, λ , such that

$$\lambda = \sum_{i=1}^k \left(\frac{\mu_i}{\sigma_i}\right)^2. \quad (5.B.8)$$

Therefore from (5.B.7), we can write PDF of $T_{\text{ED}}^{\text{H}_1}$, as

$$p\left(\frac{N_s T_{\text{ED}}^{\text{H}_1}}{\sigma^2}\right) \sim \sum_{n=0}^{N_p^{\text{ED}}-1} \mathcal{X}_{N_s}^2(\lambda), \quad (5.B.9)$$

$$\sim \sum_{n=0}^{N_p^{\text{ED}}-1} \mathcal{X}^2\left(\sum_{i=0}^{N_s-1} \frac{N_s s^2(n, i)}{\sigma^2}\right). \quad (5.B.10)$$

Since all frames are of same energy, E_p , we can write

$$p\left(\frac{N_s T_{\text{ED}}^{\text{H}_1}}{\sigma^2}\right) \sim \sum_{n=0}^{N_p^{\text{ED}}-1} \mathcal{X}_{N_s}^2(N_s \text{SNR}), \quad (5.B.11)$$

$$\sim \mathcal{X}_{N_p^{\text{ED}} N_s}^2(N_p^{\text{ED}} N_s \text{SNR}), \quad (5.B.12)$$

where in (5.B.12), the additive nature of the non-central chi-square distribution is exploited. Equations (5.B.12) and (5.B.6) can be compactly written as

$$p\left(\frac{N_s T_{\text{ED}}}{\sigma^2}\right) = \begin{cases} \mathcal{X}_{N_s N_p^{\text{ED}}}^2(N_p^{\text{ED}} N_s \text{SNR}) & \text{under } H_1, \\ \mathcal{X}_{N_s N_p^{\text{ED}}}^2(0) & \text{under } H_0. \end{cases} \quad (5.B.13)$$

If we define $N_L = N_p^{\text{ED}} N_s$, using (5.B.5), the PDF of the energy detector under H_0 , $T_{\text{ED}}^{\text{H}_0}$ can be approximated using central limit theorem (CLT) as

$$p\left(\frac{N_s T_{\text{ED}}^{\text{H}_0}}{\sigma^2}\right) \stackrel{a}{\sim} \mathcal{N}(N_L \mu_l, N_L \sigma_l^2), \quad (5.B.14)$$

where μ_l and σ_l^2 are the mean and variance, respectively of $l^2(n, i)$, since $l(n, i)$ is a standard normal with $\mathcal{N}(0, 1)$, we can write

$$\mu_l = \mathbf{E}[l^2(n, i)] = 1, \quad (5.B.15)$$

$$\sigma_l^2 = \mathbf{E}[l^4(n, i)] - (\mathbf{E}[l^2(n, i)])^2 = 2. \quad (5.B.16)$$

Therefore, (5.B.14) can be written as

$$p\left(\frac{N_s T_{\text{ED}}^{\text{H}_0}}{\sigma^2}\right) \stackrel{a}{\sim} \mathcal{N}(N_L, 2N_L). \quad (5.B.17)$$

Since $N_L = N_p^{\text{ED}} N_s$, we can write

$$p\left(\frac{N_s T_{\text{ED}}^{\text{H}_0}}{\sigma^2}\right) \stackrel{a}{\sim} \mathcal{N}(N_p^{\text{ED}} N_s, 2N_p^{\text{ED}} N_s). \quad (5.B.18)$$

From (5.B.18), for a fixed false alarm rate of the energy detector, $P_{\text{FA}}^{\text{ED}}$, we can compute the threshold, γ_{ED} , as

$$P_{\text{FA}}^{\text{ED}} = \Pr(T_{\text{ED}}^{\text{H}_0} > \gamma_{\text{ED}}), \quad (5.B.19)$$

$$\gamma_{\text{ED}} = \frac{\sigma^2}{N_s} \left[\sqrt{2N_{\text{p}}^{\text{ED}} N_s} \mathbf{Q}^{-1}(P_{\text{FA}}^{\text{ED}}) + N_{\text{p}}^{\text{ED}} N_s \right]. \quad (5.B.20)$$

Using this threshold and from (5.B.12), the probability of detection for the energy detector, P_{D}^{ED} , is given by

$$P_{\text{D}}^{\text{ED}} = \Pr(T_{\text{ED}}^{\text{H}_1} > \gamma_{\text{ED}}) \quad (5.B.21)$$

$$= \mathbf{Q}_{\chi_{\nu}^2(\lambda)}^{-1} \left(\sqrt{2N_{\text{p}}^{\text{ED}} N_s} \mathbf{Q}^{-1}(P_{\text{FA}}^{\text{ED}}) + N_{\text{p}}^{\text{ED}} N_s \right), \quad (5.B.22)$$

where $\mathbf{Q}_{\chi_{\nu}^2(\lambda)}$ is the tail probability of the non-central chi-square distribution with degrees of freedom, $\nu = N_{\text{p}}^{\text{ED}} N_s$, and centrality parameter, $\lambda = N_{\text{p}}^{\text{ED}} N_s \text{SNR}$.

5.C Performance of Amplitude Detector

In this Section, we will derive the analytical expression for the probability of detection for the amplitude detector, P_{D}^{AD} . We proceed with the same definitions for E_{p} , SNR, and σ^2 as in Appendix 5.A.

In the amplitude detector, the test statistic, T_{AD} , is compared against γ_{AD} (refer to Figure 5.3). Thus, the hypothesis test can be formulated as

$$T_{\text{AD}} \underset{H_0}{\overset{H_1}{\geq}} \gamma_{\text{AD}}, \quad (5.C.1)$$

where T_{AD} is given by

$$T_{\text{AD}} = \sum_{n=0}^{N_{\text{p}}^{\text{AD}}-1} \sum_{i=0}^{N_s-1} |r(n, i)|. \quad (5.C.2)$$

$r(n, i)$ is defined in Section 5.3. Since $r(n, i) = s(n, i) + w(n, i)$ and $r(n, i) = w(n, i)$, under H_1 and H_0 , respectively, we can write

$$T_{\text{AD}} = \begin{cases} \sum_{n=0}^{N_{\text{p}}^{\text{AD}}-1} \sum_{i=0}^{N_s-1} |s(n, i) + w(n, i)| & \text{under } H_1 \\ \sum_{n=0}^{N_{\text{p}}^{\text{AD}}-1} \sum_{i=0}^{N_s-1} |w(n, i)| & \text{under } H_0. \end{cases} \quad (5.C.3)$$

Since noise samples $w(n, i) \sim \mathcal{N}(0, \sigma^2/N_s)$, $|w(n, i)|$, has folded normal distribution [LNN61],

$$|w(n, i)| \sim \begin{cases} 2\mathcal{N}(0, \sigma^2/N_s) & \text{when } w(n, i) > 0, \\ 0 & \text{otherwise.} \end{cases} \quad (5.C.4)$$

Therefore, the amplitude detector test statistic under H_0 , $T_{\text{AD}}^{\text{H}_0} = \sum_{n=0}^{N_{\text{p}}^{\text{AD}}-1} \sum_{i=0}^{N_{\text{s}}-1} |w(n, i)|$, has a PDF given by

$$p(T_{\text{AD}}^{\text{H}_0}) = \begin{cases} 2\mathcal{N}(0, N_{\text{p}}^{\text{AD}}\sigma^2) & \text{when } T_{\text{AD}}^{\text{H}_0} > 0. \\ 0 & \text{otherwise} \end{cases} \quad (5.C.5)$$

Similarly $|r(n, i)|$ under H_1 also has a folded normal distribution with PDF of $|s(n, i) + w(n, i)|$ as

$$\begin{cases} \mathcal{N}(s(n, i), \sigma^2/N_{\text{s}}) + \mathcal{N}(-s(n, i), \sigma^2/N_{\text{s}}) & r(n, i) > 0, \\ 0 & \text{otherwise.} \end{cases} \quad (5.C.6)$$

We use same shape and energy for all the UWB frames and furthermore, we set

$$\sum_{i=0}^{N_{\text{s}}-1} s(n, i) = \alpha E_{\text{p}}, \quad (5.C.7)$$

and thus,

$$\sum_{n=0}^{N_{\text{p}}^{\text{AD}}-1} \sum_{i=0}^{N_{\text{s}}-1} s(n, i) = \alpha N_{\text{p}}^{\text{AD}} E_{\text{p}}. \quad (5.C.8)$$

Therefore, the amplitude detector test statistic under H_1 , $T_{\text{AD}}^{\text{H}_1} = \sum_{n=0}^{N_{\text{p}}^{\text{AD}}-1} \sum_{i=0}^{N_{\text{s}}-1} |s(n, i) + w(n, i)|$, has PDF, $p(T_{\text{AD}}^{\text{H}_1})$, equal to

$$\begin{cases} \mathcal{N}(\alpha N_{\text{p}}^{\text{AD}} E_{\text{p}}, N_{\text{p}}^{\text{AD}}\sigma^2) + \mathcal{N}(-\alpha N_{\text{p}}^{\text{AD}} E_{\text{p}}, N_{\text{p}}^{\text{AD}}\sigma^2) & T_{\text{AD}}^{\text{H}_1} > 0, \\ 0 & \text{otherwise.} \end{cases} \quad (5.C.9)$$

For a fixed false alarm rate, $P_{\text{FA}}^{\text{AD}}$, the threshold γ_{AD} can be computed as

$$P_{\text{FA}}^{\text{AD}} = \Pr(T_{\text{AD}}^{\text{H}_0} > \gamma_{\text{AD}}). \quad (5.C.10)$$

From (5.C.5), we can write,

$$\gamma_{\text{AD}} = \sqrt{N_{\text{p}}^{\text{AD}}\sigma^2} \mathbf{Q}^{-1}\left(\frac{P_{\text{FA}}^{\text{AD}}}{2}\right). \quad (5.C.11)$$

The probability of detection for the amplitude detector, $P_{\text{D}}^{\text{AD}} = \Pr(T_{\text{AD}}^{\text{H}_1} > \gamma_{\text{AD}})$, from (5.C.9), we can write

$$P_{\text{D}}^{\text{AD}} = \mathbf{Q}\left(\frac{\gamma_{\text{AD}} - \alpha N_{\text{p}}^{\text{AD}} E_{\text{p}}}{\sqrt{N_{\text{p}}^{\text{AD}}\sigma^2}}\right) + \mathbf{Q}\left(\frac{\gamma_{\text{AD}} + \alpha N_{\text{p}}^{\text{AD}} E_{\text{p}}}{\sqrt{N_{\text{p}}^{\text{AD}}\sigma^2}}\right) \quad (5.C.12)$$

Substituting (5.C.11) in (5.C.12) and simplifying, we can express P_D^{AD} as a function of parameters in Table 5.1 and is given by

$$\begin{aligned}
 P_D^{AD} = & \mathbf{Q} \left(\mathbf{Q}^{-1} \left(\frac{P_{FA}^{AD}}{2} \right) - \alpha \sqrt{N_p^{AD} E_p \text{SNR}} \right) \\
 & + \mathbf{Q} \left(\mathbf{Q}^{-1} \left(\frac{P_{FA}^{AD}}{2} \right) + \alpha \sqrt{N_p^{AD} E_p \text{SNR}} \right).
 \end{aligned} \tag{5.C.13}$$

UWB TOA Estimation using Kalman filter

In this chapter, we propose fusion of dynamic TOA (time of arrival) from multiple low complexity detectors like energy detectors operating at sub-Nyquist rate through Kalman filtering. We show that by having a multi-channel receiver with each channel having an energy detector, we can achieve the performance of a digital implementation with matched filter. We derive analytical expression for number of sub-Nyquist energy detector channels needed to achieve the performance of digital implementation with matched filter and demonstrate in simulation the validity of our analytical approach. Results indicate that number of energy detectors needed will be high at low SNRs and converge to a constant number as the SNR increases. We also study the performance of the strategy proposed using IEEE 802.15.4a CM1 multipath channel model and show in simulation that two sub-Nyquist detectors are sufficient to match the performance of digital matched filter. We also show that there is an order of savings in energy by using the multi-channel sub-Nyquist receiver structure compared to its digital counterpart.

6.1 Background

Narrow impulse signals that are used in IR-UWB schemes yield very fine time resolution and thus, can be used for accurate measurement of time of arrival (TOA) [GTG⁺05,SGP11]. Accurate TOA is essential in several applications including localization and communication. In localization, when the nodes are synchronized, the TOA of the signal can be used directly to obtain the range estimate. If nodes are not synchronized, TOA estimate is still needed for several ranging protocols to estimate the range. Localization information about the node can be derived from its range to anchor nodes [SGP11,MVV11]. In many IR-UWB communication systems, the message information is embedded in the location of the IR-UWB pulse. For example, pulse position modulation (PPM) and its variant modulation schemes. To demodulate the IR-UWB symbols in these modulation schemes, TOA

estimation techniques can be used [KMKK06, YDAH14, YDH14].

IR-UWB system with matched filter can provide optimal estimate of TOA for additive white Gaussian noise (AWGN) limited channels. The TOA is estimated by finding the peak location at which the filter attains the maximum value. The impulse response of the matched filter should closely approximate the transmit pulse shape. When implemented digitally, matched filter requires Nyquist-rate sampling [Coo12, Tur60]. There are several digital UWB receiver architectures for which matched filter is suitable including [OB05, BLW⁺03, NBC02]. Digital receiver structure offers several benefits such as flexibility in design, reconfigurability and scalability [CGC10]. However, UWB signal occupy extremely large bandwidth and thus requires high-speed analog-to-digital converters (ADCs). These speeds demand the use of interleaved flash ADC [NBC02] or a bank of polyphase ADCs [OB05]. In addition, the ADC must support a large dynamic range to resolve the signal from the strong narrowband interferes. These aspects makes digital UWB architecture which operates at Nyquist-rate to be costly and power hungry [NBC02, PAW07, Nam03].

The digital matched filter based detector is the method of preference, because of its superior performance in AWGN and multi-path channel. However, it requires expensive implementation so we seek low-cost alternatives. There, we consider sub-sampled energy detectors and increase the number of detector channels to compensate for the loss in performance. We show analytically that under AWGN 4 detectors channels are sufficient and under multipath even less are required. We also show that an order of gain in terms of energy efficiency can be achieved with this structure compared to single channel digital receiver. In many practical applications, TOA is dynamic in nature, thus we propose a joint fusion and tracking of estimated TOA from parallel detector channels through a Kalman filter. We assess the performance of fused TOA estimate in simulation for a dynamic TOA model from multiple energy detectors and compare it with the digital matched filter and demonstrate the validity of the claims.

This chapter is organized as follows: In Section 6.2, we discuss the signal and system model employed. In Section 6.3, we will discuss different types of detectors. Here, we will study the energy collection strategy for matched filter and energy detectors. In Section 6.4, performance analysis of these two detectors are studied for a static TOA case. Section 6.6, discusses the Kalman filter design for joint fusing and tracking of the energy detector estimates for a dynamic TOA model. Section 6.7, demonstrates the performance in simulation. Finally, Section 6.8 details the conclusions from the design and results demonstrated.

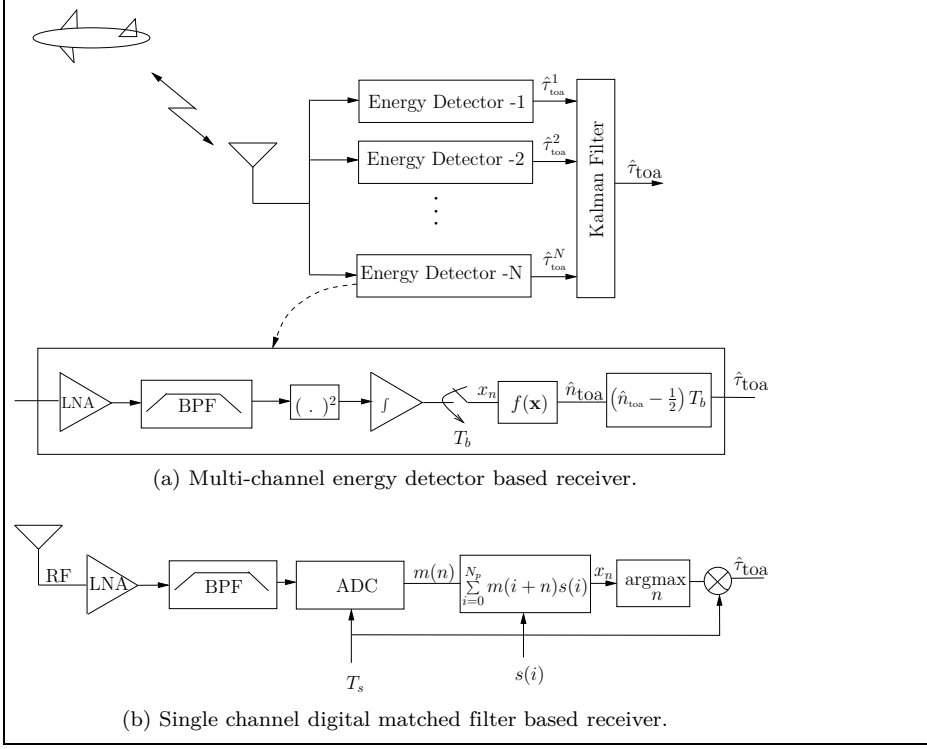


Figure 6.1: Joint fusion and tracking structure using multi-channel receiver with low cost energy detectors in each channel operating at sub-Nyquist rate, tracking a dynamic TOA of a moving target. A single channel digital receiver at Nyquist rate is also shown.

6.2 Model

6.2.1 Signal Model

The signal model comprises of N_f frames each having a unit energy pulse, $s(t)$, given by

$$\omega_{\text{tr}}(t) = \sum_{j=0}^{N_f} d_j s(t - jT_f - c_j T_c), \quad (6.2.1)$$

where each frame is of duration T_f and the frame index is represented by j . The chip duration is represented by T_c and $c_j \in \{0 \dots N_c\}$ indicates the time-hopping code. $d_j \in \{\pm 1\}$ is the polarity code, which can be used along with time-hopping to smooth the signal spectrum. We consider a sufficiently longer frame duration to

avoid inter-frame interference due to the delay spread of the channel.

A wide range of pulse shapes have been explored for UWB applications from rectangular to Gaussian. Gaussian and their derivatives, usually called monopulses, are effective due to the ease of construction and good resolution in both time and frequency. In many cost effective hardware designs, these shapes are generated without any dedicated circuits [GMHK02, MG07, YDH14, YDAH14]. For analytical and simulation analysis, we have used the 2nd order Gaussian pulse [SGI08],

$$s(t) = A \left(1 - \frac{4\pi t^2}{\zeta^2} \right) \exp \left(\frac{-2\pi t^2}{\zeta^2} \right), \quad (6.2.2)$$

The amplitude is adjusted through parameter, A , and pulse width is adjusted through parameter, ζ .

The received signal is the distorted version of the transmit pulse with multipaths. The TOA is defined as the time elapsed for the first arrival path to reach the receiver from the transmitter. The received signal can be represented by

$$\omega_{\text{rx}}(t) = \sum_{j=0}^{N_f} d_j r(t - jT_f - c_j T_c) + n(t). \quad (6.2.3)$$

where $r(t) = \sqrt{\frac{E_b}{N_f}} \sum_{l=1}^L \alpha_l r_l(t - \tau_l)$, E_b is the captured energy and $\sum_{l=0}^L \alpha_l^2 = 1$. The gain and received UWB pulse for the l -th tap is given by α_l and $r_l(t)$. The $n(t)$ is the AWGN process with zero mean and double-sided power spectral density of $N_0/2$. Without loss of generality, and for simplicity of analysis, we assume $c_j = 0$ and $d_j = 1$. TOA estimation problem is to estimate the first arrival path, $\tau_1 = \tau_{\text{toa}}$, in the received signal (6.2.3).

6.2.2 System Model and Problem Formulation

We propose a multichannel receiver structure shown in Figure 6.1a. Each channel uses a low complexity energy detector operating at sub-Nyquist rate. The energy detectors can be implemented using low cost electronics as discussed in [ADH13]. Even though, we use multiple channels to enhance the performance, the overall cost of the transceiver will still be less than a single channel digital UWB transceiver operating at Nyquist rate shown in Figure 6.1b. This is due to the requirement of extremely high speed and high dynamic range ADCs for digital UWB receivers which are expensive. The energy detectors suffer from the noise due to the square-law device, due to which the estimated TOA is sub-optimal in the mean-square-error (MSE) sense. From the collected sub-optimal estimates of the multichannel receiver, $\mathbf{y} = [\hat{\tau}_{\text{toa}}^1, \hat{\tau}_{\text{toa}}^2, \dots, \hat{\tau}_{\text{toa}}^N]$, our objective is to arrive at a single estimate, $\hat{\tau}_{\text{toa}}$, such that MSE,

$$\hat{\sigma}_{\text{toa}}^2 = \mathbf{E}\{(\hat{\tau}_{\text{toa}} - \tau_{\text{toa}})^2\}, \quad (6.2.4)$$

is minimum. where \mathbf{E} denotes the expectation operator and τ_{toa} is the true TOA. N denotes the number of channels in the receiver structure.

For joint fusion and tracking problem discussed in Section 6.1, the sub-optimal estimates from each channel are fused using a Kalman filter. This will filter out the spurious range errors due to the imperfect channel, together with achieving superior MSE performance. For dynamic TOA, we consider the following model for analysis,

$$\tau_{\text{toa}}[n] = \tau_{\text{toa}}[n-1] + v_{\text{toa}}[n-1], \quad (6.2.5)$$

$$v_{\text{toa}}[n] = \kappa v_{\text{toa}}[n-1] + u_v[n], \quad (6.2.6)$$

where the content inside square bracket indicates the time-interval, for example, $\tau_{\text{toa}}[n]$, indicates the τ_{toa} at n -th time-interval. This model represents a dynamic object moving away from the TOA receiver with a velocity v_{toa} . Equation (6.2.5) assumes the resolution of the time interval to be 0.3 seconds and $\tau[\cdot]$ is in nano-seconds. In (6.2.6), v_{toa} is defined as an AR(1) process with constant κ . The distribution of the noise in the v_{toa} measurement, is given by $u_v[n] \sim \mathcal{N}(0, \sigma_p^2)$, where \mathcal{N} denotes the Gaussian distribution.

We use the above defined dynamic TOA model to access the performance of the proposed receiver structure. The noise in each channel is assumed to be independent and identically distributed. This is due to the nature of the thermal noise generated by the electronic components of each channel. We also assume perfect synchronization for both single channel digital receiver and multi-channel sub-Nyquist receivers. Even though in practical systems there will always be synchronization errors, the effect of it will be similar in both structures. Also, this will enable us to study the performance of the proposed multi-channel receiver structure with single channel digital UWB receiver structure under similar background conditions.

6.3 Detectors

The two commonly employed receiver structures are as shown in the Figure 6.1. The received signal passes through the low noise amplifier (LNA) and band pass filter (BPF) of bandwidth B . The output signal of BPF is converted into energy samples, $\mathbf{x} = (x_1, x_2, \dots, x_{N_{\text{obs}}})$, from which TOA is estimated. Here, N_{obs} , defines the number of energy samples used in the estimation. Based on the energy collection strategy different types of detectors exists. In this chapter, we consider the matched filter which operates at Nyquist rate ($1/T_s$) and energy detectors operating at sub-Nyquist rate ($1/T_b$).

6.3.1 Matched filter

In the matched filter, energy is collected by correlating the received samples with the transmit pulse shape as shown in Figure 6.1b [VT04]. Matched filter can be

mathematically expressed as

$$x_n = \sum_{i=0}^{N_p} m(n+i)s(i), \quad (6.3.1)$$

$$\hat{n}_{\text{toa}} = \underset{n}{\operatorname{argmax}}(\mathbf{x}), \quad (6.3.2)$$

$$\hat{\tau}_{\text{toa}} = \hat{n}_{\text{toa}} T_s, \quad (6.3.3)$$

where, $s(i) = s(iT_s)$, represent the digitized transmit pulse and $m(n) = \omega_{\text{rx}}(nT_s)$, represent the digitized received signal, sampled at interval T_s . In matched filter, the energy samples, x_n , are at Nyquist rate, $1/T_s$. Energy detectors operating at the sub-Nyquist rates are an interesting alternative to digital matched filter.

6.3.2 Energy Detector

Energy detector is an interesting alternative to matched filter based detector as they are less complex and can operate at sub-Nyquist rate [ROD06, GS05, CRM⁺05]. However, these detectors suffer from the noise due to the square-law device and are sub-optimal. Performance analysis of single channel energy detector for static TOA estimation has been studied in [SGI08, GA03, GS05].

The structure for energy detector is as shown in Figure 6.1a. The structure is amenable for a low-complexity analog implementation at sub-Nyquist rates [ROD06, GS05, CRM⁺05]. In energy detector, the output signal from BPF is converted in to energy samples, $\mathbf{x} = (x_1, x_2, \dots, x_{N_{\text{obs}}})$. TOA is estimated from these energy samples using the equation below

$$\hat{n}_{\text{toa}} = f(\mathbf{x}), \quad (6.3.4)$$

$$\hat{\tau}_{\text{toa}} = \left(\hat{n}_{\text{toa}} - \frac{1}{2} \right) T_b, \quad (6.3.5)$$

where, $f(\cdot)$, is the estimator function, which estimates the block-index/sample-index of the first arriving path. The function, $f(\cdot)$, is chosen based on the channel model. We will discuss this later. Equation (6.3.5) represents $\hat{\tau}_{\text{toa}}$ as the mid-point of the corresponding estimated block and assumes that the true TOA is uniformly distributed with in this block.

Without loss of generality, we assume, T_f to be an integer multiple of T_b and the UWB pulse width is equal to T_b . Therefore, each frame consists of, $N_{\text{obs}} = T_f/T_b$, blocks, each with energy, x_n , $n \in [1, \dots, N_{\text{obs}}]$, given by

$$x_n = \sum_{i=0}^{N_f} \int_{(j-1)T_f + (n-1)T_b}^{(j-1)T_f + nT_b} |r(t)|^2 dt. \quad (6.3.6)$$

Typical variation of energy samples, x_n , verses n is as shown in the Figure 6.2. In energy detector, the energy samples are at sub-Nyquist rate, $1/T_b$.

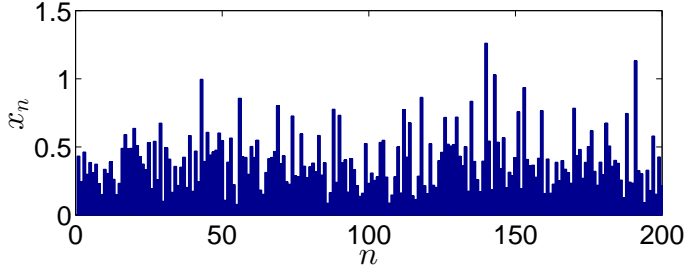


Figure 6.2: Variation of energy samples, x_n , versus block index, n . Parameters $T_f = 200$ ns, $T_b = 1$ ns, SNR = 0 dB and $N_{\text{obs}} = 200$ are considered.

6.4 AWGN Channel Analysis

The best performance in terms of mean-square-error (MSE) for an unbiased estimator is given by the Cramer Rao lower bound (CRLB) and for a TOA estimation problem, this is given by [GTG⁺05, DCW08]:

$$\sigma_\tau^2 \geq \frac{1}{8\pi^2 \text{SNR} \beta^2}, \quad (6.4.1)$$

where β is the effective signal bandwidth defined by

$$\beta^2 = \left[\frac{\int_{-\infty}^{\infty} f^2 |S(f)|^2 df}{\int_{-\infty}^{\infty} |S(f)|^2 df} \right], \quad (6.4.2)$$

where $S(f)$ is the Fourier transform of the transmit pulse, $s(t)$.

In AWGN channel model, we consider a single-path model, with $L = 1$, $\alpha_1 = 1$ and $\tau_1 = \tau_{\text{toa}}$ in (6.2.3). The probability density of x_n , for matched filter and energy detector depends on whether the particular energy sample, x_n , is signal+noise sample or noise-only sample. For matched filter it can be shown that the probability density functions under both hypotheses, $H_1 \cong x_n$ is signal+noise sample, and $H_0 \cong x_n$ is noise-only sample, are given by

$$p(x_n) \sim \begin{cases} \mathcal{N}(E_b, \sigma^2) & \text{under } H_1, \\ \mathcal{N}(0, \sigma^2) & \text{under } H_0, \end{cases} \quad (6.4.3)$$

where $\sigma^2 = N_0/2$ is the variance of the noise samples, and \mathcal{N} denotes the Gaussian distribution.

To derive the probability distribution function (PDF) of the energy samples in energy detectors case, the function $f(\cdot)$ in (6.3.4) need to be defined. Under the AWGN assumption, the received signal will have a single path, whose delay

represents the TOA. Thus, optimal TOA estimation strategy here would be to pick the energy sample having the maximum energy as \hat{n}_{toa} in (6.3.4). This selection criteria is called maximal energy selection (MES) and is given by [SGI08]

$$\hat{n}_{\text{toa}} = \arg \max_n(\mathbf{x}), \quad (6.4.4)$$

$$\hat{\tau}_{\text{toa}} = \left(\hat{n}_{\text{toa}} - \frac{1}{2} \right) T_b. \quad (6.4.5)$$

The complementary cumulative distribution function (CCDF) of energy samples, x_n , for energy detector is given by [DCW08, DCW06, GSO06, SGI08]

$$P(x_n > \eta) = \begin{cases} Q_{M'/2} \left(\frac{E_b}{\sigma}, \frac{\sqrt{\eta}}{\sigma} \right) & \text{under } H_1 \\ \exp \left(-\frac{\eta N_f}{N_o} \right) \sum_{i=0}^{M'/2-1} \frac{1}{i!} \left(\frac{\eta N_f}{N_o} \right)^i & \text{under } H_0 \end{cases} \quad (6.4.6)$$

where $Q_Z(a, b)$ denotes the Marcum-Q-function with parameter Z , P denotes the probability, and $M' \approx N_f(2BT_b + 1)$ denotes the degrees of freedom (DOF). At high SNRs the above equation can be approximated as [SGI08]

$$p(x_n) \sim \begin{cases} \mathcal{N}(\mu_{H_1}, \sigma_{H_1}^2) & \text{under } H_1, \\ \mathcal{N}(\mu_{H_0}, \sigma_{H_0}^2) & \text{under } H_0, \end{cases} \quad (6.4.7)$$

The mean and variance of x_n under both hypotheses is given by

$$\mu_{H_1} = N_f M \sigma^2 + E_b, \quad (6.4.8)$$

$$\sigma_{H_1}^2 = 2N_f M \sigma^4 + 4\sigma^2 E_b^2, \quad (6.4.9)$$

$$\mu_{H_0} = N_f M \sigma^2, \quad (6.4.10)$$

$$\sigma_{H_0}^2 = 2N_f M \sigma^4, \quad (6.4.11)$$

where $M = 2BT_b + 1$, is the degrees of freedom of noise and $\sigma^2 = N_o/2$.

If we choose the MES criteria for TOA estimation for both matched filters and energy detectors as given in (6.3.1) - (6.3.3) and (6.4.4) - (6.4.5) respectively, then an error can occur, if any one of the noise-only energy sample is higher than the signal+noise energy sample. That is

$$x_{n_{\text{no}}} > x_{n_{\text{sn}}}, \quad (6.4.12)$$

where $x_{n_{\text{sn}}}$ and $x_{n_{\text{no}}}$ are energies of signal+noise and noise only sample. For AWGN channel, there will be only one signal+noise energy sample and all other samples are noise-only. The correct selection will happen when $x_n < x_{n_{\text{sn}}}$, for all the energy samples except for the signal+noise energy sample. Thus, the probability of correct selection, P_s , and probability of error selection, P_e , is given by [GSO06]

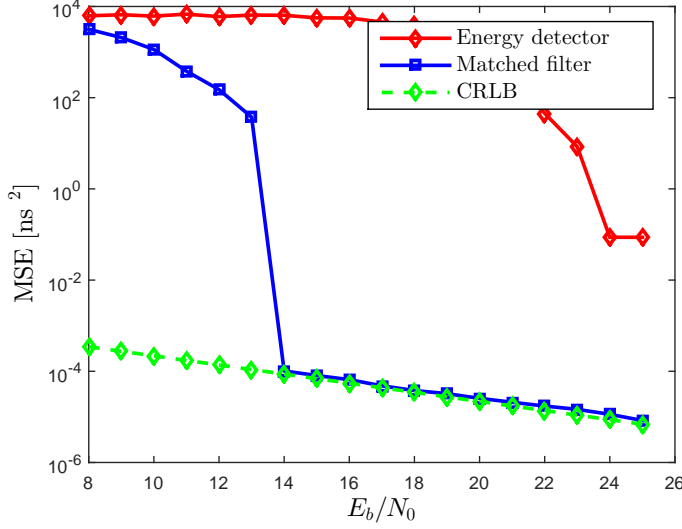


Figure 6.3: Variation of MSE with SNR for a single channel energy detector and matched filter based receivers. MSE is evaluated by averaging the estimated TOA for 1000 random τ_{toa} drawn from $\mathcal{U}[0, T_f = 200 \text{ ns}]$. Matched filter asymptotically reaches the CRLB bound.

$$\begin{aligned}
 P_s &= \int_{x_n=0}^{\infty} \left(1 - \mathbf{Q} \left(\frac{x_n - \mu_{H_0}}{\sigma_{H_0}} \right) \right)^{N_{\text{obs}}-1} p(x_n) dx_n, \\
 P_e &= 1 - P_s,
 \end{aligned} \tag{6.4.13}$$

where $p(x_n)$ is the density function of the energy samples for the detectors under hypothesis H_1 . \mathbf{Q} denotes the CCDF function of x_n . Here μ_{H_0} , denotes the mean values of x_n for matched filter and energy detectors and is given by 0 and $N_f M \sigma^2$ respectively. $\sigma_{H_0}^2$, denotes the variance of x_n for matched filter and energy detectors and is given by σ^2 and $2N_f M \sigma^4$ respectively.

It is not straight forward to arrive at the closed form expression for energy detector's P_s and P_e due to complex distribution functions (6.4.6). There is however a loss of performance in energy detectors due to squaring and integration operation at sub-Nyquist rates compared to matched filter, operating at Nyquist rate. Figure 6.3, shows the mean square error (MSE), performance for matched filter and energy detector. MSE is evaluated by averaging the estimated TOA for 1000 random TOAs (τ_{toa}) drawn from $\mathcal{U}[0, T_f = 200 \text{ ns}]$. The sampling rate ($1/T_s$) used

by matched filter is 1000 GHz¹ and sampling rate ($1/T_b$) used by energy detector is 1/1000-th that of matched filter and is equal to 1 GHz.

At high SNRs, to achieve the performance of the matched filter using multiple energy detectors, we need the covariance of the signal+noise energy sample (under hypothesis H_1) to be same. We can approximate the probability distribution of energy samples for energy detectors in to a Gaussian distribution at high SNR as shown in (6.4.7). If there are K channels each having an energy detector to independently estimate TOA, then signal+noise block in each detector will have a probability distribution given by

$$e_i \sim \mathcal{N}(\mu_{H_1}, \sigma_{H_1}^2), i \in [1, \dots, K]. \quad (6.4.14)$$

Since e_i s are independent and identically distributed, then the best estimate for the signal+noise block using K energy detectors is given by [Kay93] ,

$$e = \frac{1}{K} \sum_{k=1}^K e_k. \quad (6.4.15)$$

The probability distribution function of e is given by²

$$e \sim \mathcal{N}\left(\mu_{H_1}, \frac{\sigma_{H_1}^2}{K}\right). \quad (6.4.16)$$

Let $\sigma_{MF}^2 = \sigma^2$ and $\sigma_{ED}^2 = \sigma_{H_1}^2$ denote the variance of the x_n under H_1 for matched filter and energy detector. From (6.4.3) and (6.4.16) to achieve the performance of the matched filter using multiple energy detectors, we need

$$\sigma_{MF}^2 = \frac{1}{N_{ED}} \sigma_{ED}^2, \quad (6.4.17)$$

where, N_{ED} , is the number of energy detectors needed to have the same performance as that of matched filter. For normalized energy per bit ($E_b = 1$), and using the variance for signal+noise sample from (6.4.3), (6.4.7) and (6.4.9) we get

$$N_{ED} = \lim_{\text{SNR} \rightarrow \infty} \frac{\sigma_{ED}^2}{\sigma_{MF}^2} \quad (6.4.18)$$

$$N_{ED} = \lim_{\sigma^2 \rightarrow 0} \frac{(2M\sigma^4 + 4\sigma^2)}{\sigma^2}, \quad (6.4.19)$$

$$= 4. \quad (6.4.20)$$

¹Since TOA is continuous in time, very high sampling rate is employed to demonstrate that matched filter will indeed reach the CRLB bound without much ambiguity due to discretization of time due to sampling.

²See [PP02] to obtain the probability distribution function of a function of Gaussian random variable.

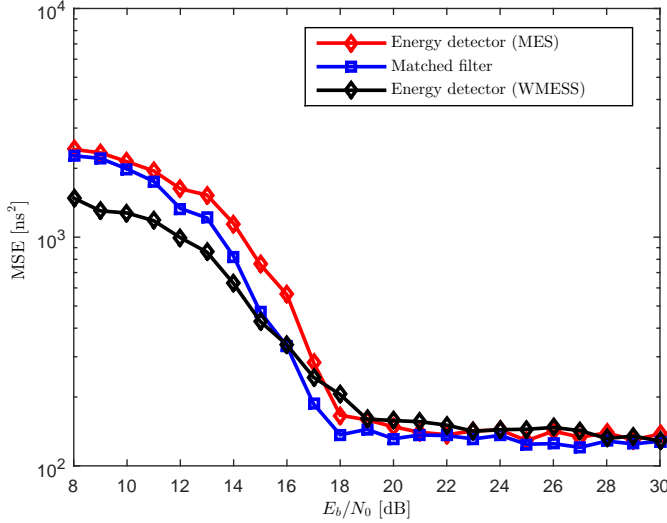


Figure 6.4: Variation of MSE with SNR for single channel energy detector (with selection criteria MES and WMES) and matched filter receivers. MSE is evaluated by averaging the estimated TOA for 1000 random τ_{toa} drawn from $\mathcal{U}[0, 100 \text{ ns}]$.

Thus, from (6.4.20), asymptotically, with the increase of SNR (E_b/N_0), the number of energy detector channels needed to achieve the same performance as digital matched filter is equal to 4. We will show in simulation that this phenomenon is indeed true in the later section.

6.5 Multipath Channel Analysis

Many UWB ranging applications have a channel response with several multipath components, i.e. the received pulse in (6.2.3) has $(\alpha_1, \alpha_2 \dots \alpha_L; \tau_1, \tau_2 \dots, \tau_L)$, where L is the number of multipaths. The TOA estimation problem is to identify the leading edge (first arriving path, τ_1). In multipath UWB channels, the matched filter performance is not optimal since the shape of the pulse is lost in the channel due to the frequency selective fading. Also, the magnitude of the energy sample containing first arriving path may be smaller than the peak energy sample, therefore, using MES criteria for TOA estimation, as represented in (6.4.4) and (6.3.2) does not always yield true TOA [MCC⁺04]. Figure 6.4, shows the performance in terms of MSE for matched filter and energy detector for 802.15.4a, residential LOS channel (CM1 model) [MCC⁺04]. MSE is evaluated by averaging the estimated TOA for

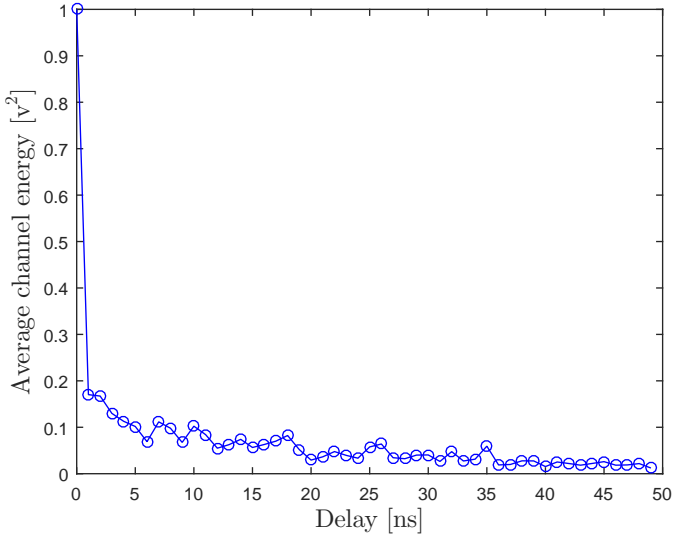


Figure 6.5: Averaged channel energy profile for 802.15.4a CM1 channel model. 100 different channel realizations are averaged.

1000 random τ_{toa} drawn from $\mathcal{U}[0, 100 \text{ ns}]$ ³. The sampling rate ($1/T_s$) used by the matched filter receiver is 8 GHz and sampling rate ($1/T_b$) used by single channel energy detector based receiver is 1/8-th that of matched filter and is equal to 1 GHz.

The performance of the energy detector can be improved by considering the *a priori* information such as power delay profile (PDP). To accomplish this, we can rephrase the TOA estimation problem as a multiple hypothesis testing problem. The energy samples vector, \mathbf{x} , is a $1 \times N_{\text{obs}}$ vector, out of which, N_e blocks are having multipath signals, $N_e T_b$, represents the excess delay of the channel. If we define H_k , as the hypothesis that the k -th sample denotes the first path arrival, then $H_k = \mathbf{x}$, with,

³Since $T_f = 200 \text{ ns}$, we assume that delay spread of the multi-path channel is $< 100 \text{ ns}$, so that there is no inter-frame interference

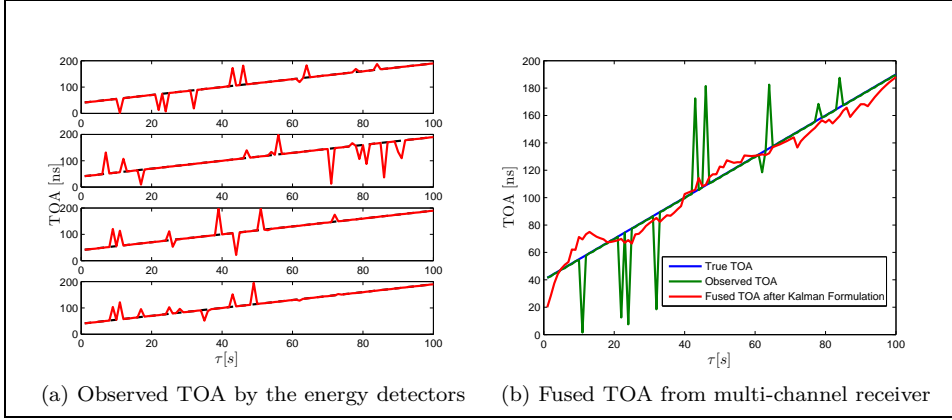


Figure 6.6: Fusion of multiple detector estimates for a dynamic TOA model using Kalman filter.

$$x(n) = \begin{cases} \int_{(n-1)T_b}^{nT_b} n^2(t).dt, \\ \text{for } n = 1, \dots, k-1 \\ \int_{(n-1)T_b}^{nT_b} |\omega_{rx}(t) + n(t)|^2.dt, \\ \text{for } n = k, \dots, k + N_e - 1 \\ \int_{(n-1)T_b}^{nT_b} n^2(t).dt, \\ \text{for } n = k + N_e, \dots, N_{\text{obs}}. \end{cases} \quad (6.5.1)$$

Here, $x(n)$, denotes the n -th element of \mathbf{x} and $H_{n_{\text{toa}}}$, is the true hypothesis [SGI08]. If the PDP for the channel is available, then we can modify the hypothesis test from MES to weighted maximum energy sum selection (WMESS), and is given by

$$\hat{n}_{\text{toa}} = \arg \max_{k \in [1, \dots, N_{\text{obs}}]} \{x(k : k + N_e) \mathcal{E}\}, \quad (6.5.2)$$

where $x(k : k + N_e)$ is a $1 \times N_e$ vector having the N_e elements from \mathbf{x} starting from k and \mathcal{E} is the $N_e \times 1$ vector denoting the a-priori channel energy information, which is similar to correlating received energy samples with PDP. Averaged channel energy profile, \mathcal{E} , for IEEE 802.15.4a residential LOS channel model is as shown in Figure 6.5. The performance of energy detector with WMESS algorithm is as shown in Figure 6.4. Even though, the WMESS estimation algorithm require more computation, its performance is better than matched filter at low SNRs for IEEE

Algorithm 6.1: Kalman filter for tracking and fusing of TOA from multiple sub-Nyquist energy detector estimates

Input: Prior state, \mathbf{s}_{init} , prior state's covariance, \mathbf{M}_{init} , and covariance of plant noise, \mathbf{Q} .

Output: Tracked and fused TOA estimates, $\tilde{\tau}_{\text{toa}}$ and variance of estimate, $\tilde{\sigma}_{\text{toa}}^2$

```

1  $\mathbf{s}[1] \leftarrow \mathbf{s}_{\text{init}}$  ▷ Initial state
2  $\mathbf{M}[1] \leftarrow \mathbf{M}_{\text{init}}$  ▷ Initial states Covariance
3  $\tilde{\tau}_{\text{toa}}[1] \leftarrow \mathbf{s}_{\text{init}}[1]$  ▷ Initial TOA estimate
4  $\tilde{\sigma}_{\text{toa}}^2[1] \leftarrow \mathbf{M}_{\text{init}}[1](1, 1)$  ▷ Initial MSE estimate
5 for  $i \leftarrow 1$  to  $I$  do
6    $\mathbf{s}_{\text{prd}} \leftarrow \mathbf{A}\mathbf{s}[i]$  ▷ Predicted state
7    $\mathbf{M}_{\text{prd}} \leftarrow \mathbf{A}\mathbf{M}[i]\mathbf{A}' + \mathbf{Q}$  ▷ Predicted MSE
8    $\mathbf{K} = (\mathbf{M}_{\text{prd}}\mathbf{H}^T)(\mathbf{C} + \mathbf{H}\mathbf{M}_{\text{prd}}\mathbf{H}^T)^{-1}$ 
9    $\mathbf{s}[i+1] = \mathbf{s}_{\text{prd}} + \mathbf{K}(\mathbf{y}[i] - \mathbf{H}\mathbf{s}_{\text{prd}})$  ▷ Update state from observations ( $\mathbf{y}[n]$ )
10   $\tilde{\tau}_{\text{toa}}[i+1] = \mathbf{s}[i+1](1)$  ▷ Save fused TOA ( $\tilde{\tau}_{\text{toa}}$ )
11   $\mathbf{M}[i+1] = (\mathbf{I}_2 - \mathbf{K}\mathbf{H})\mathbf{M}_{\text{prd}}$  ▷ Update MSE
12   $\tilde{\sigma}_{\text{toa}}^2[i+1] = \mathbf{M}[i+1](1, 1)$  ▷ Save MSE
13 return  $\tilde{\tau}_{\text{toa}}, \tilde{\sigma}_{\text{toa}}^2$ 

```

802.15.4a CM1 multipath channel model. However, at high SNR there is a loss of performance compared to matched filter.

The performance degradation at high SNR with WMESS criteria for energy detector can become a problem when the TOA of the estimated target is dynamic in nature. In the next section, we will discuss a mechanism to fuse the sub-optimal estimates from multiple energy detector channels with AWGN and multi-path channels, to achieve improved performance for a dynamic TOA system.

6.6 Multi detector Fusion Using Kalman Filter

When the estimated TOA of the target is dynamic in nature, then joint fusing and tracking using multiple independent TOA estimations from the energy detectors can yield better performance. The dynamic nature of the TOA is represented by (6.2.5) and (6.2.6). We can write this in compact form as,

$$\mathbf{s}[n] = \mathbf{A}\mathbf{s}[n-1] + \mathbf{u}[n], \quad (6.6.1)$$

where $\mathbf{s}[n]$, \mathbf{A} , and $\mathbf{u}[n]$ is given by

$$\mathbf{s}[n] = \begin{bmatrix} \tau[n] \\ v_{\text{toa}}[n] \end{bmatrix}, \quad (6.6.2)$$

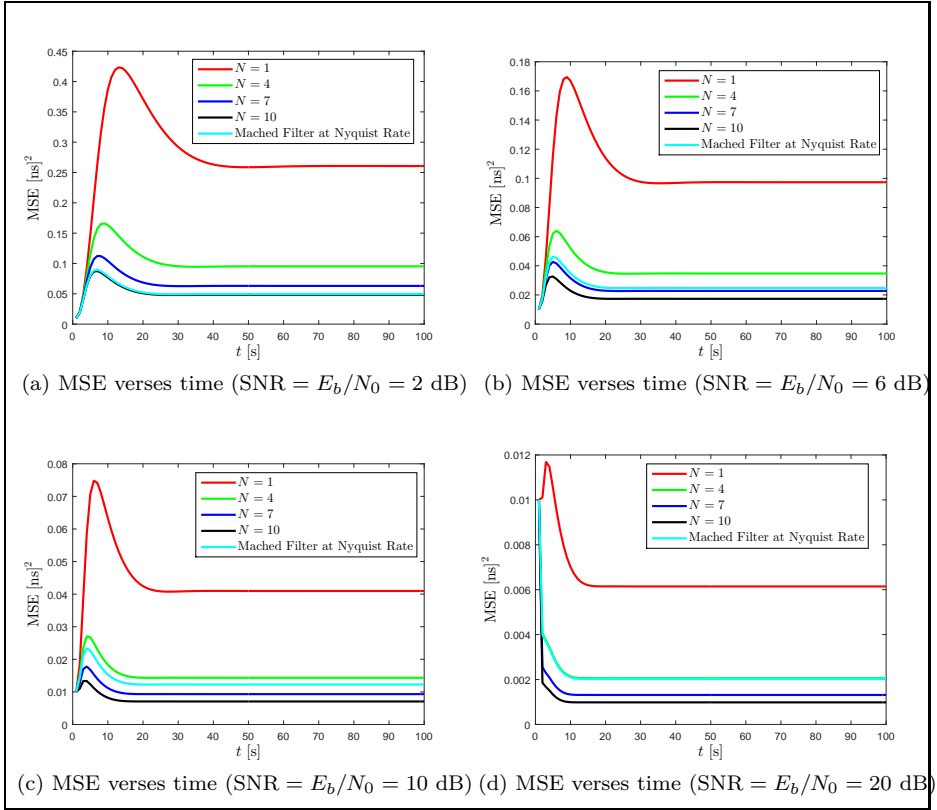


Figure 6.7: Variation of MSE with time for the TOA estimates of digital matched filter and multi-channel sub-Nyquist energy detector based receiver (N indicates number of channels).

$$\mathbf{A}[n] = \begin{bmatrix} 1 & 1 \\ 0 & \kappa \end{bmatrix}, \quad (6.6.3)$$

$$\mathbf{u}[n] = \begin{bmatrix} 0 \\ u_v[n] \end{bmatrix}, \quad (6.6.4)$$

where $u_v[n]$ is the noise with variance σ_p^2 and $\kappa < 1$ is a constant. The plant noise $\mathbf{u}[n] \sim \mathcal{N}(0, \mathbf{Q})$, where \mathbf{Q} is given by

$$\mathbf{Q} = \begin{bmatrix} 0 & 0 \\ 0 & \sigma_p^2 \end{bmatrix}. \quad (6.6.5)$$

We choose (6.6.1) as the state equation of the Kalman filter. The measurement vector, $\mathbf{y}[\mathbf{n}] = [\hat{\tau}_{\text{toa}}^1[n], \hat{\tau}_{\text{toa}}^2[n], \dots, \hat{\tau}_{\text{toa}}^N[n]]$, is the independent TOA estimates from N energy detector channels. The measurement equation of the Kalman filter is given by

$$\mathbf{y}[n] = \mathbf{H}[n]\mathbf{s}[n] + \mathbf{w}[n], \quad (6.6.6)$$

where

$$\mathbf{H}[n] = \begin{bmatrix} 1 & 0 \\ 1 & 0 \\ \vdots & \vdots \\ 1 & 0 \end{bmatrix}, \quad (6.6.7)$$

$\mathbf{w}[n] \sim \mathcal{N}(0, \text{diag}(\sigma_1^2, \dots, \sigma_N^2))$. N denotes the number of detectors and $\text{diag}(\cdot)$ indicates the diagonal matrix with diagonal elements represented inside the brackets.

With the above specified state and measurement equation, The Kalman algorithm for tracking is as shown in Algorithm 6.1. In each iteration (represented by i in the algorithm), the estimates from the energy detector channels, $\mathbf{y}[n]$, and the dynamic model represented by (6.6.1) is used to optimally evolve the system state. At each iteration, the fused estimate is extracted by

$$\tilde{\tau}_{\text{toa}}[n] = [\mathbf{s}[n]]_1, \quad (6.6.8)$$

where, $[\cdot]_i$, denotes the i -th element of the vector and its variance from the MSE matrix, \mathbf{M} (refer Algorithm 6.1), by

$$\tilde{\sigma}_{\text{toa}}^2[n] = [\mathbf{M}[n]]_{(1,1)}, \quad (6.6.9)$$

where $[\cdot]_{(i,j)}$ denotes the (i, j) -th element of the matrix.

In our analysis, we have used same kind of detectors in each channel of a multi-channel receiver and also the reliability or importance of each of the detectors are assumed same. By appropriately selecting the measurement matrix \mathbf{H} and covariance of the measurements, we can extend the Kalman filter design to accommodate different types of detectors with varying characteristics. In the next section, we will assess the performance of the proposed fusion and tracking method.

6.7 Simulation Study

6.7.1 AWGN Channel

AWGN channel is simulated with $F_s = 8$ GHz with $T_f = 200$ ns, $N_s = 1$ and $B = 4$ GHz. We set $T_b = 1$ ns, thus resulting sampling rate of the energy detector is 1/8-th the Nyquist rate. Consider a linear variation of TOA (τ_{toa}) observed by a set of four independent energy detector channels (refer Figure 6.1). The observed TOA of the four detectors are as shown in Figure 6.6a at SNR = 12 dB. The tracked TOA using the Kalman formulation is shown in the Figure 6.6b. We consider prior

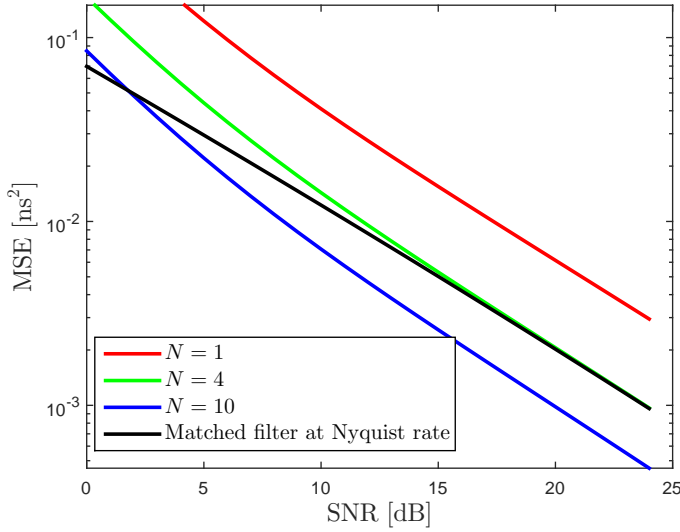


Figure 6.8: Steady state MSE versus time, for digital matched filter and multi-channel energy detector receivers (N indicates number of channels).

state, covariance of prior state and plant noise variance equal to $[20, 1]$, $0.01\mathbf{I}_2$ and $\sigma_p^2 = 0.0001$ respectively.

The mean square error (MSE) variation with time for the detection schemes with multiple energy detectors at various SNRs (E_b/N_0) are illustrated in the Figure 6.7. Notice that the steady state variance decreases with the increase in number of energy detector channels, N . Also, from Figure 6.7, at high SNRs, only few energy detector channels (operating at 1/8-th rate of matched filter) are sufficient to achieve same performance as digital matched filter.

Figure 6.8, shows the variation of steady state MSE with number of energy detector channels, N . Notice that steady state MSE of fusing 4 independent energy detector estimates reaches that of digital matched filter estimate.

Figure 6.9, shows the number of energy detector channels operating in sub-Nyquist ($F_s/8$) rate needed to match the performance of matched filter operating at Nyquist rate (F_s). At lower SNRs, more number of energy detector channels, (N_{ED}), are required to meet the matched filter performance. The number of energy detector channels, N_{ED} , reduces with the increase of SNR and asymptotically approaches to 4, confirming with the analytical derivation of the previous section.

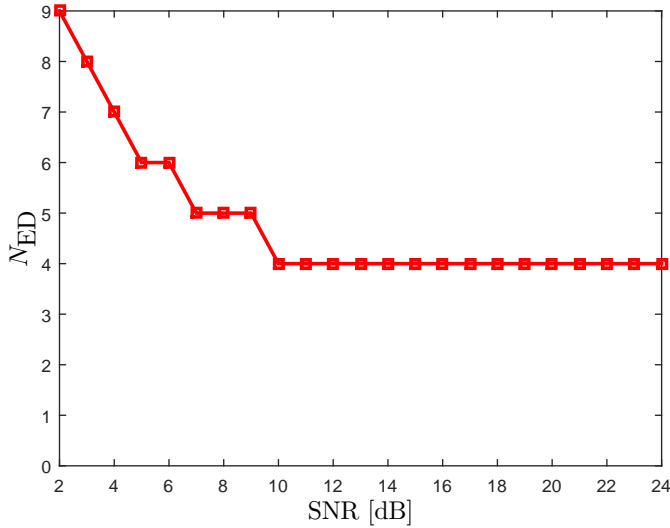


Figure 6.9: Number of sub-Nyquist energy detector channels need to match the performance of matched filter operating at Nyquist rate.

6.7.2 Multipath Channel

IEEE 801.15.4a CM1 channel model is simulated with $F_s = 8$ GHz with $T_f = 200$ ns, $N_s = 1$ and $B = 4$ GHz. We set $T_b = 1$ ns, thus resulting sampling rate of the energy detector is 1/8-th the Nyquist rate. We use WMESS algorithm discussed in the previous section to arrive at TOA estimates from the energy samples. We employ similar fusion and tracking strategy using the Kalman filter described in the previous section for the dynamic TOA model. The prior state information, covariance of prior state and other initialization parameters of the Kalman filter are kept same as in the previous section. Figure 6.10, shows the variation of MSE with time for different number of energy detector channels at 20 dB SNR. As expected the steady state variance decrease with the increase in the number of energy detector channels. Figure 6.11, shows the variation of steady state MSE with number of sub-Nyquist energy detectors, as discussed earlier a single energy detector with WMESS selection criteria outperforms the matched filter at low SNRs, however, at high SNRs more energy detectors are need to match the matched filter performance. Figure 6.11, also illustrates that fusing two energy detector channel estimates ($N_{ED} = 2$) can match the matched filter performance across the SNR region.

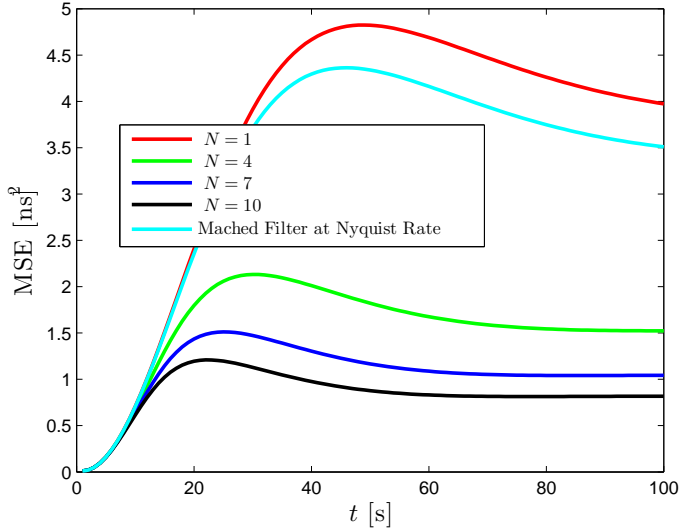


Figure 6.10: Variation of MSE with time for IEEE 802.14.4a CM1 channel model for digital matched filter and multi-channel energy detector receivers (WMESS criteria is employed, N indicates number of channels).

6.7.3 Energy Analysis

Energy of the samples used in the TOA estimation is given by, $\|\mathbf{x}\|^2$, where the samples are computed using (6.3.1) and (6.3.6). For a multi-channel receiver with N channels, the total energy is given by $N \|\mathbf{x}\|^2$. Figure 6.12 shows the averaged energy over 100 random TOA pulses for multi-channel energy detector based receiver with AWGN and IEEE 802.15.4a CM1 multipath channel.

Energy of the multi-channel receiver increases as the sampling rate, $1/T_b$, decreases. This is because of an increase in the degree of freedom, $M = 2BT_b + 1$, which will increase the mean and variance of the energy samples, x_n as per (6.4.7). Also from Figure 6.12, despite increase in the number of channels to improve the performance, the net consumed energy for similar performance is less for multi-channel receivers for AWGN and multipath channels.

6.8 Conclusion

Estimating TOA with good accuracy is very important for localization and several other applications. UWB with its large bandwidth can yield high precision ranging as evident from CRLB Equation (6.4.1). For AWGN channel, matched filter

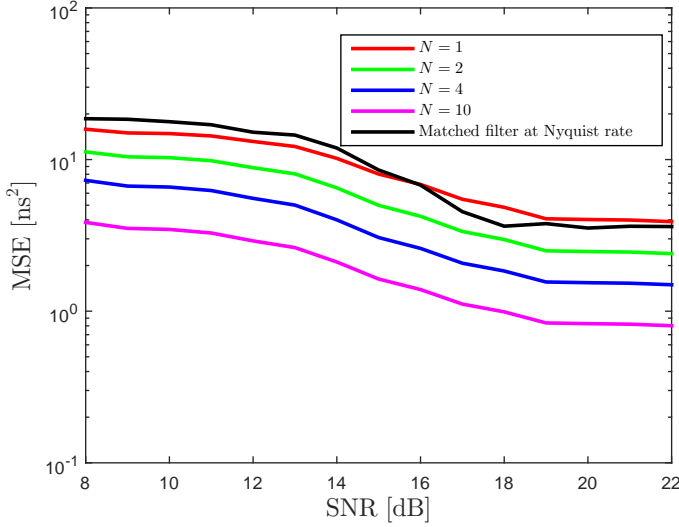


Figure 6.11: Steady state MSE verses time for IEEE 802.14.4a CM1 channel model, for digital matched filter and multi-channel energy detector based receivers (WMES criteria is employed, N indicates number of channels).

based estimation yields optimum performance at high SNRs. However, matched filter requires Nyquist-rate sampling and is inefficient in terms of cost and power consumption. Energy detectors operating at sub-Nyquist rate is an interesting alternative as it can be designed using cost effective analog circuits and is power efficient, however, it lacks the precision in range measurements. In this chapter, we showed that for an AWGN channel, we can achieve the performance of a matched filter, by using a multi-channel sub-Nyquist receiver structure. We showed that number of energy detector channels needed to meet the matched filters performance is high at low SNRs and reduces as SNR increases, and finally converges to 4 as SNR increases asymptotically. This is analytically derived in (6.4.20), and confirmed through simulations (refer Figure 6.8 and Figure 6.9). A Kalman filter with suitable choice of state-equation and measurement equations is designed to perform the dual task of tracking the TOA as well as fusing the multiple energy detector outputs. Filter equations are shown in Algorithm 6.1 and performance in terms of MSE are demonstrated in Figure 6.7 and Figure 6.8. Result indicate that for an AWGN channel, the steady state variance drops with the increase of number of detectors, and require 4 energy detectors to have the same performance as a digital matched filter.

Proposed tracking and fusion strategy of energy detectors is analyzed in simula-

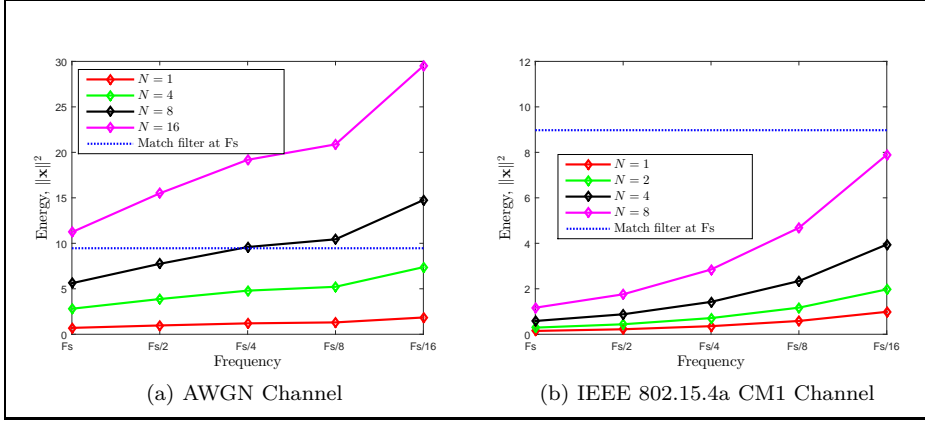


Figure 6.12: Energy of the samples used in the TOA estimation for digital matched filter and multi-channel receivers (N indicates number of channels). Averaged energy of samples, \mathbf{x} , over 100 random TOA pulses are presented.

tion for IEEE 802.15.4a CM1 multipath channel (residential LOS model) and results are demonstrated in Figure 6.4, Figure 6.10, and Figure 6.11. From Figure 6.4, we showed that by utilizing the *a priori* information like PDP about the multi-path channel, the performance of TOA estimation can be improved. Results also indicate that the two sub-Nyquist sampled energy detector estimates with WMESS criteria can outperform digital matched filter at all SNR regions.

Analysis of the energy consumed for multi-channel energy detector is studied and results are shown in Figure 6.12. It indicates the higher energy consumption at lower sampling rates. Despite this, we observe that total energy consumed for multi-channel energy detector receiver is far less compared to its digital counterpart.

Compressive Sampling Based UWB TOA Estimator

In this chapter, we discuss two compressive sampling based time of arrival (TOA) estimation algorithms using a sub-Nyquist rate receiver. We also describe a novel compressive sampling dictionary design for the compact representation of the received UWB signal. One of the discussed algorithm exploits the *a priori* information with regard to the channel and range of the target. The performance of the algorithms are compared against the maximum likelihood (ML) based receiver using IEEE 802.15.4a CM1 line of sight (LOS) UWB channel model. The proposed algorithm yields performance similar to the ML TOA estimation at high SNRs. However, the computational complexity and the sampling rate requirements are lesser compared to the ML estimator. Simulation results show that the proposed algorithms can match ML estimator performance with only 1/4-th the sampling rate at 25 dB SNR. We analyze the performance of the algorithm with respect to practical constraints like size of the holographic dictionary and sampling rates. We also discuss a new algorithm which can exploit the *a priori* information regarding the UWB channel and the geographical constraints on the target that may be available at the receiver. This algorithm can substantially boost the performance compared to the algorithm without *a priori* information at low SNRs.

7.1 Background

Compressive sampling (CS) technology has far reaching implications and concern a number of varied applications such as data compression, channel coding, medical imaging, etc. New applications for this technology are emerging constantly. In this chapter, we address a classical estimation problem concerning ultra-wideband (UWB) time of arrival (TOA) using compressive sampling technique. The compressive sampling theory suggests that from a fewer number of acquisition samples, which is less than that advocated by the Nyquist theory, an approximate reconstruction of the original signal is possible. This involves choosing an appropriate

measurement matrix for efficiently representing the received signal in lower dimension [CW08,HNT13]. The choice of reducing the sampling rate of the overall system is important as this enables digital designs for wideband systems like UWB.

Availability of unlicensed frequency spectrum at frequency band less than 10 GHz created a lot of excitement for employing UWB for various applications including TOA. However, there are several challenges in adopting UWB at these frequency bands. The two main challenges include the stringent emission regulations by the regulatory bodies like federal communications commission (FCC) [FCC02, XF12]. This had a direct impact on the range and rate of the system. Secondly, wide bandwidth requirement of UWB created bottleneck in the ADC design.

Availability of the mmWave spectrum without stringent emission requirements has benefited the evolution of UWB technology in the 30 – 50 GHz spectrum. This has improved the range and rate problems discussed earlier. However, large bandwidth coupled with high time and amplitude resolution requirements for ADCs still persist and pose significant challenge in the design of the digital UWB system.

A digital UWB transceiver can offer flexibility and scalability. Moore’s law gives us processing power for “free”, and we can make savings by using a cheaper digital front-end. However, UWB signal occupies extremely wide bandwidth, thus requiring high sampling rate. For example, TOA estimation using the proposed rake receiver structure in [LDM02], would require sampling rates in excess of 25 GHz. The ADC design for wideband systems face several challenges in order to support wide bandwidth, which include among others amplitude resolution, sampling rate, analog bandwidth, cost, etc. [NMBH13, Mur16]. High speed ADCs for UWB TOA systems can be designed using an interleaved flash ADC or bank of poly-phase ADCs [SVC09, GMH⁺09]. However, they are sensitive to timing jitter, their amplitude resolution is generally poor and are expensive in terms of the cost.

In this chapter, we propose a sub-sampled UWB receiver based on compressive sampling. With IEEE 802.15.4a CM1 as the channel model [MCC⁺04, Mol05], and Nyquist sampled maximum likelihood based UWB TOA receiver as a starting point, we show that the requirements on RF front-end sampling rate can be significantly loosened by employing recent theories on compressive sampling, without any significant loss in performance at high SNR. To accomplished this, we will represent the received UWB signal in a compact form using the columns of a carefully chosen dictionary leading to a sparse signal representation. We propose a TOA estimation method, which can estimate the TOA from this sparse representation. We also analyze the performance trade-off of the proposed algorithm in terms of the dictionary size, sampling rate and sparsity level. To the authors knowledge, compressive sampling has not before been applied to the considered problem, which is a main motivation for this chapter. In addition, we also show that *a priori* properties of the IEEE 802.15.4a channel model opens up for improvement of the receiver performance by taking statistical channel properties into account. This is a contribution that is believed to have an interest for the reader in its own right.

TOA estimation involves estimating the propagation time between transmitter and receiver. Accurate estimation of TOA is essential in several applications includ-

ing positioning and communication. In many communication systems, the message information is embedded in the location of the pulse. For example, TOA estimation methods can be used to demodulate pulse position modulated (PPM), IR-UWB symbols [YDAH14, KMKK06]. Another application of TOA is in the estimation of the position of mobile nodes in a wireless sensor network (WSN). Here, TOA values are used to calculate the range from the anchor nodes using which the location information can be derived [NZSH13, RRS⁺11].

There are several works concerning TOA estimation. Broadly, they can be classified as frequency-domain and time-domain methods. Frequency-domain methods, typically involve estimating the frequency domain channel response by sweeping the channel using a multi-carrier modulation schemes such as OFDM. Then applying a super-resolution algorithm such as root multiple signal classification (MUSIC) [DFM94] or total least square-estimation of signal parameter via rotational invariance techniques (TLS-ESPRIT) [Saa97] on the channel frequency response [Xin04]. Due to the large number of multi-paths in the UWB propagation environment, the implementation complexity of this method is extremely high [FDMW06].

In the time-domain TOA estimation methods, the TOA is estimated directly from the received time-domain signal by identifying the first multipath. UWB based positioning systems uses wide bandwidth and provides high time resolution, therefore TOA estimation using time-based ranging is the method of choice in these systems. The simplest of these methods include choosing the location of the peak in the received signal as the TOA estimate [SGI08, JV02]. The main source of error in these TOA estimation methods is due to the strongest multipath components arriving later than the first path. In UWB channels this can happen because each multipath component show delay dispersion by itself. That means a short pulse that, for example, undergoes only a single diffraction may arrive at the receiver with a larger support compared to the direct path due to NLOS and antenna effects [BKM⁺06, SGI08]. This problem is addressed using techniques such as thresholding [DCW08], using channel information [GSO06], etc. When these algorithms are implemented using digital transceivers, they require sampling rate much higher than the Nyquist rate. Our purpose in this chapter, is to develop a method which can operate at lower sampling rate using compressive sampling technique.

IR-UWB based TOA estimation using ML approach is described in [SGI08]. We will discuss this in greater detail in later section and use this method to compare the proposed schemes in this chapter. When implemented digitally, ML based TOA estimator requires Nyquist-rate sampling. Estimating the TOA in a sparse domain using the received IR-UWB signal is the main theme of this chapter.

Before we continue the discussion, the main discussion topics of this chapter are summarized as follows:

- A novel compressive sampling algorithms for the IR-UWB based TOA estimation.
- A new compressive sampling dictionary design, so that the received UWB

signal can be efficiently expressed as a linear combination of the columns of this dictionary. This results in compact representation of the received UWB signal.

- We modify the above TOA estimation algorithm to exploit the *a priori* channel information that may be available.
- We provide a performance comparison of the proposed methods with ML based TOA estimation methods.
- We analyze the performance of the methods under practical scenarios for different dictionary parameters and sampling rates.

Consequence of the above points indicate that a cost effective digital UWB TOA estimators can be developed for the practical UWB applications, thus leading to a progress beyond the state-of-the-art. Besides the achievement over the state-of-the-art, this chapter compliments the current trend in the research pertaining to UWB domain including [WLD14, BAN14, MASL⁺09, MXCZ08].

Reminder of this chapter is organized as follows. In Section 7.2, we will discuss the received multipath signal. In Section 7.3, we will discuss the maximum likelihood (ML) based TOA estimation. Section 7.4, introduces the UWB channels and discusses the challenges in estimating the TOA in multipath UWB channels. We use IEEE 802.15.4a CM1 line of sight (LOS) channel model as a reference. In Section 7.5, we briefly discuss the compressive sampling theory and present a method for sparse representation of the received UWB signal. This enables us to faithfully represent the received UWB signal at lower sampling rate. Section 7.6, discusses two TOA estimation algorithms. Section 7.7, provides the simulation results for TOA estimation under different practical scenarios. Finally, Section 7.8, discusses the conclusions from the results presented.

7.2 Signal Model

We consider a single user UWB system. The signal model comprises of N_f frames each having an unit energy pulse, $s(t)$, given by

$$\omega_{\text{tr}}(t) = \sum_{j=0}^{N_f-1} d_j s(t - jT_f - c_j T_c), \quad (7.2.1)$$

where each frame is of duration T_f , and the frame index is represented by j . The chip duration is represented by T_c and $c_j \in \{0 \dots N_c\}$ indicates the time-hopping code. The $d_j \in \{\pm 1\}$ is the polarity code, which can be used along with time-hopping to smooth the signal spectrum.

The received signal is the distorted version of the transmit pulse with multipaths. The TOA is defined as the time elapsed for the first arrival path to reach the receiver

from the transmitter. The received signal can be represented by

$$\omega_{\text{rx}}(t) = \sum_{j=0}^{N_f-1} d_j r(t - jT_f - c_j T_c) + n(t), \quad (7.2.2)$$

where,

$$r(t) = \sqrt{\frac{E_b}{N_f}} \sum_{\ell=1}^L \alpha_\ell s(t - \tau_\ell). \quad (7.2.3)$$

Here, E_b is the captured energy and $\sum_{\ell=1}^L \alpha_\ell^2 = 1$. The gain for the ℓ -th tap is given by α_ℓ . The $n(t)$ is the AWGN process with zero mean and double-sided power spectral density of $N_0/2$. Without loss of generality, and for simplicity of analysis, we assume $c_j = 0$, $N_f = 1$, and $d_j = 1$. The TOA estimation problem involves estimating the first arrival path, $\tau_1 = \tau_{\text{toa}}$, in the received signal (7.2.2). The frame duration, T_f , is chosen sufficiently larger than the delay spread of the channel to avoid any inter pulse interference, that is $T_f \gg T_d$, where T_d is the delay spread of the channel.

7.3 ML based TOA estimation

In order to be self-contained, in this section, a short review of ML based UWB TOA estimation is given [FDMW06, SGI08, WS02]. Consider a direct sampling receiver generating the sampled output of (7.2.2), defined by a vector \mathbf{r} , such that its elements $r(i) = \omega_{\text{rx}}(iT_s)$. The $N = T_f/T_s$, is the number of samples corresponding to a frame and $\mathbf{r} \in \mathbb{R}^N$. The received samples can be written as

$$\mathbf{r} = \mathbf{W}(\boldsymbol{\tau})\boldsymbol{\alpha} + \mathbf{n}, \quad (7.3.1)$$

where $\boldsymbol{\alpha} = [\alpha_1, \dots, \alpha_L]^T$ represents the path-gain, $\mathbf{n} \in \mathbb{R}^N$, are the noise samples with its elements, $n(i) = n(iT_s)$, and $\mathbf{W}(\boldsymbol{\tau}) = [\mathbf{w}_{d_1}, \mathbf{w}_{d_2}, \dots, \mathbf{w}_{d_L}] \in \mathbb{R}^{N \times L}$. The \mathbf{w}_{d_i} , is an N dimensional vector defined as

$$\mathbf{w}_{d_i} = [\mathbf{0}_{d_i}^T, \mathbf{w}^T, \mathbf{0}_{N-P-d_i}^T]^T,$$

where, \mathbf{w} denotes a vector of discrete samples representing the transmit pulse $s(t)$, with its i -th element, $w(i) = s(iT_s)$, $i = 0, \dots, P-1$. The $\mathbf{0}_{d_i}$ is a zero vector of size, $d_i = \lfloor \tau_i/T_s \rfloor$.

The ML estimation for the unknown parameter set $\boldsymbol{\nu} = [\boldsymbol{\alpha}^T, \boldsymbol{\tau}^T]^T$, can be obtained by solving the following optimization problem

$$\hat{\boldsymbol{\nu}} = \arg \min_{\boldsymbol{\nu}} \left\{ \frac{1}{N} \|\mathbf{r} - \hat{\mathbf{r}}\|_2^2 \right\}, \quad (7.3.2)$$

where the elements of $\hat{\mathbf{r}}$ are given by

$$\hat{r}(i) = \sum_{\ell=1}^L \hat{\alpha}_{\ell} s(iT_s - \hat{\tau}_{\ell}). \quad (7.3.3)$$

Solving the optimization (7.3.2) is computationally intensive as it requires a search over entire parameter space $\boldsymbol{\nu}$. However, if the multipaths in the channel are separable, then the unknown parameter estimation simplifies to [FDMW06, WS02]¹

$$\hat{\boldsymbol{\tau}} = \arg \max_{\boldsymbol{\tau}} \left\{ \sum_{i=1}^L (\mathbf{w}_{d_i}^T \mathbf{r})^2 \right\}, \quad (7.3.4)$$

$$\hat{\boldsymbol{\alpha}} = \mathbf{W}(\hat{\boldsymbol{\tau}})^T \mathbf{r}. \quad (7.3.5)$$

In this case the estimation of the TOA, τ_1 , is decoupled from the estimation of the other channel parameters. The optimization of (7.3.4), can be accomplished by maximizing each term of the sum independently. We use this method to compare the performance of the proposed algorithms.

7.4 UWB Channels

One of the most widely used channel models for indoor propagation was proposed by Saleh and Valenzuela [SV87]. This model is adopted in IEEE 802.15.4a CM1 standard for providing stochastic channel model for LOS residential conditions [MCC⁺04, Mol05]. As per this model, the discrete-time impulse-response of the UWB channel has clusters arriving in the Poisson distributed way and the multipath components (MPCs) within the cluster follows a Laplacian model. A model with C clusters having R rays (MPCs) can be expressed as

$$h(t) = \sum_{i=1}^C \sum_{j=1}^R a_{i,j} \delta(t - T_i - \gamma_{i,j}), \quad (7.4.1)$$

where T_i represents the arrival time of the i -th cluster and $\gamma_{i,j}$ represents the j -th ray in the i -th cluster. In (7.2.3), we have combined the cluster and ray arrivals, such that

$$\begin{aligned} [\alpha_1, \dots, \alpha_L] &= [a_{1,1}, \dots, a_{C,R}], \\ [\tau_1, \dots, \tau_L] &= [(T_1 + \gamma_{1,1}), \dots, (T_C + \gamma_{C,R})], \end{aligned}$$

where $L = CR$. Note that by definition $\gamma_{i,1} = 0$. Therefore, $T_1 = \tau_1 = \tau_{\text{toa}}$, denotes the arrival time of first ray of the first cluster and is the TOA for the LOS

¹Energy of the received pulse is assumed to be one.

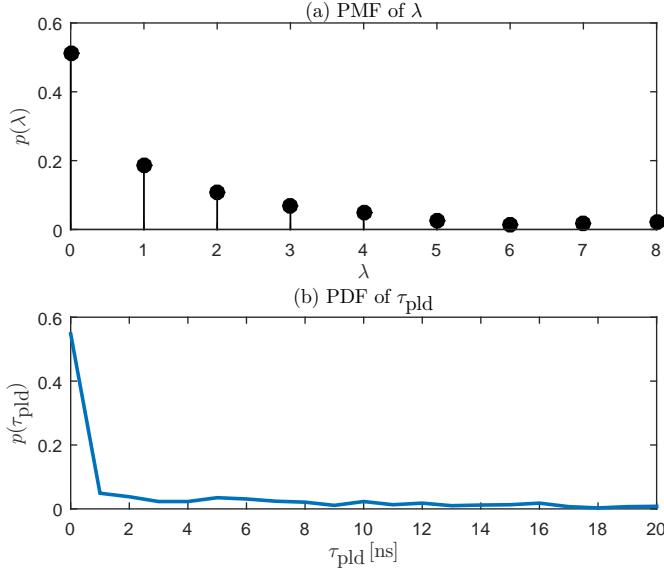


Figure 7.1: The PMF and PDF of λ and τ_{pld} respectively for IEEE 802.15.4a CM1 model. The sampling frequency of 8 GHz and 100 distinct channel realization are employed.

UWB channel. For details about the cluster and ray arrival rates, refer to the IEEE 802.15.4a CM1 model described in [IEE07].

Below, we will derive new statistical parameters for the IEEE 802.15.4a CM1 model, which can be utilized by the TOA estimation algorithm to improve the performance. For a multipath residential LOS channel proposed in IEEE 802.15.4a CM1 model, if we consider all the significant paths that constitutes 80% of the total energy, then the probability mass function (PMF) for the number of significant paths, λ , that arrives before the strongest path is shown in the Figure 7.1(a). Approximately 50% of the time the first arriving path is weaker than the strongest path. If we define τ_{pld} as the peak to first path delay, that is, $\tau_{\text{pld}} = \tau_{\text{peak}} - \tau_1$, where, τ_{peak} , is the location of the peak, then the probability density function of the τ_{pld} is shown in Figure 7.1(b).

Channel *a priori* information shown in Figure 7.1(a) and Figure 7.1(b) combined with the geographic constraint on the range can be used to improve the performance of the proposed compressive sampling algorithms. We will discuss this in the later section. In the next section, we will briefly introduce compressive sampling theory and discuss the representation of the received UWB signal, \mathbf{r} , in a sparse domain.

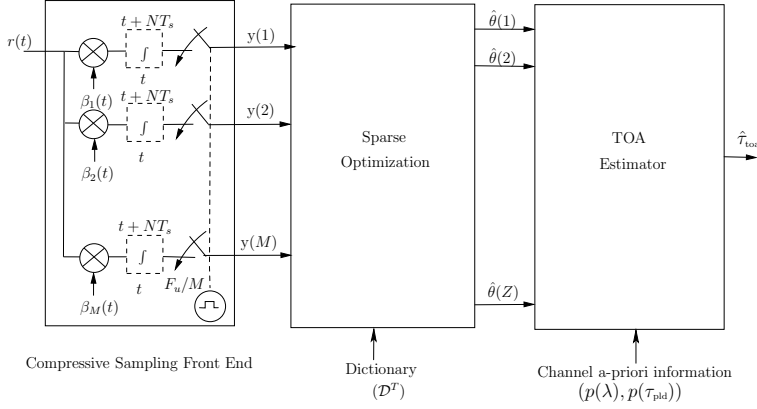


Figure 7.2: Block diagram of the compressive sampling (CS) system for TOA estimation. The $\beta_i(t)$, $i = 1, \dots, M$ denotes the continuous time i.i.d normal processes with zero mean and unit variance.

7.5 Sparse representation of UWB signal

Consider an N -point Nyquist sampled discrete-time representation of the received UWB signal, $\mathbf{r} \in \mathbb{R}^N$ obtained by sampling the received signal, $r(t)$ using an ADC at rate F_s . Consider the signal acquisition hardware shown in the Fig. 7.2. Here, the signal is acquired at an effective sampling rate of $F_u = F_s/\mathcal{U}$ and each ADCs in the M parallel paths of compressive sampling front-end will operate at a rate F_u/M . Where, $\mathcal{U} = N/M$ is the under-sampling ratio. A review on different compressive sampling front-end for wideband signals can be found in [NMBH13]. The acquired signal, \mathbf{y} , can be viewed as a projection of \mathbf{r} on a measurement matrix, Φ . The elements of Φ are i.i.ds drawn from a normal distribution. That is,

$$\mathbf{y} = \Phi \mathbf{r}, \quad (7.5.1)$$

and Φ is an $M \times N$ matrix. As shown in Figure 7.2, $\mathbf{y} \in \mathbb{R}^M$ is fed to the sparse optimization routine, which will represent \mathbf{y} in a compact form using the columns of a carefully chosen dictionary leading to a sparser signal representation.

We consider a dictionary, \mathcal{D}^T , whose dimension is $N \times Z$, whose columns, \mathbf{d}_i , are the basis vectors in space \mathbb{R}^N , in which, \mathbf{r} is sparse, that is

$$\mathbf{r} = \sum_{i=0}^S \theta_{\ell_i} \mathbf{d}_i, \quad (7.5.2)$$

where $S \ll Z$ is the sparsity of the received UWB signal in the dictionary domain. The ℓ_i is the support of vector $\boldsymbol{\theta} \in \mathbb{R}^Z$, and θ_{ℓ_i} denotes the non-zero value at the

support. The sparse optimization block of Figure 7.2, typically solves an optimization problem to represent \mathbf{y} , using a sparse vector $\hat{\boldsymbol{\theta}} \in \mathbb{R}^Z$. For example, a basis pursuit type of algorithm solves,

$$\begin{aligned} \hat{\boldsymbol{\theta}} &= \arg \min \|\boldsymbol{\theta}\|_1, \\ &\text{subject to } \mathbf{y} = \mathcal{H}\boldsymbol{\theta}, \end{aligned} \quad (7.5.3)$$

where $\mathcal{H} = \Phi\mathcal{D}$ is called holographic dictionary. From the sparse representation, an estimate of the TOA, $\hat{\tau}_{\text{toa}}$ needs to be estimated.

In the reminder of this chapter, for the proposed structure in Figure 7.2, we will discuss how to design a compressive sampling dictionary. Then we will propose a TOA estimation algorithm, which will utilize the sparse representation of the received UWB signal in the chosen dictionary domain to estimate the TOA. We will modify the algorithm to utilize the *a priori* information regarding the channel and the geographical constraints to improve the performance of the proposed TOA estimation algorithm.

7.6 Method for sub-Nyquist TOA Estimation

In this section, first, in Section 7.6.1, we design the compressive sampling dictionary for the TOA algorithms. Subsequently, two main algorithms of this chapter which uses the above designed dictionary for TOA estimation are discussed in some detail. In Section 7.6.2, we discuss the TOA estimation using a modified greedy search algorithm, then the TOA estimation based on *a priori* channel information is studied in Section 7.6.3.

7.6.1 Compressive sampling dictionary

As shown in (7.2.2), the received UWB signal is a scaled and delayed version of the transmit pulse. The transmit pulse, $s(t)$, is typically chosen as first or second order Gaussian derivative pulse [YDAH14]. To construct the dictionary, we choose each column of the dictionary, $\mathcal{C}^T(t, \Delta)$, as shifted versions of the transmit pulse, that is

$$\mathcal{C}^T(t, \Delta) = [p_0(t), \dots, p_{Z-1}(t)], \quad (7.6.1)$$

where

$$p_\ell(t) = s(t - \Delta\ell), \quad \ell = 0, 2, \dots, Z-1. \quad (7.6.2)$$

The Z defines the number of atoms (columns) in the dictionary. The offset, Δ , needs to be controlled to strike a compromise between the number of atoms needed to faithfully represent the received UWB pulse and the size of the dictionary. The Δ and Z are chosen such that $T_f = Z\Delta$. Equation (7.6.2) is expressed in terms of continuous t and Δ . In practice, both these parameters are discretized such that t is sampled at a particular sampling period T_s and Δ is a multiple of T_s . We define

\mathcal{D} as uniform sampling of the dictionary \mathcal{C} , and it is of the dimension $Z \times N$ as each atom ($p_\ell(t)$) in the dictionary is now a vector of length N . That is

$$\mathcal{D}^T = [\mathbf{w}_0, \dots, \mathbf{w}_Z] \in \mathbb{R}^{N \times Z}, \quad (7.6.3)$$

where,

$$\mathbf{w}_\ell = [\mathbf{0}_{\ell\nu}, \mathbf{w}, \mathbf{0}_{N-P-\ell\nu}]^T \in \mathbb{R}^N, \quad (7.6.4)$$

with $\ell = [0, \dots, Z-1]$ and $\Delta = \nu T_s$, where ν is an integer constant, which can be used to control the size of the dictionary.

7.6.2 TOA estimation algorithm

Consider discrete samples of the received UWB signal sampled at F_s represented as a time-domain vector, \mathbf{r} . Let $\mathbf{y} = \Phi\mathbf{r}$, denote the random projection of \mathbf{r} on the measurement matrix, Φ (refer to Figure 7.2), where Φ is a $M \times N$ matrix, with its elements $\phi_{i,j}$ drawn from $\mathcal{N}(0, 1)$. As shown in Figure 7.1(a), for a LOS UWB channel the first arrival path can be weaker than the strongest path. To locate the true TOA, one has to search backward from the peak location to locate any possible significant energy paths, which may not be strongest. To accomplish this in sub-Nyquist domain, we propose a TOA algorithm as shown in Algorithm 7.1.

Input to the Algorithm is the vector \mathbf{y} , Holographic dictionary, \mathcal{H} , and the parameter, K , which defines the number of paths to be searched. In line-7, \mathcal{H}_{I_k} , denotes the matrix composed of the columns defined in the set I_k . The $\mathcal{H}_{I_k}^\dagger$ indicates the pseudo inverse of \mathcal{H}_{I_k} . Also, all columns of \mathcal{H} , are normalized, that is $\|\mathbf{h}_i\|_2^2 = 1, \forall i \in [1, \dots, Z]$, where \mathbf{h}_i denotes the i -th column of the matrix \mathcal{H} . It can be noticed that in each iteration, the holographic dictionary, \mathcal{H} , is searched for the strongest delayed version of the transmitted signal, that is contained in the residual signal, \mathbf{e}_k . After K iteration, the lowest indexed column of the holographic dictionary, ℓ , is identified. Since each column in the dictionary is offset by Δ , the TOA is estimated as $\hat{\tau}_{\text{toa}} = \ell\Delta$.

The performance of the algorithm depends on the offset, Δ , if Δ is small, the accuracy of the TOA estimation will be better, as the atoms of the dictionary can resolve the TOA better. However, this will increase the dictionary size, Z as $Z = T_f/\Delta$, thus increasing the memory requirements for the system.

If the number of paths searched, K , in the algorithm is too high then, there is a potential problem of picking the wrong atom in the dictionary due to the noise and if K is too small then there is a possibility of missing the atom which correspond to the weaker first path. There exists an optimal K , at which the performance of the estimator is maximum.

The TOA estimation performance can be improved by increasing the number of random projections of UWB signal, since it aids better reconstruction [Don06, CRT06]. However, this leads to higher sampling rate and increases the demands on ADC resources, there by increasing the cost of the transceiver as discussed in

Algorithm 7.1: TOA estimation algorithm**Input:** $\mathbf{y}, \mathcal{H}, K, \Delta, \mathbf{e}_0 = \mathbf{y}, k = 0, I_k = \{\emptyset\}$ **Output:** TOA estimate, $\hat{\tau}_{\text{toa}}$.

```

1 repeat
2    $t = \arg \max |\langle \mathbf{h}_i, \mathbf{e}_k \rangle|, i = 1, \dots, Z$ 
3   if  $k=0$  then  $\ell = t$ ;
4   else if  $t < \ell$  then  $\ell = t$ ;
5    $k = k + 1$ 
6    $I_k = I_k \cup t$ 
7    $\mathbf{e}_k = \mathbf{y} - \mathcal{H}_{I_k} \mathcal{H}_{I_k}^\dagger \mathbf{y}$ 
8 until  $k \leq K$ 
9 return  $\hat{\tau}_{\text{toa}} = \ell \Delta$ 

```

Section 7.1. In Section 7.7, the performance of Algorithm 7.1 is studied as well as the rules-of-thumb is provided for its configuration.

7.6.3 TOA estimation with *a priori* information

If we know certain statistical properties of the channel beforehand, then we can exploit this information to improve the performance of the TOA estimator. For example, for IEEE 802.15.4a CM1 channel model, the probability distributions of number of significant paths before peak-path, λ , and peak-to-first path delay, τ_{pld} , are as shown in Figure 7.1(a) and Figure 7.1(b). From this we can notice that more than 50% of the time the peak path is the first path, and also probability that the first path is more than 20 ns away from the peak location is negligible. Another important *a priori* information could be from the geographic constraints on the range of the target, resulting in TOA values being $\tau_{\text{toa}} < \tau_{\text{toa}}^{\max}$.

The above *a priori* information can be handled by modifying Algorithm 7.1, such that, only the paths within a window interval before the peak are considered for the TOA estimation. The modified algorithm is as shown in Algorithm. 7.2. In the later section, we will show that the modified algorithm with *a priori* information outperforms the Algorithm 7.1, which is agnostic to this information.

In the next section, we will assess the performance of the proposed algorithm in simulations.

7.7 Simulation Study

In this section, the performance of the proposed methods are investigated by numerical simulations that mimic a realistic UWB link. Residential LOS UWB channels can vary depending on the environmental aspects such as plan of the building, type of walls, obstacles, etc. The IEEE 802.15.4a UWB stochastic channel models, which are developed based on actual measurements from the measurement setup described

Algorithm 7.2: TOA estimation algorithm (with *a priori* information)

Input: $\mathbf{y}, \mathcal{H}, K, \Delta, \mathbf{e}_0 = \mathbf{y}, k = 0, I_k = \{\emptyset\}, \tau_{\text{toa}}^{\max}, \tau_{\text{pld}}^{\max}$
Output: TOA estimate, $\hat{\tau}_{\text{toa}}$.
 // Search only in $\lfloor \tau_{\text{toa}}^{\max} / \Delta \rfloor$ columns of \mathcal{H}
 1 $\mathcal{H} = \mathcal{H}(:, 1 : \lfloor \tau_{\text{toa}}^{\max} / \Delta \rfloor)$
 // Bound the first path in relation to peak
 2 $\Omega = \lfloor \tau_{\text{pld}}^{\max} / \Delta \rfloor$
 3 **repeat**
 4 $t = \arg \max |\langle \mathbf{h}_i, \mathbf{e}_k \rangle|, i = 1, \dots, \lfloor \tau_{\text{toa}}^{\max} / \Delta \rfloor$
 5 **if** $k = 0$ **then** $\ell = t$;
 6 **else if** $t < \ell$ **and** $t > \ell + \Omega$ **then** $\ell = t$;
 7 $k = k + 1$
 8 $I_k = I_k \cup t$
 9 $\mathbf{e}_k = \mathbf{y} - \mathcal{H}_{I_k} \mathcal{H}_{I_k}^\dagger \mathbf{y}$
 10 **until** $k \leq K$
 11 **return** $\hat{\tau}_{\text{toa}} = \ell \Delta$

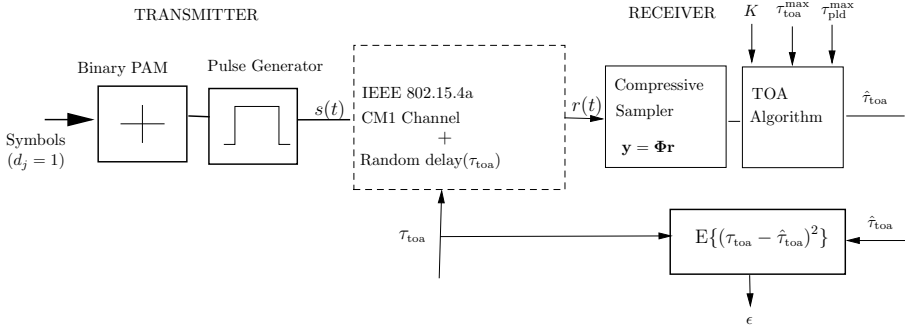


Figure 7.3: The block diagram of the simulation bed for the performance evaluation of TOA estimation algorithms.

in [MCC⁺04, Mol05] represents the practical UWB channels. Based on this channel model, a simulation bed for a single user UWB system is developed for the evaluation of the proposed TOA algorithms. The block diagram of this is as shown in the Figure 7.3. We choose $F_s = 8$ GHz, $T_f = 200$ ns, and $N_f = 1$. We used a second order Gaussian pulse of width of 1 ns as defined in [SGI08] as the transmit pulse. Thousand distinct TOA values, drawn from a uniform distribution of [0 ns – 50 ns], is employed in the simulation. The TOA modulated pulses are received using 1000, distinct realizations of IEEE 802.15.4a CM1 channel. We use the mean square error (MSE), $\epsilon = \mathbf{E}[(\tau_{\text{toa}} - \hat{\tau}_{\text{toa}})^2]$, as the metric to assess performance. Here, τ_{toa} , is the true TOA and $\hat{\tau}_{\text{toa}}$, is the estimated TOA. To give a full picture, we compare the

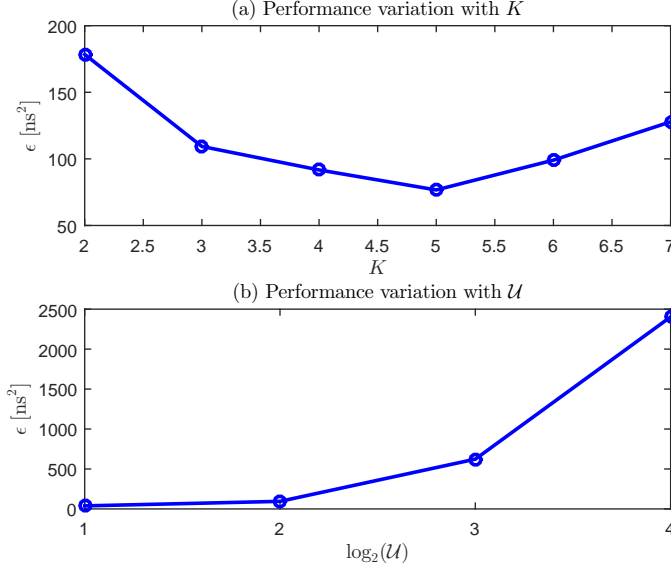


Figure 7.4: The performance of the proposed method with number of paths searched, K , and under-sampling ratio, \mathcal{U} , for a fixed SNR = 24 dB. $\mathcal{U} = N/M = 4$, and $K = 5$, is employed in (a) and (b) respectively.

performance of the proposed algorithm with the ML estimation method described in Section 7.3. The optimization described in (7.3.4) is evaluated, with $L = 10$ and $F_s = 8$ GHz.

7.7.1 Choice of K and Δ

As discussed earlier, the choice of K and Δ plays a significant role in the performance of the algorithm. If the number of paths searched, K , in the algorithm is high then there is a potential problem of picking the wrong atom (column) in the dictionary due to the noise, however, if the K , is too small then we may miss the true TOA, due to the possibility of earlier paths being weaker than the first path. Typically K can be selected by solving the optimization problem

$$\arg \min_K \mathbb{E}\{(\tau_{\text{toa}} - \hat{\tau}_{\text{toa}})^2\}, \quad (7.7.1)$$

for a fixed, \mathcal{U} , SNR. For a LOS UWB channel models like IEEE 802.15.4a model, it is difficult to arrive at the closed form equation. We measure MSE, ϵ , for various value of K as shown in Figure 7.4a, to pick optimal K . The MSE performance with under-sampling ratio, \mathcal{U} , is as shown in Figure 7.4b, as expected, the performance deteriorate with the increase in \mathcal{U} .

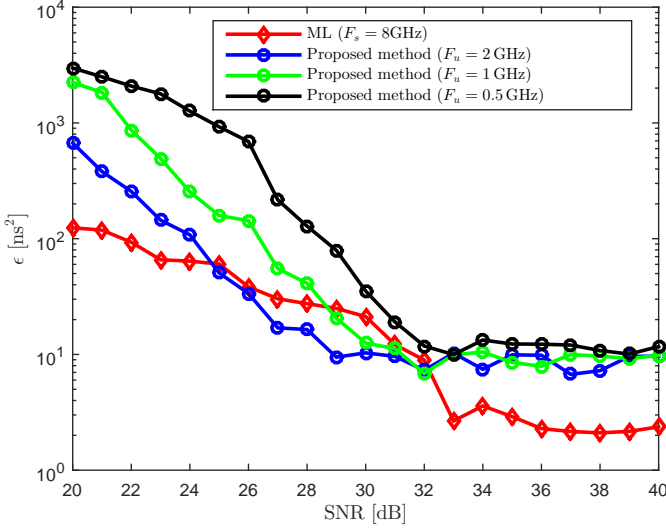


Figure 7.5: The Performance of the proposed and ML based TOA estimation algorithms. The second order Gaussian pulse of width of 1 ns is employed in the simulation and $\Delta = T_s$ is considered for the dictionary construction.

The performance of the proposed algorithm depends on the resolution, Δ , of the dictionary. This is illustrated in the Figure 7.4b. The smaller resolution yields better performance, however this requires larger dictionary size.

7.7.2 Performance with no *a priori* information

The performance of the Algorithm 7.1 is evaluated for various SNRs, under different practical settings such as dictionary size, sampling frequency, etc. We use the simulation setup as discussed in the beginning of this section. Note that Algorithm 7.1 does not assume any prior knowledge regarding the TOA range or the UWB channel.

In Figure 7.5, the performance of the algorithm is evaluated for various under-sampling ratio, \mathcal{U} . As described above second order Gaussian pulse of width 1 ns and $\Delta = T_s$ are considered for the dictionary construction. As expected, the performance degrades with the decrease of the sampling rate $F_u = F_s/\mathcal{U}$.

In Figure 7.6, the performance of the algorithm is compared with the ML estimation method described in Section 7.3 for various Δ s at under-sampling ratio, $\mathcal{U} = 4$. As described in Section 7.6.1, the larger Δ , will ease the memory requirement of the TOA system due to the reduced dictionary size, however, this will result

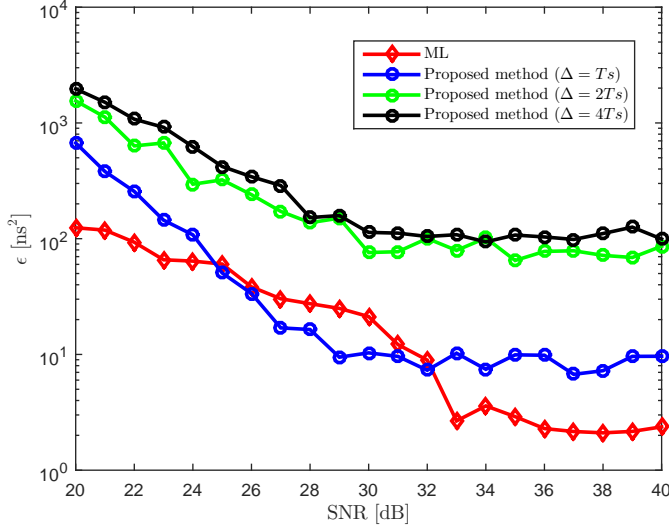


Figure 7.6: Performance of the proposed and ML based TOA estimation algorithms. The ML algorithm with sampling frequency, $F_s = 8$ GHz, and proposed method with under-sampling ratio, $\mathcal{U} = 4$, *i.e.*, $F_u = F_s/\mathcal{U} = 2$ GHz, are compared with different Δ s.

in inferior performance as shown in Figure 7.6.

The plots indicate that the proposed algorithm can yield similar performance as ML estimation, with only fraction of the sampling rate at high SNRs. Based on the environment, engineering trade offs between, Δ , \mathcal{U} , and K need to be done while employing the proposed compressive sampling TOA algorithm for TOA estimation.

7.7.3 Performance with *a priori* information

We use the same setup for the simulation as described in the beginning of this section. Notice that in our simulation setup the TOA ranges are uniformly distributed between $[0 \text{ ns} - 50 \text{ ns}]$. We also know that the channel model employed is IEEE 802.15.4a CM1 model. From Section 7.4, we notice that for this channel the probability that $\tau_{\text{pld}} > 20 \text{ ns}$ is negligible.

We evaluate the TOA estimation performance using Algorithm 7.2 with $\tau_{\text{toa}}^{\text{max}}$ set to 50 ns and $\tau_{\text{pld}}^{\text{max}}$ set to 20 ns. The variation of MSE, ϵ , with SNR is given in Figure 7.7. Notice that by exploiting the channel and geographical constraints performance of the estimation at low SNR can be significantly improved.

To summarize, we have shown that the proposed TOA estimation algorithm,

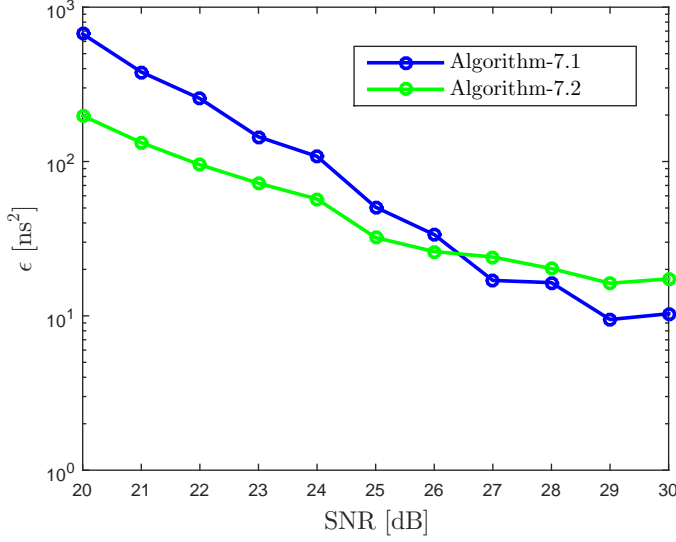


Figure 7.7: Performance comparison of Algorithm 7.2 and Algorithm 7.1 in the presence of *a priori* information such as $\tau_{\text{pld}}^{\text{max}}$ and $\tau_{\text{toa}}^{\text{max}}$. In the Algorithm 7.2, we exploited *a priori* information that $\tau_{\text{toa}}^{\text{max}} = 50$ ns and from the probability distribution of $\tau_{\text{pld}}^{\text{max}}$ for IEEE 802.15.4a channel model (refer to Figure 7.1(b)), we set $\tau_{\text{pld}}^{\text{max}} = 20$ ns.

together with the proposed compressive sampling dictionary, can achieve performance comparable to ML algorithm with only a fraction of the sampling frequency at high SNRs. TOA algorithms require a reasonable range to error ratio for it to be viable for many applications, having a slight loss of performance ($<5\%$), compared to ML estimator with a significant savings in the ADC resources make the proposed methods pertinent for many applications. At low SNRs, the performance of the proposed method can be improved by exploiting the *a priori* information.

7.8 Conclusions

A compressive sampling based TOA estimation algorithm was discussed in this chapter. The proposed algorithm along with the proposed dictionary can yield the same performance as the ML based TOA estimation with only 1/4-th the sampling rate at 25 dB SNR as shown in Figure 7.6 for IEEE 802.15.4a CM1 channel model. We also analyzed, how the performance of the algorithm varies with the choice K and \mathcal{U} . This is shown in Figure 7.4. From Figure 7.4a, we notice that there exists an

optimal K , which maximizes the performance for the choice of algorithm parameters. Impact of the sampling rate on the performance is shown in the Figure 7.5. As expected, the performance of the proposed method degrades with the decrease of the sampling rate, $F_u = F_s/\mathcal{U}$.

In certain TOA estimation scenarios, where the *a priori* information is available then the performance of the proposed algorithm can be improved. In many scenarios this can originate from the geographical constraints on the range of the target which can upper bound the TOA so that $\tau_{\text{toa}} < \tau_{\text{toa}}^{\text{max}}$, or the channel model from which we can limit the search interval by exploiting peak-to-first path lag, $\tau_{\text{pld}}^{\text{max}}$. We modified the Algorithm 7.1 to Algorithm 7.2 to exploit these *a priori* information and demonstrated the benefits through Figure 7.7.

The results are encouraging for the UWB TOA estimators working in the high SNR scenarios. The consumption of ADC resources can be significantly reduced thereby reducing the cost of the transceiver. In a typical UWB residential LOS channels, high SNRs in excess of 25 dB can be achieved by averaging over many independent received frames. The proposed TOA estimation method is sub-optimal as it does not take into consideration the frequency selective characteristics of the UWB antenna. How to address these practical issues is a topic for future research.

Compressive Sampling Based Joint PPM and TOA Estimator

Impulse radio ultra wideband (IR-UWB) signals are used in various applications which requires joint localization and communication. Due to the large bandwidth of the UWB signal, the estimation of time of arrival (TOA) and data symbols requires high sampling rates. This chapter describes a sub-Nyquist rate receiver, which can jointly estimate TOA and data symbols. We first represent the received UWB signal in a new domain in which it is sparse. Then, we design physical layer waveforms and estimation algorithms to exploit this sparsity for joint estimation of TOA and pulse position modulation (PPM) data symbols. The performance of the receiver is compared against the maximum likelihood (ML) based receiver using an IEEE 802.15.4a CM1 line of sight (LOS) UWB channel model. The proposed algorithm yields performance similar to the ML based algorithms with only a fraction of sampling rate at high SNRs (> 25 dB).

8.1 Background

There are two main constraints which preclude wide spread adaptation of IR-UWB technology. Firstly, the stringent emission regulations by the regulatory bodies like federal communications commission (FCC) [FCC02], which had a direct impact on the range and rate of the system. Secondly, wide bandwidth requirement of UWB created bottleneck in the ADC design. Availability of the mmWave spectrum without stringent emission requirements has benefited the evolution of UWB technology in the 30 – 80 GHz spectrum. This has improved the range and rate problems discussed earlier. However, large bandwidth coupled with high time and amplitude resolution requirements for ADCs still persist and pose significant challenge in the design of the digital UWB system.

Typical UWB transceiver applications, including the first responder systems discussed in [RRS⁺11], requires both data communication and ranging. The training template based methods suggested in [SGI08] coupled with maximum likelihood

(ML) estimation methods can be extended to the considered problem. However, these methods when implemented digitally require sampling rates higher than the Nyquist rate, requiring the ADCs to support sampling rates in excess of 8 GHz. This makes the cost of the transceiver prohibitively high. In this chapter, we introduce a method to jointly estimate the TOA and symbol value from the modulated received pulses, without any training pulses and also show that the requirements on RF front-end sampling rate can be significantly loosened by employing recent theories on compressive sampling, without significant loss in performance at high SNR. We present two algorithms catering to the two distinct mobility (dynamics) of the target. We compare the results with the ML estimation to demonstrate the benefits.

Reminder of this chapter is organized as follows. In Section 8.3, we briefly discuss the compressive sampling theory and present a TOA estimation technique using sub-Nyquist rate. In Section 8.4.2, we present a method for joint estimation of range and pulse position modulated (PPM) symbols for short range slowly moving (dynamic) targets. In Section, 8.4.3, we modify the signaling structure to aid joint estimation for highly dynamic targets. In Section 8.5, we discuss the numerical results of the methods proposed in a practical UWB scenario. Finally, we conclude with few key observations based on the results in Section 8.6.

8.2 System Model

We consider a single user UWB system. The signal model comprises of N_f modulated frames, having a unit energy pulse, $p(t)$, for each data symbol. The received signal is the distorted version of the transmit pulse with multipaths. The TOA is defined as the time elapsed for the first arrival path to reach the receiver from the transmitter. The received signal can be represented by,

$$\omega_{rx}(t) = \sum_{i=-\infty}^{\infty} \sum_{j=0}^{N_f-1} r_i(t - jT_f) + n(t), \quad (8.2.1)$$

where,

$$r_i(t) = \sqrt{\frac{E_b}{N_f}} \sum_{\ell=1}^P \alpha_{\ell} p'(t - \Delta s_i - \tau_{\ell}). \quad (8.2.2)$$

Each frame is of duration T_f , and the frame index is represented by j . The $s_i \in \{0, \dots, L-1\}$ denotes the i -th PPM symbol and L denotes the modulation order.

Here, E_b , is the captured energy and $\sum_{\ell=1}^P \alpha_{\ell}^2 = 1$. The gain for the ℓ -th tap is given by α_{ℓ} . $p'(t)$ is the distortion of the received pulse due to the antenna and channel effects. We consider a sufficiently longer frame duration to avoid inter-frame interference due to the delay spread of the channel. The $n(t)$ is the AWGN process with zero mean and double-sided power spectral density of $N_0/2$ ¹. Without

¹We have assumed a LOS multipath channel with resolvable multi-paths, as observed in IEEE 802.15.4a CM1 channel model.

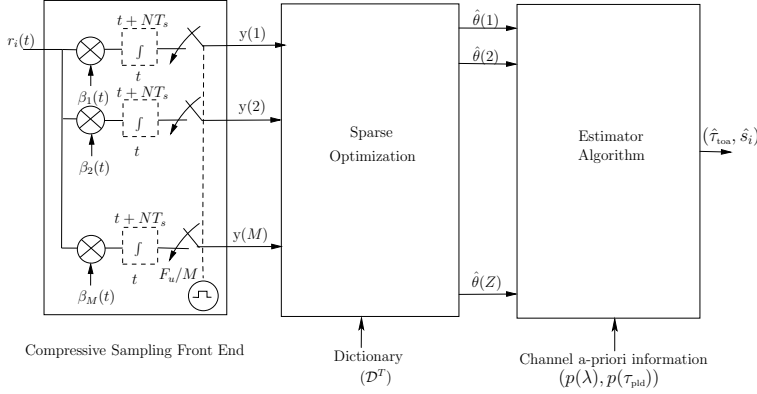


Figure 8.1: Block diagram of the compressive sampling (CS) system for TOA estimation. The $\beta_i(t)$, $i = 1, \dots, M$, denotes the continuous time i.i.d normal processes with zero mean and unit variance.

loss of generality, we consider $N_f = 1$ for the rest of the discussion.

8.3 Sub-Nyquist TOA Estimator

Consider an N -point Nyquist sampled discrete-time representation of the received UWB frame for the i -th symbol, $\mathbf{r}_i \in \mathbb{R}^N$, which is obtained by sampling the received signal, $r_i(t)$, at the Nyquist rate, F_s . Consider the signal acquisition hardware shown in the Fig. 8.1. Here, the signal is acquired at an effective sampling rate of $F_u = F_s/U$ and each ADCs in the M parallel paths of compressive sampling front-end will operate at a rate F_u/M . Where $U = N/M$ is the under-sampling ratio. A detailed review on wideband sampling schemes can be found in [NMBH13]. The acquired signal, \mathbf{y}_i , can be viewed as a projection of \mathbf{r}_i on a measurement matrix, Φ . The elements of Φ are i.i.ds drawn from a normal distribution. That is,

$$\mathbf{y} = \Phi \mathbf{r}_i, \quad (8.3.1)$$

and Φ is an $M \times N$ matrix. As shown in Figure 8.1, $\mathbf{y} \in \mathbb{R}^M$ is fed to the sparse optimization routine, which will represent \mathbf{y} in a compact form using the columns of a carefully chosen dictionary leading to a sparser signal representation from which TOA, $\hat{\tau}_{\text{toa}}$, and data symbol value, \hat{s}_i , are estimated.

8.4 Joint TOA and PPM Symbol Estimation

In this section, first, in Section 8.4.1, we design the compressive sampling dictionary. Subsequently, two main topics of this chapter, which include algorithms for jointly

estimating the $(\hat{\tau}_{\text{toa}}, \hat{s}_i)$ by utilizing the designed dictionary for varying mobility of the target nodes are discussed.

8.4.1 Dictionary construction

As shown in (8.2.1), the received multipath UWB signal constitutes a scaled and delayed versions of the transmit pulse. Since most practical indoor UWB channels have resolvable multipaths, to construct the dictionary, we choose each column of the dictionary, $\mathcal{C}^T(t, \Lambda)$, as shifted versions of the transmit pulse, that is,

$$\mathcal{C}^T(t, \Lambda) = [p_0(t), \dots, p_{Z-1}(t)], \quad (8.4.1)$$

where

$$p_\ell(t) = p(t - \Lambda\ell), \quad \ell = 0, 1, \dots, Z - 1. \quad (8.4.2)$$

The Z defines the number of atoms (columns) in the dictionary. The offset, Λ , needs to be controlled to strike a compromise between the number of atoms needed to faithfully represent the received UWB signal and the size of the dictionary. The Λ and Z are chosen such that $T_f = Z\Lambda$. Equation (8.4.2) is expressed in terms of continuous t and Λ . In practice, both these parameters are discretized such that t is sampled at a particular sampling period T_s , and Λ is a multiple of T_s . We define \mathcal{D} as uniform sampling of the dictionary, \mathcal{C} , and is of dimension $Z \times N$ as each atom $(p_\ell(t))$ in the dictionary is a vector of length N . That is

$$\mathcal{D}^T = [\mathbf{w}_0, \dots, \mathbf{w}_Z] \in \mathbb{R}^{N \times Z}, \quad (8.4.3)$$

where

$$\mathbf{w}_\ell = [\mathbf{0}_{\ell\nu}, \mathbf{w}, \mathbf{0}_{N-P-\ell\nu}]^T \in \mathbb{R}^N, \quad (8.4.4)$$

with $\ell \in [0, \dots, Z-1]$ and $\Lambda = \nu T_s$. Here, ν is an integer constant, which can be used to control the size of the dictionary. The \mathbf{w} is the sampled pulse shape used in the transmission, that is, the i -th element of the vector, \mathbf{w} , $w(i) = p(iT_s)$, $i \in 1, \dots, N_p$. We construct the holographic dictionary using the transformation $\mathcal{H} = \Phi\mathcal{D}$, which will be used later in the first multipath detection algorithm.

8.4.2 Quasi-static scenario

Consider a semi-static target, where the TOA can be assumed to be constant for the duration of a block of N_b symbols. We propose a method to demodulate the block of N_b symbols together with its associated TOA, τ_{toa} . Consider the signaling structure shown in Fig. 8.2. We propose a TOA estimator from the PPM modulated signal as follows:

$$\hat{\tau}_{\text{toa}} = \frac{1}{N_b} \sum_{i=1}^{N_b} \left(\tau_i - \frac{L-1}{2} \Delta \right), \quad (8.4.5)$$

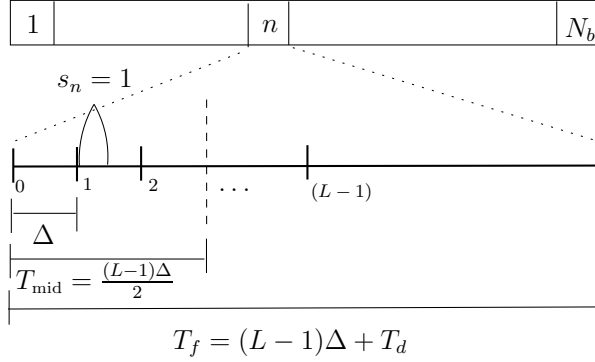


Figure 8.2: Transmit signal for the proposed Algorithm 8.1. The T_d is the delay spread of the channel and Δ is the PPM modulation index (width of the PPM-bins).

where τ_i is the first multipath for the i -th symbol. If we assume that the i -th transmit frame (refer to Fig. 8.2) contains symbol s_i , then $\tau_i = s_i\Delta + \tau_{\text{toa}}$. Therefore,

$$\hat{\tau}_{\text{toa}} = \tau_{\text{toa}} - \frac{L-1}{2}\Delta + \frac{\Delta}{N_b} \sum_{i=1}^{N_b} s_i. \quad (8.4.6)$$

In most communication systems, the all symbols are equally likely. Therefore, s_i is uniformly distributed between $[0, L-1]$. Thus,

$$\mathbb{E}(s_i) = \frac{L-1}{2}, \quad (8.4.7)$$

$$\text{Var}(s_i) = \frac{(L-1)^2}{12}. \quad (8.4.8)$$

Where $\mathbb{E}(\cdot)$ and $\text{Var}(\cdot)$ denote the mean and variance of s_i respectively. Using (8.4.7) and (8.4.8) in (8.4.6), and employing the fact that for any constant c , $\mathbb{E}(cs_i) = c\mathbb{E}(s_i)$ and $\text{Var}(cs_i) = c^2\text{Var}(s_i)$, we get,

$$\mathbb{E}(\hat{\tau}_{\text{toa}}) = \tau_{\text{toa}}, \quad (8.4.9)$$

$$\text{Var}(\hat{\tau}_{\text{toa}}) = \frac{\Delta^2(L-1)^2}{12N_b}. \quad (8.4.10)$$

Therefore, the estimator is unbiased. Also, from (8.4.6), and for large N_b , one can apply central limit theorem to show that the $\hat{\tau}_{\text{toa}}$ is Gaussian, that is $\hat{\tau}_{\text{toa}} \sim \mathcal{N}\left(\tau_{\text{toa}}, \frac{\Delta^2(L-1)^2}{12N_b}\right)$.

Algorithm 8.1: TOA estimation algorithm

Input: $\mathbf{Y}, \mathcal{H}, K, \Lambda, N_b, \Delta$
Output: TOA estimate, $\hat{\tau}_{\text{toa}}$, demodulated symbols, $\hat{\mathbf{d}}$.

```

1 for  $i \leftarrow 1$  to  $N_b$  do
2    $\mathbf{e}_0 \leftarrow \mathbf{Y}(:, i), \mathbf{y} \leftarrow \mathbf{Y}(:, i), k \leftarrow 0, I_k \leftarrow \{\emptyset\}$ 
3   repeat
4      $t \leftarrow \arg \max_p |\langle \mathbf{h}_p, \mathbf{e}_k \rangle|, p = 1, \dots, Z$ 
5     if  $k == 0$  then  $\ell \leftarrow t$ ;
6     else if  $t < \ell$  then  $\ell \leftarrow t$ ;
7      $k \leftarrow k + 1$ 
8      $I_k \leftarrow I_k \cup t$ 
9      $\mathbf{e}_k \leftarrow \mathbf{y} - \mathcal{H}_{I_k} \mathcal{H}_{I_k}^\dagger \mathbf{y}$ 
10  until  $k \leq K$ 
11   $\tau(i) \leftarrow \ell \Lambda$ 
12   $\eta \leftarrow \eta + (\tau(i) - \frac{L-1}{2} \Delta)$ 
13  $\hat{\tau}_{\text{toa}} \leftarrow \eta / N_b, \hat{\mathbf{d}} = (\boldsymbol{\tau} - \hat{\tau}_{\text{toa}}) / \Delta$ 
14 return  $\hat{\tau}_{\text{toa}}, \hat{\mathbf{d}}$ 

```

For a consistent estimator the distributions of the estimates become more and more concentrated near the true value of the parameter being estimated as the number of data points (N_b) increases. That is,

$$\lim_{N_b \rightarrow \infty} \hat{\tau}_{\text{toa}} = \tau_{\text{toa}}. \quad (8.4.11)$$

This is true for the proposed estimator of (8.4.5) because the variance of the Gaussian estimates, $\left(\hat{\tau}_{\text{toa}} \sim \mathcal{N} \left(\tau_{\text{toa}}, \frac{\Delta^2 (L-1)^2}{12 N_b} \right) \right)$, tends to zero as N_b tends to infinity. Symbols are demodulated by removing the TOA bias ($\hat{\tau}_{\text{toa}}$), that is,

$$\hat{s}_i = (\tau_i - \hat{\tau}_{\text{toa}}) / \Delta. \quad (8.4.12)$$

The joint demodulation and TOA estimation algorithm is as shown in Algorithm 8.1. Input to the algorithm is the matrix, \mathbf{Y} , with its i -th column $\mathbf{Y}(:, i)$, $i \in [1, \dots, N_b]$ having a sub-Nyquist samples corresponding to the i -th frame², Holographic dictionary, \mathcal{H} , with its columns $\mathbf{h}_p, p = 1, \dots, Z$, and the parameter, K , which defines the number of paths to be searched. The inner loop of the Algorithm 8.1 tries to identify the lowest indexed support from the set of K significant energy columns of the holographic dictionary. The first multipaths of the received frames are collected in, $\boldsymbol{\tau}$ (refer to line 11). The estimated TOA, $\hat{\tau}_{\text{toa}}$, for the block of N_b symbols is obtained by averaging the difference between T_{mid} and the first multipath, $\boldsymbol{\tau}$. The demodulated symbols are computed after removing the bias (τ_{toa})

²Frame and symbol are interchangeably used since $N_f = 1$ is considered. The algorithm assumes LOS resolvable channel, as observed in 802.15.4a channel for indoor LOS environment (CM1).

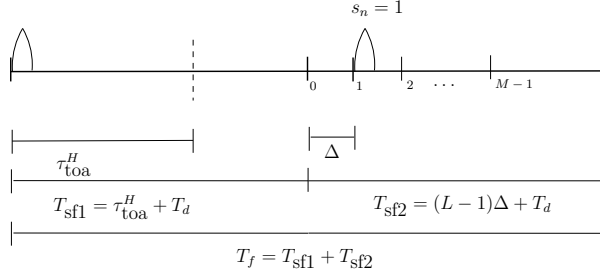


Figure 8.3: Transmit signal for the proposed Algorithm 8.2. The T_d is the delay spread of the channel, Δ is the PPM modulation index (width of the PPM-bins) and $N_b = 1$ is considered.

Algorithm 8.2: TOA estimation algorithm

Input: $\mathbf{Y}, \mathcal{H}, K, \Lambda, N_b, \Delta$

Output: TOA estimate, $\hat{\tau}_{\text{toa}}$, demodulated symbols, $\hat{\mathbf{d}}$.

```

1 for  $i \leftarrow 1$  to  $N_b + 1$  do
2    $\mathbf{e}_0 \leftarrow \mathbf{Y}(:, i), \mathbf{y} \leftarrow \mathbf{Y}(:, i), k \leftarrow 0, I_k \leftarrow \{\emptyset\}$ 
3   repeat
4      $t \leftarrow \arg \max_p |\langle \mathbf{h}_p, \mathbf{e}_k \rangle|, p = 1, \dots, Z$ 
5     if  $k == 0$  then  $\ell \leftarrow t$ ;
6     else if  $t < \ell$  then  $\ell \leftarrow t$ ;
7      $k \leftarrow k + 1$ 
8      $I_k \leftarrow I_k \cup t$ 
9      $\mathbf{e}_k \leftarrow \mathbf{y} - \mathcal{H}_{I_k} \mathcal{H}_{I_k}^\dagger \mathbf{y}$ 
10  until  $k \leq K$ 
11   $\tau(i) \leftarrow \ell \Lambda$ 
12   $\hat{\tau}_{\text{toa}} \leftarrow \tau(1), \hat{\mathbf{d}} = (\tau(2 : \text{end}) - \hat{\tau}_{\text{toa}}) / \Delta$ 
13 return  $\hat{\tau}_{\text{toa}}, \hat{\mathbf{d}}$ 
```

as shown in line 13. The performance of the proposed algorithm is studied in Section 8.5. The choice of K and Λ plays a significant role in the performance of the algorithm. If the number of paths searched, K , in the algorithm is high then there is a potential problem of picking the wrong atom (column) in the dictionary due to the noise, however, if the K is too small then we may miss the true first multipath, due to the possibility of it being weaker than the estimated first path. It is shown in [YH16] that $K = 5$ provides an optimal performance in terms of mean square error (MSE) for first multipath detection schemes at high SNR scenarios ($\text{SNR} > 25$ dB).

8.4.3 Dynamic scenario

If the nodes are highly dynamic in nature then TOA values may vary rapidly and thus, N_b need to be small for the above transmit scheme. Therefore averaging the difference between first multipath to the middle of the frame, T_{mid} , with a small N_b will not yield the true TOA. Thus, we propose an alternate signaling structure, where this can be controlled effectively. Here, we start the frame with an unmodulated frame, which can be used for TOA estimation, followed by N_b symbols. The N_b can be chosen based on the rate at which the TOA of the target node needs to be estimated³. An illustration of this signaling with $N_b = 1$ is shown in Figure 8.3. The unmodulated frame is represented by T_{sf1} , and the data symbol carrying frame is represented by T_{sf2} . The signaling structure is similar to dirty template structure proposed in [L. 04].

The sub-Nyquist domain estimation method for TOA and the data symbols are shown in the Algorithm 8.2. The inner loop computes the first multipath from the received frames. From the first unmodulated frame TOA, $\hat{\tau}_{\text{toa}}$, is estimated, which is used to demodulate the subsequent frames as given in line 12 of Algorithm 8.2.

8.5 Numerical Results

The IEEE 802.15.4a UWB stochastic channel models, which are developed based on actual measurements from the measurement setup described in [MCC⁺04] represent most practical UWB channels. In the numerical study, we employ IEEE 802.15.4a CM1 channel model for indoor LOS channel, with the sampling rate, $F_s = 8$ GHz, and a second order Gaussian pulse of width of 1 ns as the transmit pulse.

8.5.1 Quasi-static scenario

We study the performance of the Algorithm 8.1, with $T_f = 200$ ns, $L = 4$, and $\Delta = 50$ ns. We use the symbol error rate (SER) and MSE ($\epsilon = \mathbf{E}[(\tau_{\text{toa}} - \hat{\tau}_{\text{toa}})^2]$), to assess symbol and TOA estimation performance. The 100,000 random symbols are PPM modulated with 100 random TOA values, drawn from a uniform distribution of $[0 \text{ ns} - 100 \text{ ns}]$, with each block having $N_b = 1000$ symbols, as explained in Section 8.4.2 is used in the simulation. The SER at various acquisition rates, $F_u = F_s/\mathcal{U}$, is studied. We compare the results with the ML estimator described in [FDMW06, WS02]. Figure 8.4, shows the variation of the TOA and SER at various SNRs for the under-sampling ratio $\mathcal{U} = 4, 8$ and ML based estimation at 8 GHz. From Figure 8.4, we notice that the performance of a compressive sampled receiver above 25 dB is manageable for most applications, and thus provides a good trade-off with respect to sampling frequency.

³We assume that TOA does not vary during N_b symbols.

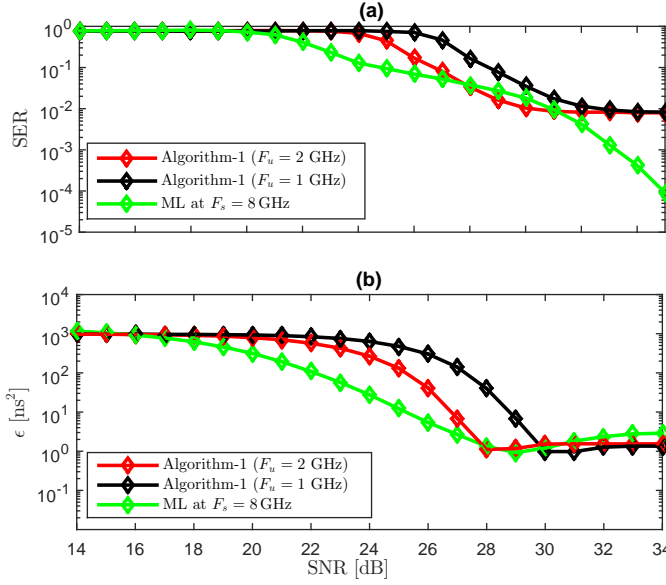


Figure 8.4: The performance of Algorithm 8.1 and ML method at various SNRs. For ML estimation, sampling rate of $F_s = 8$ GHz is employed. For compressive sampling algorithm sampling rates of $F_u = 2$ GHz, and 1 GHz are employed. The $\Lambda = T_s$.

8.5.2 Dynamic scenario

We study the performance of the Algorithm 8.2, with $T_f = 400$ ns, $L = 4$ and $N_b = 1$ ($T_{\text{sfl1}} = 200$ ns, $T_{\text{sfl2}} = 200$ ns) as described in Section 8.4.3. The 100,000 frames each having random TOA and PPM symbols as described in Section 8.4.3 are used in the simulations. Each frame is passed through a randomly chosen IEEE 802.15.4a CM1 channel from the set of 1000 distinct channels. The symbol error rate at various acquisition rates and dictionary constructions are shown in Figure 8.5(a) and Figure 8.5(b).

From Figure 8.5, the performance of Algorithm 8.2 at high SNR is one to two orders of magnitude worse than ML. From Figure 5(b), we notice that performance at high SNRs deteriorates rapidly with the dictionary parameter Δ . The performance benefit of Algorithm 8.2 with 1/4 of the sampling rate ($\mathcal{U} = 4$) and $\Delta = T_s$, provides 99% accurate symbol detection for SNRs higher than 30 dB. For many applications, this is an acceptable SER and the benefits of reduced sampling rate by a factor of 4 outweigh the improvement in the SNR by using ML at higher sampling rate.

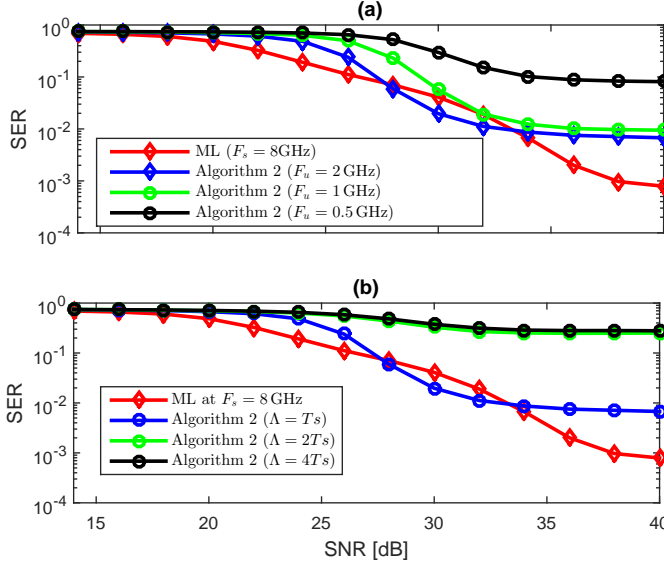


Figure 8.5: The performance of Algorithm 8.2 and ML method at various SNRs. For ML estimation, the sampling rate of $F_s = 8$ GHz is employed.

8.6 Conclusions

Data communication and ranging are the two main applications of the IR-UWB systems. In many IR-UWB transceivers this can be accomplished jointly using the proposed signaling structure. Due to the wide bandwidth of the IR-UWB signal, ADCs employed in the UWB transceiver should support high sampling rates. This issue can be resolved by using compressive sampling design with a careful choice of dictionary, signaling structure and estimation algorithms. We show that a performance degradation for 90% accurate symbol estimation is about 2 dB from the ML for an undersampling ratio of $\mathcal{U} = 4$, however, with the following benefits.

- Lower cost of transceiver due to the cheaper ADC as the cost of the ADC increases with the sampling rate.
- Lower power consumption as the power increases linearly with the sampling rate for the pipelined and sigma-delta ADCs [BKKC14].

The proposed algorithms also provide trade-off between sampling rate, memory (dictionary size) and performance. In contrast to the proposed methods, the ML based estimation performance monotonically improves with the SNR. However, at high SNRs, the benefit of lower sampling rate outweighs the loss of performance.

Summary and Future Research

Ultra-wideband (UWB) technology has an unprecedented opportunity to impact future communication systems. Large bandwidth enables high precision localization and robust communication systems. The propagation physics of UWB can aid several applications which have harsh propagation environments such as first responder systems, search-and-rescue, and mining. There are many GPS deficient environments such as shopping malls, building, tunnels, etc., which require high precision localization. UWB is an ideal technology for localization as it has unique spectral characteristics coupled with a robust indoor propagation environment. The possibility of efficient implementation of UWB transceivers using analog energy detectors has made UWB an important contender for low-complexity, low-power and low-cost communication and localization systems.

In this thesis we have focused on the physical layer and signal processing aspects of UWB signals. While there are several research contributions in this area, there are also many aspects which are still not completely understood. In the discussions from Chapter 1 to Chapter 8, we have tried to highlight these gaps and have provided solutions to some of them. Furthermore, there are several aspects which are not addressed in this thesis. We have summarized them in Section 9.2. Below we summarize the main conclusions from the results discussed in the previous chapters.

9.1 Conclusions

The main conclusion from Chapter 3, is that by designing the UWB signaling based on the constraints of the underlying low-cost hardware, one can achieve high data rate for short range communication. We proposed two signaling schemes which are variant of PPM signaling for IR UWB communication. The results of the proposed signaling methods indicate the possibility of achieving a higher bitrate in excess of 150 Mbps with low probability of error in detection, as suggested by the performance curves using the parameters from our transceiver hardware (discussed in Chapter 1). One of the signaling schemes called with-memory signaling required memory and more complexity in the modulator and demodulators. However it can increase the

range fourfolds compared to no-memory signaling. We also derived the theoretical closed form expression for hard decision demodulators for the proposed signaling schemes. We also showed that with-memory signaling can improve the detector performance by approximately 1 dB at 10^{-2} SER compared to no-memory signaling.

Many communication systems require both localization and communication. The synergy between communication and localization can benefit each other. In Chapter 4, we discussed a methodology for utilizing the range information to arrive at the transmission schedules for accessing the shared common channel in a fully connected sensor network. We posed this as an optimization problem, the solution of which is NP-hard. We proposed three sub-optimal algorithms CA, TSP and IPA for solving them. The results indicate that throughput can be increased on average by **3 – 10** times for typical network configurations compared to traditional methods. The complexity analysis for the proposed algorithms is also analyzed, which indicates that the proposed methods are practically viable.

The main conclusion from Chapter 5 is the fact that when the multiple detector outputs from a hardware platform are available, then fusing their results can yield better performance in hypothesis testing than relying on a single detector output. For example, comparing the performance of the energy detector alone with the MAP fusion rule for multiple detectors indicates that a gain of 4 dB in terms of signal to noise ratio (SNR) can be achieved for probability of detection greater than 95% with low probability of error ($< 5\%$).

Estimating TOA with good accuracy is highly important for localization. Wide bandwidth of UWB makes the cost of the digital transceivers prohibitively high. Energy detectors operating at sub-Nyquist rate is an interesting alternative as it can be designed using cost effective analog circuits and is power efficient. However, it lacks the precision in range measurements. In Chapter 6, we propose a multi-channel receiver with each channel having a low-cost energy detector operating at a sub-Nyquist rate. We showed that the number of energy detector channels needed to meet the digital matched filters performance is high at low SNRs and reduces as SNR increases, and finally converges to 4 as SNR increases asymptotically. We showed that a Kalman filter with suitable choice of state and measurement equations can perform the dual task of tracking the TOA as well as fusing the multiple energy detector outputs. Another interesting result is that the net power consumed by the multi channel receiver is lower than its digital counterpart.

Chapter 7 and Chapter 8 a compressive sampling technique to overcome the ADC issue due to the wide bandwidth of UWB signals. In Chapter 7, a new acquisition front end is proposed, using which the sampling rate of the ADC can be significantly reduced. Two algorithms are proposed in this chapter which can operate on the acquired sub-Nyquist samples to estimate the TOA. Results indicate that the performance can match the ML based TOA estimation with only 1/4-th the sampling rate. Also, we noticed that by using the *a priori* information from channel and geography one can improve the performance at low SNRs.

Chapter 8 extended the idea of Chapter 7 towards joint estimation of TOA and PPM symbols. Here two signaling methods based on the dynamicity of the target

are proposed. From the results, one can notice performance degradation for 90% accurate symbol estimation is approximately 2 dB from the ML based estimation, however with a significant saving in ADC resources.

9.2 Future Research

In this section, we will highlight the aspects that are relevant to future research directions. In Chapter 3, a hardware aware signaling is proposed using constraints from the low cost in-house hardware. Extending the work towards other hardware platforms and evaluating the realtime performance could be a topic for further study. In Chapter 4, utilizing the range information for the all-to-all communication assumes a fully connected network. How to extend the ideas presented in this chapter to a partially connected network is still an open problem. The impact of the non-idealities pertaining to synchronization and timing estimation on the methods proposed in Chapter 5 and Chapter 6 are of interest. Also, in Chapter 6, the Kalman filter performance can be further improved by using not only the dynamic motion model, but also utilizing the maps on which the target is moving.

It is not possible to design an antenna for UWB with uniform gain across its wide bandwidth. The effect of this renders the proposed algorithms discussed in Chapter 7 and Chapter 8 sub-optimal. This is because the compressive sampling dictionary design in these chapters does not take into account the effect of frequency selective characteristics of the UWB antenna. In Chapter 7, a new acquisition front end is proposed, using which the sampling rate of the ADC can be significantly reduced. A circuit implementation of this front end could be an interesting problem.

In this thesis, the TOA estimation methods are designed for a LOS UWB channel. The performance of the proposed methods are evaluated using the multi-path propagation models proposed in the IEEE 802.15.4a CM1 channel model. However, extending the methods to the NLOS scenario is a topic for further research. Also, the performance of proposed schemes on different channel models that may arise due to the operation in mmWave band needs further investigation. All the algorithms and methods are evaluated in simulations. It would be of interest to see how these algorithms perform in real environments using UWB hardware. The ideas discussed in this thesis are applicable to the future evolution of the flexible UWB hardware platform discussed in Chapter 1. This platform can be used for joint ranging and communication applications. The platform has a digital processing section comprising an FPGA, where the proposed techniques of this thesis can be implemented. Even though in this thesis the applicability of the techniques are demonstrated in simulation, the results provide an early insight into the achievable performance.

Based on the above discussion, we foresee broadly three research directions which hold much promise.

UWB circuit design: Accurate localization with a high refresh rate are key for practical UWB systems. Many application scenarios can be opened provided the

accuracy levels are within a few centimeters and refresh rates are within a few milliseconds. This means a transceiver circuit should be able to generate pulses of a few nanoseconds and make TOA measurements which are accurate up to a few nanoseconds. The footprint of the circuit should be small enough to ensure portability.

Signal Processing: Most of the UWB research in signal processing assumes that the signal is in the 0–10 GHz band, However, availability of an unlicensed spectrum with relaxed regulatory restrictions in mmWave band has brought renewed impetus to UWB technology. The signal processing methods for UWB transceivers that operate in this band are still largely unexplored.

Medium Access Control: UWB has significant potential to be one possible candidate for the 5G Internet-of-things (IOT). These networks are low-cost, low-power, and they do not have a planned deployment. The problem of providing medium access in a new type of network utilizing properties such as location, failure detection and reconfiguration, among others, has high research potential.

Bibliography

- [ADGC11] A. De Angelis, M. Dionigi, R. Giglietti, and P. Carbone. Experimental Comparison of Low-Cost Sub-Nanosecond Pulse Generators. *Instrumentation and Measurement, IEEE Transactions on*, 60(1):310–318, Jan 2011.
- [ADH13] A. De Angelis, S. Dwivedi, and P. Händel. Characterization of a Flexible UWB Sensor for Indoor Localization. *Instrumentation and Measurement, IEEE Transactions on*, 62(5):905–913, 2013.
- [ADM⁺09] A. De Angelis, M. Dionigi, A. Moschitta, R. Giglietti, and P. Carbone. Characterization and Modeling of an Experimental UWB Pulse-Based Distance Measurement System. *Instrumentation and Measurement, IEEE Transactions on*, 58(5):1479–1486, May 2009.
- [AIS⁺14] P. Agyapong, M. Iwamura, D. Staehle, W. Kiess, and A. Benjebbour. Design considerations for a 5G network architecture. *Communications Magazine, IEEE*, 52(11):65–75, Nov. 2014.
- [All16] WiMedia Alliance. <http://www.wimedia.org/>, 2016.
- [APM04] Ian F. Akyildiz, Dario Pompili, and Tommaso Melodia. Challenges for Efficient Communication in Underwater Acoustic Sensor Networks. *ACM SIGBED Review - Special issue on embedded sensor networks and wireless computing*, 1(2):3–8, July 2004.
- [AR98] Mark Anderson and Andrew Robbins. Formation flight as a cooperative game. In *Guidance, Navigation, and Control and Co-located Conferences*, pages 244–250. American Institute of Aeronautics and Astronautics, August 1998.
- [AR09] Bazil Taha Ahmed and Miguel Calvo Ramon. Coexistence between UWB and other communication systems - tutorial review. *International Journal of Ultra Wideband Communications and Systems*, 1(1):67–80, 2009.
- [BA02] A. Bharathidasan and V. Anand. Sensor Networks: An Overview. Technical report, Dept. of Computer Science, University of California at Davis, 2002.

- [BAN14] T. Ballal and T. Y. Al-Naffouri. Low-sampling-rate ultra-wideband digital receiver using equivalent-time sampling. In *Ultra-WideBand (ICUWB), 2014 IEEE International Conference on*, pages 321–326, Sept 2014.
- [BBD⁺10] Anuj Batra, Jaiganesh Balakrishnan, Anand G. Dabak, Ranjit Gharpurey, Paul Fontaine, and Heng Lin. Time-frequency interleaved orthogonal frequency division multiplexing ultra wide band physical layer, 2010.
- [BKKC14] B. Bakaloglu, S. Kiaei, H. Kim, and K. Chandrashekar. *Design of Power, Dynamic Range, Bandwidth and Noise Scalable ADCs*, chapter 2, pages 29–81. Springer Berlin Heidelberg, Berlin, Heidelberg, 2014.
- [BKM⁺06] M.G. Di Benedetto, T Kaiser, A.F. Molisch, I Oppermann, C. Politano, and D.Porcino. *Ultra-wideband Communication Systems: A Comprehensive Overview*. Hindawi Publishing Corporation, New York, 2006.
- [BLW⁺03] R. Blazquez, F.S. Lee, D.D. Wentzloff, P.P. Newaskar, J.D. Powell, and A.P. Chandrakasan. Digital architecture for an ultra-wideband radio receiver. In *Vehicular Technology Conference, 2003. VTC 2003-Fall. 2003 IEEE 58th*, volume 2, pages 1303–1307 Vol.2, Oct 2003.
- [BP00] P. Bahl and V.N. Padmanabhan. Radar: an in-building rf-based user location and tracking system. In *INFOCOM 2000. Nineteenth Annual Joint Conference of the IEEE Computer and Communications Societies. Proceedings. IEEE*, volume 2, pages 775–784, 2000.
- [BT97] Dimitris Bertsimas and Johnn Tsitsiklis. *Introduction to Linear Optimization*. Athena Scientific, 1st edition, 1997.
- [BV04] S. Boyd and L. Vandenberghe. *Convex Optimization*. Cambridge University Press, New York, NY, USA, 2004.
- [CGC10] Pedro Cruz, Hugo Gomes, and Nuno Carvalho. *Advanced Microwave and Millimeter Wave Technologies Semiconductor Devices Circuits and Systems*. InTech Publishers, 2010.
- [CMR15] D. Ciuonzo, A. De Maio., and P.S. Rossi. A Systematic Framework for Composite Hypothesis Testing of Independent Bernoulli Trials. *Signal Processing Letters, IEEE*, 22(9):1249–1253, Sept 2015.
- [Com16a] BeSpoon Company. <http://www.bespoon.com/>, 2016.
- [Com16b] Decawave Company. <http://www.decawave.com/>, 2016.

- [Com16c] Timedomain Company. <http://www.timedomain.com/>, 2016.
- [Com16d] Ubisense Company. <http://www.ubisense.net/>, 2016.
- [Com16e] Zebra Company. <http://www.zebra.com/>, 2016.
- [Coo12] Charles Cook. *Radar signals: An introduction to theory and application*. Elsevier, 2012.
- [Cot14] S.L. Cotton. A Statistical Model for Shadowed Body-Centric Communications Channels: Theory and Validation. *Antennas and Propagation, IEEE Transactions on*, 62(3):1416–1424, March 2014.
- [CR14] D. Ciuonzo and P. S. Rossi. Decision Fusion With Unknown Sensor Detection Probability. *Signal Processing Letters, IEEE*, 21(2):208–212, Feb 2014.
- [CRM⁺05] P. Cheong, A. Rabbachin, J. Montillet, Kegen Yu, and I. Oppermann. Synchronization, TOA and position estimation for low-complexity LDR UWB devices. In *Ultra-Wideband, 2005. ICU 2005. 2005 IEEE International Conference on*, pages 480–484, Sept 2005.
- [CRT06] E.J. Candes, J. Romberg, and T. Tao. Robust uncertainty principles: exact signal reconstruction from highly incomplete frequency information. *Information Theory, IEEE Transactions on*, 52(2):489–509, Feb 2006.
- [CSB14] R. Chavez-Santiago and I. Balasingham. Ultrawideband Signals in Medicine [Life Sciences]. *IEEE Signal Processing Magazine*, 31(6):130–136, Nov 2014.
- [CW08] E.J. Candes and M.B. Wakin. An Introduction To Compressive Sampling. *Signal Processing Magazine, IEEE*, 25(2):21–30, March 2008.
- [DAH12] S. Dwivedi, A. De Angelis, and P. Händel. Scheduled uwb pulse transmissions for cooperative localization. In *2012 IEEE International Conference on Ultra-Wideband*, pages 6–10, Sept 2012.
- [DAZH15] S. Dwivedi, A. De Angelis, D. Zachariah, and P. Händel. Joint Ranging and Clock Parameter Estimation by Wireless Round Trip Time Measurements. *Selected Areas in Communications, IEEE Journal on*, 33(11):2379–2390, 2015.
- [DCW06] D. Dardari, Chia-Chin Chong, and M.Z. Win. Analysis of threshold-based TOA estimators in UWB channels. In *14th European Signal Processing Conference (EUSIPCO 2006), Florence, Italy,, 2006*.

- [DCW08] D. Dardari, Chia-Chin Chong, and M.Z. Win. Threshold-Based Time-of-Arrival Estimators in UWB Dense Multipath Channels. *Communications, IEEE Transactions on*, 56(8):1366–1378, Aug. 2008.
- [DFM94] L. Dumont, M. Fattouche, and G. Morrison. Super-resolution of multipath channels in a spread spectrum location system. *Electronics Letters*, 30(19):1583–1584, Sep 1994.
- [Don06] D.L. Donoho. Compressed sensing. *Information Theory, IEEE Transactions on*, 52(4):1289–1306, April 2006.
- [DW1] DW1000. - *DecaWave's Precise Indoor Location and Communication Chip*, [online]. Available: <http://www.decawave.com/>.
- [DZAH13] S. Dwivedi, D. Zachariah, A. De Angelis, and P. Händel. Cooperative Decentralized Localization Using Scheduled Wireless Transmissions. *Communications Letters, IEEE*, 17(6):1240–1243, June 2013.
- [EGE02a] Jeremy Elson, Lewis Girod, and Deborah Estrin. Fine-grained Network Time Synchronization Using Reference Broadcasts. *SIGOPS Oper. Syst. Rev.*, 36(SI):147–163, December 2002.
- [EGE02b] Jeremy Elson, Lewis Girod, and Deborah Estrin. Fine-grained network time synchronization using reference broadcasts. *SIGOPS Oper. Syst. Rev.*, 36(SI):147–163, December 2002.
- [ER15] Ericsson Mobility Report: On the pulse of the Networked Society. <https://www.ericsson.com/res/docs/2015/mobility-report/ericsson-mobility-report-nov-2015.pdf>, Nov 2015.
- [FCC02] First report and order, revision of part 15 of the commission's rules regarding ultra-wideband transmission systems. Technical report, FCC, Washington-DC, ET Docket 98-153, 2002.
- [FDMW06] Chiara Falsi, Davide Dardari, Lorenzo Mucchi, and Moe Z. Win. Time of Arrival Estimation for UWB Localizers in Realistic Environments. *EURASIP J. Appl. Signal Process.*, 2006:152–152, January 2006.
- [FKO⁺] R Fisher, R Kohno, H Ogawa, H Zhang, K Takizawa, M Mc Laughlin, and M . Welborn. Ds-ubw physical layer submission.
- [FZTS11] Federico Ferrari, Marco Zimmerling, Lothar Thiele, and Olga Saukh. Efficient network flooding and time synchronization with glossy. pages 73–84. IEEE, 2011.
- [GA03] I. Guvenc and H. Arslan. Performance evaluation of UWB systems in the presence of timing jitter. In *Ultra Wideband Systems and Technologies, 2003 IEEE Conference on*, pages 136–141, Nov 2003.

- [GKS03] Saurabh Ganeriwal, Ram Kumar, and Mani B. Srivastava. Timing-sync Protocol for Sensor Networks. In *Proceedings of the 1st International Conference on Embedded Networked Sensor Systems*, SenSys '03, pages 138–149, New York, NY, USA, 2003. ACM.
- [GMH⁺09] J. Goodman, B. Miller, M. Herman, G. Raz, and J. Jackson. Polyphase Nonlinear Equalization of Time-Interleaved Analog-to-Digital Converters. *IEEE Journal of Selected Topics in Signal Processing*, 3(3):362–373, June 2009.
- [GMHK02] Mohammad Ghavami, Lachlan B. Michael, Shinichiro Haruyama, and Ryuji Kohno. A novel UWB pulse shape modulation system. *Wireless Personal Communications*, 23:105–120, 2002. 10.1023/A:1020953424161.
- [GMPK07] S. Gezici, A.F. Molisch, H.V. Poor, and Hisashi Kobayashi. The Trade-off Between Processing Gains of an Impulse Radio UWB System in the Presence of Timing Jitter. *Communications, IEEE Transactions on*, 55(8):1504–1515, Aug 2007.
- [GQMT07] Nan Guo, Robert C Qiu, Shaomin S Mo, and Kazuaki Takahashi. 60-ghz millimeter-wave radio: Principle, technology, and new results. *EURASIP Journal on Wireless Communications and Networking*, 2007:068253(1):1–8, 2007.
- [GS05] I. Guvenc and Z. Sahinoglu. Threshold-based TOA estimation for impulse radio UWB systems. In *Ultra-Wideband, 2005. ICU 2005. 2005 IEEE International Conference on*, pages 420–425, Sept 2005.
- [GSO06] I. Guvenc, Z. Sahinoglu, and P.V. Orlik. TOA estimation for IR-UWB systems with different transceiver types. *Microwave Theory and Techniques, IEEE Transactions on*, 54(4):1876–1886, June 2006.
- [GTG⁺05] S. Gezici, Zhi Tian, G.B. Giannakis, Hisashi Kobayashi, A.F. Molisch, H.V. Poor, and Z. Sahinoglu. Localization via Ultra-Wideband Radios: A look at positioning aspects for future sensor networks. *Signal Processing Magazine, IEEE*, 22(4):70–84, July 2005.
- [Gwa16] *Broadband Omnidirectional Antenna - Elite-2460*, [online]. Available: <http://www.greenwavescientific.com/>, 2016.
- [Hel00] K. Helsgaun. An effective implementation of the Lin–Kernighan traveling salesman heuristic. *European Journal of Operational Research*, 126(1):106–130, 2000.
- [HHK05] C. Hsu, F. Hsu, and J. Kuo. Microstrip bandpass filters for Ultra-Wideband (UWB) wireless communications. In *Microwave Symposium Digest, 2005 IEEE MTT-S International*, pages 1–4, June 2005.

- [HHKK04] Jason Hill, Mike Horton, Ralph Kling, and Lakshman Krishnamurthy. The platforms enabling wireless sensor networks. *Commun. ACM*, 47(6):41–46, June 2004.
- [HNT13] H. Hayashi, M. Nagahara, and T. Tanaka. A User’s Guide to Compressed Sensing for Communications Systems. (*IEICE Trans. on Communications*, E96-B(3):685–712, Mar 2013.
- [HT02] R. Hoor and H. Tomlinson. Delay-hopped transmitted-reference RF communications. In *Ultra Wideband Systems and Technologies, 2002. Digest of Papers. 2002 IEEE Conference on*, pages 265–269, 2002.
- [IA04] H. Ishida and K. Araki. A design of tunable UWB filters. In *Ultra Wideband Systems, 2004. Joint with Conference on Ultrawideband Systems and Technologies. Joint UWBST IWUWBS. 2004 International Workshop on*, pages 424–428, May 2004.
- [IEE07] IEEE. 802.15.4: Wireless Medium Access Control (MAC) and Physical Layer (PHY) Specifications for Low-Rate Wireless PANs. Technical report, IEEE P802.15.4a-2007, (Amendment 1) Std., 2007.
- [IEE09] IEEE. 802.15.3c Millimeter Wave Alternative PHY. Technical report, IEEE 802.15.3c-2009 Std, 2009.
- [JH00] Roy Want Jeffrey Hightower, Gaetano Borriello. Spoton: An indoor 3d location sensing technology based on rf signal strength. Technical report, UW CSE Technical Report, 2000.
- [Joh82] D.S. Johnson. The NP-completeness column: An ongoing guide . *Journal of Algorithms*, 3(2):182 – 195, 1982.
- [JV02] E. R. Jativa and J. Vidal. Coarse first arriving path detection for subscriber location in mobile communication systems. In *Signal Processing Conference, 2002 11th European*, pages 1–4, Sept 2002.
- [Kay93] S.M. Kay. *Fundamentals of Statistical Signal Processing: Estimation Theory*. Fundamentals of Statistical Signal Processing. Prentice-Hall, 1993.
- [Kay98] S.M. Kay. *Fundamentals of Statistical Signal Processing: Detection theory*. Prentice Hall Signal Processing Series. Prentice-Hall PTR, 1998.
- [KLO10] Fabian Kuhn, Nancy Lynch, and Rotem Oshman. Distributed Computation in Dynamic Networks. In *Proceedings of the Forty-second ACM Symposium on Theory of Computing*, STOC ’10, pages 513–522, New York, NY, USA, 2010. ACM.

- [KMH11] W. Kleunen, N. Meratnia, and P.J.M. Havinga. A Set of Simplified Scheduling Constraints for Underwater Acoustic MAC Scheduling. In *Advanced Information Networking and Applications (WAINA), 2011 IEEE Workshops of International Conference on*, pages 902–907, March 2011.
- [KMKK06] N.V. Kokkalis, P.T. Mathiopoulos, G.K. Karagiannidis, and Christos S. Koukourlis. Performance analysis of M-ary PPM TH-UWB systems in the presence of MUI and timing jitter. *Selected Areas in Communications, IEEE Journal on*, 24(4):822–828, April 2006.
- [KMPK13] Alex Kushleyev, Daniel Mellinger, Caitlin Powers, and Vijay Kumar. Towards a swarm of agile micro quadrotors. *Autonomous Robots*, 35(4):287–300, 2013.
- [KNX⁺12] H. Khani, Hong Nie, Weidong Xiang, Zhimeng Xu, and Zhizhang Chen. Low complexity suboptimal monobit receiver for transmitted-reference impulse radio UWB systems. In *Global Communications Conference (GLOBECOM), 2012 IEEE*, pages 4084–4089, 2012.
- [KWA⁺04] J. Karedal, S. Wyne, P. Almers, F. Tufvesson, and A.F. Molisch. UWB channel measurements in an industrial environment. In *Global Telecommunications Conference, 2004. GLOBECOM '04. IEEE*, volume 6, pages 3511–3516, Nov 2004.
- [L. 04] L. Yang and G. B. Giannakis. Blind UWB timing with a dirty template. In *Acoustics, Speech, and Signal Processing, 2004. Proceedings. (ICASSP '04). IEEE International Conference on*, volume 4, pages 509–512, May 2004.
- [Lap92] G. Laporte. The traveling salesman problem: An overview of exact and approximate algorithms. *European Journal of Operational Research*, 59(2):231 – 247, 1992.
- [Law76] E. Lawler. *Combinatorial Optimization: Networks and Matroids*. Saunders College Publishing, Fort Worth, 1976.
- [Law85] Eugene Lawler. *The Traveling Salesman Problem: A Guided Tour of Combinatorial Optimization*. Wiley, New York, 1985.
- [LDM02] V. Lottici, A. D’Andrea, and U. Mengali. Channel estimation for ultra-wideband communications. *Selected Areas in Communications, IEEE Journal on*, 20(9):1638–1645, Dec 2002.
- [LG90] Lennart Ljung and Svante Gunnarsson. Adaptation and Tracking in System Identification - A survey. *Automatica*, 26(1):7 – 21, 1990.

- [LLH03] K.S. Low, K.M. Lye, and P.K.M. Ho. Method and apparatus for ultra wide-band communication system using multiple detectors, August 2003. US Patent 6,611,223.
- [LN04] J. Lerdworatawee and Won Namgoong. Low-noise amplifier design for ultrawideband radio. *Circuits and Systems I: Regular Papers, IEEE Transactions on*, 51(6):1075–1087, June 2004.
- [LNN61] F. C. Leone, L. S. Nelson, and R. B. Nottingham. The folded normal distribution. *Technometrics*, 3(4):543–550, 1961.
- [Lov79] L. Lovász. Combinatorial Problems and Exercises. *Akadémiai Kiadó, Budapest*, 1979.
- [LR03] Koen Langendoen and Niels Reijers. Distributed localization in wireless sensor networks: a quantitative comparison. *Computer Networks*, 43(4):499 – 518, 2003. Wireless Sensor Networks.
- [LT02] W.M. Lovelace and J.K. Townsend. The effects of timing jitter and tracking on the performance of impulse radio. *Selected Areas in Communications, IEEE Journal on*, 20(9):1646–1651, Dec. 2002.
- [Lue12] Luecken. *Communication and Localization in UWB Sensor Networks*. PhD thesis, ETH ZURICH, 2012.
- [MASL⁺09] J. Meng, J. Ahmadi-Shokouh, H. Li, E. J. Charlson, Z. Han, S. Noghanian, and E. Hossain. Sampling rate reduction for 60 GHz UWB communication using compressive sensing. In *Signals, Systems and Computers, 2009 Conference Record of the Forty-Third Asilomar Conference on*, pages 1125–1129, Nov 2009.
- [MCC⁺04] A.F. Molisch, D. Cassioli, C.C. Chong, S. Emami, A. Fort, B. Kannan, J. Karedal, J. Kunisch, H.G. Schantz, and K. Siwiak. IEEE channel model - Final report. <http://ieee802.org/15/pub/TG4a.html>, Sep 2004.
- [MG07] R. Kohno M. Ghavami, L.B. Michael. *Ultra Wideband Signals and Systems in Communication Engineering*. John Wiley, West Sussex, UK, 2007.
- [MGF⁺05] F. Mondada, L.M. Gambardella, D. Floreano, S. Nolfi, J.-L. Deneuborg, and M. Dorigo. The cooperation of swarm-bots: physical interactions in collective robotics. *Robotics Automation Magazine, IEEE*, 12(2):21–28, June 2005.
- [MGK02] L. B. Michael, M. Ghavami, and R. Kohno. Multiple pulse generator for ultra-wideband communication using Hermite polynomial based orthogonal pulses. In *Ultra Wideband Systems and Technologies, 2002. Digest of Papers. 2002 IEEE Conference on*, pages 47–51, May 2002.

- [Mol05] A.F. Molisch. Ultrawideband propagation channels-theory, measurement, and modeling. *Vehicular Technology, IEEE Transactions on*, 54(5):1528–1545, 2005.
- [MS06] M. Molins and M. Stojanovic. Slotted FAMA: a MAC protocol for underwater acoustic networks. In *OCEANS 2006 - Asia Pacific*, pages 1–7, May 2006.
- [MSR15] G.R. Maccartney, M.K. Samimi, and T.S. Rappaport. Exploiting directionality for millimeter-wave wireless system improvement. In *Communications (ICC), 2015 IEEE International Conference on*, pages 2416–2422, June 2015.
- [Mur16] B. Murmann. ADC Performance Survey 1997-2014. <http://web.stanford.edu/murmann/adcsurvey.html>, 2016.
- [MVV11] S.Y. Monir Vaghefi and R.M. Vaghefi. A novel multilayer neural network model for TOA-based localization in wireless sensor networks. In *Neural Networks (IJCNN), The 2011 International Joint Conference on*, pages 3079–3084, July 2011.
- [MXCZ08] X. P. Mao, K. Xu, B. Cao, and Q. Y. Zhang. A Nonuniform Low Sampling Rate Receiver in UWB Communications. In *Wireless Communications and Mobile Computing Conference, 2008. IWCMC '08. International*, pages 831–836, Aug 2008.
- [Nag07] P. Nagvanshi. *Analysis of multiple antenna ultra-wideband and millimeter wave communication systems*. PhD thesis, University of California, San Diego, 2007.
- [Nam03] Won Namgoong. A channelized digital ultrawideband receiver. *Wireless Communications, IEEE Transactions on*, 2(3):502–510, May 2003.
- [NBC02] P.P. Newaskar, R. Blazquez, and A.P. Chandrakasan. A/D precision requirements for an ultra-wideband radio receiver. In *Signal Processing Systems, 2002. (SIPS '02). IEEE Workshop on*, pages 270–275, Oct 2002.
- [NJ07] T. Nagayama and B.F. Spencer Jr. Structural health monitoring using smart sensors. Technical report, NSEL Report, Series 001, 2007. [online] Available : <http://hdl.handle.net/2142/3521>.
- [NMBH13] C. Nader, W. Van Moer, N. Björzell, and P. Händel. Wideband radio frequency measurements: From instrumentation to sampling theory. *IEEE Microwave Magazine*, 14(2):85–98, March 2013.

- [NP09] H. Nikookar and R. Prasad. *Introduction to Ultra Wideband for Wireless Communications*. Signals and Communication Technology Series. Springer, London, 2009.
- [NRP⁺05] J. Nembrini, N. Reeves, E. Poncet, A. Martinoli, and A. Winfield. Mascarillons: flying swarm intelligence for architectural research. In *Swarm Intelligence Symposium, 2005. SIS 2005. Proceedings 2005 IEEE*, pages 225–232, June 2005.
- [NZSH13] J.O. Nilsson, D. Zachariah, I. Skog, and P. Händel. Cooperative localization by dual foot-mounted inertial sensors and inter-agent ranging. *EURASIP Journal on Advances in Signal Processing* 2013, Dec. 2013:164–174, 2013.
- [OB05] Ian D. O'Donnell and R.W. Brodersen. An ultra-wideband transceiver architecture for low power, low rate, wireless systems. *Vehicular Technology, IEEE Transactions on*, 54(5):1623–1631, Sep 2005.
- [Orn20] Aaron Michael Orndorff. Transceiver Design for Ultra-Wideband Communications. Master's thesis, Electrical and Computer Engineering, Virginia Polytechnic Institute and State University, 2004-05-20.
- [PAW07] J.L. Paredes, G.R. Arce, and Z. Wang. Ultra-Wideband Compressed Sensing: Channel Estimation. *Selected Topics in Signal Processing, IEEE Journal of*, 1(3):383–395, Oct 2007.
- [Per94] Jukka Perttunen. On the Significance of the Initial Solution in Travelling Salesman Heuristics. *The Journal of the Operational Research Society*, 45(10):1131–1140, 1994.
- [PH96] R. Prasad and S. Hara. An overview of multi-carrier CDMA. In *Spread Spectrum Techniques and Applications Proceedings, 1996., IEEE 4th International Symposium on*, volume 1, pages 107–114 vol.1, Sep 1996.
- [PP02] Athanasios Papoulis and S Unnikrishna Pillai. *Probability, random variables, and stochastic processes*. Tata McGraw-Hill Education, 2002.
- [PR14] Dan Shan Paul Richardson, Weidong Xiang. UWB outdoor channel environments: analysis of experimental data collection and comparison to IEEE 802.15.4a UWB channel model. *International Journal of Ultra Wideband Communications and Systems*, 3(1), 2014.
- [PSJ04] Santashil PalChaudhuri, Amit Kumar Saha, and David B. Johnson. Adaptive clock synchronization in sensor networks. In *Proceedings of the 3rd International Symposium on Information Processing in Sensor Networks*, IPSN '04, pages 340–348, New York, NY, USA, 2004. ACM.

- [PZD⁺14] B. Panzner, W. Zirwas, S. Dierks, M. Lauridsen, P. Mogensen, K. Pajukoski, and Deshan Miao. Deployment and implementation strategies for massive MIMO in 5G. In *Globecom Workshops (GC Wkshps), 2014*, pages 346–351, Dec. 2014.
- [Rap09] T.S. Rappaport. *Wireless Communications: Principles and Practice*. Prentice Hall communications engineering and emerging technologies series. Dorling Kindersley, 2009.
- [Ree93] C.R. Reeves, editor. *Modern Heuristic Techniques for Combinatorial Problems*. John Wiley & Sons, Inc., New York, NY, USA, 1993.
- [RFSL15] H. Ramezani, F. Fazel, M. Stojanovic, and G. Leus. Collision Tolerant and Collision Free Packet Scheduling for Underwater Acoustic Localization. *IEEE Transactions on Wireless Communications*, 14(5):2584–2595, May 2015.
- [RHFME10] J. Rantakokko, P. Handel, M. Fredholm, and F. Marsten-Eklöf. User requirements for localization and tracking technology: A survey of mission-specific needs and constraints. In *Indoor Positioning and Indoor Navigation (IPIN), 2010 International Conference on*, pages 1–9, 2010.
- [RLK⁺09] Ill-Keun Rhee, Jaehan Lee, Jangsub Kim, Erchin Serpedin, and Yik-Chung Wu. Clock Synchronization in Wireless Sensor Networks: An Overview. *Sensors*, 9(1):56–85, 2009.
- [ROD06] A. Rabbachin, I. Oppermann, and B. Denis. ML Time-of-Arrival estimation based on low complexity UWB energy detection. In *Ultra-Wideband, The 2006 IEEE 2006 International Conference on*, pages 599–604, Sept 2006.
- [Ros73] G. F. Ross. Transmission and reception system for generating and receiving base-band duration pulse signals without distortion for short base-band pulse communication system. U.S. Patent 3,728,632, April 1973.
- [RP89] R. Ramaswami and K.K. Parhi. Distributed scheduling of broadcasts in a radio network. In *INFOCOM '89. Proceedings of the Eighth Annual Joint Conference of the IEEE Computer and Communications Societies. Technology: Emerging or Converging, IEEE*, pages 497–504, April 1989.
- [RRS⁺11] J. Rantakokko, J. Rydell, P. Strömbäck, P. Händel, J. Callmer, D. Tornqvist, F. Gustafsson, M. Jobs, and M. Gruden. Accurate and reliable soldier and first responder indoor positioning: multisensor systems and cooperative localization. *Wireless Communications, IEEE*, 18(2):10–18, Apr. 2011.

- [RSL77] D. J. Rosenkrantz, R. E. Stearns, and P. M. Lewis. An Analysis of Several Heuristics for the Traveling Salesman Problem. *SIAM Journal on Computing*, 6(3):563–581, 1977.
- [RSM⁺13] T.S. Rappaport, Shu Sun, R. Mayzus, Hang Zhao, Y. Azar, K. Wang, G.N. Wong, J.K. Schulz, M. Samimi, and F. Gutierrez. Millimeter Wave Mobile Communications for 5G Cellular: It Will Work! *Access, IEEE*, 1:335–349, 2013.
- [RvdV15] R.T. Rajan and A.J. van der Veen. Joint Ranging and Synchronization for an Anchorless Network of Mobile Nodes. *Signal Processing, IEEE Transactions on*, 63(8):1925–1940, April 2015.
- [Saa97] Saarnisaari, H. TLS-ESPRIT in a time delay estimation. In *Vehicular Technology Conference, 1997, IEEE 47th*, volume 3, pages 1619–1623, May 1997.
- [Sch93] R.A. Scholtz. Multiple access with time-hopping impulse modulation. In *Military Communications Conference, 1993. MILCOM '93. Conference record. Communications on the Move., IEEE*, volume 2, pages 447–450 vol.2, 1993.
- [SDAH11] Dino Strömberg, Alessio De Angelis, and Peter Händel. A Low-Complexity Adaptive-Threshold Detector for Pulse UWB Systems. In *Int. Workshop ADC Modelling, Testing Data Converter Analysis Design/IEEE.*, 2011.
- [SGI08] Z. Sahinoglu, S. Gezici, and G. Ismail. *Ultra-wideband Positioning Systems: Theoretical Limits, Ranging Algorithms, and Protocols*. Cambridge University Press, New York, 2008.
- [SGP11] H. Soganci, S. Gezici, and H.V. Poor. Accurate positioning in ultra-wideband systems. *Wireless Communications, IEEE*, 18(2):19–27, April 2011.
- [SHN03] A Saito, H. Harada, and A Nishikata. Development of band pass filter for ultra wideband (UWB) communication systems. In *Ultra Wideband Systems and Technologies, 2003 IEEE Conference on*, pages 76–80, Nov 2003.
- [SJ01] Park Soonchul and Lim Jaesung. A Parallel Transmission Scheme for All-to-All Broadcast in Underwater Sensor Networks. *IEICE Transactions on Communications*, Vol.E93-B(9):2309–2315, 2010/09/01.
- [Sko08] M. Skolnik. *Radar Handbook, Third Edition*. Electronics electrical engineering. McGraw-Hill Education, New York, USA, 2008.

- [SV87] A.A.M. Saleh and R.A. Valenzuela. A Statistical Model for Indoor Multipath Propagation. *Selected Areas in Communications, IEEE Journal on*, 5(2):128–137, February 1987.
- [SVC09] S. Shahramian, S. P. Voinigescu, and A. C. Carusone. A 35-GS/s, 4-Bit Flash ADC With Active Data and Clock Distribution Trees. *IEEE Journal of Solid-State Circuits*, 44(6):1709–1720, June 2009.
- [TAW05] F. Troesch, F. Althaus, and A. Wittneben. Pulse position precoding exploiting UWB power constraints. In *Signal Processing Advances in Wireless Communications, 2005 IEEE 6th Workshop on*, pages 395–399, 2005.
- [Tdm16] *Time Domain PulsON (P400) Ranging and Communications Module (RCM)*. [Online]. Available: <http://www.timedomain.com>, 2016.
- [TMR11] E. Torkildson, U. Madhow, and M. Rodwell. Indoor millimeter wave mimo: Feasibility and performance. *Wireless Communications, IEEE Transactions on*, 10(12):4150–4160, December 2011.
- [Tra16] *TransferJet Overview Whitepaper* [online]. Available: <http://www.transferjet.org/tj/transferjetwhitepaper.pdf>, 2016.
- [Tur60] G.L. Turin. An introduction to matched filters. *Information Theory, IRE Transactions on*, 6(3):311–329, June 1960.
- [Ubi16] *The Series 7000 Ubisense UWB sensors*. [Online]. Available: <http://www.ubisense.net/>, 2016.
- [Urk67] Harry Urkowitz. Energy detection of unknown deterministic signals. *Proceedings of the IEEE*, 55(4):523–531, April 1967.
- [Vit95] Andrew J. Viterbi. *CDMA: Principles of Spread Spectrum Communication*. Addison-Wesley, 1995.
- [VT04] Harry L Van Trees. *Detection, estimation, and modulation theory*. John Wiley & Sons, 2004.
- [Wan11] T. Wang. Adaptive UWB Pulse Allocation for Distributed Detection in Sensor Networks. *Communications, IEEE Transactions on*, 59(5):1357–1367, May 2011.
- [WLD14] Y. Wang, G. Leus, and H. Delic. Time-of-arrival estimation by UWB radios with low sampling rate and clock drift calibration. *Signal Processing*, 94:465 – 475, 2014.
- [WLJ⁺09a] K. Witrisal, G. Leus, G. Janssen, M. Pausini, F. Troesch, T. Zasowski, and J. Romme. Noncoherent ultra-wideband systems. *Signal Processing Magazine, IEEE*, 26(4):48–66, July 2009.

- [WLJ⁺09b] K. Witrisal, G. Leus, G. J M Janssen, M. Pausini, F. Troesch, T. Zaslowski, and J. Romme. Noncoherent ultra-wideband systems. *Signal Processing Magazine, IEEE*, 26(4):48–66, 2009.
- [WLW09] H. Wymeersch, J. Lien, and M.Z. Win. Cooperative Localization in Wireless Networks. *Proceedings of the IEEE*, 97(2):427–450, Feb 2009.
- [WS98] M.Z. Win and R.A. Scholtz. Impulse radio: how it works. *Communications Letters, IEEE*, 2(2):36–38, Feb 1998.
- [WS00] M.Z. Win and R.A. Scholtz. Ultra-wide bandwidth time-hopping spread-spectrum impulse radio for wireless multiple-access communications. *Communications, IEEE Transactions on*, 48(4):679–689, 2000.
- [WS02] M.Z. Win and R.A. Scholtz. Characterization of ultra-wide bandwidth wireless indoor channels: a communication-theoretic view. *Selected Areas in Communications, IEEE Journal on*, 20(9):1613–1627, Dec 2002.
- [WWZ14] Q. Wan, Q. Wang, and Z. Zheng. Design and analysis of a 3.1-10.6 GHz UWB low noise amplifier with forward body bias technique. *AEU - International Journal of Electronics and Communications*, 9(1):119–125, Jan 2014.
- [XF12] Lv. X. and Bai. F. Review of Ultra-Wideband Communication Technology Based on Compressed Sensing . *Procedia Engineering* , 29:3262 – 3266, 2012. 2012 International Workshop on Information and Electronics Engineering.
- [Xin04] Xinrong Li and Pahlavan, K. Super-resolution TOA estimation with diversity for indoor geolocation. *Wireless Communications, IEEE Transactions on*, 3(1):224–234, Jan 2004.
- [YDAH13] V. Yajnanarayana, S. Dwivedi., A. De Angelis, and P. Händel. Design of impulse radio UWB transmitter for short range communications using PPM signals. In *Electronics, Computing and Communication Technologies (CONECCT), 2013 IEEE International Conference on*, pages 1–4, 2013.
- [YDAH14] V. Yajnanarayana, S. Dwivedi, A. De Angelis, and P. Händel. Spectral efficient IR-UWB communication design for low complexity transceivers. *EURASIP Journal on Wireless Communications and Networking*, 2014:158(1):1–13, 2014.
- [YDH14] V. Yajnanarayana, S. Dwivedi, and P. Händel. Design of impulse radio UWB transmitter with improved range performance using PPM

- signals. In *Electronics, Computing and Communication Technologies (IEEE CONECCT), 2014 IEEE International Conference on*, pages 1–5, Jan 2014.
- [YDH16] V. Yajnanarayana, S. Dwivedi, and P. Händel. IR-UWB detection and fusion strategies using multiple detector types. In *2016 IEEE Wireless Communications and Networking Conference (WCNC)*, pages 1–6, April 2016.
- [YGCZ03] R. Yao, G. Gao, Z. Chen, and W. Zhu. UWB multipath channel model based on time-domain UTD technique. In *Global Telecommunications Conference, 2003. GLOBECOM '03. IEEE*, volume 3, pages 1205–1210, Dec 2003.
- [YH02] Lie-Liang Yang and L. Hanzo. Residue number system assisted fast frequency-hopped synchronous ultra-wideband spread-spectrum multiple-access: a design alternative to impulse radio. *Selected Areas in Communications, IEEE Journal on*, 20(9):1652–1663, 2002.
- [YH16] V. Yajnanarayana and P. Händel. Compressive Sampling Based UWB TOA Estimator. *CoRR*, abs/1602.08615, 2016.
- [YZC03] R. Yao, W. Zhu, and Z. Chen. An efficient time-domain ray model for UWB indoor multipath propagation channel. In *Vehicular Technology Conference, 2003. VTC 2003-Fall. 2003 IEEE 58th*, volume 2, pages 1293–1297, Oct 2003.
- [Zac13] D. Zachariah. *Estimation for Sensor Fusion and Sparse Signal Processing*. PhD thesis, KTH Royal Institute of Technology, 2013.
- [ZADH13] D. Zachariah, A. De Angelis, S. Dwivedi, and P. Händel. Self-localization of asynchronous wireless nodes with parameter uncertainties. *IEEE Signal Processing Letters*, 20(6):551–554, June 2013.
- [ZNCO⁺14] Y. Zahedi, R. Ngah, U.A.K. Chude-Okonkwo, S. Nunoo, and M. Mokayef. Modeling the RMS delay spread in time-varying UWB communication channels. In *Intelligent and Advanced Systems (ICIAS), 2014 5th International Conference on*, pages 1–5, June 2014.
- [ZOS⁺09] J. Zhang, P.V. Orlik, Z. Sahinoglu, A.F. Molisch, and P. Kinney. UWB Systems for Wireless Sensor Networks. *Proceedings of the IEEE*, 97(2):313–331, 2009.
- [ZSM05] L. Zhu, S. Sun, and W. Menzel. Ultra-wideband (UWB) bandpass filters using multiple-mode resonator. *Microwave and Wireless Components Letters, IEEE*, 15(11):796–798, Nov 2005.

- [ZSZ10] Anfu Zhu, Fu Sheng, and Anxue Zhang. An implementation of step recovery diode-based UWB pulse generator. In *Ultra-Wideband (ICUWB), 2010 IEEE International Conference on*, volume 2, pages 1–4, 2010.